Radiation Damage on Multiple Length Scales in Uranium Dioxide

Mahima Gupta

A dissertation submitted in partial fulfillment of the requirements for the degree of

Doctor of Philosophy

(Nuclear Engineering and Engineering Physics)

At the

University of Wisconsin-Madison

2015

Date of Final Oral Examination: 4/20/2015

This dissertation was approved by following members of the oral committee
Dr. Todd Allen, Nuclear Engineering and Engineering Phyiscs
Dr. Michael Corradini, Nuclear Engineering and Engineering Phyiscs
Dr. James Blanchard, Nuclear Engineering and Engineering Phyiscs
Dr. Kumar Sridharan, Nuclear Engineering and Engineering Phyiscs
Dr. Paul Evans, Material Science and Engineering

Contents

List of Figures

List of Tables

Acknowledgements

First and foremost, I would like to thank Dr. Todd Allen, who has been a mentor, a friend and an inspiration over the course of my Ph.D. I am grateful for all of our conversations (except the baseball related ones) and for all the guidance he has provided me. This work would have been impossible without Dr. Allen's support and continued participation in my thesis. I am glad to have a rockstar of an adviser! Secondly, I would like to thank Dr. Steven Conradson, who has mentored me over the last 3 years in performing and understanding EXAFS experiments and calculations. He is a "behind the scene" adviser and has always been there to answer my simplest questions. I would also like to thank Dr. Kumar Sridharan for his guidance during this thesis.

During the last two years, I have been an intern at the Idaho National Laboratory at the Materials and Fuels Complex and at the Center for Advanced Energy Studies. This wouldn't have been possible without my mentors Dr. James Cole and Dan Ogden who have consistently supported my research endeavors and helped with all my work at CAES. I would also like to thank Dr. Jian Gan and Dr. Brandon Miller for their insightful suggestions. At CAES, Joanna Taylor, Jatu Burns and Bryan Forsmann have been incredibly kind for working with my schedule to help with sample prep and analysis. Also, I would also like to specially thank Taylor Dressen for helping me with IT problems on my INL laptop that occurred almost every single day. I couldn't have done this without the support of the CAES family.

Janne Pakarinen and Lingfeng He have been incredible colleagues and mentors during the last few years at the University of Wisconsin. Both Janne and Lingfeng have patiently worked with me on this research project, helping me all along the way. I couldn't have

asked for better colleagues, who are also good friends. I would specially like to thank Beata Tyburska-Puschel who is a great friend and an excellent scientist. She has conducted two ion irradiations on my behalf and helped with sample handling at University of Wisconsin, while I was at the INL. I would also like to thank Kim Kriewaldt and Ben Maier for their help with ion irradiations and Bob Agasie for helping with shipping and handling of my radioactive samples.

Technically, none of this would have been possible without my parents, had they not had me. So big thanks to my parents. Jokes aside, they have been incredibly understanding, supportive and loving throughout my thesis work and I am very grateful to have such an amazing family cheering for me all the way from India. Their resistance to using technology and my resistance to answering cell phone calls makes for complicated communication, but we have still managed to share a unique bond of love, respect and friendship that is becoming more special with time.

Lastly, I would like to thank my partners in crime: Justin Ammerlaan and Snow Gupta. Adopting Snow is easily the best decision I have made. She is the best dog in the world, the fastest running buddy and has patiently listened to all my research presentations. Justin has been my best friend, my ski and rock climbing buddy and my biggest supporter throughout my thesis. From discussions on oxygen interstitials to parallel universes to drinking copious amounts of wine on a Tuesday night, Justin has been the best partner I could have asked for. Words don't do justice to how much I appreciate all that Justin has done for me in the last three years. Therefore, this thesis is dedicated to him.

1 Introduction

The properties of ceramic nuclear fuel, UO_2, are crucial to the fleet of current and future nuclear power plants operating globally. As the primary nuclear fuel, UO_2 has been extensively studied through the years to determine its optimum design and enrichment to cope with high temperatures and degrading radiation environment. Despite large empirical databases for UO_2, there is a lack of scientific understanding of its property evolution under irradiation. This document will enrich the scientific basis of radiation induced damage formation in UO_2, the ultimate goal being the understanding of the irradiation microstructure evolution starting from the point defect scale. Irradiation damage in UO_2 resulting from ion irradiations has been characterized using a combination of state-of-the-art theoretical and experimental methods. Ultimately, this study provides a novel explanation for formation of defect structures on multiple length scales using H^+, He^{2+} and Kr ion irradiations.

Radiation damage in UO_2 has been well studied but there exists little correlation between point defect accumulation, lattice structure changes and microstructure. This is partly because irradiated nuclear fuel is highly radioactive and its defect chemistry is extremely complicated resulting from fission of the material and consequent fission products being embedded in the fuel matrix [66]. To adequately study the evolution of defects from point defects through to microstructure features, the resulting defects have to be intentionally simplified for characterization. Ion accelerators have the unique capability of creating simple microstructure features using specific ions, without the added complication of fission and neutron activation from nuclear reactors. As an example, H^+ ions have been used to create (only) a distribution of dislocations that were studied using various techniques. The ability

to tune the energy or type of the ion to achieve desirable implantation depth and ideally simple microstructure renders it a lucrative instrument for this type of analysis.

X-ray diffraction (XRD) studies and transmission electron microscopy (TEM) have been utilized to study extended structure changes and microstructure evolution. Ion beam irradiations create displacements and displacement networks, voids, surface fracturing, gas bubbles and several other microstructure changes to model nuclear reactor damage [65]. Using an ion accelerator, it has been possible to isolate these radiation induced defects and study their subsequent evolution with increasing dose. Insofar, since all of the phenomena caused by radiation damage originate from point defects, the elucidation of radiation effects on the atomic scale is crucial. This is rendered complicated due to aperiodic irradiation defects. This lack of periodicity renders standard approaches, such as TEM and XRD ineffective, as these methods probe average structure over tens of Angstroms. Therefore, techniques that are sensitive to short range order are required to understand the defect detail on atomic scale. X-ray absorption fine structure spectroscopy (XAFS) measures the population-weighted local structure and chemical speciation of the examined elements making it perhaps the most incisive method for determining the local range order in irradiated materials. In this study, Extended X-ray Absorption Fine Structure (EXAFS) measurements have shed significant insight into the local chemistry evolution from irradiation damage in UO_2.

With the aforementioned defect characterization techniques, this project has developed three significant scientific conclusions:

1. Irradiation of UO_2 creates changes with some similarity to oxidation, but the increase in lattice parameter (as compared to oxidation) indicates differences in microstructure.

2. TEM invisible defect clusters are predominantly responsible for lattice structure changes in UO_2, confirmed using EXAFS and Cluster Dynamics simulation.

3. The combination of EXAFS, Cluster Dynamics, CrystalMaker Analysis, MD and Raman measurements support the existence of hyper and hypo-stoichiometric regions in the material after irradiations.

4. The lattice parameter, the microstructure visible to TEM and the lattice structure invisible to TEM all scale with DPA.

2 Background

2.1 Introduction to our Material: Uranium Dioxide (UO_2)

Because of its role as nuclear fuel uranium dioxide continues to be of scientific and technological interest [2]. The fission of uranium dioxide produces fragments or daughter nuclei that carry the original nuclear energy as kinetic energy that is subsequently transformed into heat as they collide with neighboring atoms. These collisions of the heavy fission products, unlike collisions with lighter particles, displace lattice atoms from their positions in the crystal lattice. Although, almost all of these displaced atoms return to lattice sites restoring the crystal structure, a small number do not [7]. This results in small, local defects such as Frenkel pairs of vacancies and interstitials that accompany the irreversible defects caused by the forced incorporation of the fission products into the UO_2 lattice. Nuclear burn differs from other forms of combustion in that its products remain in the fuel instead of being expelled in an exhaust stream. As these point defects accumulate over time, the stresses they induce in combination with others originating in the thermal gradient across the fuel element, trigger the irreversible formation of larger scale damage structures such as voids and dislocation loops [66]. This inhibits the recombination of their constituent atomic scale defects. Ultimately these microscopic radiation effects and the larger scale damage, such as cracking, to which they contribute, reduce the thermal conductivity and overall performance of the fuel pellets.

As fission causes damage in the fuel material, it is crucial to understand the underlying mechanisms that govern the lattice damage, recovery and its susceptibility to various extreme environments. The overview of these underlying mechanisms starts with the atomic structure of UO_2. This gives insight into its complex geometry and structure, that has a high

propensity to exist as a hyperstoichiometric oxide [57]. The atomic level interactions that render UO_2 off stoichiometric are a result of electronic processes due to uranium's partially filled 5f orbital [101]. The complexities regarding the electronic properties are yet to be fully characterized but are nonetheless discussed in this study.

Uranium dioxide is one of the most complex oxide materials due to the unstable stoichiometry resulting from rapid and reversible oxygen ion mobility [36]. As the most commonly used nuclear fuel, there has been significant research to understand defect structure in the UO_2 complex, following nuclear reactor irradiation. Characterization of UO_2 stoichiometry has been undertaken since the 1960s and is still far from complete [95]. Although uranium dioxide is UO_2 in composition and fluorite in structure, it almost always demonstrates a higher degree of oxidation, i.e., UO_{2+x} **[14]**. The presence of UO_2 in atmosphere results in oxidation of the material due to its negative oxygen interstitial formation energy and therefore, it exists as UO_{2+x} **[57]**. Uranyl ion, UO_{2+x}, is similar to a smaller divalent metal ion. The phase digram of UO_2 is shown in Fig. 2 and shows that the UO_{2+x} phase is stable at room temperature.

2.2 Atomic and Electronic Structure of UO_2

2.2.1 Atomic Structure of UO_2

Aside from its application as a fuel for nuclear reactors, UO_2 has unique properties as an actinide oxide and is used as a catalyst in chemical processes due to uranium's delocalized f and d shell electrons [78]. Structurally, UO_2 is a fluorite and has a face centered cubic (FCC) structure shown in Fig.1, similar to calcium fluorite (CaF_2) and an $Fm\bar{3}m$ space

group [98]. In FCC structure, oxygen fills the tetrahedral interstices of the close-packed cation sub-lattice of uranium. This results in a cubic arrangement of oxygen atoms with uranium atoms placed between the cubes. The lattice parameter of UO_2 is subsequently 5.47 Å [67].

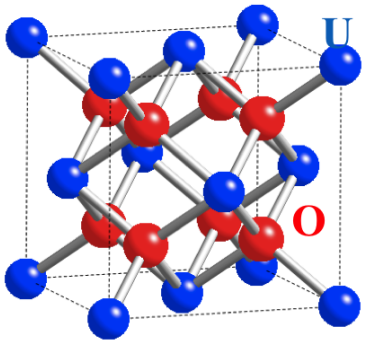

Figure 1: Face Centered Cubic Structure of UO_2

Several crystalline phases of UO_2 exist at varying temperatures and partial pressures of oxygen [3]. The knowledge of these phases is key to understanding chemistry of the nuclear fuel during reactor operation as it is subjected to a range of temperatures during fission (800-1600 K) and oxygen partial pressures. The phase diagram for various UO_2 phases is shown in Fig. 2. Stoichiometry evolution in the nuclear reactor is further controlled by the constantly evolving chemistry resulting from fission of the uranium nucleus [72]. While the uranium atom fissions, and effectively decreases in concentration, the oxygen atoms remain relatively constant in the reactor fuel. The resulting UO_{2+x} stoichiometry requires the uranium atom

to have multiple bonds with existing oxygen atoms, thereby complicating the fuel material structure. The resulting complex molecules of U and O have a larger ionic charge due to excess electrons in the system [76]. This can serve as a ligand to electron deficient fission products and form complex species that have proven difficult to separate in used nuclear fuel processing [83]. Therefore, structure evolution following irradiation in a nuclear reactor is crucial to stability of the final used nuclear fuel, especially in case of extended storage at reactor sites.

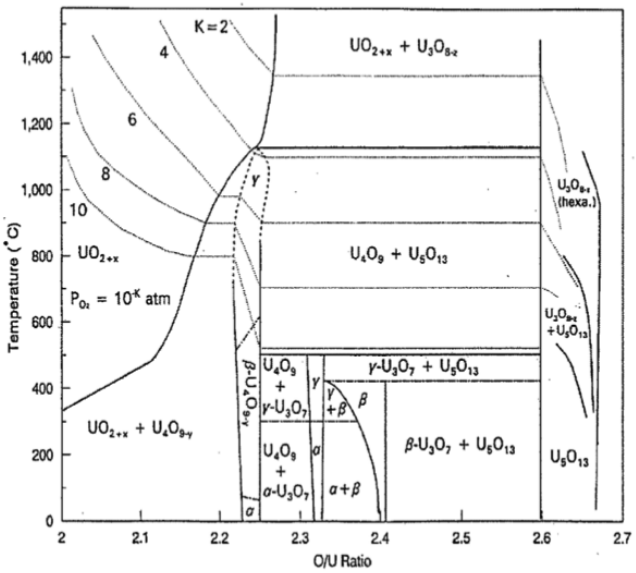

Figure 2: UO_2 phase diagram [60]

A remarkable property of UO_2 is the process of accommodation of excess oxygen ions in the lattice, which doesn't distort the lattice structure and the U sublattice maintains its

original FCC geometry [79]. The oxidation mechanism in UO_2 has been understood to result from formation of oxygen interstitials leading to a cuboctohedral type (COT) structure [95]. The oxygen atoms migrate into the UO_2 lattice as clusters and further displace the existing O atoms from their sites and it is widely accepted that the presence of oxygen clusters is energetically more favorable for the lattice than individual oxygen interstitials [**?**]. This mechanism was theorized by BTM Willis in the 1960s and has been well understood since then and widely used in several studies aiming at understanding the UO_{2+x} chemistry. Willis Structure, Fig. 3: explains the formation of oxygen cluster in UO_2 resulting from 2 oxygen interstitials, 2 displaced oxygen ions and resulting 2 vacancies. The interstitial oxygen ions are displaced from their (1/2, 1/2, 1/2) position along [110] axis and lattice oxygen are displaced along the [111] axis. This model is referred to as a 2:2:2 model [96]. Repeating this 2:2:2 cluster results in 4:3:2 and eventually higher defect cluster configurations.

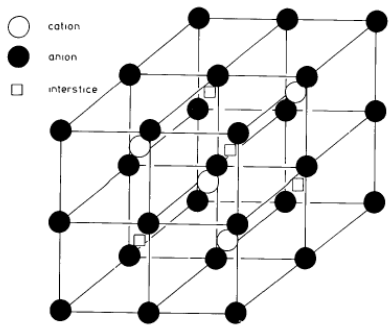

Fig. 1. Unit cell of UO_2 showing the cubic-coordinated cation sites, the tetrahedrally coordinated anion sites, and the cubic-coordinated interstitial sites.

Figure 3: Willis structure showing the 2:2:2 oxygen cluster in UO_{2+x} [95]

Understanding the changes in stoichiometry is crucial in a non-stoichiometric material such as UO_2 since, with increasing 'x' in UO_{2+x} from UO_2 to U_3O_8 to final UO_3, thermal conductivity of the material decreases [29]. This attribute can be related to the partially filled 5f orbital in uranium, which plays a significant role in determining thermal transport and local structure changes resulting from irradiation [54].

U-O is one of the most complicated binary systems known. At least 16 distinct crystallographic phases of uranium oxides from U(IV)O_2 to U(VI)O_3 have been reported, with some groups counting more [3]. It demonstrates negative oxygen interstitial formation energy [37], resulting in the formation of UO_{2+x} with x ranging from 0 to somewhere between 0.33 and 0.5, with U_2O_3 forming below the lower boundary and layered U_3O_8 above the upper. Well below the superionic transition[46] where they become much less ordered because of their mobility, the adventitious O atoms are not randomly distributed but instead form clusters within the grains, giving crystallographically phase separated $UO_{2+\delta}$: $U_4O_{9-\delta}$ and $U_4O_{9+\delta}$:$U_3O_{7-\delta}$ mixtures [74, 6]. The U sublattice is conserved, with a $< 1\%$ contraction of U_4O_9 relative to UO_2 that is reversed, accompanied by a tetragonal distortion that can initially be -1% but after some time is $+2\%$, in U_3O_7 [19]. Because the equilibrium U:O ratio depends on the chemical potential, the $\geq$ 600-1000 K thermal gradient across the 5 mm radius of the fuel pellet of poorly conductive UO_2 causes thermomigration that establishes a parallel composition gradient, not only for O but for all of the fission products as well. This process plays a role in creating stresses in the material that ultimately degrades of its material properties.

The principal issue for UO_{2+x} has been the location and effects of the adventitious O.

This is intuitively relevant to the radiation damage problem because the interstitial atoms pose the same question as to where and how they reside in the lattice. The original proposal by Willis in 1964 [95] has been followed by a large number of both experimental and theoretical refinements. This model involves the addition of O into the cubic holes in the open fluorite structure accompanied by a concomitant displacement of one, or more recently two, neighboring O ions from their cube vertex positions to adjacent holes to give, respectively the cuboctahdedral or di-interstitial [4] type structures. Recent studies by Geng et al. suggest that di-interstitial clusters, which coalesce to form quad-interstitial oxygen clusters, have a higher stability than the postulated cuboctohedral ones [30]. These differ primarily in their long range order since the cuboctahedra are not only initially more regular but also easily maintain translational symmetry when extended [30]. Both, however, retain the U sublattice essentially intact. The near neighbor U-O distribution is single peaked with an average bond length still near 2.36 Å [5, 38], with the shortest U-O distance for the nine-coordinate U(V)-type sites still ~ 2.2 Å. Both models also utilize clustering of the adventitious O and consequent phase separation of UO_2 and $U_4O_{9-\delta}$ type domains and are therefore consistent with the observed behavior of the diffraction patterns and the interpretation that the O-enriched domains that grow as "x" increases are very similar to U_4O_9 [95].

These theories of COT type clusters were, however, contradicted by XAFS measurements that clearly showed a much broader U-O distribution extending to 1.7 Å, a bond length that is only consistent with uranyl type bonds [103]. The uranyl type bond exists as a trans dioxo consisting of two oxo groups double bonded to the uranium atom with a bond angle of approximately 180°. This group is highly symmetric resulting from the incorporation of O to the existing UO_2 molecule. Although the presence of uranyl has been attributed to

the formation of oxygen interstitial clusters resulting from oxidation of the material, the Extended X-ray Absorption Fine Structure (EXAFS) measurements on ion irradiated UO_2 have shown a similarly short U-O bond distance of ~1.9 Å. Further, the lack of additional oxygen atoms to account for this lattice disturbance are explained in this study. A recent study, however, explains that the formation of the defect cluster is contingent upon the oxygen concentration in the lattice [30]. The presence of COT clusters is then just as likely as quad-interstitial type defects and uranyl defects depending on the precise stoichiometry. Therefore, naturally occurring UO_{2+x} likely has a distribution of various types of oxygen defect clusters that are stable at their own equilibrium conditions. The geometry of the various oxygen defect clusters such as the COT cluster, the di-interstitial cluster and the split di-interstitial cluster (two of which make the split quad interstitial cluster) are shown in Fig. 4.

Atomic defects including point defects and clusters control diffusion properties and can accommodate fission products and lead to stoichiometry variations [20]. However, the defects on atomic scale to a large extent result from electronic interactions in UO_2 which are discussed in detail in the next section. While off-stoichiometric samples of UO_2 have been highly researched, there is very limited information on atomic defects in irradiated UO_2. Discussion of the results of UO_{2+x} species is pertinent to characterizing similar defect structure due to ion damage and also to explain any preexisting atomic phenomenon governing mechanics of defect interaction. The resulting atomic structure evolution from varying irradiation dose is key to understanding defect structure evolution in a nuclear reactor where several different ions constantly damage the nuclear fuel lattice.

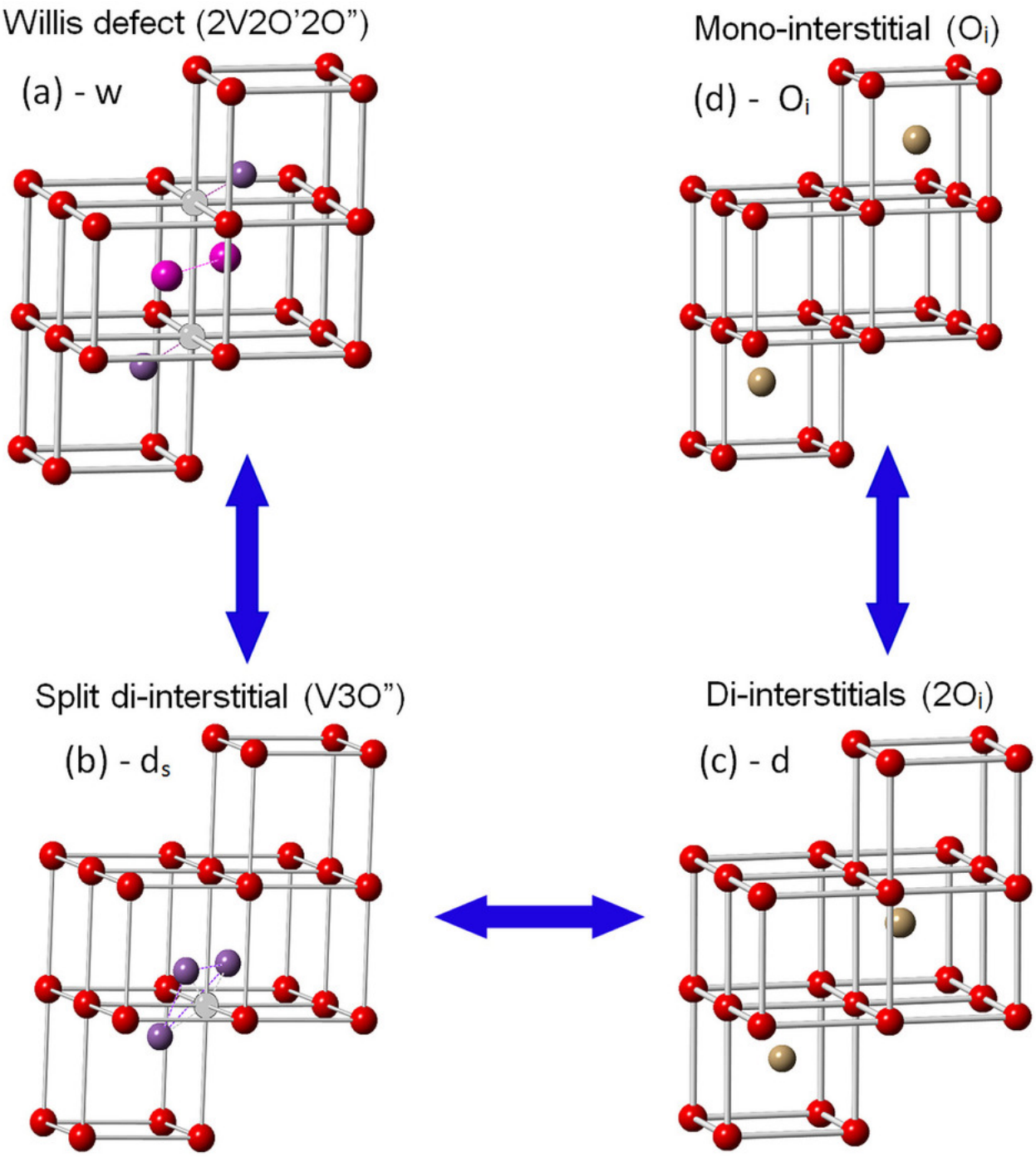

Figure 4: The Willis defect cluster (a) serves as a transition state for rapid diffusion of the split di-interstitial defect (b). The latter can also migrate through a di-interstitial (c). Di-interstitial can dissociate to two immobile mono-interstitials (d).

2.2.2 Electronic Structure of UO_2

A discussion of electronic structure of UO_2 properties help better explain electrical conductivity, chemistry and stoichiometry preferences. Uranium, like other actinide metals, is characterized by an incomplete 5f orbital, which provides the molecule it's magnetic properties. At 0 K, UO_2 is an insulator and at higher temperatures, it changes to a semi-conductor. Below its Neel temperature of 30 K, UO_2 exists as anti-ferromagnetic and for this reason it is referred to as a Mott-Hubbard insulator [82].

Actinide atoms have partially filled 5f orbital resulting in strong Coulomb repulsion in their outer electron shells [101]. To better model ground state characteristics of bulk materials, lattices, point defects and more in UO_2, Density functional theory (DFT), a quantum mechanical technique has been used. DFT is rather advanced compared to other existing techniques in the way that it considers the interacting electrons using a single electron density rather than utilizing many body wave functions. Localized density approximation (LDA) is used to estimate the electron correlation interaction but this cannot successfully describe the varying density changes. Generalized gradient density approximation includes the charge density gradient which describes the effect due to spatially varying charge density. DFT with LDA and GGA, despite their detailed electronic approximations, cannot completely describe the structure of strongly correlated materials including UO_2 [45].

A fully developed understanding of irradiation damage, including defect formation and migration, in UO_2 is incomplete without involving a first principles approach. Existing first principles density functional theory approximations utilize the localized density approximation (LDA) and the generalized gradient approximation (GGA), which have not been

able to account for strong correlations in the hybridized 5f electrons in uranium. Uranium is known to transition from antiferromagnetic state below 30 K to a ferromagnetic metallic state above that temperature. The existing LDA and GGA approximations have successfully predicted the presence of the ferromagnetic state but fail to account for the Mott-Hubbard insulator and antiferromagnetic behavior below 30 K. Therefore, there has been an effort to explain this strong correlation between 5f electrons by including a Hubbard-U (DFT+U and DFT+DMFT) term in recent calculations [24].

The DFT + U approximation (LDA + U or GGA + U) had an enhanced treatment of the strongly correlated 5f electrons by adding a correction term to the standard DFT term as

$$\mathrm{E}^{DFT+U} = \mathrm{E}^{DFT} + \mathrm{E}_{Hub} - \mathrm{E}_{dc}$$

In this equation, E_{DFT} is the standard DFT term with LDA and GGA components. E_{Hub} corrects for electron-electron interaction taking into consideration the higher correlations in electrons and is similar to the Hubbard U term and E_{dc} is the double counting correlation.

The partial and full density of states of the U 5f and O 2p orbitals are shown in Fig. 5 and it gives a different perspective on the electronic structure and the orbital interactions resulting in the specific UO_2 chemistry. In this figure, the flat bands appear from the U 5f orbitals implying that these 5f electrons are partially localized. Looking into this further, the top two valence bands appear more depressed than the unoccupied f bands with a band gap of approximately 2 eV. This shows that the U 5f orbitals may hybridize with neighboring atomic orbitals including in this case with the 2p orbital of oxygen. The

magnetic moments of UO_2 can be attributed to this split 5f band. Further, the wide band gap in UO_2 has characteristics of a semiconductor and has been probed via photo-excitation measurements [82]. These recent synchrotron diffraction measurements predict the formation of photo-stabilized ordered structures with domains similar to O-enriched domains in UO_{2+x} at low x, above ground state phonon density of states. This occurs due to the creation of quasiparticles called U (IV) oxo polarons, tunneling through the lattice to create aggregates of defect clusters, giving the properties of Bose-Einstein Condensates. Therefore, the density of states at and above 3 eV could result in the formation of stabilized oxo defect structures that are detected in synchrotron light source measurements.

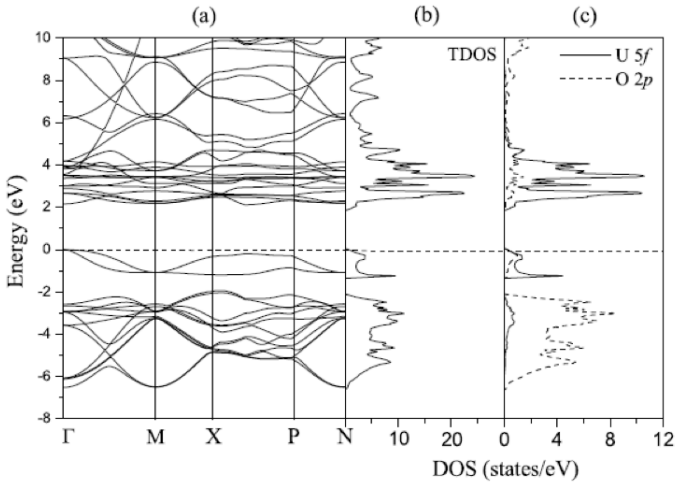

Figure 5: Density of State in UO_2 with (a) energy band structure, (b) the total density of states of UO_2 and (c) partial density of states of U $5f$ and O $2p$ orbitals [101]

LSDA + U calculations have predicted the predominance of oxygen related defects in UO_2 over uranium ones due to strong correlation in the uranium 5f electrons. Uranium defects result in increase in overall volume whereas oxygen defects result in reduction in volume in all but one type of defect structures [57], which is energetically more favorable for the lattice and reduces the overall lattice energy. Detailed DFT calculations suggest that hyperstoichiometry in UO_2 is due to the oxygen atoms migrating into the UO_2 lattice as clusters and further displacing the existing O atoms from their sites. Fig. 6 shows the various point defect formation energies in UO_2 where, the oxygen interstitial formation energy is consistently negative for all the unit cells used for computation.

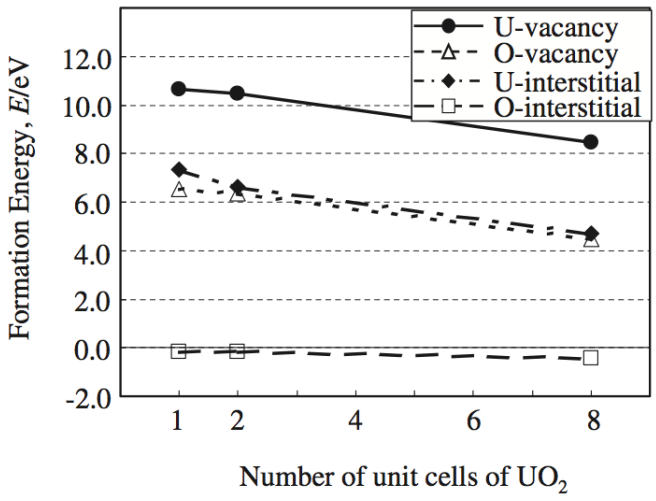

Figure 6: Formation energy in eV of various point defects in UO_2 in super cells of size U_4O_8, U_8O_{16} and $U_{32}O_{64}$ [57].

Andersson et al, studied oxygen clustering and migration mechanism in UO_2 using DFT calculations [5]. The previously postulated cuboctohedral oxygen clusters have shown to form higher density configurations similar to split quad interstitials which are stable in comparison to single oxygen interstitials in UO_{2+x}. Therefore, there is still an ongoing effort to fully understand the effect of oxygen mobility in crystalline UO_2 and in irradiated UO_2.

2.3 Radiation Defect Formation and Analysis

During nuclear reactor operation, the damage to the lattice structure of the internal reactor components is continuous and in many cases, results in irreversible non-equilibrium structures. Therefore, the study of radiation damage is crucial to fully understand the structural challenges and further, to find a way to engineer stronger, more radiation resistant components.

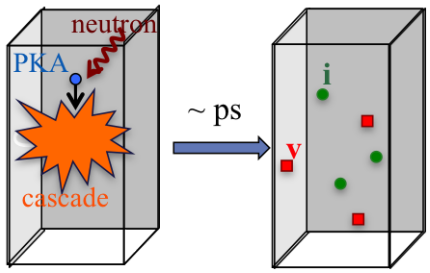

Figure 7: The process of damage cascade in the material due to neutron irradiation

Radiation damage occurs in a material when an incoming ion of sufficient energy interacts

with it, by imparting to the material the ion's energy and disturbing its original structure [11]. Defect formation from irradiation results in a chain reaction called damage cascade. The first lattice ion to start the damage cascade is termed the Primary Knock-on Atom (PKA), which in turn imparts its energy to further atoms in the lattice, which recursively start their own cascades. Fig 7. shows the process of a neutron creating a PKA and starting the damage cascade. The damage cascade results in displaced lattice atoms known as interstitials and the resulting vacant sites of these atoms are called vacancies. This pair of an interstitial and a vacancy is known as a Frenkel disorder (or a Frenkel pair). Another type of defect resulting from vacancies is a Schottky defect, which consists of two charge compensating vacancies. Interstials and vacancies are together known as point defects and a larger collection of point defects results in microscopic and macroscopic defects in the target material. Fig. 8 shows an illustration of these point defects. It is worth noting here that a majority of the defect clusters resulting from cascade damage annihilate on pico-second scale [80] and only the remaining defects give rise to larger defect microstructures.

Simply put, defects arise from disruption of crystalline structure of the material and can significantly alter its properties including, but not limited to, electric conductivity, thermal conductivity, heat capacity, density, optical properties, diffusion coefficients and overall structural integrity [32].

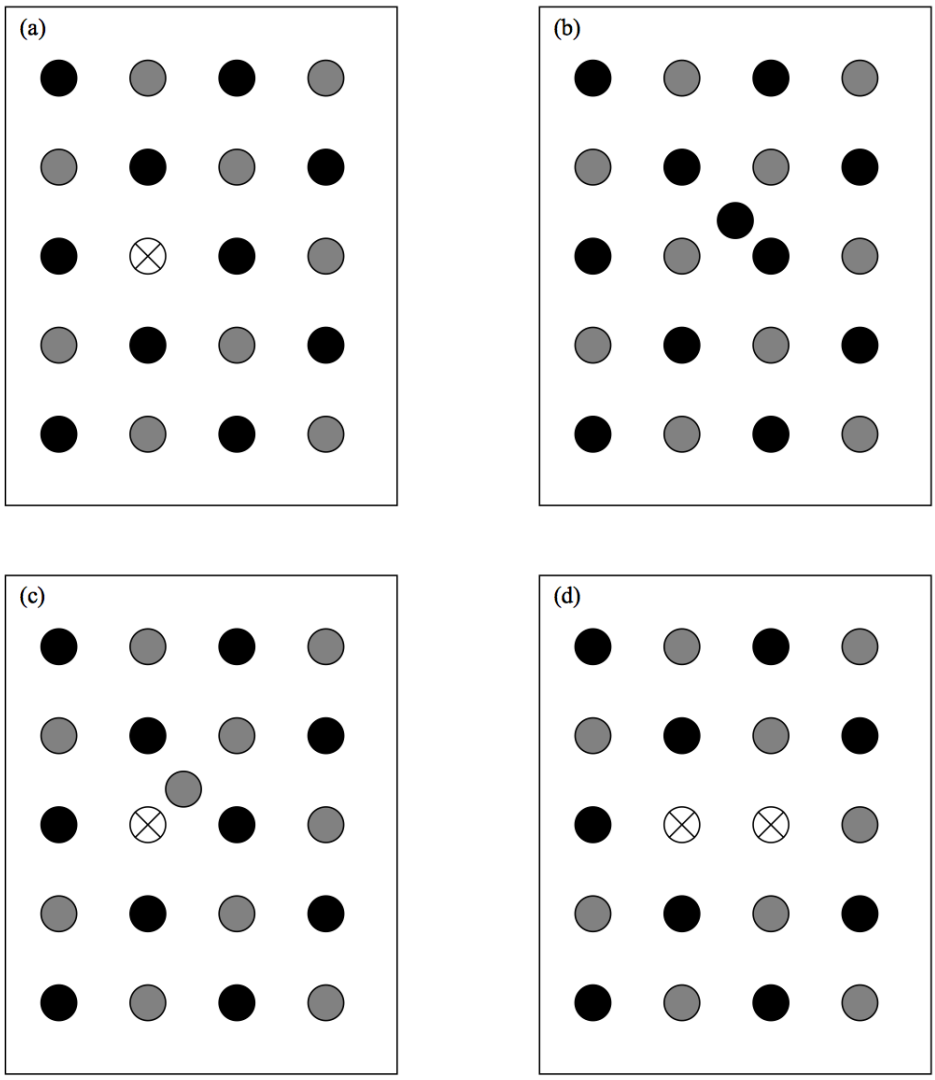

Figure 8: Point defects with their defect complexes: a) vacancy, b) interstitial, c) Frenkel pair and d) Schottky defect

During nuclear reactor operation, fission products of high energies between 167-171 MeV [50] emerge and proceed to damage the atomic structure of the materials inside the reactor

vessel. The resulting microstructure of the reactor materials is complicated because the fission products that interact with it, possess a range of masses and energies. Therefore, ion irradiations are designed by keeping in mind that the damage morphology is different for various types of ions that cause the primary damage as shown in Fig. 9. Electron irradiation results in Frenkel pairs, protons result in small damage clusters that also include Frenkel pairs, heavy ions and neutrons produce larger cluster of damage regions [90]. Based on this, it can be concluded that the damage due to neutrons is different from damage due to protons and heavy ions. It is worth mentioning here that as a part of basic sciences initiative, this difference between damage regions was considered and simultaneously, an attempt to compare the effects of isolated defects on microstructure of the fuel was undertaken in this work.

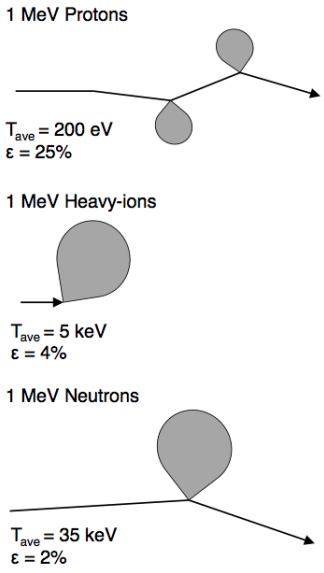

Figure 9: Variation in average recoil energy, damage profiles and displacement efficiency for different ions of 1MeV in Nickel. (Adapted from [90])

Mathematically speaking, radiation damage in a material can be quantified using the damage rate equation (R_d):

$$R_d = N \int_{\hat{E}}^{\check{E}} \phi\left(E_i\right) \sigma_D(E_i)\, \mathrm{d}E_i$$

Here, N is the atom density in the lattice of the target material, $\phi(E_i)$ is the energy dependent particle flux and $\sigma_D\left(E_i\right)$ is the energy dependent displacement cross section. Further, each atom in the lattice can be displaced by the incoming ions with a probability determined by the displacement cross section,

$$\sigma_d\left(E_i\right) = \int_{\hat{T}}^{\check{T}} \sigma\left(E_i, T\right) v(T)\, \mathrm{d}T$$

Here, $\sigma\left(E_i, T\right)$is the probability that a particle of energy E_i will impart a recoil energy T to a struck lattice atom, and $v(T)$ is the resulting number of atoms displaced from this collision. These equations highlight how the damage rate is depended on the type and energy of the incident ion.

2.4 Radiation Induced Defects in UO_2

2.4.1 Microstructure Defects in Irradiated UO_2

The first defects that form following radiation damage are point defects following a damage cascade event. Majority of these defects annihilate due to thermal lattice recovery and diffusion of defects in the material lattice. However, the defects that do survive and remain stable are energetically more favored to cluster and form either small defect clusters [59], or they could arrange themselves into linear formations and form dislocations that could be seen using TEM [88]. Arrangements of defects can result in bi and tridimensional extended defect structures, that could be nanometers or even microns in size [58].

Fission of UO_2 in a nuclear reactor results in high energy fission products that end up populating the fuel matrix and causing radiation damage. Some of the highest concentration fission products include krypton and xenon fission gases that have a large yield (close to 25%) and have low solubility in UO_2. During the reactor operation, the embedded krypton and xenon gasses precipitate into bubbles facilitated by high temperatures during fission. The gas atoms that do not form bubbles then proceed to leave the UO_2 fuel, thereby causing microstructural damage due to the voids they leave behind in the volume of the sample.

The release of gas in-pile is due to a variety of factors including thermally enhanced diffusion such as release of fission products and emission by the fuel due to interaction with incoming fission fragments. When the fission gases do release from the fuel matrix, large voids are left behind as microstructure features in the fuel that weaken the fuel coherence. Fig. 10 shows a micrograph of the high burn up fuel following fission gas release, revealing large voids across the fuel surface. The release of accumulated fission gases isn't just limited to fuel reactor operation, but in fact continues throughout extended fuel storage [97].

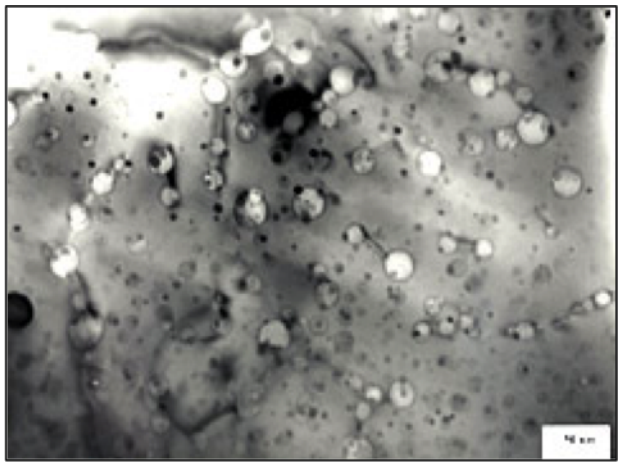

Figure 10: Voids in UO_2 following fission gas release

The formation of fission gas bubbles can seriously challenge the fuel properties, as it can result in fuel swelling, which causes the fuel and the cladding to interact and subsequently damage both the fuel and the clad. This has led to significant research funding directed toward understanding and development of accident tolerant fuel, where the clad fuel and clad interactions are the focal point [21]. Fission gas bubbles can also affect the thermal transport ability of the fuel, which is the key step in producing efficient power from nuclear fuels and further, reducing the radiation damage annihilation capability in the fuel and other

reactor materials [49]. Finally, due to decreased thermal transport, the nuclear fuel will not be able to dissipate heat as efficiently and could ultimately result in an accident and fuel meltdown as a worst case scenario, which is highly undesirable for nuclear reactors. Several studies have been performed to understand the evolution of fission gas bubbles in UO_2 using krypton and xenon gases and some of the resulting micrographs are shown in Fig. 11 and 12. Most notably, studies done using cerium oxide, CeO_2, a surrogate material for UO_2, predict the various differences in bubble characteristics using the two gas atoms. These studies have been performed using ion accelerators to emulate the accumulation of fission gas in the UO_2 matrix in a reactor to a similar dose level.

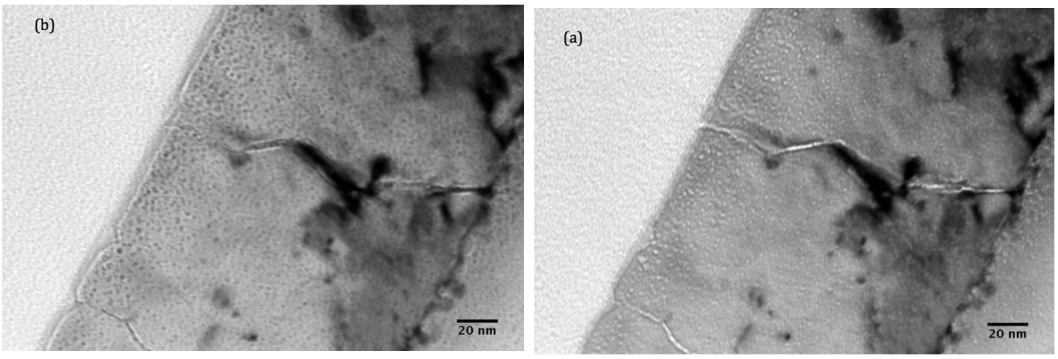

Figure 11: Bubbles seen in krypton implanted CeO_2 [99]

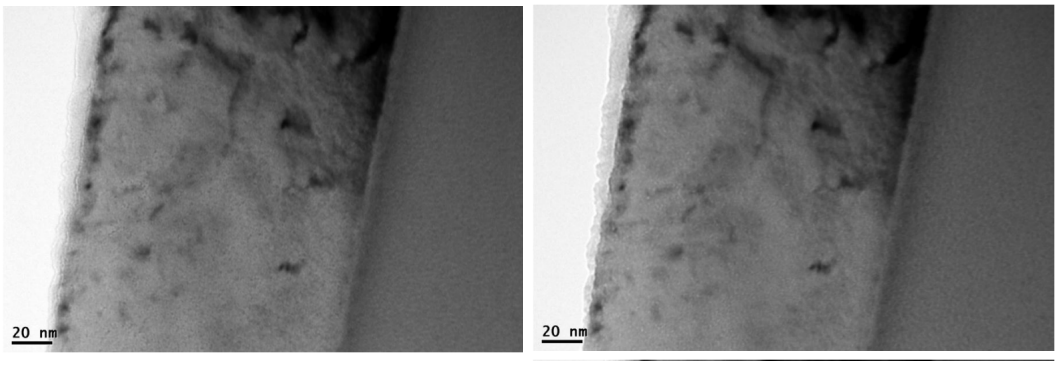

Figure 12: Xenon gas bubbles in CeO_2 [99]

Another one of the noble fission gases is helium which causes radiation damage as a fission product and simultaneously from radioactive decay of heavier fission products into lighter elements. Furthermore, the natural decay of isotopes continues throughout the lifetime of the fuel, even in used nuclear fuel storage. Therefore, it is crucial to understand the damage ability of helium within the nuclear reactor during fuel operation and in used nuclear fuel storage, where it could result in unstable isotopes and challenge material stability in extended storage. Irradiation of helium has been used to understand radiation induced microstructure evolution in several material types. Helium ions, or alpha particles, are one of the highest concentration fission product and therefore a prime candidate for radiation damage studies in fission ceramics. Transmission electron microscopy studies are consistent across materials and show a steady growth of dislocation loop size with helium atom dose. Further, while the coalescence of helium defects into helium gas has been predicted for low temperature UO_2 irradiations, there are no experimental proofs of the same. This study shows the evolution of microstructure, including helium bubbles, along with lattice structure and dislocation growth in helium implanted UO_2. TEM micrograph of He^{2+} ion precipitate in UO_2 is shown in Fig. 13.

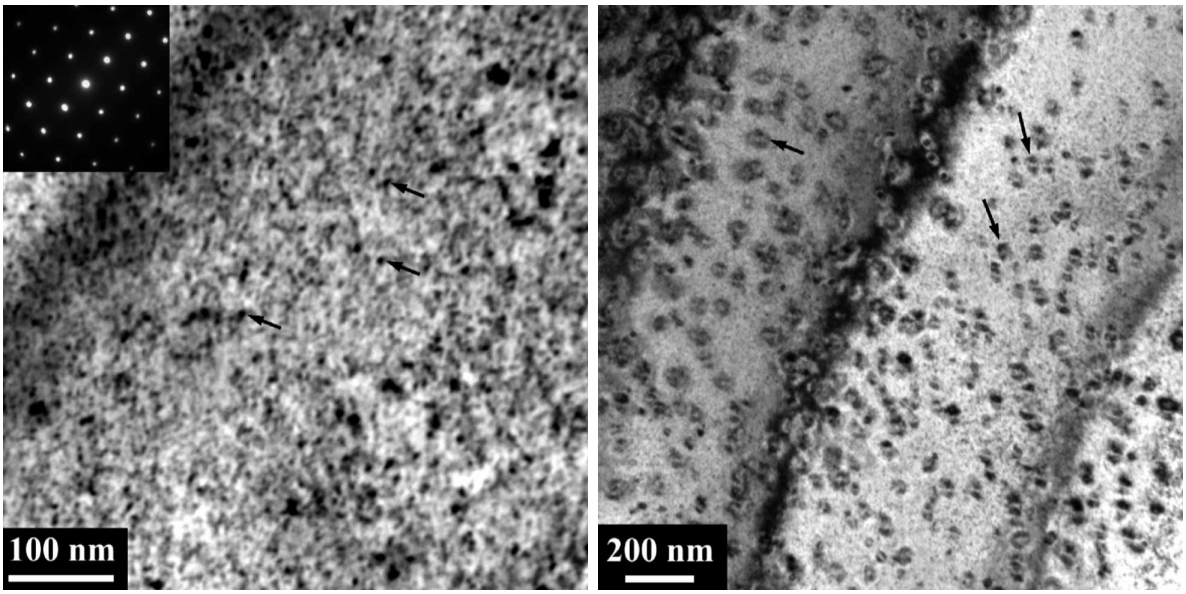

Figure 13: Dislocation loops and helium ion precipitates in UO_2irradiated to a fluence of 7 $\times$ 10^{15} ions/cm^2 [27]

In extended fuel storage, large quantities of helium gas are produced as a result of alpha decay of the isotopes in used nuclear fuel. The accumulation of helium in the spent fuel can affect the integrity of the fuel rods during storage and during transportation of the fuel. Studies have shown that a high level of damage occurs using helium atoms at a DPA of 1.2 and the surface of the UO_2 samples can start flaking at about 1 at % of helium atoms. Over time in extended storage, the helium decay induced damage could reach up to 3 DPA which causes grain subdivision and significant changes to the microstructure of the fuel [89]. The radiation induced damage simply due to the decay of alpha particles can result in high concentration of dislocations, helium ion precipitates and bubbles and lattice expansion in the used fuel materials. It is also likely that over the storage time of the fuel, the material properties evolve from crystalline to amorphous causing the helium gas to pressurize the

storage canister, potentially resulting in failure [71]. Long term effects of helium dose in used fuel materials have not been studied due to time limitations but can be predicted using accelerated measurement techniques. The dose rate in extended fuel storage is similar to the ones performed in this study and therefore predict the radiation damage in the used nuclear fuel adequately. Fig. 14 gives an expected idea of radiation dose due to alpha decay in various fuel compositions in extended storage.

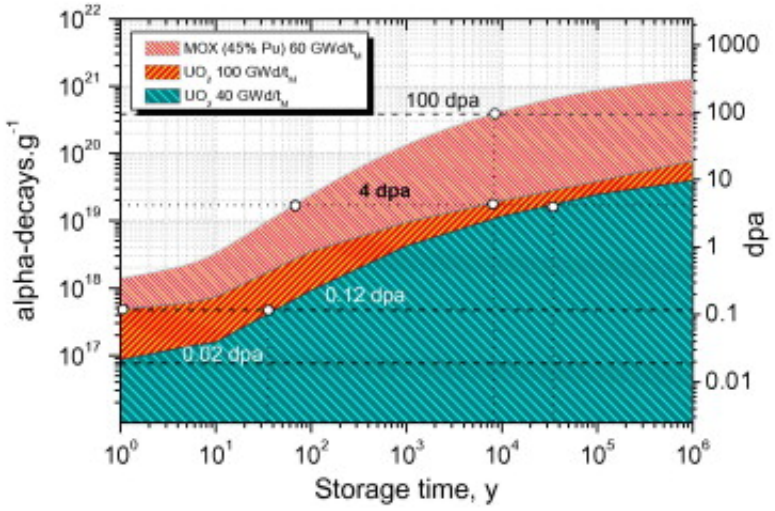

Figure 14: Alpha particle dose in various composition of used nuclear fuel in units of DPA over the fuel storage lifetime [61].

Aside from Transmission Electron Microscopy investigation of helium implanted UO_2 several studies have been performed to study the distribution of the helium ions along with the resulting phase changes in the material. One of the studies using X-ray diffraction shows a dramatic expansion in the UO_2 lattice as the implantation dose is increased **[91]**. The study further demonstrates the saturation of lattice expansion due to helium ions at a concentration of 1 atom %. The primary reason for lattice expansion in UO_2 is due to the

formation of point defects, specially the Frenkel pairs of U and O along with contribution due to small vacancy clusters of helium defects. X-ray Diffraction, while powerful in determining the lattice expansion due to individual point defects, cannot sufficiently determine the atomic level interactions between atoms that cause the point defects. Extended X-ray Absorption Fine Structure measurements used in this study help understand the ordering of atoms that causes the lattice expansion, along with the near neighbor distances resulting from a variety of radiation atoms and doses.

Finally, proton irradiation in ceramics, even though limited, is known to create isolated defect structures in other ceramic materials including SiC, ZrC [100]. The evolution of dislocation microstructure in proton irradiated ZrC to 5 dpa is shown in Fig. 15. The microstructure is predominantly dislocation loops and Frenkel loops, with their density increasing with increasing proton dose. Unlike fission gases used in this study, protons do not form fission gas bubbles or material dependent voids and therefore the resulting microstructure is relatively simple. Using protons is an ideal way to perform a basic science study to relate irradiation dose in the sample to resulting lattice structure and microstructure changes. Therefore, proton irradiations were the first set of experiments done in this study and will be discussed in the experimental section.

In general, it is seen that with increasing radiation dose in UO_2 thermal transport in the fuel dramatically decreases. What has been a remarkable discovery is that while the damage in UO_2 is large, its lattice recovery is also high, such that the overall structure is maintained. This feature of high radiation resistance is a characteristic of FCC actinide oxides including CeO_2, PuO_2, etc. Therefore, it is to be expected that with radiation, local differences in microstructure cause variation in thermal transport and mechanical properties in the fuel,

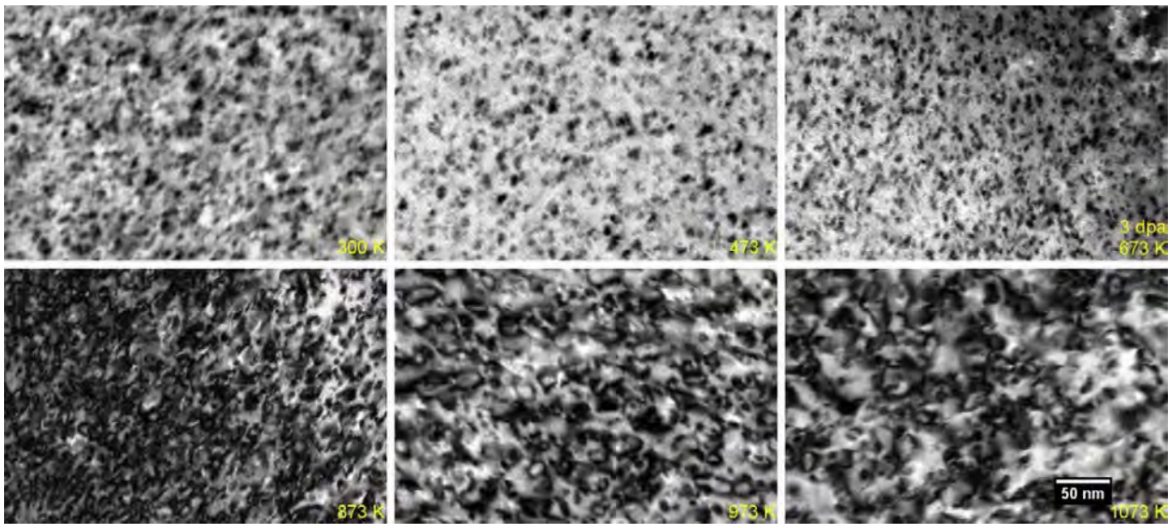

Figure 15: TEM bright field micrographs of dislocation evolution in proton irradiated ZrC to 5 dpa.

while the fuel continues to exist as a ceramic fluorite with insignificant amorphization. The details of the lattice structure evolution with dose are discussed in the next section.

2.4.2 Atomic defect structure in Irradiated UO_2

The study of atomic defect production due to ion irradiation and annealing in a reactor are crucial to improving fuel performance and endurance. Following reactor irradiation, the fuel undergoes a variety of microstructural changes including, but not limited, fuel swelling, grain growth and bubble formation, which finally lead to loss of adequate thermal conductivity [93]. Some of these complicated networks of microstructural features are known to be self-recovering at elevated temperatures [64]. Methods to study these microstructural effects have led to a sound understanding of radiation damage in UO_2. Intermediary microstruc-

tural features and atomic defects arising from crystal imperfections are yet to be completely understood with the latter of the two being minimally studied experimentally.

The process of fission produces high levels of atomic displacement damage, which produces solid and gaseous fission products in the fuel. The fission products emerging at high energies distort the lattice of UO_2 and compromise its crystal structure. Following irradiation, UO_2 stoichiometry changes to UO_{2+x} due to the fissioning of uranium ions [32]. Irradiation damage and change in stoichiometry independently and simultaneously contribute to the deterioration in heat transport in the fuel to the reactor coolant. Atomic structure evolution of UO_2 under irradiation should give the necessary insight into the process of lattice change from fission particles and chemistry changes.

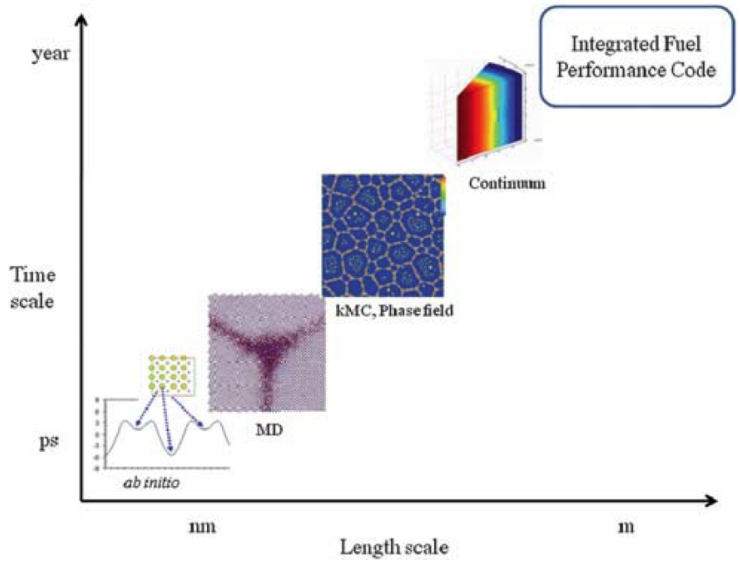

Figure 16: Computer simulation techniques are able to simulate defect formation at varying length and time scales [69].

DFT ab initio calculations provide insight into the electronic states of the damaged material, but to simulate the onset and result of the damage cascade, Molecular Dynamics (MD) calculations have high utility [8]. Fig. 16 shows the various simulation techniques used to understand fuel performance over various length and time scales. Using MD, it is possible to simulate a cascade resulting from a PKA of selected energy which displaces additional atoms through secondary recursive recoil events. Fig. 17 shows the point defects following a damage cascade resulting from an 80 keV PKA . The end of the cascade results in a large number of point defects (interstitials and vacancies). Therefore, using MD it is possible to comment on the size of the cascade, the type of the cascade and the final composition of point defects. However, MD is an approximation of a real cascade and amongst other things, doesn't take into account electronic energy loss regime. Further, all the MD calculations are based on rigid interatomic potentials that significantly vary in the final results of the cascade. Thus, it is necessary to validate the simulation models with experimental data to accurately understand the nature of point defects in the irradiated material.

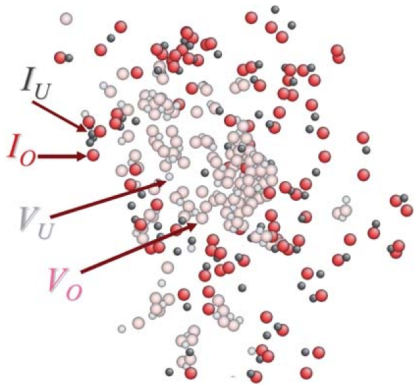

Figure 17: Molecular dynamics (MD) simulation (using 80 keV PKA) shows the distribution of the point defects including oxygen interstitials (I_O), uranium interstitials (I_U), oxygen vacancies (V_O) and uranium vacancies (O_U). It is evident from this image that vacancies congregate toward the center of the cascade while the interstitials are located on the outside.

X-ray Diffraction (XRD) analysis done on UO_2 polycrystalline samples irradiated using 5 MeV alpha particles to an irradiation dose of 0.06 dpa suggests lattice expansion as a result of the ion dose [92]. Similar study on single crystal UO_2 also suggests lattice parameter increase in the material with increasing ion fluence [91]. Fig. 18 shows a comparison between alpha particle irradiation on both single and polycrystalline samples.

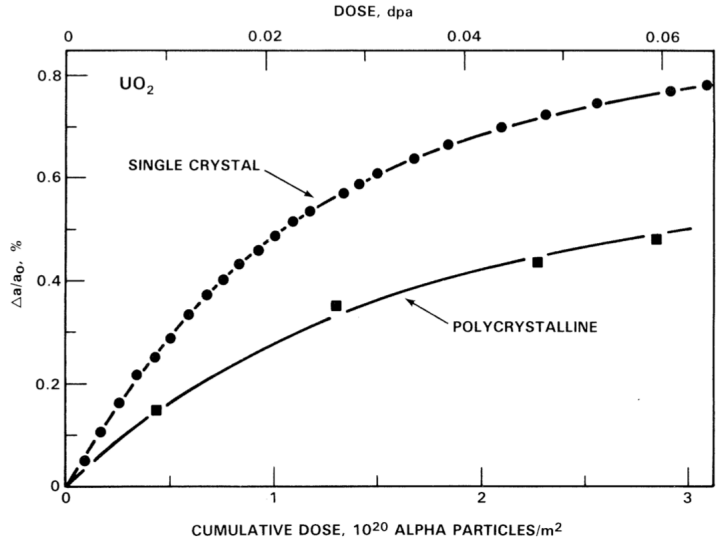

Figure 18: Lattice parameter increase in single and polycrystalline UO_2 when irradiated with alpha particles

Recent observations made by Raman spectroscopy on UO_2 irradiated with 25 MeV He^{2+} ions predict the formation of new defect physics in ion irradiated UO_2. He^{2+} irradiation is noted to directly form the quasi-particle known as polaron, that acts as an electron energy carrier and undergoes relaxation at a later time following electronic excitation, via a process that creates defects in the uranium sublattice. The Raman spectra gives evidence of Magneli type defects [22] in UO_2 that are separate domains with U(III) and U(V) that form complex defect structures on the oxygen sublattice [51]. The U(V) corresponds to regions with locally high O compositions and U(III) would be present in O-depleted ones. The separate U(III) and U(V) regions occur in tandem and elucidate the presence of UO_{2-x} and U_4O_9 type domains due to ion irradiation. This possible new mechanism for formation of radiation stabilized defects, shown in Fig. 19, occurs in these steps:

- Dynamical polaron is formed by electronic excitation
- Self trapped defects on U (STD-U) sublattice form
- Accumulation of STD-U lead to formation of O displacements and defects on neighboring U sublattices

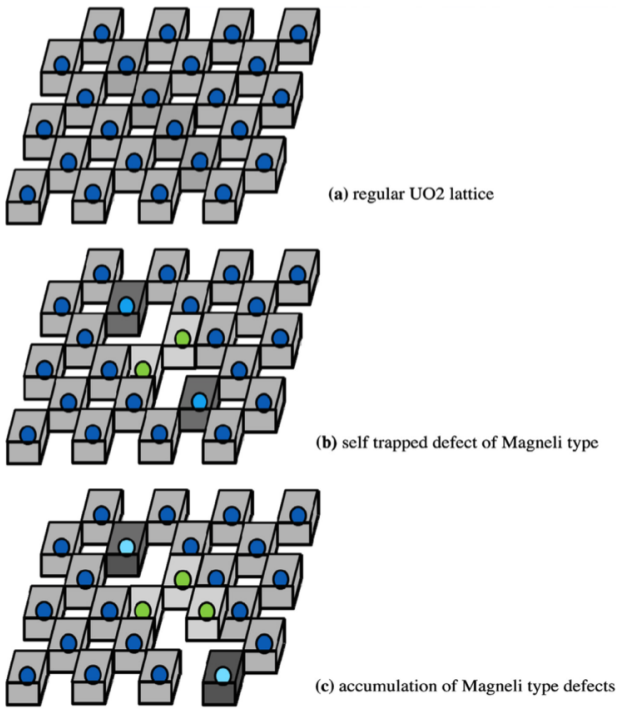

Figure 19: Magneli type defects are shown to occur (b) and start accumulating (c) due to radiation damage in UO_2

UO_2 chemistry has been vastly studied over the last 6 decades but there is a lack of atomic level understanding of property evolution under irradiation. Some of the historical synchrotron results obtained from UO_2 are summarized in the next section.

2.5 Historical EXAFS UO_2 Results

The EXAFS technique has been used on a set of systematic off stoichiometric samples that inspired this study to a great extent. Conradson, et al performed an EXAFS analysis on UO_{2+x} compounds for x = 0 – 0.20 (UO_2-U_4O_9) to study the local structure changes from additional oxygen. The off stoichiometric powder samples were prepared under strict conditions at JRC Institute for Transuranium Elements in Karlsruhe, Germany and the EXAFS studies were made at SSRL, Menlo Park, CA. The EXAFS measurements were recorded in fluorescence mode.

In the XANES analysis, there is a demonstrated increase in electron binding energy with an increase in charge on the cation, which further results in a higher energy shift for the absorption edge. Increasing valence in hyperstoichiometric UO_2 results in a shoulder on the higher energy side of the peak along with the peak undergoing a significant dampening of the amplitude, due to the evolution from spherically symmetric geometry of lower valence to oblate geometry of higher valence indicating the presence of dioxo groups.

In the analysis of the UO_{2+x} specimen analyzed (for $0 \leq x \leq 2.00$), there appeared to be an absence of edge shift toward higher energies and a small (~0.5 eV) shift increase in peak energy. Changes in the peak energy have a greater significance to determine effects due to valence changes in actinates. The arctangent function is used to fit the edge and the Gaussian function used to fit the high energy asymmetry of the peak. Using this fitting technique, satisfactory fits were obtained along with monotonic progression between the second Gaussian and edge energies.

The EXAFS spectra of the samples showed several changes to the local structure of the off stoichiometric samples. The primary oxygen and uranium peaks at 2.36 and 3.8 Å are well

defined in the pristine stoichiometric sample and are in good agreement with literature values for the UO_2 lattice. With increasing x in UO_{2+x} there is a consistent loss in amplitude of the primary crystallographic peaks that indicate a loss of structure due to additional oxygen interstitials as show in Fig. 20. Further, with increasing x, a shoulder begins to form and grow on the low R side of the primary oxygen peak and the primary peak diminishes in magnitude. At higher oxidation states, this shoulder appears to be larger than the primary peak indicating the first hint of a possible multisite distribution of oxygen atoms.

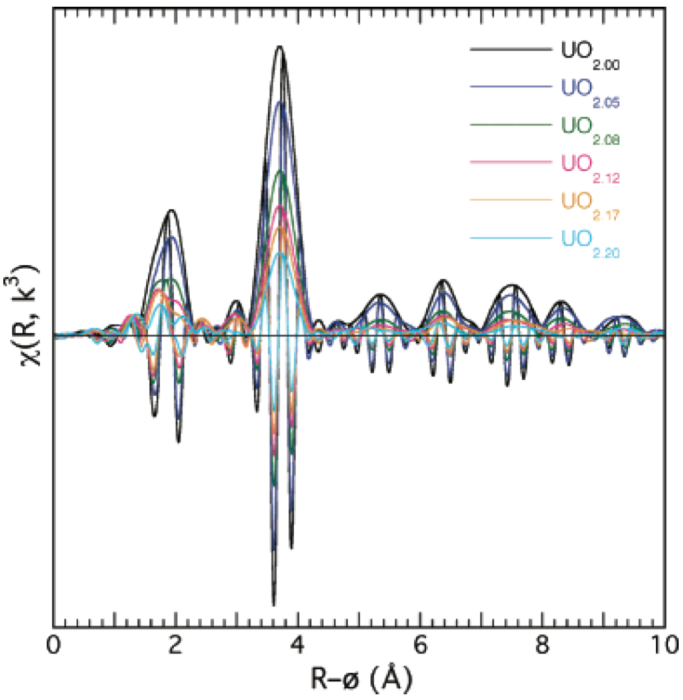

Figure 20: Fourier transforms of k^3- weighted EXAFS spectra of the off stoichiometric EXAFS samples along with their modulus and real part.

Analysis of the shoulder on the low-R side of the crystallographic oxygen peak reveals not just one but several smaller peaks appearing, that can be fit accurately with oxygen. This confirms the presence of multisite distribution of oxygen atoms from the oxidation of UO_2. The reduction of the U-U primary peak in each of the samples also simultaneously indicates the loss of overall structure due to loss of neighboring U atoms. The amplitude reduction in the EXAFS spectra is not limited to the first two nearest neighbors but is a consistent decrease through the mid range structure as well. This indicates that while the addition of oxygen atoms is distorting the lattice, the overall crystal structure is still well maintained.

Garrido et al performed neutron diffraction studies on U_4O_9 to compare U-O bond distances obtained by Conradson, et al. These results do not agree with Conradson, et al who suggested that the U sub-lattice in UO_2 consists of ordered portion and a spectroscopically silent glassy part. Garrido et al performed neutron diffraction studies on U_4O_9 to determine the presence of oxo type groups for R $<$ 2 A which was predicted by Conradson, et al using EXAFS measurements. The neutron diffraction results do not give any evidence for the presence of U-O bond distances for less than 2.2 Å for U_4O_9 system ($UO_{2.20}$). The EXAFS measurements done by Conradson, et al were compared to a similar study by Jones, et al, which corroborated Garrido et al's results as no U-O bond distances less than 2.2 Å, were found[25]. Further, Jones, et al's measurements led to a correlation function similar to the one found by Garrido's neutron diffraction measurements determined from the first U-O peak.

The comparison between neutron diffraction and EXAFS is shown in Fig. 21. The lack of O-O peak in EXAFS is due to its inability to detect O-O correlations, however the U-U

and U-O peaks are accurately plotted here. Using the result of fits from Conradson, et al, neutron correlation function is shown in Fig. 21 as T_{conr}. The disagreement between neutron correlation and EXAFS measurements are evident from this figure. There appears to be no U-O distances in the 1.7 Å range in the neutron diffraction measurements, which have been defined as oxo type groups by Conradson, et al. The area under the correlation function for $R < 2.6$ Å is greater by a factor of two for neutron diffraction results. Further, Garrido, et al did not see any evidence of glassy disordered portion exceeding 1% or 2% in the U_4O_9 measurements because there was no contribution to distinct scattering as would be expected from spectroscopically silent glassy disordered part.

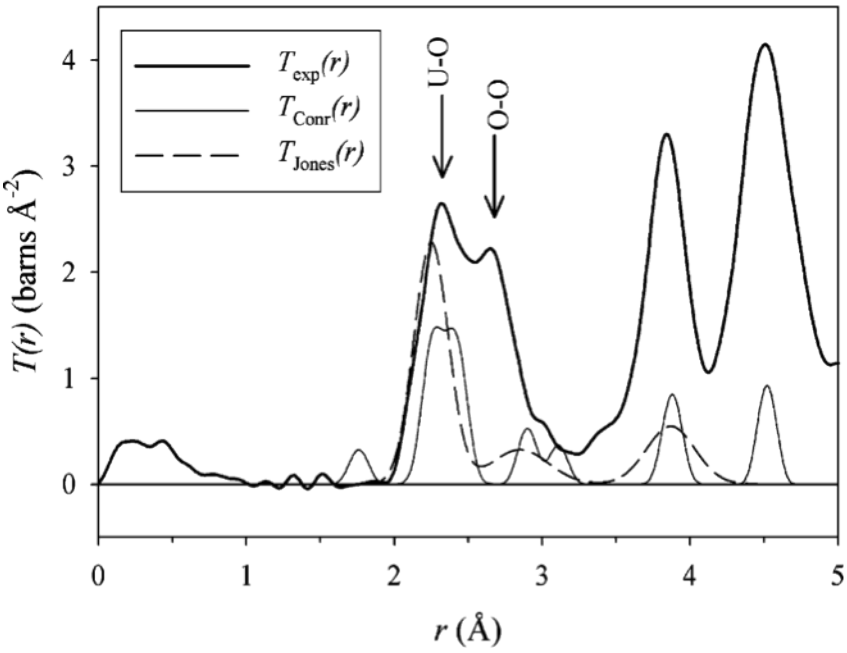

Figure 21: Comparison of neutron correlation obtained from neutron diffraction measurements by Garrido, et al (T_{exp}), fitted neutron correlation function for EXAFS measurements by Conradson, et al (T_{conr}) and calculated correlation function for measurements by Jones, et al (T_{Jones}) [40][25]

In Garrido's 2003 study [28], neutron diffraction was employed to study the lattice structure of U_3O_7 when UO_2 was oxidized to obtain it. Cuboctohedral oxygen clusters are known to form around the holes in fluorite lattice to give rise to U_4O_9 when UO_2 is oxidized. Rietveld refinement of the neutron diffraction data [25] showed that the fluorite positions of the uranium atoms remained unchanged during the oxidation from UO_2 to U_3O_7 and the lattice change is predominantly due to oxygen atoms. In fluorite geometry, the oxygen atoms occupy the fluorite positions in UO_2 leaving 30% unoccupied sites in the lattice. The addi-

tional O atoms occupy the non fluorite positions in the lattice displaced by 310 pm along the (1 1 0) directions from the cation lattice holes.

The resulting structure from the addition of O ions in the fluorite lattice is consistent with the cuboctohedral clusters. The existing cube of oxygen atoms in the fluorite lattice is replaced with a cuboctohedron and this has 12 O atoms (instead of original 8) at its vertices located along the 12 (1 1 0) direction from the hole [28].

2.6 Summary

The background section gives a detailed understanding of the characteristics of UO_2 from subatomic physics to larger mechanical defects that form in UO_2 due to its natural structure and due to interaction with extreme environments. The study of this material has been undertaken for many decades due to its expansive use as a global nuclear fuel and even more so, due it its remarkable chemical property evolution. The transmission electron microscopy measurements give insight into the microstructure features resulting from radiation damage and the x-ray measurements indicate how the lattice of the material evolves with irradiation. Atomistic simulations, the next big frontier in material characterization, have proven to be a powerful tool in explaining the defect formation mechanism in UO_2, and has provided a detailed understanding in an area where experiments fail to explain the radiation and material interactions at an atomic level.

Given the extensive characterization of irradiation induced microstructure changes in the surrogate material CeO_2, the effects of radiation damage can be anticipated to some extent in UO_2. Therefore, the irradiation doses, ion types and the temperature of the experiment

for this study were selected using the information produced in CeO_2 under similar irradiation conditions. The difference between CeO_2 and UO_2, however, arises from the interaction of irradiation conditions with the inherent lattice dynamics in UO_2. In simpler words, the extent of the effect of oxygen stoichiometry change and the naturally oxidizing nature of UO_2 on the microstructure features due to irradiation in this material is largely uncertain. Therefore, there exists a gap in the knowledge of proper radiation induced structure evolution from smaller length scales to larger microstructure features and this thesis will address this question.

The onset of radiation damage in UO_2 has been characterized to large extent using molecular dynamics type simulation techniques. The damage cascade study using these simulations has predicted the formation of point defects that, by and large, annihilate in UO_2 leaving behind smaller point defect clusters. However, the results of the calculations depend on atomistic potentials used to define the UO_2 structure in the simulation methods in use [42]. As an example, the cuboctohedral type defects predicted using neutron diffraction measurements [25] have been simulated using only one potential type in molecular dynamics known as Basak Potential [8]. As a result, there is insufficient proof for the presence of the postulated cuboctohedral type defects since the majority of the molecular dynamics calculations have not been able to simulate this type of cluster and the neutron diffraction calculations have not been verified using any other experimental or simulation measurements. Therefore, irradiation induced defect clusters forming in UO_2, are yet to be fully characterized and validated by multiple analysis techniques.

By understanding the limitations of the characterization techniques and maximizing the use of available resources, this study aims to fill in the gaps in the knowledge of radiation

induced structure changes in UO_2 on multiple length scales by using specific analysis probes. The study attempts to identify the distribution of radiation induced defect structures and probe the relationship, if any, between individual point defects, defect clusters and larger microstructure features. To deconvolute the effect of irradiation species on the final damage state, H, He and Kr ions were used to damage UO_2 to various DPAs and the resulting structure was studied using length scale specific measurement techniques. The process of irradiation of UO_2 closely resembles that of oxidation in the material. Therefore, empirical and simulation methods were used to identify the similarities between irradiated UO_2 and UO_{2+x}. Finally, this study aims to develop a general understanding of defect clusters that form due to radiation in UO_2 and use experimental and simulation techniques to validate their existence.

3 Instrumentation and Modeling Techniques

3.1 Ion Implantations at Accelerator Facilities

Ion accelerators demonstrate a unique capability of producing ion beams of specific fluences on a selected target area in the specimen being irradiated. Using an ion beam, it is possible to accelerate the radiation damage in a material in comparison to nuclear reactors, which take months to produce the same extent of radiation induced effects. Therefore, ion irradiations save experimental time and are significantly cheaper to execute while simultaneously giving the user the ability to have larger control of the experiment. For example, the target material can be irradiated to ensure low resulting activity, at a selected temperature, using specific ions to create a calculated extent of radiation damage.

A sophisticated Monte Carlo based interface called Stopping Range of Ions in Materials (SRIM) [104] is widely used to estimate the deposition profile of incoming ions from ion accelerators in the desired target and its associated damage rate. Based on the energy of the incoming ion, the code separates effects on the material via electronic and nuclear stopping powers. Primary inputs of the code include target material description including its dimension, stoichiometry, density and constituent displacement energies and incoming ion type and energy. Displacements Per Atoms (DPA) is used to describe radiation damage and is defined as the average number of times an atom is displaced from a lattice site for a given ion fluence. SRIM is used to give an approximation of the final DPA in the material and therefore, all the ion beam experiments performed in this study are based on the SRIM estimates. It is therefore pertinent to provide accurate inputs to SRIM based on available literature data.

The purpose of this study is to study the evolution of radiation damage with dose and ion

type in UO_2, which necessitates the use of ion accelerators to create isolated microstructure defects in target material. University of Wisconsin – Madison Ion Beam Lab houses a National Electric Corporation Pelletron Accelerator (Fig. 20) that uses a SNICS and TORVIS source. This accelerator was used to irradiate UO_2 samples with H^+ and He^{2+} ions. The temperature during the course of the irradiation was continuously monitored using thermocouples and an infra-red camera. For Krypton ion implantation, University of Illinois Urbana Champagne ion accelerator was used to perform ex-situ irradiations on d-UO_2 samples.

Material Density	10.97
Material Dimension	3 mm, 5 mm
Stoichiometry	UO_2
Ion type	H^+, He^{+2}, Kr
Ion energy	2.6 MeV, 3.9 MeV, 1.8 MeV

Table 1: SRIM input parameters for UO_2 ion irradiation

SRIM input parameters for irradiation simulation are summarized in Table 2 for UO_2. A study done by C. Meis, et. al [55] estimated the displacement energy for UO_2 based on crystallographic orientation for sub-lattice displacement. These are shown in Table 3. Ion irradiations on depleted UO_2 were first done on single crystal samples oriented in (1 1 0) direction and therefore corresponding displacement energies of $E_d(O) = 20eV$ and $E_d(U) = 81$ were used. Henceforth, while irradiating polycrystalline sample, $E_d(O) \sim 20eV$ and $E_d(U) \sim 50eV$ were used for further calculation .

(u v w)	(1 0 0)	(1 1 0)	(1 3 0)	(1 5 0)	(2 1 4)	(3 1 3)	(1 4 1)	(2 3 2)
E_d(O) (eV)	_	16	28	_	21	_	22	18
E_d(U) (eV)	52	85	46	44	79	43	55	74

Table 2: Threshold displacement energies in Uranium Dioxide calculated by C. Meis et. al using Mott Littleton approach [55]

3.2 Transmission Electron Microscopy

Transmission electron microscopy (TEM) techniques benefit from the small de Broglie wavelength of electrons, making them capable of imaging dramatically higher resolution than traditional optical microscopes. Due to the ability to image such high resolutions, it is possible to observe materials down to a single column of atoms using electron microscopy. TEM techniques are crucial and highly accurate in determining microstructure damage to the irradiated material. The illuminating system, the objective lens and stage and the imaging system are collectively the three main components of the TEM. The electron gun in the TEM is directed using a series of lenses and focused on the the specimen holder to image defects in the sample. The assembly of magnetic lenses in the vertical column are maintained in vacuum at 10^{-5} torr or less. In the center of the TEM the specimen interacts with the electron beam and subsequently sample images and their diffraction patterns are obtained. These images and diffraction patterns can be magnified to obtain extremely detailed measurements of defect structures. The objective, one of the most important parts of the microscope, is responsible for producing images of higher quality. The imaging system comprises of several lenses which are used to magnify the image and diffraction patterns and further help focus the sample on the fluorescent viewing screen or using a CCD camera on the computer screen.

Fig. 22 shows the set up for a TEM in diffraction mode and image mode.

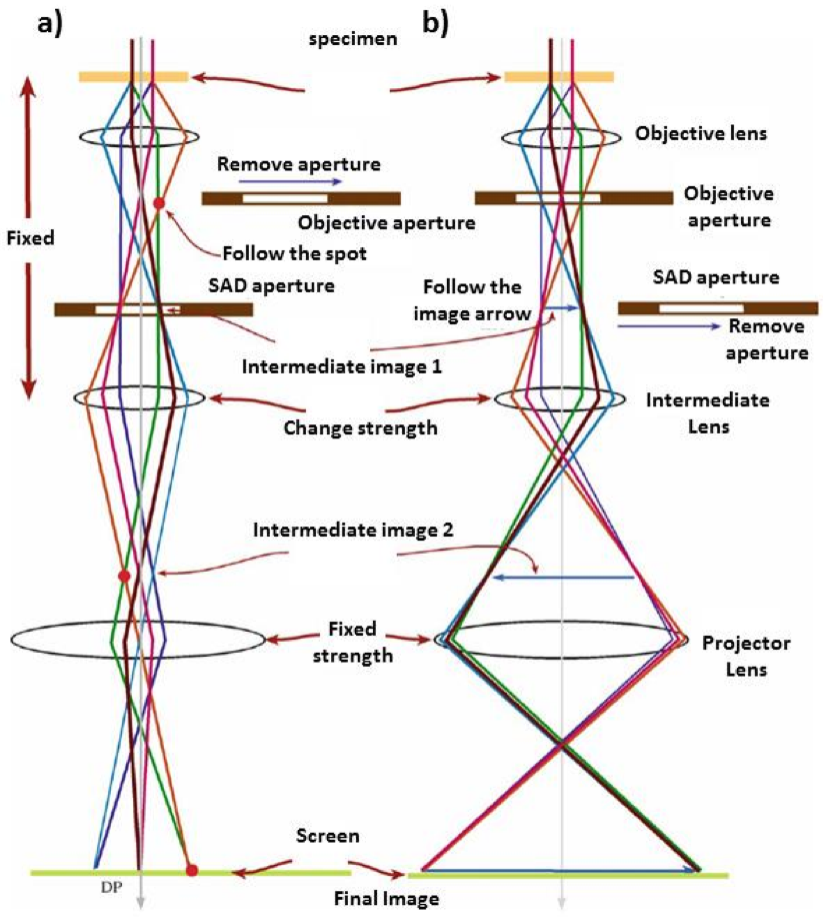

Figure 22: TEM set up for imaging in a) Diffraction mode b) Real image

Ex situ TEM characterization was performed at the Microscopy and Characterization suite at the Center for Advanced Energy Studies, Idaho Falls, ID. The TEM is a Technai TF30-FEG ST with STEM, a high-resolution analytical transmission electron microscope, which can be used for crystal defect analysis and for elemental analysis. The TEM has a double tilt holder is available with the TEM which allows for +/- 45 degree tilt in both X

and Y axes. High accelerating voltage of 300 kV results in small electron wavelength, the coherent electron source due to the Schottky field emission electron gun (FEG) and finally, the high mechanical and electrical stability of the TEM make this ideal for high resolution studies with information resolution of 0.14nm.

Depending on the material characteristic to be probed, TEM imaging methods can be modified by the user to utilize the information provided by the electron waves exiting the sample area to form an image. The interrogated damage structure consisted primarily of dislocation loops and networks and inert gas bubbles. Therefore, the TEM techniques that were used were a combination of methods to understand these various damage features. One of the TEM technique that has been utilized to explain relation of atomic defects to microstructural defects is High Resolution Transmission Electron Microscopy (HRTEM). HRTEM is an extremely powerful tool that allows us to probe atomic scale resolution of materials [94] because, at very high magnification, crystalline material's lattices can be easily studied and individual atomic columns can be imaged. Presently, sub nanometer resolution or approximately 0.2 nm can be obtained routinely on the microscopes which makes it possible to obtain atomic resolution in sufficiently thin samples. In contrast to conventional TEM, HRTEM does not employ electron wave absorption by the specimen to form an image. Instead, the contrast arises from interference in the image plane of the electron wave itself. Once the electron beam penetrates the specimen, the amplitude of the electron wave function is unperturbed, however, the phase is modified resulting in phase-contrast imaging. For successful HRTEM examination, high quality samples with very thin areas are needed. The final image produced using HRTEM is still not a certain representation of the crystal structure of the material. There are associated errors arising

from the aberrations of the microscope and the non-linear relationship between exit wave and the image wave that could result in the indication of an atomic column being present at a different location.

Another transmission electron microscopy technique used to study radiation damage in this study is the application of diffraction contrast. Diffraction contrast is studied by inserting an aperture in the back focal plane of the objective lens. This aperture ensures only one electron beam to pass through, which then produces the final image. A bright field image is produced by letting the transmitted beam pass through the sample and, a dark-field image is produced by letting the diffracted beam through. The image obtained from diffraction contrast technique is a highly magnified variation of the intensity of the selected beam across the bottom surface of the sample. This makes diffraction contrast an ideal technique for imaging crystal defects, precipitates, dislocations, etc [94].

To have strong diffraction contrast for imaging in both bright-field and dark-field modes, the specimen has to be tilted to obtain two beam condition, such that only one diffracted beam is strong. Bragg condition is required to have strong signal in the dark field imaging mode. Precise tilting of the specimen is critical for two beam condition, which is manipulated using a double-tilt eucentric sample holder. This is because dark field images can form from any of the strongly diffracted beams and each of these images depend on the selected beam, making them all very different from one another.

To further refine the images of defects using TEM, even more so than two beam condition, a technique known as weak-beam microscopy is employed in this study. Using this method, it is possible to resolve smaller dislocations that would be present in lower dose samples and could be mistaken as impurities or precipitates. Using weak beam imaging in dark field

setting, the smaller dislocations become clear and visible, which can be used to understand the extent of radiation damage in the material.

Several techniques can be utilized to prepare electron thin specimen for TEM analysis. The primary technique utilized in this study for sample preparation is done using a focused ion beam, which is discussed in detail in the next section.

3.3 Focused Ion Beam (FIB)

Analyses by transmission electron microscopy are performed on samples that are electron transparent, and therefore, very thin. Since sample preparation has to be performed prior to sample examination, the preparation technique must keep the surface of the sample intact and prevent the selected area from any damage. Along with minimizing damage to the sample surface, the need for isolated examination of regions of interest led to the use of focused ion beam (FIB) for extracting lamellae from a localized zone of the sample with a spatial accuracy of ~10 nm [56]. The FIB method to perform TEM sample preparation employs the following steps:

1. Area of choice is selected in the FIB and focused in the SEM and FIB imaging mode. Further, it is important to ensure that the image corresponds to the sample location in both SEM and FIB

2. Using the FIB, two trenches are made on either sides of the sample top. The depth of the trench is equivalent to the desired lamella height

3. The omniprobe extractor is welded on the lamella top and the lamella is cut free from the original sample. Omniprobe needle is then extracted.

4. The lamella is then welded on to the FIB grid which will be used for analyses in the TEM. The omniprobe needle is cut free from the lamella

Using these steps, a FIB lamella can be mounted on to a grid which can be used in the TEM for imaging. The FIB can be used to perform rigorous thinning of the sample to ensure electron transparency without causing high damage to the sample surface.

For TEM specimen preparation in this study, a FEI Quanta 3D FEG DualBeam FIB/SEM located at the Center for Advanced Energy Studies (CAES) at the Idaho National Laboratory was used. During the lift-out procedure, a thin cap of platinum was deposited on the surface of the sample, to avoid charging effects and to minimize contamination in the region of interest. Material is removed from both the sides of the platinum cap, shaping a thin lamella (~2μm thick). Once the lamella is shaped, it can be cut free after one of its sides is welded with platinum to a needle. The lamella is then attached to a copper Omniprobe® Lift-Out Grid, which are grids specifically designed to accept the TEM lamellas milled out by FIB systems. These grids have a typical thickness of 25-30 μm with a diameter of 3mm. The final product is an electron transparent lamella from the region of choice of the sample. It is important to note here that there is FIB induced damage in the lamellae during the extraction and cleaning process that is visible during TEM. A good microscopy practice is then to identify this damage as "noise" using a reference (unirradiated) sample and look for different features caused by ion accelerator damage in irradiated specimen.

3.4 X-ray Diffraction (XRD)

Microstructure determination in a polycrystalline material became popular when Paul Scherrer discovered peak broadening in the X-ray diffraction peak due to the presence of finite small crystallites present inside the material [77]. Further, theory of line broadening in XRD analysis incorporated the effects due to lattice strain making it more precise. Microstructural changes in irradiated materials alter the XRD peak profiles and can give valuable information about average structure deformation which makes X-ray Diffraction a key tool for studying irradiated materials. Using XRD, it is possible to correctly measure the average lattice parameter and phase of the material being studied.

X-ray Diffraction is a highly important and relevant technique for studying the crystal properties of materials and in the case of this study, irradiated material lattice spacing can be adequately understood using this technique. X-ray Diffraction can be defined as coherent elastic scattering of the X-ray beam from the crystal of the sample and is understood using Bragg's law given by,

$$2d_{hkl} \cdot sin\theta_{hkl} = \lambda$$

Here d_{hkl} is the lattice spacing between crystallographic planes (hkl) that produce the said Bragg peak, θ_{hkl} being the angular position of the Bragg peak and λ is the X-ray wavelength. The peak is observed at the 2θ angle from the incident beam direction. In XRD, the angle at which a peak in the material of interest occurs is given by Bragg's law. Fig. 23 illustrates the theory of Bragg diffraction from the plane of a crystal lattice. Using the Bragg's law, lattice parameter can be calculated as a function of the planar lattice spacing.

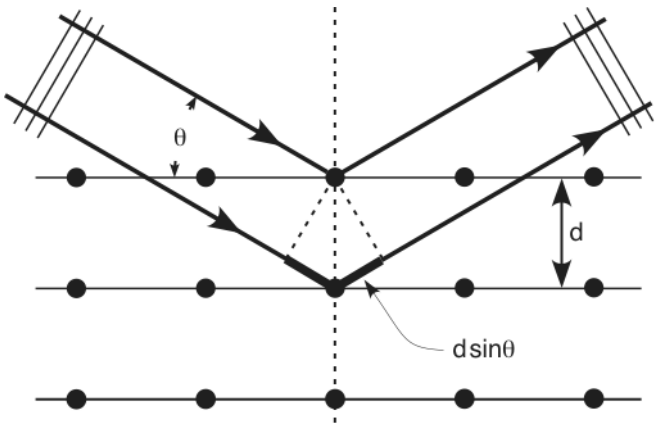

Figure 23: X-ray diffraction by crystal illustrates Bragg's law

The local lattice parameter can be calculated using the equation here:

$$a = d\sqrt{h^2 + k^2 + l^2}$$

Therefore, using Bragg's law, this equation can be written as

$$a = \frac{\lambda}{2sin\theta}\sqrt{h^2 + k^2 + l^2}$$

Where, a is the local lattice parameter, θ is the incident X-ray angle, λ is the X-ray wavelength and (h,k,l) are the miller indices of the Bragg peak of the sample being interrogated. Using this equation lattice parameter has been successfully determined for the ion irradiated UO_2 samples.

While x-ray diffraction is capable of providing accurate average lattice information, it is not an ideal tool for studying atomic defects in irradiated materials. This technique derives its information from summing over contributions of thousands of angstroms and thus provides average structure information from coherent parts of the material. XRD is typically not highly sensitive to lighter atoms and also, determination of structure is not straightforward. Ultimately, average lattice information obtained from XRD needs to be presented in conjunction with more local, atomic level data to fully understand the structure of the material.

3.4.1 XRD Experimentation

X-ray Diffraction studies were carried out at the University of Wisconsin-Madison using a Siemens Stoe X-ray diffractometer that uses Cu Kα radiation (40kV, 2.5mA) in omega-2theta geometry. The diffractometer used in this set of experiments is located at the University of Wisconsin - Madison Material Science Center. It is set up in the standard Bragg-Brentano geometry where the detector and the sample move such that the detector is at an angle of 2θ around the sample and the sample surface always at angleθ from the incident X-ray beam. Since the samples used in this experiment were bulk samples with an irradiated layer that varied in depth from 1μ m to 40 μ m, most of the experiments were conducted in grazing incidence geometry such that the X-ray beam would interrogate only the irradiated layer of the specimen. X-ray source used for this set of measurements was a copper based source using Cu K_α radiation (40kV, 2.5mA) that was monochromatized to give a higher resolution. XRD peak position for the (224) reflection was used to calculate the lattice parameter of the target samples prior to and after the ion irradiations. This high order reflection of (224) was

chosen so that the probing depth of the X-rays was about 1.6 μm into the sample surface and also to reduce any uncertainty from varying displacement dose as a function of depth.

3.5 EXAFS

In order to interrogate the local structure evolution, EXAFS technique was used to study the effect of radiation on UO_2 lattice. Extended Xray Absorption Fine Structure (EXAFS) is a spectroscopic measurement technique that principally utilizes the X-ray absorption edge, which is specific to the element being probed. EXAFS is used to determine near-neighbor characteristics of target atoms including local chemistry, distance and coordination number and is capable of detecting material constituents in very dilute quantities. This makes EXAFS highly sensitive to lattice disorder in the target material and was therefore a major part of this study to understand atomic structure changes in irradiated UO_2.

3.5.1 EXAFS Introduction

EXAFS is a modification of the photoelectron's final state due to the molecular field surrounding the absorbing atom. This phenomena was first noticed and studied by Kronig in 1931 in his paper "Quantum Mechanics of Electrons in Crystal Lattices" [44]. One of the commonly accepted theories treats the photoelectron as a spherical wave that is partially scattered by point approximation of the atoms around the absorbing atom [26]. The interference between the outgoing photoelectron wave and the backscattered waves modulate the absorption coefficient which gives rise to Extended X-ray Absorption Fine Structure. The

fine structure is measured by dipole transition between initial photoelectron core-state and final state. Fig. 24 shows the process of the creation of a core hole and excitation of a core electron. The process of de-excitation of this electron releases an X-ray characteristic to the transition energy from the higher energy shell to the lower energy shell of the electron, which is modulated by the location and type of surrounding atoms. This gives insight into the local structure of the atom being probed.

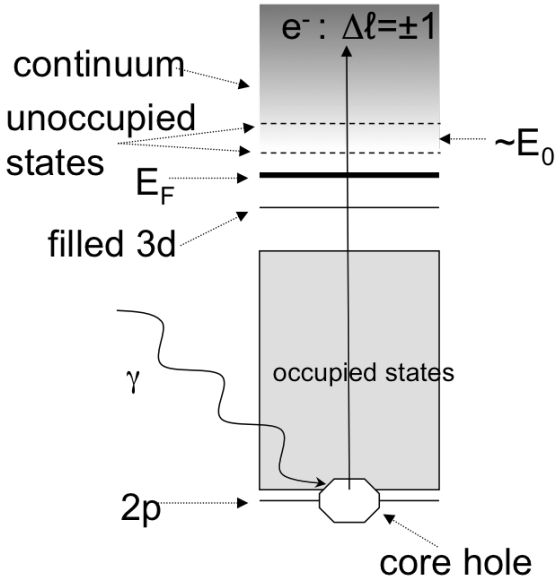

Figure 24: Electronic excitation in an atom due to EXAFS

XAFS originates from Einstein's Nobel Prize winning concept of the Photoelectric Effect. When an incoming X-ray posses greater energy than the binding energy of the electron, the X-ray is absorbed and the electron leaves its original quantum state for a higher energy state. The Beer-Lambert law gives the extent of X-ray absorption in the sample,

$$I = I_0 e^{-\mu t}$$

In this equation, I_0 is the initial X-ray intensity, I is the intensity transmitted through the sample, t is the sample thickness and μ is the absorption coefficient of the material [63]. Over the range of X-ray energies used to probe the samples, the absorption coefficient is usually seen as a smooth function of energy given by,

$$\mu(E) = \frac{\rho Z^4}{A E^3}$$

Here, ρ is the density of the target material, E the incoming X-ray energy, Z the atomic number of the target and A is the atomic mass. The strong dependence of $\mu(E)$ on the atomic number Z and E (Fig. 2.3) is a fundamental property of X-rays and gives rise to EXAFS phenomenon. Therefore, EXAFS can simply be explained as the modulation of the X-ray absorption probability due to the physical and chemical state of the atom. X-ray Absorption Fine Structure (XAFS) region is a total of two subregions, which constitute their own measurement techniques, and they probe complementing features of the target specimen. These are,

1. X-ray Absorption Near Edge Structure (XANES), typically 30 - 50 eV about the absorption edge. This contains information on local electronic structure, oxidation state and coordination chemistry.

2. Extended X-ray Absorption Fine Structure (EXAFS), starts after the absorption edge and extends up to 1000 eV past it. EXAFS gives information regarding near neighbor distances, coordination number and species of the neighboring atoms.

Elements have well-defined binding energies for their core electrons. Therefore, it is possible to probe specific elements using X-rays equal to the absorption edge energies, making EXAFS an element specific technique. X-ray absorption taking place in the nucleus is merely an electronic transition between two quantum states. Due to scatter of X-rays from neighboring atoms, EXAFS can identify thermal and static disorder in bond distances. Even if the neighboring atoms are different from the absorbing atoms, EXAFS adds up the contributions of all atoms in the coordination sphere.

3.5.2 EXAFS Equation

Mathematically, EXAFS can be understood as

$$X(k) = \frac{\mu - \mu_0}{\mu_{0j}} = \sum_j \frac{N_j f_j(k) e^{-2k^2\sigma_j^2}}{kR_j^2} sin[2kR_j + \delta_j(\mathrm{k})]$$

This equation is known as the standard EXAFS equation [62] and is the basis of all EXAFS calculations. Here, $\triangle\mu = \mu - \mu_0$ is the oscillatory part of the absorption coefficient which is normalized per atom by μ_0, the absorption for a singular atom. Further, $f(k)$ and$\delta(k)$ are the scattering properties of the atoms surrounding the exciting atom (for this study, the absorbing atom is uranium), N is the total number of atoms surrounding the absorbing atom, R is the distance to the neighboring atoms and σ^2 is the Debye Waller factor which gives the disorder in the distance of the near-neighbor atoms (O, U) from the absorbing atom (U). Using this equation, it is possible to determine the N, R and σ^2 if the scattering amplitude $f(k)$ and the phase shift $\delta(k)$ are known. The scattering properties are inherent to the atom being interrogated and is dependent on the atomic number of the species. The orientation of the sample is spherically averaged and the photoelectron wave vector is defined as,

$$k = |k| = \frac{2m_e}{\hbar} \left(\hbar\lambda - E_0\right)^{\frac{1}{2}}$$

where λ is the X-ray wavelength, m_e is the electron mass and E_0 is the final ionization threshold energy for the photoelectron. The modification of the final state of the photoelectron, known as EXAFS, takes the form of a damped non-linear sine wave.

3.5.3 EXAFS Data Analysis

The first step in EXAFS data analysis requires the isolation of the extended XAFS from the entire spectra using sophisticated background subtraction routines over the region. The EXAFS spectra is superimposed on a background of an atom of the target element in the absence of any other absorption edges. The background is removed by extrapolated Victoreen or other polynomial fit to the pre-edge region below the absorption edge. Above the absorption edge, the atom-like background consists of a monotonically decreasing part and a slowly oscillating part at low values of the photoelectron wave vector, k.

Assumption regarding the frequency of the EXAFS being greater than the background contributions can be maintained by neglecting the first few coefficients in the Fourier synthesis. In this study, the background is approximated using a weighted smooth polynomial spline function determined by the least squares fit of the EXAFS region. The spline, a series of semi-independent functions allows, a better approximation than other background subtraction techniques by avoiding contributions due to anomalous data points in the background. Adequate fitting of the spline polynomial is a tedious and a crucial part of EXAFS analysis of radiation damaged samples. Care is taken to ensure that the spline parameters are similar for all the samples in each set to ensure consistent results, especially with that

of the reference sample.

Finally, there could still be residual background components present even after thorough background subtraction and Fourier filtering. The effects due to these components on the data can be minimized using a variable background fit to the low frequency components during curve fitting. Alternatively, background from a structurally and chemically similar standard can be used for background subtraction.

After background removal, a spline polynomial is used to normalized the EXAFS amplitude relative to the absorption edge height. This step is necessary for the determination of the number of neighboring scattering atoms. The extrapolated value of the background using subtraction techniques near the absorption edge and the decrease in the elemental absorption of the target is used as an approximation to determine the atom-like absorption, μ_0.

Fourier transforms are widely used for the presentation of EXAFS data. Using Fourier analysis, EXAFS data from its original k-space (Å^{-1}) is transformed to radial structure function of the scattering atoms around the absorbed in R-space (Å). In this Fourier transform, the peaks correspond to the scattering amplitude from each shell. The location, size and shape of the peak is dependent on the absorber-scatterer distance, the type and the number of atoms in each crystallographic shells and the Debye Waller factors (σ^2). Further, a Fourier filtering technique can be used to isolate the contribution from individual shells by back-transforming the Fourier transform over the limited range of a single feature in the Fourier spectra.

Transforms of EXAFS weighted by a power of k. For scatterers of $Z < 36$, the transforms are usually weighted by k^3 (as was done in this study) since this method best nullifies the

k^{-1} dependence of the EXAFS and the energy dependence of the amplitude, making the EXAFS amplitude consistent over the entire energy range. Using a lower power of k to weight the EXAFS increases the contribution of the lower k-region to the Fourier transform, thus maximizing the contribution of the low-Z atoms. Increase in the relative size of a Fourier transform weighted with higher power of k indicates a higher Z element in the scattering shell. The position of the low-Z elements tends to shift more than high-Z as a function of the k-weight power. Therefore, the radial distribution function from the Fourier transform is a function of the k-weighting factor. These basic steps of EXAFS data analysis are outline in Fig. 25 through Fig. 26.

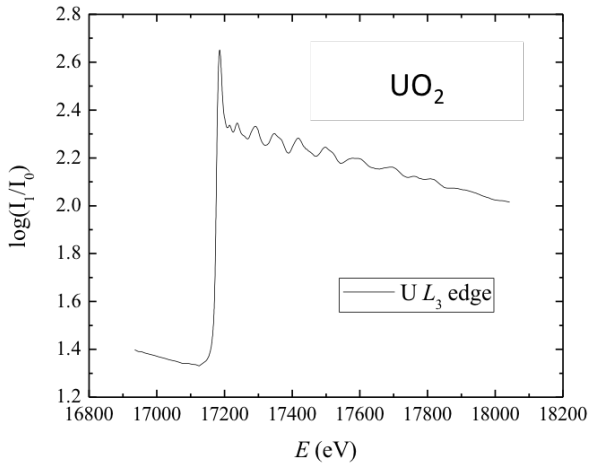

Figure 25: Absorption spectra for UO_2 with U L_{III} edge step at 17163.24 eV

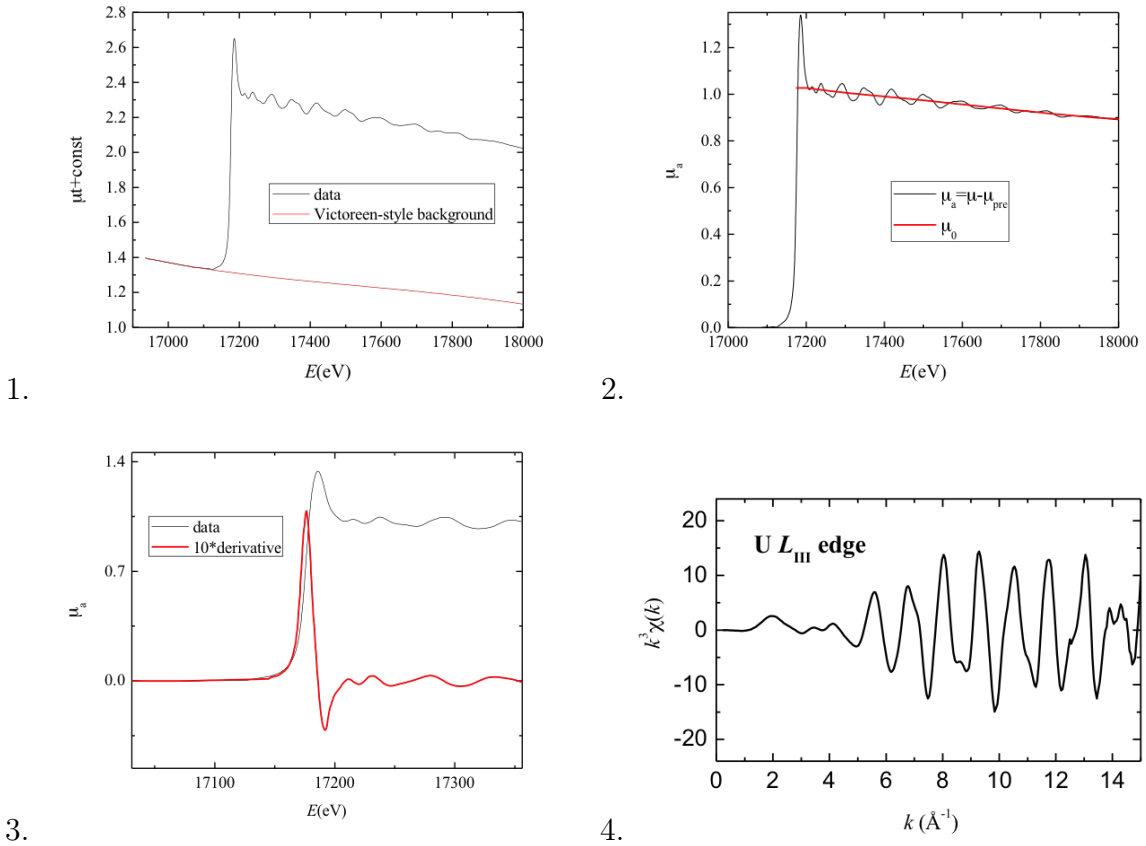

1. 2. 3. 4.

Figure 26: Figure 24.1-24.4 show the background subtraction and EXAFS fitting process in the post edge regime. Fig. 24.1 demonstrates the technique of background subtraction using a Victoreen. Fig. 24.2 shows fitting of the post edge region with a polynomial and Fig. 24.3 isolates the edge energy for the data. Finally, Fig. 24.4 is the calculated k^3 weighted EXAFS spectra for the UL_{III} edge.

3.5.4 EXAFS Experimentation

Ion irradiated samples were loaded on dedicated samples holders for the EXAFS measurements at Stanford Synchrotron Radiation Lab. Each set of irradiated samples was measured along with a pristine UO_2 sample that was derived from the same original material as the

irradiated samples. A pristine sample acts as a reference and any structural deviation from this is an indication of radiation damage due to ion implantation. The samples were mounted in a glove box at University of Wisconsin Ion Beam Lab for H^+ and He^{2+} irradiated samples and at the Idaho National Lab for the Krypton implanted samples. The sample holder was then lined with an Indium wire to act as a vacuum seal and was then checked for any vacuum leaks using a vacuum desiccator. Experiment geometry for the samples was again dependent on the ion implantation depth in the same. To study radiation damage, only the implantation depth must be interrogated by the synchrotron X-rays and therefore the samples were adequately turned to select X-ray incidence angles. Proton implanted samples were at the usual 45^o, He^{2+}samples were angled at $60^o$to the incident beam, and the Krypton irradiated samples have an implant depth of 1 μm and were therefore studied at a shallow incidence angle of 10° from the incident beam. In order to avoid the blockage of the beam by the sample holder, an aluminum plate was put in the holder to elevate the samples for accurate measurements. Fig. 27 shows an unassembled and assembled sample holder for EXAFS measurements.

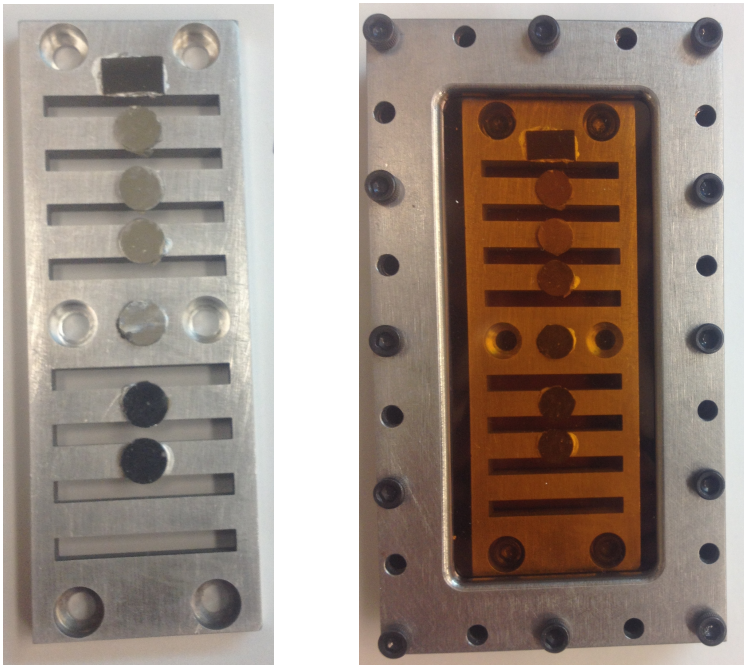

Figure 27: Unassembled and assembled sample holder with Krypton irradiated d-UO_2 samples for EXAFS measurements. The first sample is a piece of silicon for identification of the order of samples. The samples are then in increasing order of radiation dose. The unassembled sample holder is an image of the samples loaded on an aluminum plate to raise the height of the samples so that the outsides of the sample holder don't block the beam.

EXAFS measurements are typically done at synchrotrons as they provide a full range of high energy X-rays and high quality detectors. A Silicon [220] monochromator that uses Bragg diffraction to select a particular energy was used. The monochromator is required to have a high energy resolution of ~ 1 eV for 10 keV. Samples are measured at a temperature of ~70 K as the samples are inserted in a liquid nitrogen cooled chamber to minimize thermal affects on the structure determination. Collimating slits ensure the beam is accurately sized to study the irradiated region of the sample. An illustration of the EXAFS beam and sample set up is shown in Fig. 28 and Fig. 29.

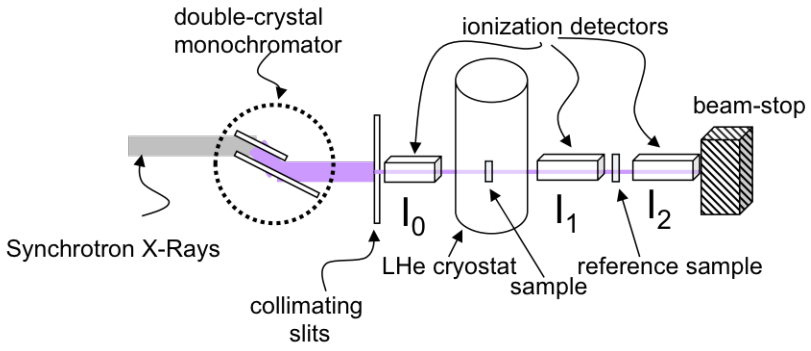

Figure 28: EXAFS setup

EXAFS spectra for the samples in this study were measured at the Stanford Synchrotron Radiation Laboratory under dedicated operating conditions (3.0 GeV, 50 - 100 mA) on end stations 11 - 2 and 4 - 1. Sample holders are attached to a cold finger of liquid nitrogen cryostat to ensure low sample temperate of 80 K. Harmonics in the detection were eliminated with a flat Pt-coated mirror tilted to a cutoff energy of 20 - 25 keV. The spectra were recorded using a state-of-the-art multi-element Germanium detector and digital amplifiers. Dead time correction of 1 μs was applied to adjust the absorption peak to match the transmission data. The edge energy of the sample (UL_{III}) is approximately 17163.24 eV which was interrogated in this study. The typical accuracy of the energies collected in a given EXAFS experiment are within 0.2 - 0.3 eV

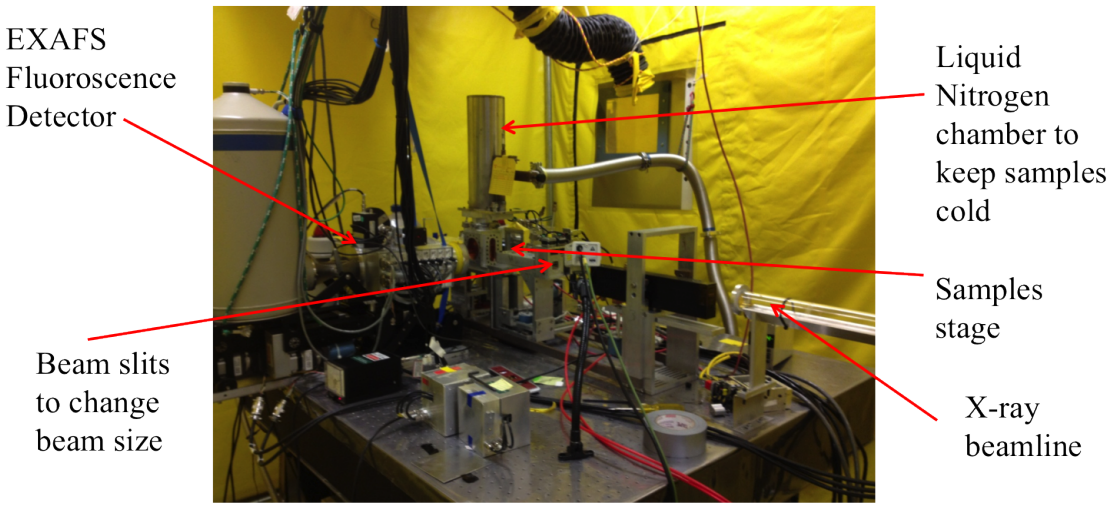

Figure 29: SSRL beamline Hutch setup

3.6 Simulation and Theoretical Calculation

Experimentation is crucial for validation of theoretical understanding of the evolution of radiation damage from onset to fully developed stage. However, in this case theoretical calculations were performed to verify the empirical data from the various measurement techniques. Close comparison with molecular dynamics (MD and CD) results in ion implanted UO_2 is performed to understand the distribution of point defects following an irradiation spike event and their evolution and annihilation with time. Therefore, MD is an excellent tool to study the interaction of defects and to simulate the kinetics of the process governing microstructure growth following irradiation. Cluster dynamics (CD), a simulation technique based on rate theory equations, can model the evolution of point defects to larger scale defects over extended time frames, similar to that of experiments [43]. CD can further interrogate the stoichiometry and relative concentration of the microstructure defects, such

as voids and dislocation loops, which have been simulated using experimental information. Therefore, CD has been used to understand the relationship between larger scale defects seen in a transmission electron microscope and smaller scale defects observed using EXAFS techniques.

Further, FEFF-9 software was used to generate EXAFS spectra for UO_2 unit cells to compare to the irradiated samples and to generate a list of atomic positions for the atoms in the unit cells **[70]**. These atomic positions were then inserted into Artemis and Athena software for EXAFS data interpretation to create simulations on creating interstitials and vacancies in the lattice structure [39]. This was done to understand the effect of individual point defects on the overall EXAFS spectra generated by the bulk samples. Finally, basic calculations were performed to understand the fundamental relationship between radiation induced defects on large and small length scales (explained in the Discussion section). These calculations, while rudimentary, have provided unique information regarding the differences in the effect of stoichiometry of large defects and small defects on EXAFS measurements.

3.7 Summary of Instrumentation

To adequately address the science of radiation damage so as to answer the questions in this study, suitable instrumentation and techniques were identified and employed. The analysis methods used were targeted to study the evolution of structure on smaller length scales to investigate point defect clustering and lattice damage, and the also targeted towards larger length scale structure evolution in the material. Transmission Electron Microscopy techniques have been employed for dislocation, bubble and other larger scale damage studies.

X-ray Diffraction measurements were used to then identify the change in lattice parameter and the difference in phase of irradiated UO_2. Extended Xray Absorption Fine Structure measurements were used to study the changes in near neighbor correlations, the relative position of atoms and the spread of atoms due to ion damage. Simulation methods were crucial in validating the empirical results, and giving a more visual understanding of radiation damage on various stages after its onset. Collectively, the chosen techniques give a wholesome idea of the extent and difference in radiation damage on various length scales resulting from varying irradiation conditions.

The next few sections discuss the experiments performed and the results obtained in this study.

4 Proton Experiments

Abstract: Radiation damage in the nuclear fuel is largely responsible for decline of fuel efficiency and thermal transport over the course of reactor operation [93]. Neutrons in the reactor emerge at high energies resulting from fission and proceed to not only sustain a nuclear chain reaction but also create radiation induced microstructures in the fuel material. Several studies relate the damage mechanism due to H^+ (or proton) irradiation to neutron irradiations in a nuclear reactor environment [33]. Therefore, the effect of low temperature proton irradiation was examined as function of radiation dose (in DPA) in polycrystalline UO_2. Radiation damage on lattice and microstructure scale was studied by a systematic evolution of H^+ dose in UO_2 using Extended X-ray Absorption Fine Structure measurements, X-ray Diffraction and Transmission Electron Microscopy. XAFS measurements indicate an expansion of the lattice coupled with modified local structure at all dose levels. At higher doses, mid range features also begin to get distorted resulting from lattice damage and phase reorganization in UO_2. XAFS results are corroborated by XRD analysis that shows a consistent lattice expansion with increase in radiation dose in UO_2. TEM micrographs reveal that H^+ irradiation almost exclusively produces dislocation dominant microstructure in UO_2 with the density and size of dislocations increasing with increasing ion dose. Overall, the damage structure analysis reveals the presence of off-stoichiometric regions that on average give the appearance of a stoichiometric fluorite but in fact, show variation from UO_2 phase locally.

4.1 Sample Preparation

Sample preparation of oxide ceramics offers a unique challenge in terms of cutting samples into the right sizes and further polishing them to a mirror finish to continue interrogation. Unlike metals, ceramics are brittle and tend to flake off when friction is applied. To make things even more challenging, the ceramic UO_2 samples in this case are radioactive and need special handling including new set of equipment, separately designated rooms to conduct sample preparation and special waste mitigation solutions. Protocols unique to conducting sample preparation in laboratories was put in place for smooth execution of sample handling.

4.1.1 High Dose (0.4 - 0.5 DPA) Samples

The samples were obtained from Chalk River Lab and were fabricated by heating fused UO_2 with hyperstoichiometric UO_2at 1900 K in a hydrogen atmosphere. The lattice constant was determined to be a = 5.473 $\pm$ 0.001 Å by neutron scattering measurements at room temperature, implying that the O/U ratio was very close to 2. These samples were further prepared at the Materials Fuels Complex at the Idaho National Lab (INL). At the INL, these UO_2 samples were cut into disks about 3 mm in diameter and 700 µm in thickness. This was followed by polishing the sample surface to a mirror finish by hand polishing.

Due to the brittle nature of ceramics, performing ion irradiations can also be a significant challenge. Following the irradiations samples of higher fluences had undergone surface blistering due to the high concentration of the incoming ion that led to lattice strain and compromised the surface integrity of the samples. There existed regions in the sample that were not affected by blistering of the sample surface and were therefore chosen as areas

for further analysis. The blistering of the sample at 0.5 DPA was then established as the maximum dose level in this experiment. All sample dose levels were maintained below this maximum level to avoid extraneous effects due to blistering and lattice strain resulting from the blistering.

4.1.2 Intermediate Dose (0.2 - 0.3 DPA) Samples

Intermediate dose irradiation samples were obtained at the Idaho National Lab. The UO_2 sample preparation was performed at Center for Advanced Energy studies by first cutting the depleted UO_2 pellets into squares of 2 mm length using a diamond saw in a glove box. The samples were subsequently polished to 0.5 µm finish by hand polishing the surface of the samples that was to be irradiated. Sample polishing was also performed in a glovebox environment. The cutting and the polishing of samples is shown in Fig. 30. These samples were subsequently transferred into membrane box containers and shipped to the University of Wisconsin Ion Beam Lab for ion irradiation.

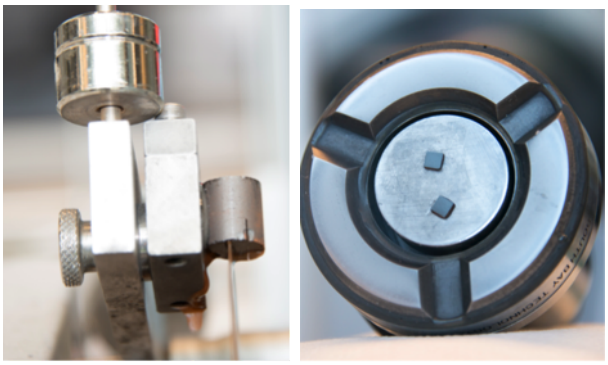

Figure 30: Samples prep at CAES for d-UO_2 samples for 0.2 DPA proton irradiation

4.1.3 Low Dose (0.01-0.1) DPA Samples

The UO_2 samples used for low dose irradiation were sintered at Los Alamos National Lab. The feedstock powders were prepared by milling depleted UO_2 powder with 0.25 wt.% ethylene bis-stearamide in alumina SPEX mill for 15 minutes before sieving through a 200 screen mesh. Typical powder impurities were below the detection limit of the inductively coupled mass spectrometer measurement, with the exception of 11 ppm Al content. About 1 gram of the UO_2 powder was pressed in a 6.22 mm single action die at roughly 80 Mpa and held for 60 seconds. Densification of the pellets was performed in a tungsten metal furnace where the UO_2 pellets were placed on a tantalum foil inserted on top of tungsten furnace trays. These pellets were then sintered in partial pressure of argon containing 5-10 ppm of oxygen for four hours at 1650^oC. The atmosphere was changed to argon containing 6% hydrogen during furnace cooling so as to have minimal change of UO_2 stoichiometry. This process produces 5.2 mm diameter pellets, 4.3 mm in height within 95-96% of theoretical density. These pellets were then sliced into 0.6 mm thickness slices using a low speed diamond saw at the Idaho National Lab and then polished to a mirror finish using diamond suspensions (15-0.25 µm) prior to ion irradiations. All the ion irradiation and EXAFS parameters were verified against the UO_2 crystal and stoichiometric powder samples to make sure there are no outlying effects due to the difference in sample source.

4.2 H^+ Implants

The University of Wisconsin Ion Beam Laboratory was used to produce a steady current of protons, which were accelerated to 2.6 MeV using a Pelletron tandem, Van de Graaff type

accelerator (proudly shown in Fig. 31) . A source of Negative Ions Sputtering (SNICS) produced H^+ions for the high dose (0.4-0.5 DPA) irradiation using a TiH cathode. In case of the intermediate dose and the low dose irradiations, a toroidal volume ion source (TORVIS) was used to produce H^+ ions for the irradiation. The beam was rasterized across the sample to achieve a uniform distribution of ions over the specimen surface. Beam current was recorded throughout the irradiation and the temperature of the samples was between 300 and 400 ^oC. The temperature of the samples was due to beam assisted heating only.

Samples were prepared from the region with steady damage profile and measurements were made such that only the damage plateau was interrogated. Sample temperatures during the irradiation were controlled by heating and cooling the stage when necessary. To cool the samples, both air cooling and water cooling was utilized via cooling lines attached to the stage. Temperature monitoring was performed using thermocouples and a thermal imaging camera device. Three k-type thermocouples were spot welded to the side of the samples to determine the temperature during the course of the irradiation. The thermal imaging camera that was used as an additional temperature validation source, utilized an infra-red pyrometer, which is calibrated for the irradiation temperature range and the emissivity of the material. The camera was employed to ensure consistent beam assisted heating along the sample surface during the course of the irradiation.

Figure 31: University of Wisconsin – Madison Ion Accelerator that was used to perform 2.6 MeV H^+ and 3.9 MeV He^{2+} irradiations.

The irradiation stage was made of molybdenum and copper due to their high thermal conductivity and resistance to sputtering. During the course of this study, various materials were employed to improve thermal transport and maintain sample integrity. Some of the materials include alumina paste, which offers a matrix for the samples during irradiation, and also silver backing gel, used for high thermal conductivity.

Apertures were used to control the beam distribution on irradiation targets and the irradiation region area. Fig. 32 shows the irradiation stage setup with apertures in place ready to be installed in the ion accelerator prior to irradiations. Ion beam emerging through the accelerator on the target is rasterized across target surface to ensure uniform irradiation conditions. Ceramic stands are used to electrically isolate the apertures from the irradiation surface. A sophisticated LabVIEW system (National Instruments product) was designed to monitor beam current as a function of time, temperature monitored via thermocouples while simultaneously calculating total fluence on the material. This setup provides the temperature

and beam current history by recording values during the course of the irradiation.

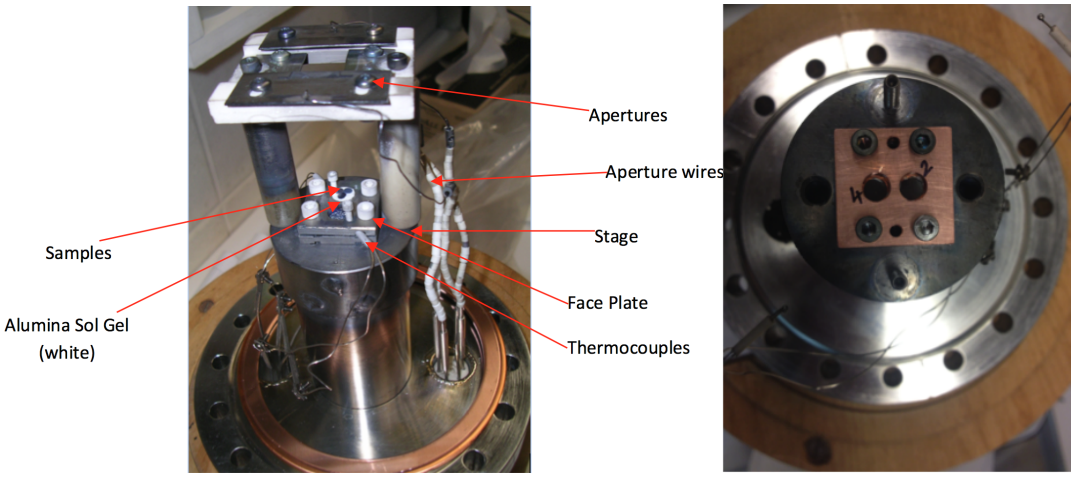

Figure 32: Fully assembled irradiation stage set up ready to be loaded in the ion accelerator at University of Wisconsin Ion Beam Lab.

Stopping Range of Ions in Matter (SRIM) based on the quick Kinchin-Pease model [84] was used to calculate the associated damage rate and the proton irradiations were performed at the University of Wisconsin Ion Beam Lab . The resulting radiation damage profile was almost flat up to 30 µm deep from the irradiation surface. The threshold displacement energies were set to 20 and 40 eV for oxygen and uranium respectively. The depth dependent radiation damage is shown in Fig. 33.

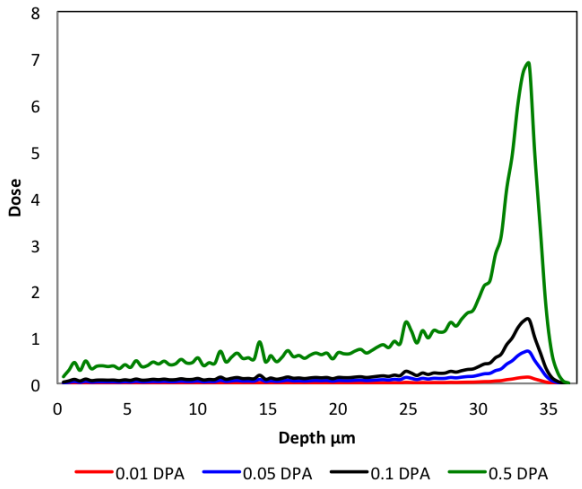

Figure 33: SRIM DPA profile of dUO2 with H+ ions.

The final set of proton implantations were performed to bridge the data gap between the 0.4 - 0.5 DPA and the 0.01 - 0.1 DPA implants, hence the dose of these set of samples was 0.2 DPA. The irradiations were also performed under the dedicated conditions of the University of Wisconsin Ion Beam Laboratory where protons were accelerated to 2.6 MeV using an ion accelerator. All the conditions were made to be consistent with the other two ion irradiations, such as temperature, beam current, sample stage, etc. This was done to eliminate any effects on radiation damage measurements due to any of the previously mentioned factors.

4.3 EXAFS on H^+ Irradiated Samples

The Extended X-ray Absorption Fine Structure measurements were performed at the Stanford Synchrotron Radiation Lab for the low dose (0.01-0.1 DPA) and the high dose (0.4-0.5 DPA) samples. Both sets of samples were analyzed at beam end station 11-2 at an angle of

45^o to the X-ray beam. The long ion implantation depth of 30 µm in case of H^+ irradiation ensures that the X-ray probing volume is of a consistent damage profile. Harmonics were eliminated with a flat, Pt coated mirror tilted to a cutoff energy of 20-25 keV. The measurements were performed in fluorescence mode using a multi-element Ge detector. Calibration of energy was performed by measuring the spectrum of a Zr foil, either as a part of the U spectrum or immediately before U spectrum, defining the energy of the first inflection point as 17999.35 eV. The accuracy associated with this technique is ± 0.2 - 0.3 eV. Dead time correction of 1 µs was applied to adjust the absorption peak heigh to match that of the transmission data. All the data obtained was analyzed by curve fitting using amplitudes and phases calculated by FEFF9 code **[70]**. The results of the curve fits are presented in Table 4. Results for individual spectra contain an error that was derived by varying the parameter until the least squares error was higher than the best fit by 10% of the difference between the best fit and the fit without the shell in question. Results for all the spectra where the crystallographic UO_2 shells and the anharmonic O shell that are fit have been reported.

In case of the 0.2 DPA samples were collected at the 10-BMB MRCAT beamline at the Advanced Photon Source. An undulator produced polychromatic X-rays and wavelength was selected using a Si(111) double crystal monochromator. Higher harmonics were removed using a detuning rocking curve at 50%. The energy was calibrated to the U K-edge (17163 eV) of a UO_2 and Zr foil run in fluorescence and transmission geometry respectively with incident and transmitted X-ray monitored by ionization detectors. The irradiated UO_2 samples were measured in fluorescence geometry using an element Vortex detector. The I_0 ion chamber used 85% N2 : 15% Ar, the I_t and the fluorescence ion chamber used 100% Ar as the fill gas.

The extended X-ray absorption fine structure was extracted from the spectra by first

subtracting out the absorption edge using a sum of arctangent and gaussian fit to the edge and the peak. A polynomial spline was then fit to the remaining spectrum to approximate the smooth absorption of an atom. The spline knots were optimized by minimizing the area of the Fourier transform modulus of the EXAFS from 0 to 1.2 Å. Effort was made to ensure similar values for the spline knots for all the sample spectra to minimize the effects of background noise on data analysis. The E_0 for the spectra during data analysis was set to 17172.0 eV [87]. Results are discussed in terms of N, the number of atoms in each shell, r, the U-O/U distances, and σ, the pairwise Debye-Waller factors, which were obtained by curve fits of the $\chi(k)$ data over the ranges depicted in figures, which utilized the full spectral range available.

Fourier transforms $(\chi(R))$, were performed over the same range, using k^3 weighting to enhance the accuracy for the O shells, especially at higher R, and a sine window. Pairwise U-O and U-U curve fitting parameters were obtained using FEFF9 code as mentioned previously. Using this, the total spectrum for the three samples was obtained and was best scaled to match the experimental data. The number of shells was kept limited to four, with three corresponding to the crystallographic shells in UO_2 and fourth shell was to fit the small oxygen type distribution on the low R side (at approximately 1.8 Å) of the original O peak. Debye-Waller factors were set to 0.045 for the non-crystallographic O shell, similar to the original O peak. All other parameters were allowed to float unless they were exceptionally large or small.

The XAFS parameters of N, r and σ were derived by calculating the difference in the least squares errors between spectra with contribution from all shells and the spectra without a particular shell for each of the fit shells. The number of independent parameters were

calculated for k = 2.7 - 14.9 Å^{-1} and R = 1.2 - 4.6 Å fitting ranges for these experiments is 28. It is imperative to perform direct comparison of all the resulting parameters to the reported values to adequately validate the results of the fits. Subsequently, real part of the spectra and the moduli of the transforms are necessary for identification of the oxo groups and partial radial distribution functions are used for verifying values for each shell.

4.4 Results

This section reports the results of EXAFS spectra collected at the Stanford Synchrotron Radiation Laboratory to determine the cumulative effect of disrupted short range order and the microstructure due to H^+ ion irradiation. Inspection of the $\chi(R)$ reveals aspects of the changes to the average local structure of the target element, in this case as a function of increasing H^+ ion dose. The pristine sample with no dose and the lowest dose sample at 0.01 DPA have a spectra of cubic, fluorite type oxide. The first near neighbor crystallographic O peak is due to contribution of eight nearest neighbor O atoms, well separated from the more distant second nearest neighbor metal peak of uranium whose larger amplitude reflects its higher Z and 12 atoms. The higher R features in these samples are seemingly well ordered again similar to the fluorite oxide. As the ion dose increases, the amplitudes of all the peaks decreases monotonically, indicative of diminished order via displacement of U and O atoms from their lattice sites coupled to the incorporation of the non stoichiometric O atoms into interstitial, defect sites. The loss of amplitude is remarkably seen to occur uniformly throughout the range of the spectra. Randomly located defects would result in a more significant amplitude loss, which hasn't been seen in this set of samples. This could indicate

that the radiation induced defects tend to cluster so that a significant fraction of the lattice retains its original UO_2 structure with potentially smaller cluster regions of defects. Defect clustering in UO_2 has been studied and is predominantly due to oxygen atom clustering to form interstitial clusters and small, nano domains of U_4O_9 [74].

The nearest neighbor O peak is the only large feature that displays any behavior that differs from this simple loss of amplitude As the H^+ ion dose increases, a shoulder on the low R side becomes more prominent relative to the rapidly diminishing primary O peak. In case of the highest dose sample of 0.5 DPA, the shoulder peak on the low R side is a fully resolved independent peak next to the original O peak. This implies that the underlying near neighbor distribution is splitting into a dual site oxygen distribution. Initial interpretation of this data also indicates that oxygen ions are rearranging as uranyl type bonds that are highly stable due to their oblate geometry as a result of irradiation (and not oxidation). The increase in the height of the shoulder peak is so significant that if analyzed in isolation, these features would be unequivocally assigned to structural components due to their large size relative to the original oxygen peak.

Curve fitting features can only refine the particular model used (in this case, UO_2) and it is unable to introduce features that are not present initially. This assumes that the average number of nearest neighbors does not vary significantly from that found in the starting $UO_{2.00}$, and these atoms are arranged so that they all make distinct identifiable contributions to the spectrum. This constraint gave good fits, but for all the irradiated spectra these fits included small shoulder features on the low R side of the original O peak. The total number of atoms in the fitting process for any of the peaks wasn't fixed, but instead allowed to float.

There is good long-range order in the irradiated irradiated samples but the near neighbor

U-U amplitude at 3.87 Å is seen to decrease consistently with increasing dose. Simultaneously, the oxygen shell fit at 1.8 Å increases with increasing dose. This 1.8 Å oxygen shell results in the aforementioned multisite distribution of oxygen ions closer to the absorbing atom (uranium) than the original crystallographic position of oxygen at 2.36 Å. In stoichiometric, pristine UO_2 there are three crystallographic shells fit using EXAFS: 8 atoms in the first shell of oxygen (U-O) at 2.36 Å, second shell of uranium (U-U) at 3.86 Å with 12 uranium atoms and third shell of oxygen at 4.5 Å with 24 oxygen atoms. The new 1.8 Å shell has become evident and consistently more prominent with increasing irradiation dose. Of the 6 proton irradiated samples, the pristine and low dose samples have long-range order similar to documented UO_2. Disruption in local structure is evident in low and high dose samples and it increases with dose. The high dose proton irradiated sample has highly damaged structure overall and appears to be significantly affected by ion implantation. The summary of all the fit parameters is shown in Table 3.

Sample		U-O (1.8 Å)	U-O (2.36 Å)	U-U (3.85)	U-O (4.5)
Crystal	R		2.36	3.85	4.52
	N		8	12	24
Reference sample	R		2.35	3.85	4.48
	N		8	12	24
	σ		0.047	0.002	0.073
0.01 DPA	R	1.9± 0.02	2.35± 0.02	3.85± 0.1	4.45± 0.7
	N	0.12± 0.01	7.12± 2.2	11.43± 2.7	20.66± 3.7
	σ	0.045	0.05± 0.01	0.05± 0.01	0.06± 0.01
0.05 DPA	R	1.88± 0.02	2.36± 0.02	3.85± 0.1	4.45± 0.2
	N	0.21± 0.03	6.96± 1.4	11.02± 2.6	18.85± 3.1
	σ	0.05	0.045± 0.01	0.045± 0.01	0.06± 0.01
0.1 DPA	R	1.87± 0.02	2.36± 0.02	3.87± 0.1	4.44± 0.6
	N	0.29± 0.04	5.28± 1.1	9.11± 2.1	18.73± 3.1
	σ	0.05	0.045± 0.01	0.04± 0.01	0.045± 0.01
0.2 DPA	R	1.84	2.356± 0.02	3.87± 0.1	4.543± 0.4
	N	0.56	5.07± 1.03	8.24± 1.8	17.92± 3.1
	σ	0.04	0.04± 0.01	0.04± 0.0	0.05± 0.01
0.4 DPA	R	1.81± 0.02	2.36± 0.02	3.87± 0.1	4.54± 0.2
	N	0.98± 0.2	4.61± 0.8	7.44± 1.3	16.42± 2.6
	σ	0.04	0.043± 0.01	0.029± 0.005	0.03± 0.008
0.5 DPA	R	1.82± 0.02	2.358± 0.02	3.867± 0.1	4.47± 0.2
	N	1.05± 0.8	3.82± 0.08	6.67± 1.2	13.94± 1.9
	σ	0.04	0.044± 0.01	0.035± 0.008	0.025± 0.006

Table 3: Fitting parameters for the krypton implanted UO_2 samples.

The presence of the O type distribution on the low R side of the peak suggests the presence of oxygen moeties with irregular valence to exist as stable aggregates alongside the original peak. One possible explanation if the presence of a very short U-O corresponding to a contracted, non-bridging uranyl moiety. The uranyl moiety, also seen in XAFS studies done on UO_{2+x}, is highly stable due to its oblate shape and can therefore form due to lattice excitation in UO_2 resulting from ion irradiation [31]. Uranyl type molecules are also commonly found in used nuclear fuel in storage and can form complex molecules with

neighboring actinides [15], and therefore their presence in irradiated UO_2 doesn't come as a surprise. In fact, recent analysis of the Fukushima-Daiichi accident shows the presence of series of uranyl peroxide compounds in the form of nanoscale cage clusters of uranyl ions bonded to form complicated compounds. Another possibility, as indicated by the monotonic loss of spectral amplitude is the presence of defect clusters in the lattice. The presence of randomly located defects would cause a faster loss of spectral features, something that hasn't been seen in this case.

In Fig. 34, the pristine sample was fit to stoichiometric UO_2 therefore the first distinct peak is that of oxygen in its crystallographic position followed by higher peak of uranium due to its high Z. The zero dose material has the same features as literature UO_2 [19], with primary contributions from the three crystallographic shells. The errors in the fit are within experimental error of the crystallographic reported data and the low dose samples exhibit similar distances to stoichiometric UO_2 lattice. The low dose materials (Fig. 35-36) resemble UO_2 in their long-range order and seems to have an oxo type of shell at 1.8 Å, and there are also some small differences from the control sample, such as mid range features beginning to change. Through increasing in ion dose, there are consistent trends with loss of spectral amplitude and increase in the magnitude of the oxygen shoulder. This is seen in Fig 37-40. This evolution of lattice structure with dose indicates that the radiation is consistently distorting the lattice. Therefore, high dose sample (0.5 DPA) demonstrates a significant level of local structure disorder. The high R peaks are gone and there are significant contributions to the EXAFS in addition to the three crystallographic shells as seen in Fig. 40.

By isolating the oxo shoulder at 1.8 Å, it can be seen that again in Table 8, with increasing proton dose, the ratio of the number of atoms to the Debye-Waller factor increases

with increasing proton dose. This indicates the clustering of oxygen defects at low-R while simultaneously the primary peak diminishes implying a disorder in the lattice structure due to radiation damage. There is more detailed explanation regarding the type of disorder in the discussion section.

The H^+ irradiated UO_2 are fit with the three nearest neighbor shells of UO_2, O at 2.36 Å, U around 3.87 Å, second O around 4.54 Å, which is slightly greater than literature values of UO_2 as shown in Fig. 41. The near neighbor distances in these samples are 0.01 Å larger than stoichiometric UO_2, indicating that the irradiation is in fact increasing the size of the lattice locally with increasing ion dose. This change is consistent with measurements done using He^{2+} atoms in UO_2 showing an expansion of the lattice in XRD measurements. Therefore, ion irradiation is not just simply distorting the lattice, but is creating complex defect structures that result in local lattice expansion.

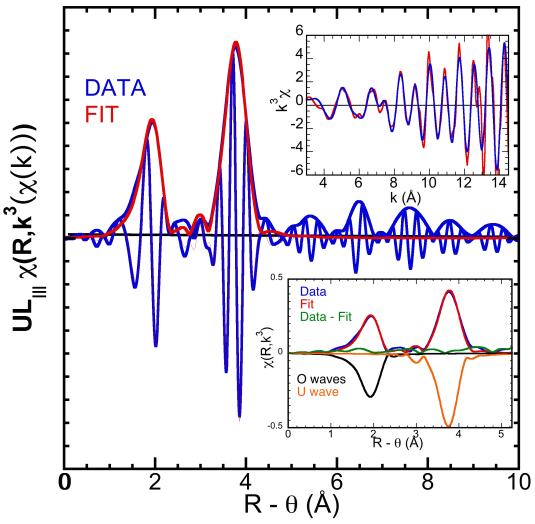

Figure 34: Reference sample is identical to the literature UO_2 as seen in the Fourier transform with negligible difference between "Data" and "Fit".

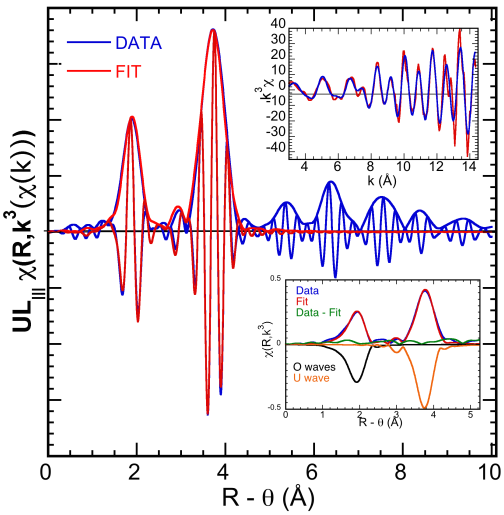

Figure 35: 0.01 DPA lowest dose sample has same peak positions as the reference sample with well ordered structure. The peak amplitude loss is insignificant at this dose level.

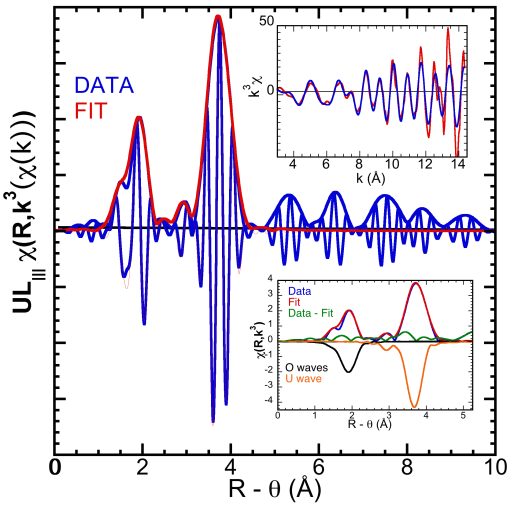

Figure 36: 0.05 DPA Intermediate dose sample shows the onset of oxo shoulder on the low R side of the original oxygen peak.

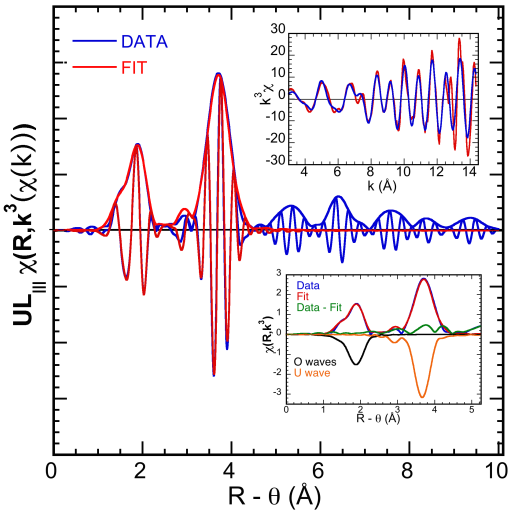

Figure 37: 0.1 DPA sample shows that the oxo shoulder is becoming more prominent and the overall peak amplitude has significantly decreased.

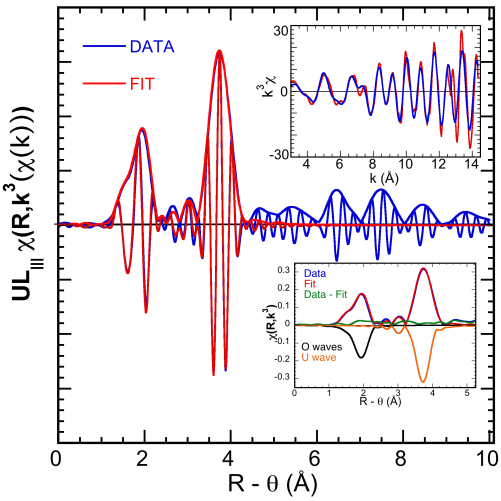

Figure 38: 0.2 DPA samples were studied at the Advanced Photon Source. This sample shows loss of amplitude and rise of oxo shoulder in sync with the other proton implanted samples.

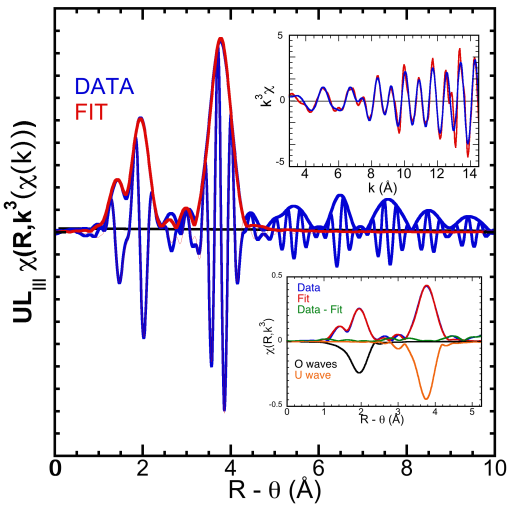

Figure 39: 0.4 DPA sample shows that the peak amplitude decrease continues along with distinct non crystallographic oxygen peak at 1.8 Å.

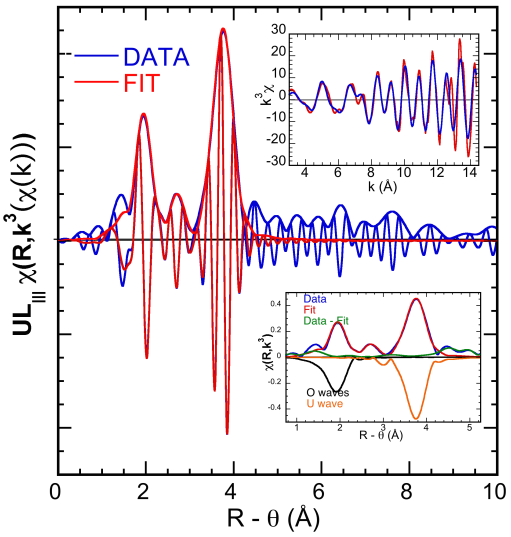

Figure 40: 0.5 DPA highest dose sample shows damage in intermediate structure along with loss of amplitude and rise in prominence of low-R oxygen shoulder.

Looking at Fig. 40, it can be seen that the lowest dose sample (0.01 DPA) has the

higher amplitude in the first O shell and almost the same amplitude as the intermediate dose sample (0.05 DPA) in the second U shell. With ion increasing dose, this amplitude quickly decreases and hence the highest dose sample (0.5 DPA) has the lowest amplitude for both the crystallographic O and U shells. This decrease in amplitude with dose is reversed for the 1.8 Å O shoulder where increasing dose results in a more prominent O-shoulder implying a higher amplitude. This trend of amplitude loss and rise of prominence of the oxygen shoulder continues through to the higher dose levels of 0.4 and 0.5 DPA samples. This trend is clearly seen in Fig. 41.

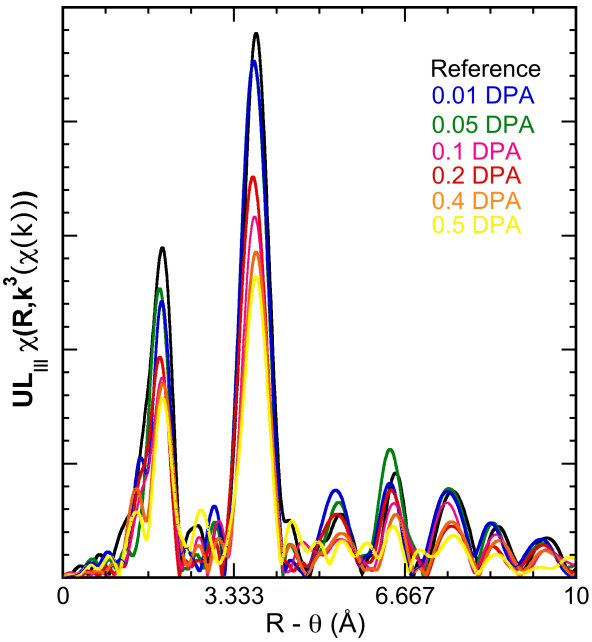

Figure 41: Modulus of all the peaks

It is imperative to study the relative size of the oxygen shoulder (at 1.8 Å) with increasing dose and consequently diminishing original oxygen peak (at 2.35 Å). This is done by multiplying the primary O peak in the irradiated samples with the ratio of the peak heights of the

control sample to the irradiated sample increases the contribution of the irradiated samples to match that of the pristine sample showing high significance of the oxo shoulder at 1.8 Å as shown in Fig. 42. This ensures that the modulus of the amplitudes for the crystallographic O peak are identical. In the case of the lowest dose (0.01 DPA) sample, this feature is non existent and the primary oxygen peak dominates. This O shoulder exists in the remaining four of the proton irradiated samples and grows with increasing ion dose as the primary O peak decreases. By multiplying the ratios it is evident that this peak isn't greater than the primary O peak (at 2.36 Å) but it does have a distinct shape and position that can be fit by a separate shell of oxygen atoms indicating a heightening secondary oxygen distribution due to irradiation.

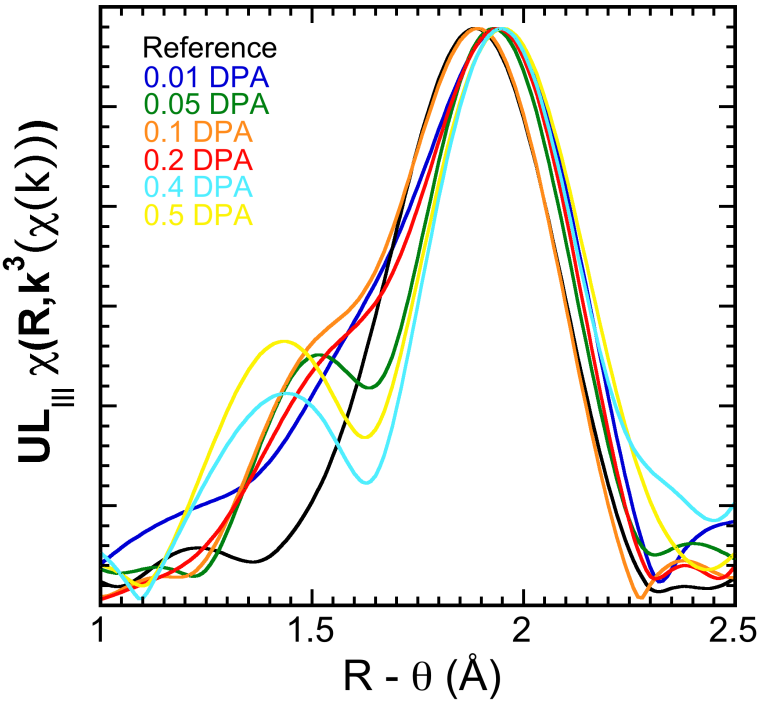

Figure 42: Fourier transform of low dose proton irradiated sample EXAFS

The Debye-Waller factors were obtained by curve fitting the $\chi(k)$ over the k range 2.7-14.95 using the full usable spectra. The Debye-Waller factors account for the structural and thermal disorder in the atoms of the molecule. Since the DW-factors give information regarding the vibration dynamics in a crystal, they tend to increase with increasing disorder. Further, while fitting the EXAFS samples, an increase in Debye-Waller factor results in a decrease in the number of atoms fit in each shell. To accurately comment on the state of disorder due to irradiation, Fig. 43 and 44 show the ratios of the number of atoms fit in each shell to the DW-factors. Using this approach, it can be seen that the the number of atoms in each shell is in fact decreasing and this can be attributed to the disorder in the lattice from

proton irradiation. However, it is worth noting that this decrease in amplitude is consistent across all the primary crystalline peaks but not in the oxygen shoulder at approximately 1.9 Å, where the amplitude increases with irradiation dose. The decrease in amplitude does not reflect the loss of atoms in the sample as the sample is a fully dense material. This loss of spectral peak is due to loss of atoms in their original crystallographic positions. Therefore, the atoms haven't been removed from the UO_2 sample due to ion irradiation, and the disorder is indicative of lattice damage resulting from local clustering of point defects that can be observed as the prominence of the non-crystallographic oxygen peak. The ratio of the number of atoms fit and the DW factor have also been shown in Table 4.

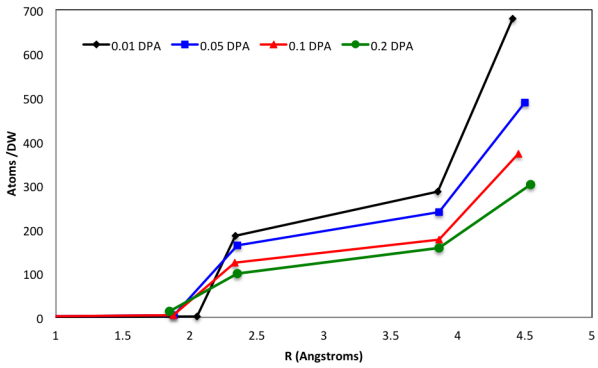

Figure 43: Atoms to Debye Waller factor ratio consistently decreases with increase R as seen for low dose samples.

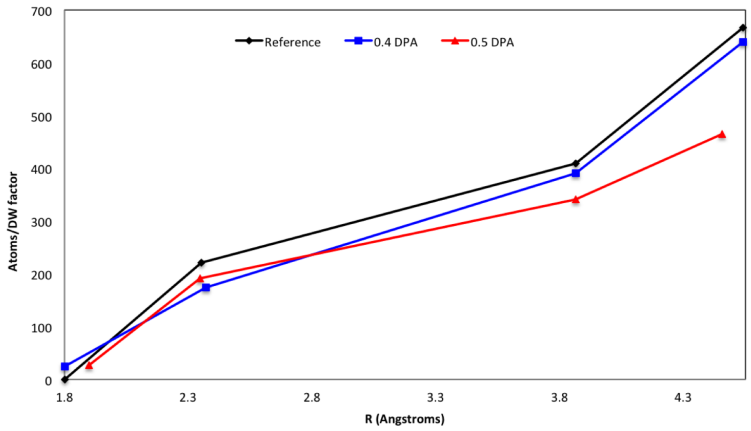

Figure 44: Similar to Fig. 42, the ratio of Atoms/ DW factor is shown (separately for clarity) to decrease with increasing ion dose in higher dose samples.

Table 4 shows the ratio of the number of atoms fit to the Debye-Waller factor for the 1.9 Å shoulder. This table shows that with increasing ion dose, the ratio of the number of atoms fit in the shoulder to the DW factor increases with increasing ion dose. This increase of the ratio in the shoulder occurs with the decrease in this ratio overall, implying that due to irradiation, defects are forming near the absorbing ion (uranium) at a distance of approximately 1.8 Å and this defect cluster appears to be growing in magnitude with higher irradiation dose. For the zero dose sample, this ratio is 2.8 which is quite small and continues to increase to 26.31 for the highest dose material.

Sample	Atom/ DW factor at 1.9 Å
0	0
0.01 DPA	2.66
0.05 DPA	4.25
0.1 DPA	5.87
0.2 DPA	14.45
0.4	24.5
0.5	26.25

Table 4: Ratio of number of atoms fit at 1.9 Å to the Debye Waller factor at that R increases with dose.

4.5 X-ray Diffraction

X-Ray Diffraction is sensitive to the lattice expansion or contraction of the specimen and can detect various phases that could be present. Diffraction scans were performed on all the proton implanted samples along with the reference samples for comparison. The comparisons were made with the (224) peak due its larger probing depth. There was no average stoichiometry change observed due to ion irradiation in the material. However, due to irradiation induced damage to the lattice, a clear diffraction peak shift was observed to smaller 2θ angles relative to the reference sample as illustrated in Fig. 45. The lattice expansion due to proton irradiation agrees with historical data done using He^{2+} ion implants but lower in magnitude (as a function of dose). Therefore, ion implantation creates regions of small local defects that cause local lattice expansion in UO_2 that can be detected via XRD technique, which is sensitive to average disorder in the material. Expansion in the lattice, also seen in EXAFS results, is corroborated now by XRD, as the lattice parameter increases with increase in H^+ ion dose in the material. Diffraction measurements also indicate that

the overall structure of the lattice still remains as FCC fluorite along with smaller defect regions that cause the peak to shift to lower 2θ angles. This, in fact, suggests that the UO_2 structure is consistently incorporating smaller phases of UO_{2+x} that have their XRD peak reflections at smaller 2θ angles. Therefore, XRD results show agreement with all the EXAFS measurements in H^+ implanted UO_2 samples.

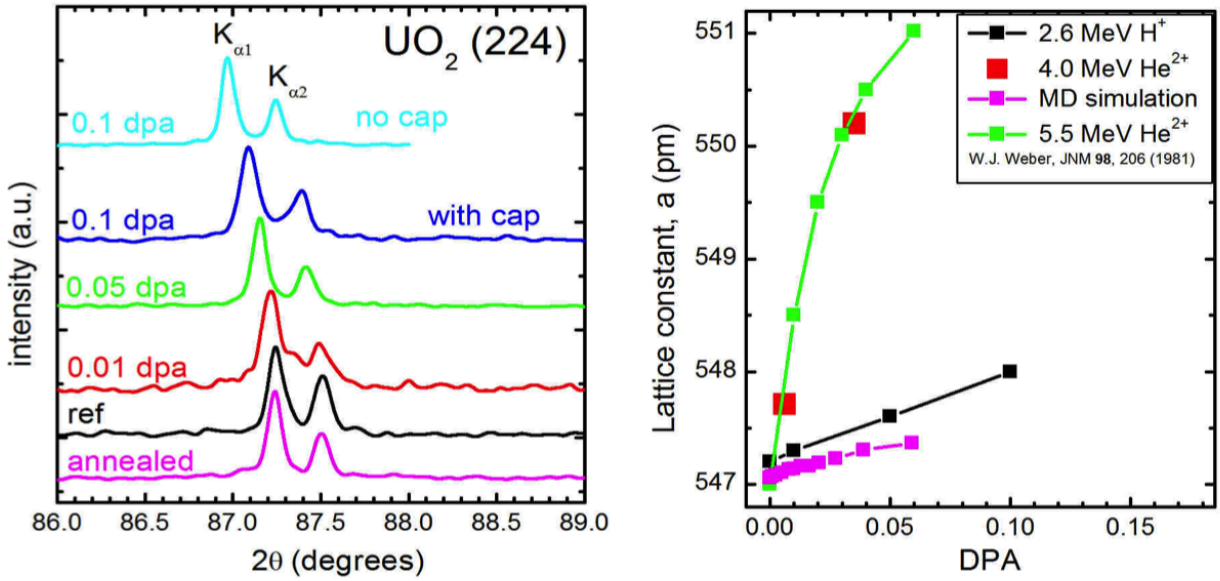

Figure 45: X-ray Diffraction study on proton irradiated UO_2 samples shows that with increasing dose, the lattice parameter consistently grows. The lattice parameter shift is in good agreement with historical data by Weber, et al (shown in green in the plot of lattice constants), with the Helium irradiated samples and also follow the same trend as the Molecular Dynamics simulation.

4.6 TEM Images

Radiation induced damage to the microstructure of this fuel material was investigated via Transmission Electron Microscopy (TEM). The TEM measurements were performed using the Technai TF30-FEG TEM housed at the Center for Advanced Energy Studies. Focused Ion Beam instrument, also at CAES was used to extract samples perpendicular to the ion beam, approximately 10 µm × 10 µm in size. The size of the lamellae, which were extracted by FIB, ensures that the entire sample has a consistent damage profile. This is because, the radiation damage plateau, which offers a zone of consistent damaged structure is approximately 30 µm in length. Using FIB, the sample was thinned to approximately 100 nm using 30 kV Ga ions and the final cleaning was performed using an even lower ion energy of 2 kV Ga ions.

Small scale irradiation induced features at the plateau region shows a consistent evolution of damage structure features. These dislocation loops were well-defined regions throughout the range of H^+ ion dose and have excellent contrast in conventional bright field TEM. Damage structure for all the H^+ implanted samples has been interrogated close to the (0 1 1) pole with g = [-1 -1 1] and this region consisted predominantly of dislocation loops. These are shown in Fig. 46. Using proton irradiations, it has been possible to introduce relatively simple microstructures in the target material.

Estimates for displacement density were made for the set of irradiated samples to understand the evolution of microstructure with dose. Sample thickness for the FIB lamellae was made based on the thickness fringes at the foil edge and the dislocation loop density was calculated in 10 locations on the sample. FIB milling and cleaning is known to create lattice damage in the specimen being prepared [47]. Therefore, comparison of the microstruc-

ture in the irradiated sample was compared to reference sample prepared by FIB to remove contributions from milling.

H^+ produces distinct microstructures of predominantly dislocation loops that are easily resolved. With evolution in dose, the predominant microstructure still continued to be dislocations. The density of these dislocation loops grew as the dose increased from 3.06×10^{21} to $9.4\ \times10^{22}$ loops/cm^3. Simultaneously, the loop size increased with ion dose from 7.9 nm to 15.7 nm at 0.01 and 0.5 DPA respectively. These results are summarized in Table 5. Increase in the density of dislocation loops is consistent with increased diffusion of the atoms at high irradiation doses. Subsequently, the diffusion of oxygen atoms in clusters has twice the probability than the singular oxygen atoms, which further diffuse easier than uranium atoms. Therefore, the dislocation loops are likely to be oxygen interstitial rich, which, in fact, has been suggested by several studies performed on irradiated actinide oxides [12]. The increase in microstructure concentration suggests greater local structure and average structure damage and therefore corroborates the EXAFS and XRD results that show increased lattice disorder with increasing ion dose.

Dose	Loop Size (nm)	Loop Density (#/cm^3)
0	-	-
0.01	7.9 ± 0.4	$3.06\times\ 10^{21}$
0.05	8.3 ± 0.4	$4.24\ \times10^{21}$
0.1	10.5 ± 0.4	7.38×10^{22}
0.4	14.2 ± 0.4	$8.02\times\ 10^{22}$
0.5	15.7 ± 0.4	$9.4\ \times10^{22}$

Table 5: Comparison of loop area and density evolution with increasing H^+ ion dose.

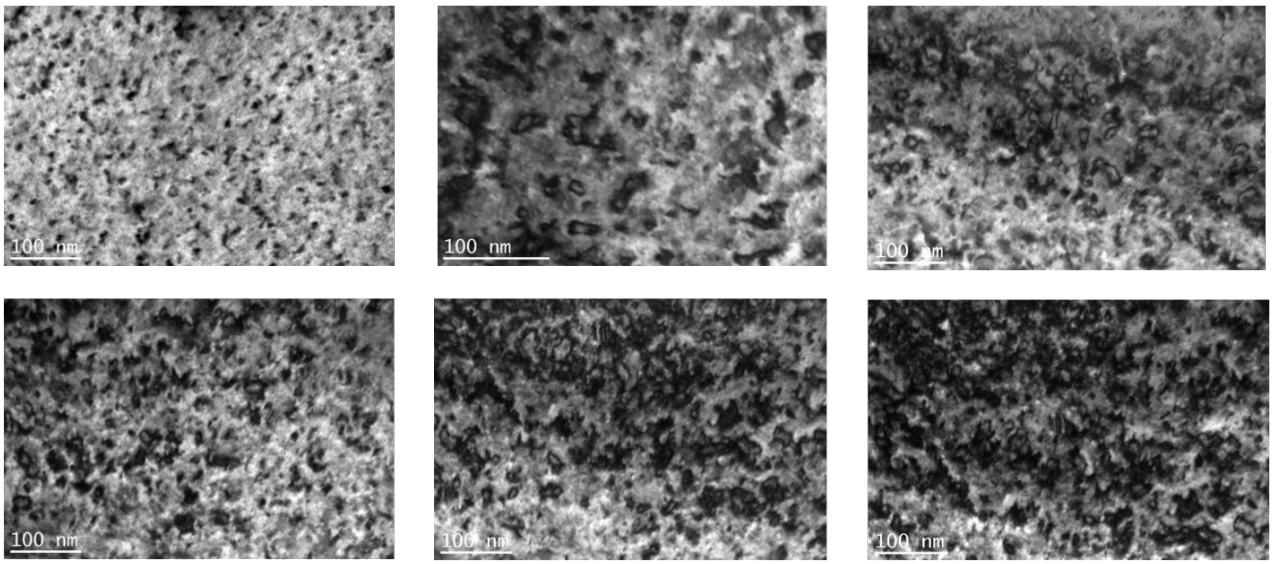

Figure 46: Evolution of dislocation in H^+ irradiated UO_2

The results seen due to proton irradiation can be reasonably compared to the spatially resolved Raman spectroscopy measurements done in He^{2+} implanted samples. Raman measurements clearly show the presence of defects as a function of depth in the UO_2 indicating differences in damage plateau and damage peak regions. Investigation of the radiation damage plateau indicates that there is deviation from a perfect fluorite lattice due to incorporation of defects from irradiation. Raman spectroscopy measurements also proposed that the defect structure consisted of hypo and hyper stoichiometric clusters in the overall stoichiometric UO_2 lattice. These measurements are surprisingly consistent with the results from EXAFS analysis that suggest clustering of local defects to form oxygen rich and oxygen poor region. However, these defects haven't been identified in the TEM analysis. Through high resolution microscopy, it was proposed to study these defect clusters using TEM.

High resolution microscopy is one of the only techniques that allows direct imaging of

atomic defects in materials. Therefore, to probe the relationship between atomic structure and lattice structure defects, the HRTEM imaging method has been employed. Fig. 47 shows a high resolution TEM images where the evolution of dislocation loops is clearly visible due to contrast in atomic columns and has been shown to increase with radiation dose. HRTEM micrographs clearly show the presence of dislocations on the lattice that have formed due to ion irradiations in UO_2. However, it wasn't possible to identify the constitution of these defective regions to show oxygen rich and oxygen poor type behavior. Based on the size and density of dislocation loops, Appendix A, shows a detailed analysis of potential atoms in the material being affected from dislocation type microstructure defects. The results of the analysis suggest that there is a distribution of damage cluster type defects that exist in the irradiated samples that cannot be detected via TEM measurements. Therefore, using TEM micrographs, while it is possible to see atomic scale defects due to H^+ irradiation, it isn't possible to completely characterize all defects that cause changes to the lattice. For this, one has to rely on techniques highly sensitive to atomic level defects, such as XRD and XAFS. Fig. 48 shows the Fourier transform filter placed on dislocation loops, giving a clearer image of the defect style.

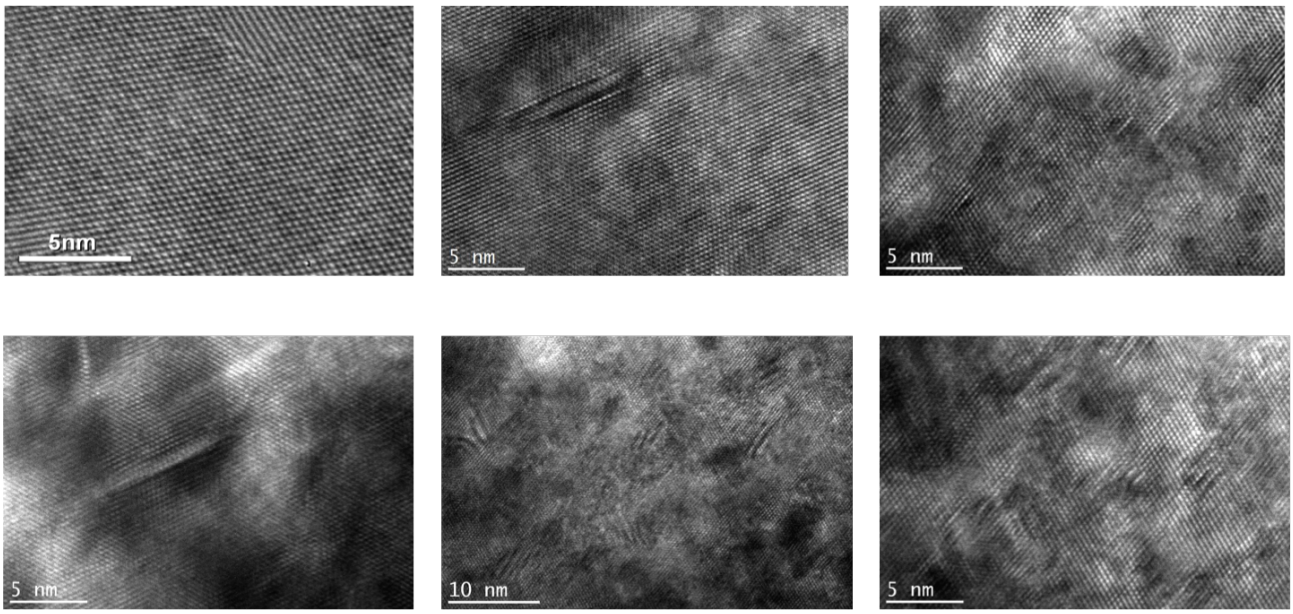

Figure 47: HRTEM micrographs of evolution of dislocation population in UO_2

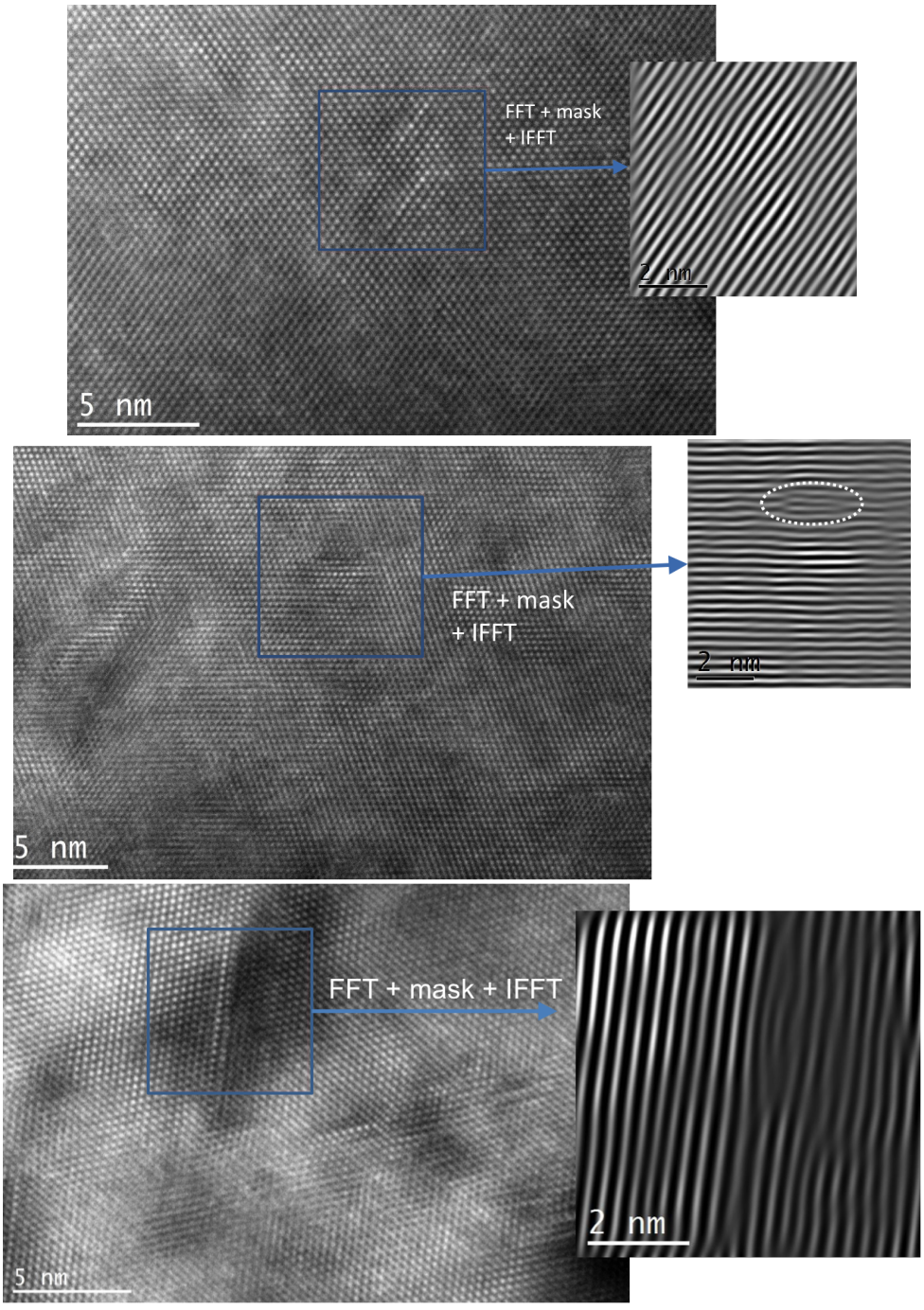

Figure 48: FT masks placed on the HRTEM dislocation images shows a clear dislocation loop

4.7 Summary

H^+ irradiation in UO_2 was performed so as to mimic radiation damage due to neutrons and to develop a mechanism to create simple microstructures in the target sample. The evolution of lattice and microstructure in H^+irradiated UO_2 has been investigated by EXAFS, XRD and TEM. While the TEM micrographs show an evolution of dislocation dominant microstructure, EXAFS and XRD results show a variation in the local structure and average lattice structure. The key results can be summarized as

1. Increase in lattice parameter as detected by XRD is corroborated by EXAFS results that show an increase in near neighbor distances with increasing ion dose.

2. The loss of spectral amplitude across the Fourier transform with proton dose indicates incremental distortion of lattice from the pristine structure

3. Concomitant with the loss of oxygen crystallographic peak height, there is an increase in the non crystallographic oxygen shoulder at U-O distance of 1.8-1.9 Å indicating a stable position for oxygen atoms to cluster.

4. With increasing dose, there is a total loss of short range and intermediate range order in the UO_2 lattice as is demonstrated by the 0.5 DPA sample.

5. Increase in ion dose comes with an increase in complexity of dislocation distribution. The density and size of dislocations increase with proton dose.

The results indicate visible and measurable changes in the damage structure of the UO_2 samples. Radiation damage due to protons creates the loss of overall structure with increasing dose with a drastic change in oxygen distribution in the form of oxygen clusters and a subtle change in uranium distribution by removing the U atoms away from the crystallographic sites but not in the form of a cluster of defects. Further explanation of the results is in the "Discussion" section.

5 Helium Experiments

ABSTRACT: Accumulated radiation damage in UO_2 significantly degrades thermal conductivity and fuel integrity during reactor operation, motivating studies of the microscopic damage mechanisms. The effects of such damage on the local structure and chemical speciation have been investigated via U L3 edge Extended X-ray Absorption Fine Structure (EXAFS) spectroscopy measurements on two polished, polycrystalline pellets of UO_2 irradiated with a 3.9 MeV helium ion beam to an average of 0.006 and 0.035 displacements per atom (DPA) over its 9 μm penetration depth. Analysis of the EXAFS showed substantial similarities between the effects of this ion irradiation and oxidation to UO_{2+x} that corroborate recent Raman spectroscopy experiments [22]. EXAFS provides a much more detailed description of this process, including 1) a reduction of the amplitude of the overall UO_2 spectrum concomitant with retention of its longer range order that is indicative of the aggregation of the defects and resulting phase separation of fully ordered UO_2 from domains containing the defect aggregates; 2) an apparent reduction in the number of U neighbors despite conservation of the bulk density; and 3) the formation of a multisite U-O pair distribution in terms of the formation of an oxo-type neighbor with, most remarkably, a U-O bond length of around 1.9 Å that is longer than that in UO_{2+x} and could signify an asymmetrically bridging or U(V)-oxo moiety. Microscopic collective and cooperative phenomena in which O-interstitial type defects are stabilized in proximity to each other so that they either migrate towards each other or their recombination and annihilation with vacancies is inhibited near existing defects to give the implicit aggregation observed in these experiments therefore appear to be a crucial part of the radiation damage mechanism in UO_2. These results are further supported by transmission electron microscopy measurements of radiation induced microstructures revealing

the presence of oxygen rich dislocation loops and inert gas bubbles. X-ray diffraction shows an increase in lattice parameter, consistent with literature data and EXAFS measurement results.

5.1 Sample Preparation

The polycrystalline samples used for the low temperature helium irradiations were sintered in Los Alamos National Laboratory with the procedure outlined in [41] using the Ellingham diagram as shown in Fig. 45. The sintered pellets were approximately 5.2 mm in diameter and 4.3 mm high with a theoretical density of 95-96%. The O/U ratio was set at 2 by cooling the sintered pellets from 1650^o C in a Ar-6% H mixture. These samples were further sliced into 5.2 mm diameter pellets with 0.6 mm height using a low speed diamond saw and polished to a mirror finish using a 0.1 µm grit size polishing paper, prior to the irradiations. The final sample details are summarized in Table 6. Estimates for the ion beam current required, the ion energy and the implantation depth were made using SRIM calculations as shown in Fig. 49.

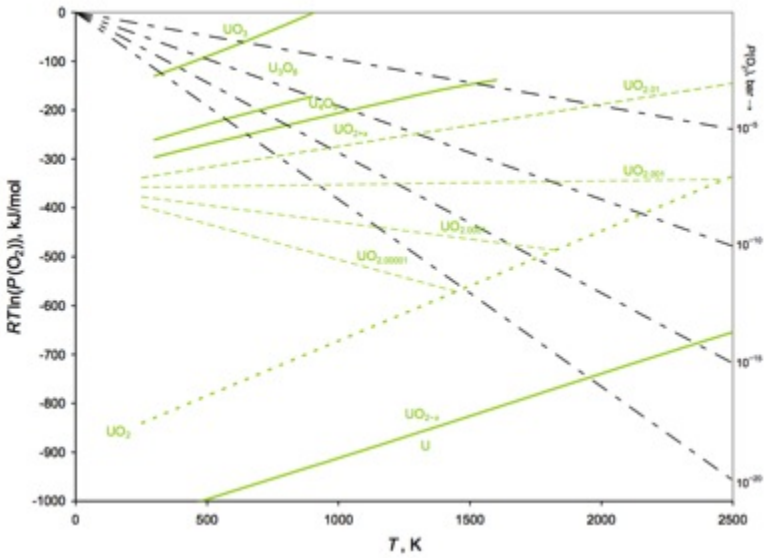

Figure 49: Stability of oxidation for UO_2 (Enhanced Thermal Conductivity in Oxide Fuels -2005)

5.2 Helium Implants

The ion irradiations were performed at the University of Wisconsin-Madison Ion Beam Lab which houses a Pelletron® tandem accelerator. A toroidal volume ion source (Torvis) produced He^{2+}ions, which were accelerated to 3.9 MeV with a Pelletron tandem accelerator. Similar to the proton irradiations, the temperature monitoring was performed using K-type thermocouples attached to the sample stage and in contact with the samples being irradiated. To consistently monitor the thermal distribution across the target sample surface during the course of the irradiation, a thermal imaging camera was used. The temperature

was maintained between 150° C and 200° C and the ion beam current was 1 μA on the UO_2 sample surface. The He^{2+} ions were rastered across the sample surface and the ion fluence was monitored using the LabView system as a function of time. The vacuum in the irradiation chamber was maintained in the range of 10^{-6} - 10^{-7} bar. It should be noted here that the reduction of UO_2 under vacuum conditions is negligible and in order to proceed towards measurable hypostoichiometry, a reducing gas agent must be used in the vacuum chamber or the temperature should be higher than 1200 ^{o}C **[73]**. Therefore, none of the noticeable effects discussed in this study originate from vacuum chamber atmosphere, or the lack thereof.

Disk ID	Fluence (ions/cm^2)	DPA (plateau)	He at % (plateau)	T (^oC)
1	0	0	0	-
2	$0.9{\cdot}10^{16}$	0.007	< 0.001	< 200
3	$5{\cdot}10^{16}$	0.038	< 0.001	< 200

Table 6: Description of UO_2 samples prior to He^{2+} irradiation: Summary of the irradiation conditions for the two samples being irradiated along with information on the radiation dose of each sample and other irradiation conditions

Two samples of UO_2 were irradiated to doses of 0.006 and 0.035 displacements per atom (DPA), with these numbers calculated as the integrated dose over one attenuation length of the incident x-ray beam. Although the penetrability is somewhat greater for the emission line than the original beam just above the U L_3 absorption edge, nevertheless the bulk of the signal will come from the volume well below the peak in the energy loss so that the material being probed can be considered homogeneous without concern about signal from the high

defect density region at the end of the ion track making a sufficiently large contribution to the total spectrum to affect the results. The details of these samples are summarized in Table 6. The Stopping Range of Ions in Matter (SRIM) [104] simulation code was used to estimate the final ion dose, the implanted ion depth and the profiles of atomic displacements in UO_2. A quick Kinchin-Pease calculation was made as outlined in [84] and the result is shown in Fig. 50.

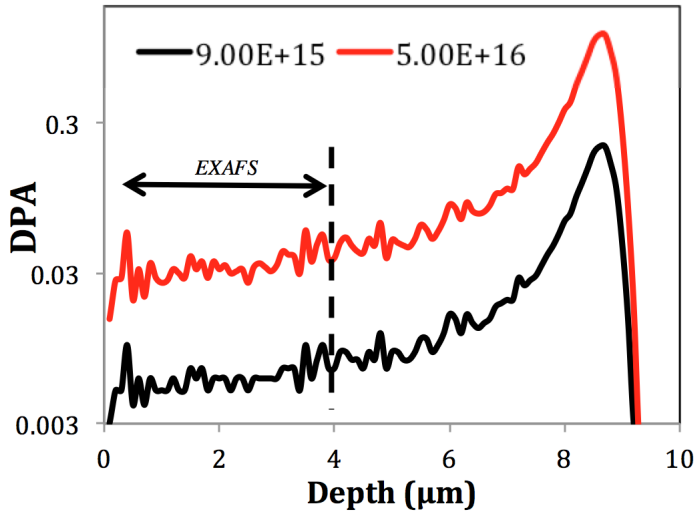

Figure 50: Ion damage profile as obtained from SRIM. The dashed line corresponds to one attenuation length of the beam just above the U L3 absorption edge at the angle of the sample with respect to the beam.

5.3 EXAFS on Helium Implanted UO_2 Samples

Extended X-ray Absorption Fine Structure measurements were performed at the Stanford Synchrotron Radiation Lab at beam end station 11-2 with operating conditions of 3.0 GeV, 300 mA in the fluorescence mode on these opaque samples using an ionization type detector with a Sr filter to reduce scatter, a minimal problem with pure UO_2. Sample holders were attached to a cold finger of liquid nitrogen cryostat to give a sample temperature of ~80 K to reduce the Debye-Waller factors. The samples were fixed at 45° relative to the incident beam to analyze the damage plateau region of the UO_2 samples. This corresponds to ~ 4 µm in depth for 1/e of the incident photons, magnified by the greater attenuation of the emitted x-rays. Comparison with Fig. 46 shows that the fluences do not depart too far from a constant over this range, with one absorption length being well below the final peak in the damage profile, and that in this probed region the fluences are well below the average value that is increased by the peak at the end of the ion track. Silicon [220] crystals were used to produce a monochromatic beam, running fully tuned with harmonics being eliminated by a flat, Rh-coated mirror tilted to give a cutoff around 20–22 keV. The energies were calibrated by defining the first inflection point of a Y foil measured periodically as 17032.08 eV. Spectra were normalized by offsetting them so that the value of a second order polynomial fit through the pre-edge region was 0 and then scaled so that the value of a third order polynomial fit through the post-edge region was unity at 17185 eV. The photoelectron wave vector was calculated by setting the ionization energy, E_0, to 17163 eV. The EXAFS were obtained by first subtracting out the absorption edge from the spectra using a sum of an arctangent and a Gaussian fit to the white line and the edge to eliminate the ripple in the spline function resulting from it abrupt change in slope when it passes through these

features. The EXAFS were calculated as the difference between the resulting spectra and a polynomial spline function approximating the smooth atomic absorption. The location of the spline knots was varied to minimize the area of the Fourier transform modulus of $k^3\chi$ below 1.2 Å. The range of variation was, however, subject to ensuring similar knots for all of the spectra to ensure that any differences would be real and not artifacts of the background. Metrical parameters were obtained via non-linear least squares curve-fits over the range k = 2.7−14.52 Å using amplitudes and phases calculated with FEFF9 [70] to model the waves from each neighbor shell individually, varying N, R, σ, and ΔE_0, with ΔE_0 constrained to within $\leq$1 eV of each other for the O shells and 3 eV for the U. The k^3 weighting was used to enhance the contribution of the O shells.

Final fits were performed with four neighbors, the crystallographic O shells at 2.36 Å and 4.52 Å and the U shell at 3.85 Å and the new, non-crystallographic oxo shell at around 1.9 Å. The Debye-Waller factors for all the first three shells was allowed to float except when the resulting number of atoms in these shells was unphysically large or small, in which case it was constrained over a narrow range or fixed at a specific value. The oxo shell seen as a shoulder on the low R side of the primary O shell at 2.36 Å was also fit with an O shell and the Debye Waller factor for this was fixed at 0.05 Å. The results are summarized in Table 8 for the interatomic distance, R, the number of atoms fit in each shell, N and the pairwise Debye-Waller factors, σ. The errors were calculated by removing each shell from the fit to determine its overall contribution and then individually varying each of its parameters until the increase in the error was 10% of this amount.

Extended X-ray Absorption Fine Structure measurements were performed at Stanford Synchrotron Radiation Lab at beam end station 11-2 with operating conditions of 3.0 GeV,

300 mA. Sample holders are attached to a cold finger of liquid nitrogen cryostat to give a sample temperature of 80 K to reduce the Debye-Waller factors. A Silicon [220] monochromator that uses Bragg diffraction to select a particular energy was used. The energies were calibrated by defining the first inflection point of a Y foil measured periodically as 17032.08 eV. The photoelectron wave vector was calculated by setting the ionization energy, E0, to 17160 eV. The EXAFS measurements were performed in fluorescence mode with a 45° angle between the incident beam and the sample. Lytle detector was used to measure the fluorescent x-rays from the samples.

5.4 EXAFS Results

Comparing the three spectra as the Fourier transforms shows (Fig. 53) that their features are almost all identical over their entire range within the noise limit of the data, with the principal difference being in their amplitude that decreases monotonically with increasing helium ion dose. That this diminution in amplitude is proportionately equal across the entire spectrum so that the relative amplitudes of the features remain constant indicates that the locally ordered part of the structure that gives these spectra is identical for all, i.e., UO_2 in its fluorite form. The amplitude reduction therefore indicates that the ion irradiation does not, as could be expected, result in randomly located defects that break down the order on increasingly shorter length scales as more of them occur. Instead, it disrupts larger amounts of the originally fully ordered UO_2, even while the remaining UO_2 is intact and unaffected. This could only occur if the irradiation-induced defects that would form randomly along the He^{2+} tracks do not rapidly recombine and annihilate but instead move and aggregate.

Furthermore, because no new, non-UO_2 related spectral features are observed, these defect-containing domains must be so highly disordered that they are invisible to EXAFS. The spectra for the reference sample is shown in Fig. 51 and for the irradiated specimen is given in Fig. 52.

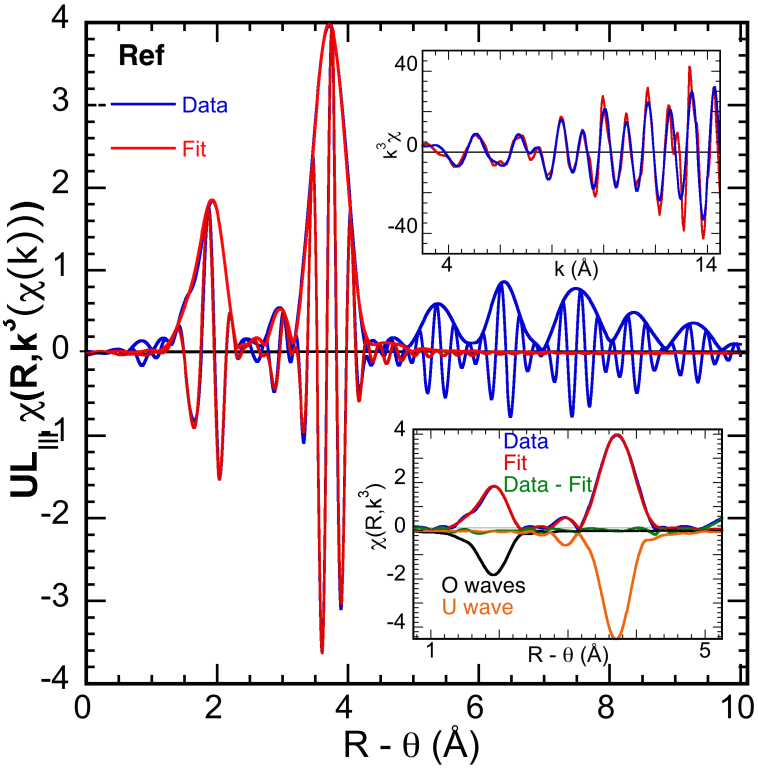

Figure 51: Fourier transform of reference sample

In this way the irradiation process closely resembles that of oxidation where the insertion of O into the UO_2 lattice also gave spectra identical to $UO_{2.00}$ at higher R except for

a constant reduction in amplitude [17]. In that case it is known from diffraction that the adventitious O atoms cluster to give UO_2-U_4O_9 phase separation within the grain, permitted by the minimal (<1%) difference in lattice parameter. The exception to this overall proportional spectral amplitude reduction is the region on the low R side of the nearest neighbor O peak at R = 1.9 Å. Here the relative amplitude increases, although it never becomes a resolved shoulder, and the zero crossing of the real component shifts to lower R (Fig. 52, 53). This behavior is also very similar to that of oxidation of UO_2, where this feature was shown to originate in an U(VI) oxo or uranyl-type species and the formation of a multi-site nearest neighbor U-O distribution with increasing x.

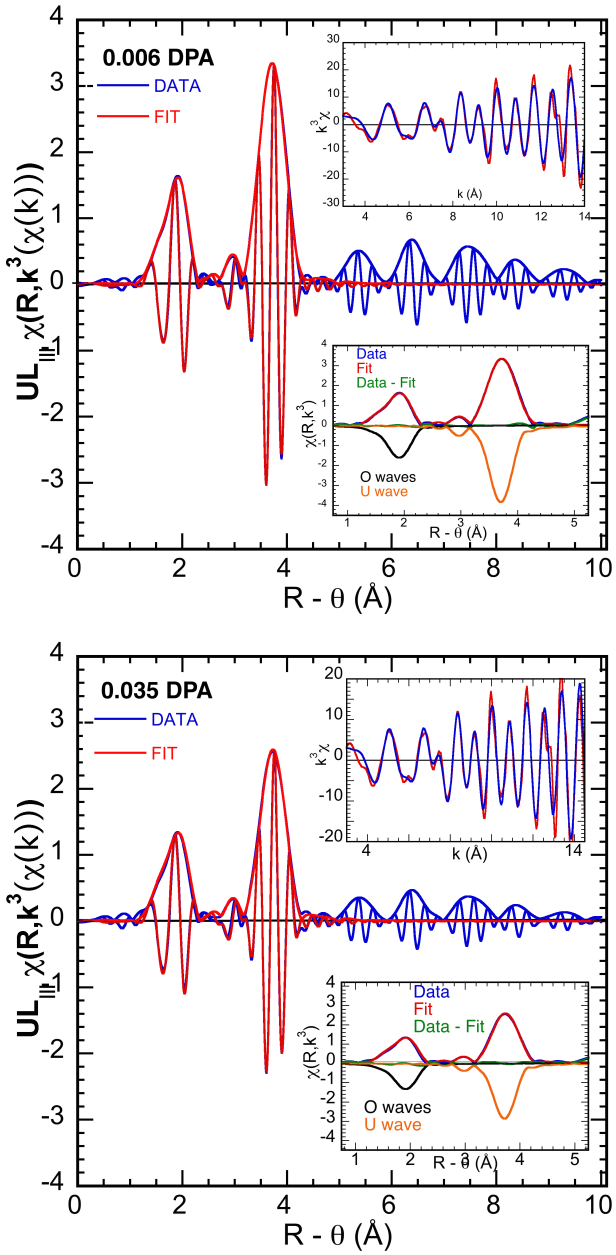

Figure 52: The $k^3\chi$(R) EXAFS of UO_2 irradiated to 0.006 dpa with He^{2+} ions and UO_2 irradiated to 0.035 dpa also with He^{2+} ions. The modulus of the real part of the transform of both data and fit are shown in the plots. The insets show the $k^3\chi$ spectra overlaid with curve-fit (top) and the moduli (bottom) of the data, fit, difference between data and fit, and the individual contributions to the fit (inverted for clarity).

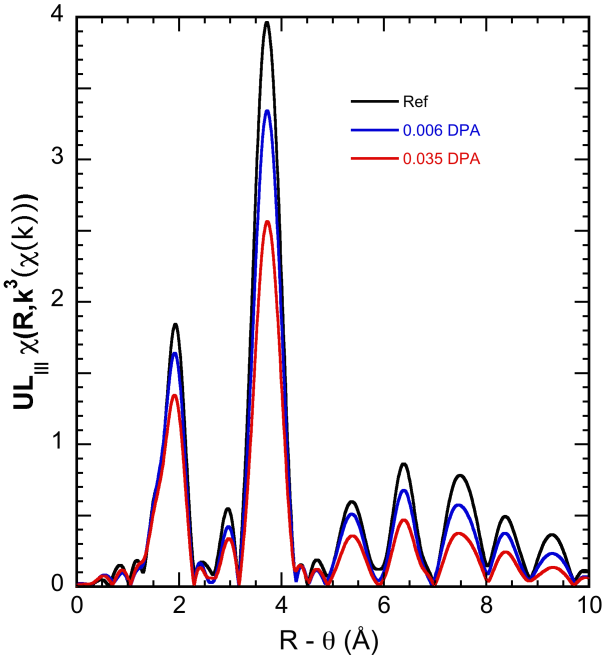

Figure 53: This shows the modulus of the Fourier transforms of the k^3- weighted EXAFS spectra of indicated samples. Transforms were performed over k - range of 2.70 – 14. 52 $Å^{-1}$.

This interpretation of the spectra is corroborated by the curve-fits. With the exception of the region around R = 2.3 Å where the amplitude is almost at the baseline because there are no structural features giving waves with those frequencies at that location, the curve-fits model the contributions from the first three crystallographic O, U, and O shells almost perfectly (Fig. 52-53). The residuals are minimal throughout this region and the nodes of the real components of the data and the fit align to better than the width of the lines. In addition, the distances found for these shells are within experimental error of the crystallographic ones and the changes in distance between the samples are even less (Table 7).

Of interest then is the behavior associated with the amplitude reductions. For the crystallographic nearest neighbor O at 2.36 Å, the numbers of atoms decrease and the Debye-Waller factors increase monotonically with increasing dose, albeit by small amounts and with only these three data points. A somewhat different result is obtained from a log-ratio analysis (Fig. 54). This shows negligible reduction in amplitude for 0.006 dpa sample but a very similar increase in Debye-Waller factor for both samples. The discrepancy between the two results is evident in the much larger deviation from linearity of the log-ratio of the 0.035 dpa residual spectra. Although both, a loss of atoms from the 2.36 Å U-O shell and an increase in Debye-Waller factor are implicated – and certainly the addition of oxo-type atoms would have to be mirrored by depletion of the original shell – it is likely that the U-O distribution becomes more complicated with increasing numbers of O in defect sites. This again duplicates the behavior in UO_{2+x} with its multisite U-O distribution whose behavior was not monotonic with increasing x, which made it difficult to quantify the number of oxo atoms.

For the nn U, there is a substantial jump in the Debye-Waller factor on irradiation, which does not increase further with higher dose. Instead, the curve-fits find that the continued diminution of amplitude for the contribution of this shell results from a larger drop in the number of atoms. This was confirmed by log-ratio analysis of the amplitudes of the U-U wave (Fig. 54) as performed previously for UO_{2+x} [19]. These ratios are reasonably close to the straight line over their extended range that is expected because a multisite distribution is not formed, with negative slopes that are similar to each other but a significantly lower intercept for the 0.035 DPA sample.

The decrease in the number of U neighbors for the 0.006 dpa sample is around 1/3 for both curve-fits and this more graphic analysis, whereas that for the O is only ~10%, at the

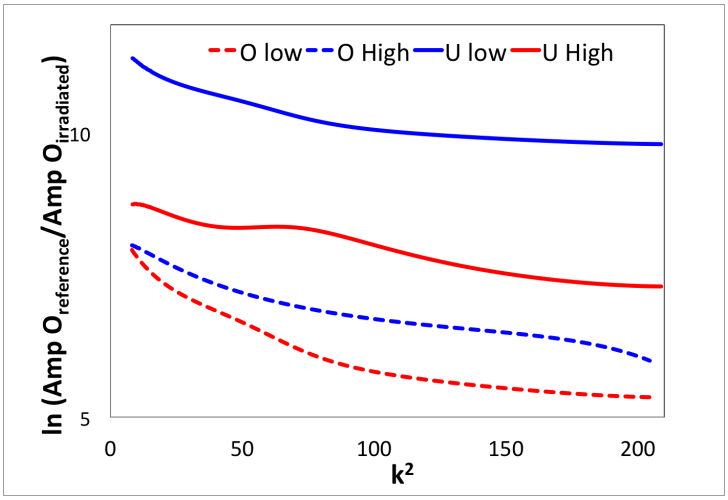

Figure 54: Logarithms of ratio of U-U near neighbor and O-O near neighbor amplitudes of helium irradiation $UO_2$from subtracting out all U-O components to that of reference sample

limit of significance. The radiation damage over this range therefore causes only a limited increase in disorder for the O that is most likely the initiation of a multisite distribution, but an increase in both harmonic and anharmonic disorder for the U neighbor where the connection is weaker. "Anharmonic" disorder is defined as disorder that gives an apparent decrease in the number of neighbor atoms even while the material remains almost fully dense so that it is not a loss of atoms but rather a rearrangement into a distribution that results in their being invisible in EXAFS. This behavior is also similar to what was observed for oxidation and may therefore be subject to the same constraints in terms of the types of U-U distributions that can cause this effect.

By ratioing the atoms fit for the near neighbors to their respective Debye-Waller factors the consistent loss of structure with irradiation is seen in the case of helium irradiated samples as well (Fig. 55). With increasing helium ion dose, the number of atoms in each shell decrease and it indicates that the overall lattice structure is being distorted. This loss

of atoms fit is seen only in the case of the original crystallographic peaks and not for the first U-O distance of 1.9 Å, in which case, this ratio increases with increasing dose.

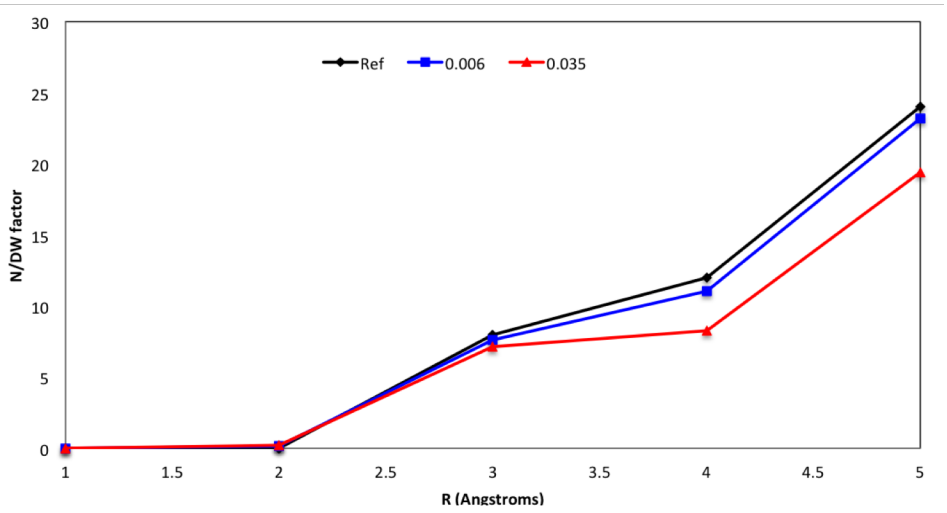

Figure 55: Ratio of number of atoms fit in each shell (including the 1.9 Å shoulder) to the DW factor for each of those shells shows a decrease in this ratio with increasing ion dose except for the U-O shoulder at 1.9 Å.

The exception to the retention of the UO_2 structure as the sole locally ordered fraction of the material is in the region below the nearest neighbor O. Close inspection of this region (Fig. 53) shows an increase in the relative amplitude of this shoulder feature coupled to a change in the real component in $\chi(R)$ with increasing dose. This is observed more easily when the spectra are rescaled so that the modulus amplitudes are identical (Fig. 56). This increase, and the simultaneous absence of a shift in the nodes of the real component that demonstrate that it results from a change in the amplitude of the given feature, would originate in a structural feature at a distance ~ 0.4 Å shorter than the principal nearest neighbor O shell

at 2.36 Å. Since this must be within the sample it can only be another O, and curve-fits in fact find an O shell at 1.92 Å containing 0.2 atoms with Debye-Waller factors only slightly lower than the fluorite nn shell. Because of the low relative amplitude of the U-oxo waves in the EXAFS, especially at high k where the U-U wave dominates, the Debye-Waller factors for this O shell were fixed to 0.05 Å for both the irradiated samples instead of allowing them to float. The small number of atoms in this shell and the likelihood that the U-O distribution is becoming complicated even as it is fit with just these two well separated O shells accounts for the uncertainties in obtaining consistent results from the curve-fits and log-ratio analysis that would be expected to be mirrored in the number of O atom in the principal neighbor shell. Despite the difficulties in quantification, e.g., an uncertainty of 2.4/7.6 in the number of O atoms at 2.35 Å in the 0.006 dpa sample, this figure and Fig 47-59 clearly show the loss of UO_2 concomitant that is paralleled by the increase in this U-oxo type moiety.

Sample		U-O (1.8 Å)	U-O (2.36 Å)	U-U (3.85)	U-O (4.5)
Crystal	R		2.36	3.85	4.52
	N		8	12	24
Reference sample	R		2.35±0.02	3.86±0.01	4.48±0.02
	N		8	12	24
	σ		0.047±0.02	0.002±0.0	0.073±0.019
0.006 dpa	R	1.92±0.02	2.35±0.02	3.87±0.01	4.48±0.02
	N	0.19±0.04	7.6±2.4	11.02±2.6	23.19±6.1
	σ	0.05	0.052±0.02	0.0199±0.014	0.0752±0.017
0.035 dpa	R	1.93±0.02	2.36±0.02	3.87±0.01	4.52±0.025
	N	0.2±0.03	7.15±2.0	8.29±2.02	19.41±5.9
	σ	0.05	0.061±0.018	0.02±0.017	R±0.017

Table 7: Crystallographic distances (R) and curve fitting results for N (number of atoms) and σ (Debye Waller factor) obtained on the UO_2 samples

Table 8 shows the ratio of number of atoms fit to the Debye-Waller factor which is increasing with increasing dose. This effect is attributed to the clustering of oxygen ions similar to UO_{2+x} at low-R distances from the absorbing atom. The increase in the size of this oxygen cluster occurs simultaneously with the loss of number of atoms in the original oxygen peak.

Sample	Atom/ DW factor at 1.9 Å
0.01	0
0.05	2.9
0.1	3.98

Table 8: Ratio of the number of atoms to the Debye Waller factor increasing in value to indicated the total number of atoms in at the 1.9 A distance are growing

The accumulation of randomly located defects typically results in a faster decrease in the amplitude of the Fourier transform peaks at longer distances than at shorter ones because the sequential breakdown in order begins at long range with the loss of structural coherence on the distal side of a defect propagating into broader, anharmonic pairwise distance distributions. Here, we observe the opposite, that the proportional loss in amplitude is identical throughout the full range of R. This indicates that the defects are not randomly distributed throughout the lattice but instead are clustering so that the UO_2 domains where they do not reside retain their fully ordered fluorite structure. The only locally ordered component found in these spectra that can be attributed to the domains containing the oxygen defects is therefore the O shell with the 1.9 Å U-O distance. In addition to UO_{2+x}, this effect has

also been noted in PuO_{2+x} where EXAFS also showed similar collective behavior of oxygen defects including an O shell 1.8–1.9 Å from the Pu ion [17].

The phase separation of ordered UO_2 from the domains containing the defects is the transformation of the latter into another structure. This is analogous to the phase separation and micro / nano domains in UO_{2+x} that indicate the propensity of UO_2 to proceed towards the more stable U_4O_9 and U_3O_7 phases **[4]** and heterogeneity rather than forming random solid solutions of defects. These domains have been postulated to address the oxygen defect formation mechanism in UO_2 as the addition of oxygen results in oxygen defect clusters. The formation of these defect clusters due to irradiation could be due to the greater diffusion coefficient of oxygen in UO_2 **[?]**when ion irradiation increases the oxygen ion mobility and therefore results in oxygen ions clustering locally, a phenomenon detected by EXAFS analysis. The locally disordered structure in the O-enriched regions is then closer to U_4O_9[74], implying that the O-depleted regions would be U_2O_3-like. An additional factor, however, is that their formation most likely indicates that these clusters are stabilized by some mechanism in addition to any kinetic trapping.

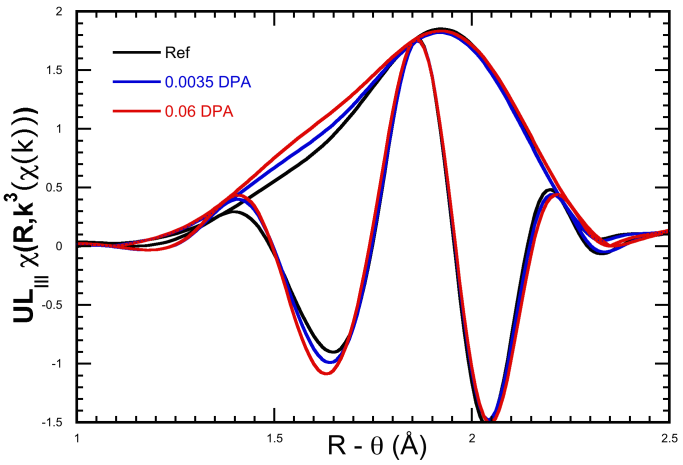

Figure 56: Low R features in He samples compared to two reference samples. The spectra from the irradiated samples have been rescaled so that the peak amplitudes are all identical, facilitating the comparison of the lower R feature.

Debye-Waller factors are expected to increase when the distribution of atoms is asymmetric. One-dimensional simulations of the structure were performed to address the less localized distribution of U atoms and their apparent decrease in the EXAFS fitting routine similar to the analysis of UO_{2+x} [19]. Here, the U atoms were divided into three subshells with an occupancy ratio of 1:2:1. When the separation between these three shells was increased, it resulted in a significant loss of amplitude in the principal contribution to the EXAFS, similar to what has been shown in Fig. 53. Further, it was noted in the same set of simulations that a component of the U distribution was becoming amorphous and not contributing to the EXAFS. Therefore, ion irradiation is separating the U atoms into at least two populations that may correspond to the UO_2 and U_4O_9-like domains. As noted, this process implies the formation of O-depleted domains as well, which do not contribute to

the EXAFS either because they are invisible analogous to U_4O_9 or because O vacancies do not disrupt the UO_2 lattice whether they are randomly distributed or clustered. In the first of these, not completely identical to UO_{2+x}, the distribution remains harmonic and centered on its crystallographic position, but also becoming somewhat broader. In the second the other U atoms must be becoming "glassy" and therefore invisible to EXAFS analysis. The non-glassy U atoms tend to spread over 0.4 Å around their position, which did contribute to the EXAFS analysis.

These results corroborate similar observations by Raman spectroscopy on UO_2 indicate the formation of U(III) and U(V) species resulting in oxygen rich and depleted regions on the oxygen sublattice [22]. The occurrence of the two types of features effectively balances out the charge but continues to give the appearance of regions of hyper and hypo-stoichiometry. The formation and description of these Magneli type defect has been discussed in the background section.

5.5 X-ray Diffraction

X-Ray Diffraction studies done on the set of the He^{2+} implanted samples was done using the (224) XRD reflection for comparison. The (224) reflection has a high probing length of 1.6 μm which interrogates the damaged plateau region thus not including effects in the peak region. With increasing He^{2+} ion dose, lattice peak shift was observed to lower 2θ angles as is shown in Fig. 57. The increase in lattice constant is consistent with results by Weber, et al [92] and with agrees with the lattice parameter trend seen with proton irradiated d-UO_2 samples.

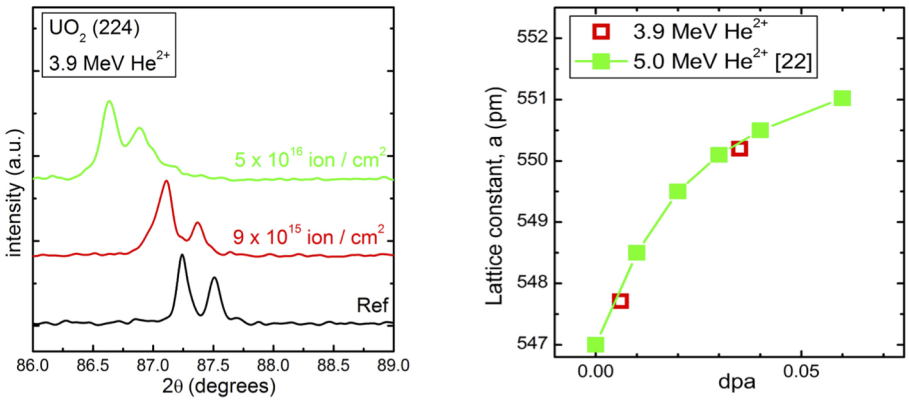

Figure 57: Lattice parameter increase with increasing He^{2+} ion dose as measured for the XRD (224) peak

5.6 Transmission Electron Microscopy

The irradiation damage on microstructure scale was studied using Transmission Electron Microscopy. The samples for TEM were prepared by Focussed Ion Beam sample milling as was explained in experimental techniques. The damage plateau gives evidence of consistent microstructure between both dose levels. This could be a result of very small ion dose and minor difference between the two dose points. Bright field image of the helium implanted sample (0.035 DPA) shows several dislocation loops oriented edge on along the <111> plane in Fig. 58. The dislocation loop images have been extracted from the damage plateau region which appears to be fairly consistent in the microstructure change. These loops grow with irradiation dose and therefore alter the local chemistry of the material. Average loop size is < 10 nm, so they are relatively small. This could also be attributed to lower dose levels in the samples. High resolution image of the dislocation loops is shown in Fig. 59.

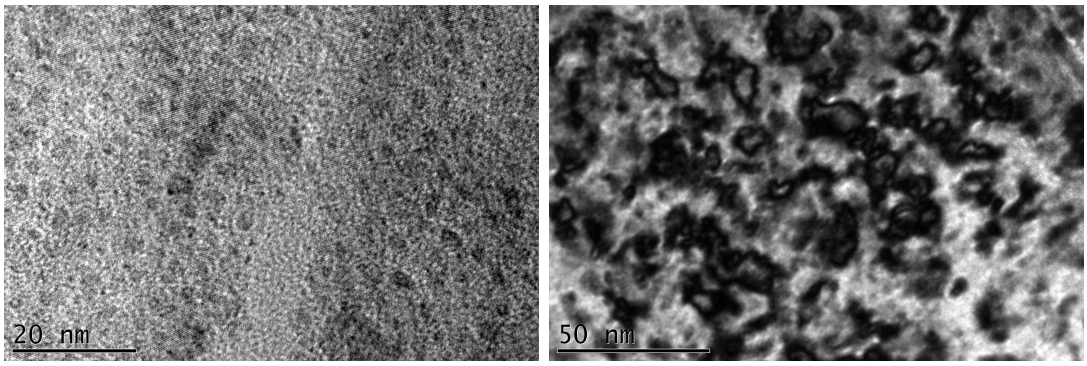

Figure 58: Edge on dislocation loops along <111> plane in He^{2+} implanted UO_2 . The network of dislocations is seen in both low and high dose samples.

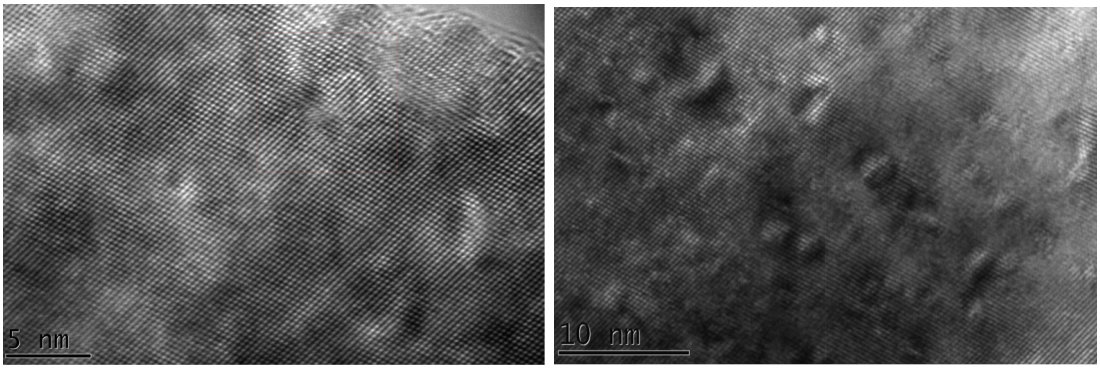

Figure 59: High Resolution images of low dose (0.006 DPA) and high dose (0.035 DPA) helium implanted samples showing growing concentration of dislocation loops. Summary of dislocation loop characteristics is give in Table 9.

The thickness of the TEM foils was calculated using thickness fringes at the edge of the FIB foils. The average density of loops was estimated in ten different regions for all the samples in this study. The average loop density and size is summarized in Table 9. With increase in irradiation dose, the average loop density and diameter increase in size and concentration in the sample. This indicates the propensity of He^{2+} samples to develop incrementally complicated microstructure with increase in radiation dose.

Sample	Loop Density	Average Loop Diameter
Ref	-	-
0.006 DPA	$6 \pm 0.8 \times 10^{21}$loops/m^3	7.3 nm
0.035 DPA	$13 \pm 0.8 \times 10^{21}$loops/m^3	8.5 nm

Table 9: Summary of dislocation loops in helium implanted dUO_2samples

Further TEM investigation of the helium implanted samples along the damage plateau region of the samples shows a distribution of bubbles of helium gas along the sample. The helium gas bubbles were imaged by changing the focus level of the TEM from under focus point to an over focus point. The images were extracted at the same level of under focus and over focus across both samples. This is the first known evidence of helium gas bubbles observed at lower temperatures in TEM. The nucleation and growth of helium bubbles is facilitated by temperature, however, in this case, the 150^o C temperature was sufficient to cause helium ions to coalesce to form gas bubbles. This is because helium precipitates at very low concentrations and readily form bubbles. While this does not alter the near neighbor structure of UO_2 as seen in EXAFS, it does cause the structure of UO_2 to be unstable, which contributes to lattice expansion as seen in XRD results and could give some energy needed to oxygen atoms to form uranyl type bonds in the sample locally. Fig. 60 shows a progression of focus across the two samples.

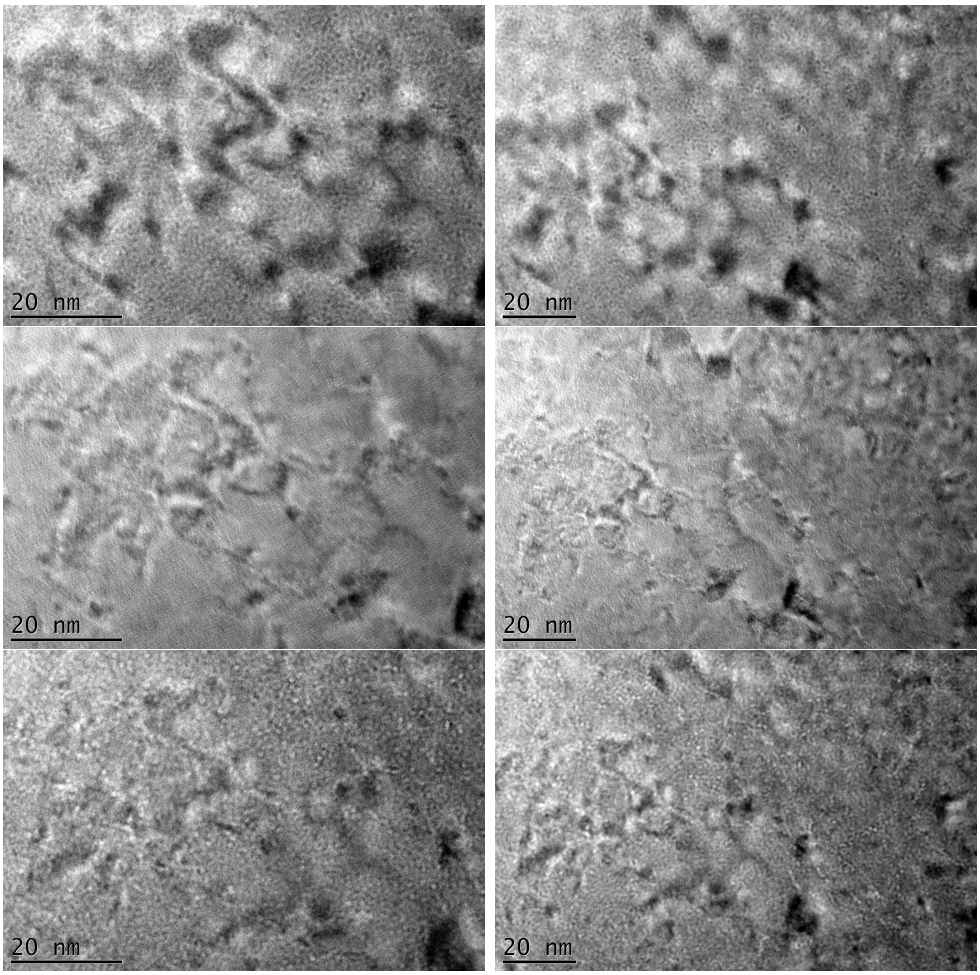

Figure 60: Over focus and under focus images of low (first column) dose and high dose (second column) helium implanted UO_2 give evidence of helium gas bubbles.

Table 10 shows the increase in bubble density and diameter with increasing radiation dose in the UO_2samples. The nucleation of helium bubbles is known to occur in the large grain areas and not in the grain boundary region. This is in agreement with the observations shared in this study. The helium bubble density is a lot slower within the grain than at the grain boundaries, inducing the formation of He^{2+} gas bubbles. It has been shown previously

that the overall helium release from the damaged sample is a decreasing function of helium fluence and therefore, the damage in the material. Ion irradiation produces vacancies and vacancy clusters for which He atoms have large affinity, and will therefore nucleate at these vacancy sites within the grains of the sample.

Sample	Bubble Density	Bubble Diameter
Ref	-	-
0.006 DPA	$5 \pm 0.3 \times 10^{23}$ /m^3	1.3 nm
0.035 DPA	$9 \pm 0.3 \times 10^{23}$/m^3	1.6 nm

Table 10: Increase in concentration of He bubbles with dose in helium implanted UO_2samples

Therefore, He^{2+}irradiation results in the formation of relatively simple microstructure in UO_2that consists of dislocations that increase in density and diameter with increasing ion dose. Also, the formation of inert gas bubbles in UO_2 as demonstrated in this study supports the TEM study that predicts their nucleation at a fluence of ~10^{15}ions/cm^2.

5.7 Summary

Helium irradiation in UO_2 was done to model the alpha particle damage during nuclear reactor irradiation and also to study the effect of low dose self irradiation of fuel in extended storage. Low doses used in this study are sufficient to create measurable microstructure damage and distinctive lattice structure changes. These changes were measured using XRD to study the evolution of lattice parameter with dose, the variation in lattice structure was studied using EXAFS and radiation induced microstructure was quantified by TEM. The key results from all the techniques are:

1. Monotonic loss of peak height suggests a distortion of structure, which is evident from reduced number of atoms fit.

2. With increasing dose, a short U-O distance forms at non crystallographic distance of 1.9 Å from U, which develops into a shoulder peak increasing in magnitude.

3. The near neighbor distances are longer than pristine lattice by 0.01 Å, corroborating XRD results of lattice parameter expansion with increasing He^{2+} ion dose.

4. TEM results show a distribution of dislocation loops along [111] plane in UO_2

5. He^{2+} bubbles were observed to form in the UO_2 lattice with bubble density decreasing with dose and size increasing.

The low dose He^{2+} irradiations show the evolution of radiation damage on multiple length scales in UO_2. The presence of the oxygen shoulder indicates O clustering in the material along with the U atoms changing into a distribution around the crystallographic position. The dislocations are classically located along [111] zone, supporting the theory behind propensity of UO_2 to form defects along the large fluorite defect site. These results are explained in more detail in the "Discussion" section.

6 Krypton Experiments

Abstract: Fission products during nuclear reactor operation emerge at high energies and proceed to damage the structure of the nuclear fuel. To study radiation damage due to fission gases, an ion accelerator was used to produce a steady current of Kr ions, a common fission product, on UO_2target specimen. Polycrystalline UO_2 disks were irradiated with 1.8 MeV Kr ions at doses ranging from 5 $\times$ 10^{13} ions/cm^2 to 1 $\times$ 10^{15} ions/cm^2 at room temperature and at 800$^o C$. These irradiations were conducted in-situ and ex-situ using an ion accelerator. The post irradiation examination was conduced using Extended X-ray Absorption Fine Structure (EXAFS) at the UL_{III} edge and using Transmission Electron Microscopy (TEM). The microscopy identified the presence of krypton bubbles and complex network of dislocations increasing in density with ion dose. EXAFS analysis revealed the presence of a multisite U-O pair distribution that started at 1.8 Å and is indicative of the highly stable uranyl bond. Further, with increasing krypton ion dose, there is an increase in the oxygen cluster concentration locally, which begins to form a multisite U-O distribution and results in a monotonic decrease in amplitude of the overall UO_2 spectra. Finally, X-ray diffraction measurements were performed to study the lattice parameter evolution with ion dose in UO_2. XRD results show the disappearance of significant crystalline features due to ion irradiations. These results suggest the formation of radiation stabilized atomic features in UO_2 that are characterized by a bi-modal oxo distribution on the U sublattice, rendering those regions hyper and hypo stoichiometric. The extent of the off stoichiometry is seemingly depending on ion dose and increases with higher dose.

6.1 Background

Krypton is one of the most common fission products in nuclear reactors. As a nobel gas, krypton does not interact chemically with the fuel materials and other reactor materials it comes in contact with. However, due to its inactivity, it forms inert gas bubbles inside the fuel and can result in void swelling, which can eventually challenge the fuel and reactor material integrity. To study the radiation damage in nuclear fuel due to krypton gas, an ion accelerator was used to generate a current of krypton ions impacting the UO_2 sample surface. As mentioned previously, the ion accelerator produces krypton ions to mimic nuclear reactor damage, without the complication of neutron activation that is expected in a reactor. This study enables us to understand the evolution of microstructure and damage structure with increasing krypton ion dose and can help in understanding the exclusive effect of krypton on the nuclear fuel material.

Transmission Electron Microscopy is widely used to understand the location, form and size of microstructure features in krypton implanted UO_2 **[102]**. Simultaneously, there is a lack of understanding of atomic level changes and stoichiometry evolution in krypton irradiated UO_2 that can be used to complement the microstructure evolution measurements using TEM. Previous studies have revealed the presence of krypton gas bubbles and complex networks of dislocations that grow with krypton ion dose. The bubble size typically is known to increase with dose and the subsequent bubble density shows a marked decrease. These studies were performed at a higher temperature of 800^o C [35] and, therefore can result in increase ion diffusion and mobility in the material, thereby causing bubbles to coalesce to form larger features. The study discussed here focuses on room temperature krypton ion irradiation of UO_2 to minimize the coalescence of defects and lattice recovery that is aided

by temperature of the system.

Density Functional Theory calculations reveal the extent of point defect formation and migration in UO_2 during and after krypton ion implantation [48]. These studies reveal that the solubility of Kr in UO_2 is extremely low, which results in almost all the krypton ions to precipitate into small bubbles. Therefore, the lattice structure of the material following ion irradiation is combination of the original UO_2 FCC structure along with dislocation networks and krypton gas bubbles that form as a result of irradiation. It is important to determine the characteristics of these bubbles in the material along with the subsequent alteration to the atomic structure of UO_2 resulting from this irradiation.

While the EXAFS analysis in this study cannot be performed in-situ, a separate study was launched to perform systematic analysis of microstructure evolution in UO_2 using krypton ions at various doses. This in-situ experiment helps understand the dynamic evolution of dislocations in polycrystalline UO_2 at 800^o C. The focus of this irradiation was to understand the progression of microstructure around the grain boundaries of the material, which act as a sink of microstructure defects.

6.2 Sample Preparation

6.2.1 Ex-situ samples with EXAFS analysis

Polycrystalline samples of depleted UO_2 were used for krypton implants. The polycrystalline samples were prepared at Los Alamos National Lab and are from the same set of samples as used for the helium irradiations. The pellets were approximately 5.2 mm in diameter and 4.3 mm high with a theoretical density of ~96%. These samples were subdivided into 5.2 mm diameter and 0.6 mm high samples using a low speed diamond saw in a glove box to

ensure no contamination. The surface of these disks was then polished to a mirror finish using a 0.1 µm grit size polishing paper. The samples were then checked for imperfections using a scanning electron microscope to ensure no polishing damage occurred prior to ion implantation.

6.2.2 In-situ samples at 800^o C

For the in-situ irradiation of polycrystalline UO_2 samples, the material was obtained from Los Alamos National Laboratory, from the same set of samples as the ex-situ irradiation. To isolate the microstructure interaction with grain boundaries, FIB was used to extract lamella from a desirable location in the sample. A lamella was first coarse trenched to dimensions of 15 µm × 10 µm × 1 µm and then welded on to a molybdenum TEM grid. Once welded, the lamella was thinned using the FIB to electron transparency for adequate TEM measurements. The final thickness of the sample was approximately 100 nm using 30 keV gallium ions. Finally, the sample was cleaned using 2 keV Ga ions while on the grid in the FIB. The sample was studied using Technai TF30-FEG TEM to characterize any pre-irradiation damage due to the FIB.

6.3 Krypton Implants

6.3.1 Ex-situ samples with EXAFS analysis

The University of Illinois Urbana Champagne (UIUC) ion accelerator was used to implant 1.8 MeV Krypton ions into the six polycrystalline d-UO_2 samples. The temperature of the irradiation was monitored using thermocouples and was maintained at room temperature.

The ex-situ irradiation set up at UIUC made it possible to perform successive irradiations ranging from 5×10^{13}ions/cm^2 to 1×10^{15}ions/cm^2(corresponding to 0.18 DOA - 3.69 DPA) without removing the six samples from the irradiation chamber. Stopping Range of Ions in Matter (SRIM) atomic displacement and radiation damage simulation code was used prior to the experiment to create an estimate of the irradiation conditions. Quick Kinchin-Pease method was used to estimate the damage profile using SRIM and this method has been outlined as an update to the previously accepted model [84]. Fig.61 shows the SRIM calculation performed to the ion irradiation for the sample irradiated to 3.69 DPA. The implant layer from this irradiation was approximately 1.1 μm. Due to Krypton being a heavier ion, there was insignificant distinction between the damaged plateau and peak region.

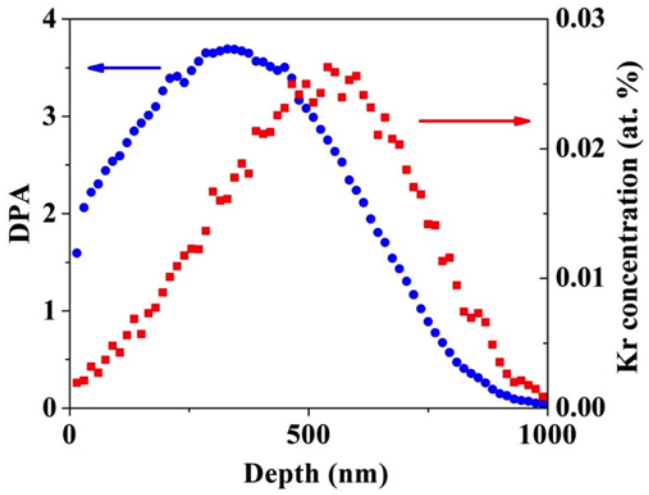

Figure 61: SRIM generated profile of Kr induced radiation damage in UO_2. The plot shows the DPA in the sample at the ion dose level of 1×10^{15} ions/cm^2 and the krypton ion concentration in the sample at the same dose level.

The details of both the single crystal and polycrystalline samples are summarized in Table 11.

Disk Number	Thickness (mm)	Temperature	Fluence (ions/cm^2)	Dose (DPA)
1	0.590	RT	5×10^{13}	0.18
2	0.594	RT	1×10^{14}	0.37
3	0.594	RT	3×10^{14}	1.11
4	0.594	RT	5×10^{14}	1.85
5	0.594	RT	8×10^{14}	2.95
6	0.594	RT	1×10^{15}	3.69

Table 11: Description of $dUO_{2\nu}$ samples prior to Kr irradiation

6.3.2 In - situ samples at 800^o C

For the in-situ irradiations, samples of UO_2 from the same material were used as in the case of the ex-situ irradiation. The in-situ irradiation was executed at the IVEM-Tandem facility at the Argonne National Laboratory. The ions were implanted using a Tandem implanter, which implants ions into the polycrystalline sample inside a 300 kV Hitachi 900 NAR TEM. The incident ion beam at 1 MeV and 150 keV is at an angle of 15 degrees from the surface of the UO_2 samples. The samples were first heated to, and maintained at, a temperature of 600^o C and 800^o C for 30 minutes before the start of the krypton implantation.

6.4 EXAFS Experiments

Ion irradiated samples were loaded on dedicated samples holders for the EXAFS measurements at the Stanford Synchrotron Radiation Lab. The irradiated samples was measured

concurrently with a pristine UO_2 sample that was derived from the same batch as the irradiated samples to ensure consistent results in comparison to crystalline, pure UO_2. The Krypton implanted samples were mounted at the Idaho National Lab on EXAFS specific sample holders. The sample holder was then lined with an indium wire to act as a vacuum seal and was then checked for any vacuum leaks. The difference in the measurement of data for the Krypton irradiated samples was the angle at which the samples were interrogated. Krypton, being a much heavier ion than H^+ and He^{2+} had an implant layer of less than 1.1 μm. EXAFS interrogation volume is typically greater than 1μm and therefore the signal would be an average of unirradiated and irradiated regions. To avoid this, samples were analyzed at a grazing incidence angle at about 10^o to the incident X-ray beam. To avoid the blockage of the beam by the edges of the sample holder, a raising aluminum plate was put in the holder to elevate the samples . Fig. 62 shows an unassembled and assembled sample holder for EXAFS measurements.

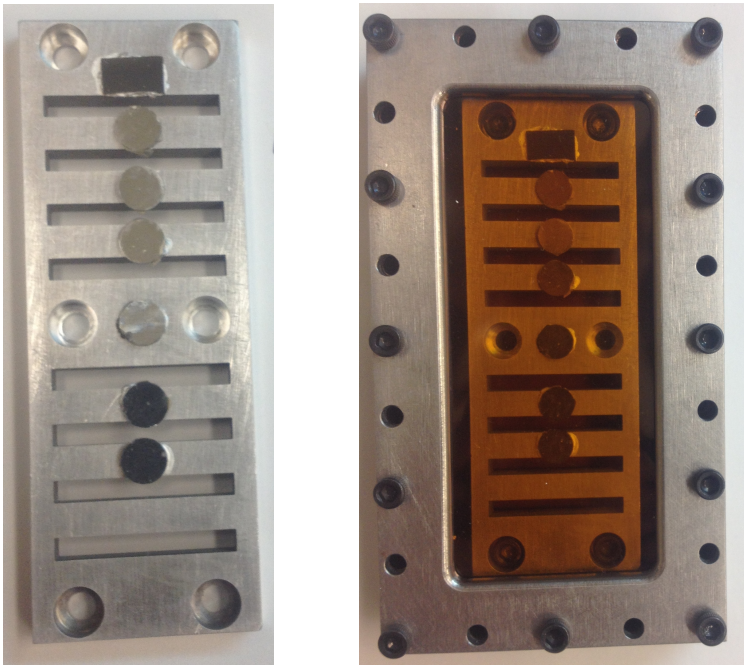

Figure 62: Unassembled and assembled sample holder with Krypton irradiated d-UO_2 samples for EXAFS measurements. The first sample is a piece of Silicon for identification of the order of samples. The samples are then in increasing order of radiation dose. The unassembled sample holder is an image of the samples loaded on an aluminum plate to raise the height of the samples so that the outsides of the sample holder don't block the beam.

EXAFS analysis was carried out under similar conditions to the proton and helium irradiated samples at beamline 11-2 at SSRL, Menlo Park, CA. The data was collected using a multi-element Ge detector placed at an angle of 90^o to the sample. A Zr foil was used to calibrate U spectra with the first inflection point of 17999.35 eV. The edge energy for the uranium (UL_{III}) in the UO_2 samples is approximately 17163.24 eV, which was the target element in the samples. The Curve fitting was done using an in-house software operating on FEFF9 routine. Fourier transforms were performed over the range of 2.50 – 14.70 Å. The

curve fitting results for all the samples are shown in Table 12. Two separate shells were used to fit the O distribution below R $<$ 2.4 Å. This is explained in the results in more detail.

6.5 Results

The χ(R) spectra and the Fourier transforms of the krypton irradiated samples can be summarized in three predominant aspects. First, the spectral features are well defined and represent an FCC lattice as of the unirradiated sample. Therefore, the average structure of the material continues to be in fluorite form. The features of the crystallographic shells are at original locations and fit by the crystallographic atoms as in pristine UO_2. There are, however, variations in the local structure of the samples. Therefore, secondly, the Fourier transforms reveal a general trend of loss of spectral amplitude across the entire range of samples, with the crystallographic features being fit with a decreasing number of atoms in each respective shell with increasing krypton ion dose. The loss of amplitude across the spectrum is monotonic as a function of increasing radiation dose. There exist no regions in the spectra wherein the subsequent loss of amplitude is significantly larger in one R region than another. This indicates the presence of regions of defect clusters, rather than randomly located defects, which however could be present, albeit in much smaller number than the defect aggregates causing monotonic amplitude loss. While irradiation dose doesn't seem to alter the overall fluorite lattice arrangement of the target specimen, there are differences in the local structure, primarily involving the oxygen distribution. Therefore, these oxygen defects alter the lattice just enough that the FCC geometry isn't perturbed. These oxygen defects have been demonstrated in EXAFS of UO_{2+x} not affecting the lattice, as the oxidation

of $UO_{2.00}$ progresses via $UO_{2.25}$ and $UO_{2.3}$ with a growing multisite O distribution, when finally the lattice structure transitions from Fm3m to P62m. Since there is no evidence of a new phase in the irradiated UO_2 samples yet, the defects due to irradiation are limited to local structure changes and oxygen interstitial type defects. Finally, similar to the UO_{2+x} and PuO_{2+x} studies, radiation damage is resulting in oxygen interstitial defects that present the only significant point of difference between the spectra of the irradiated samples. With increasing radiation dose, these oxygen interstitial defects cluster, with a U-O bond of 1.9 Å and can be fit by separate shell of oxygen atoms in EXAFS analysis. These oxygen features start as a small shoulder on the lower R side of the crystallographic peak, thereby, quickly growing in magnitude to its own independent peak in the Fourier transform of χ(R).

The general trend of loss of spectral amplitude is observed across the entire range for the 6 irradiated samples as shown in Fig. 69. The samples have been fit using four atomic shells: three crystallographic shells at 2.35 Å (U-O), 3.85 Å, (U-U) and 4.5 Å (U-O) and one non-crystallographic shell at 1.9 Å. Features corresponding to the fluorite structure of UO_2 are seen throughout the range of samples, even when the dose increases to higher values with the only significant difference being the appearance and increase of the non crystallographic peak at 1.9 Å from the uranium atom. This peak has been identified to be an oxygen peak, fit using an oxygen shell of atoms and has resulted from the incorporation of nonstoichiometric O atoms in the interstitial sites in UO_2. There are empty octahedral sites in the UO_2 lattice that present a good location for the excess oxygen interstitials [52] and these interstitials form clusters by interacting with the crystallographic oxygen ions. Therefore, there seems to be a steady increase in the number of atoms fit in the non crystallographic oxo peak, in comparison to the U-O peak at 2.35 Å. The details of the curve fits on the irradiated samples,

along with a non-irradiated sample from the similarly prepared UO_2 and theoretical results from UO_2 crystal structure, are given in Table 12.

At lower krypton ion doses there appears to be a U – O shoulder forming on the low-R side of the primary oxygen peak. This shoulder begins to transform into an independent peak, which grows in amplitude as the ion dose and subsequently, the radiation damage increases. At higher doses in the χ(R) spectra, the nearest neighbor O region shows two clearly resolved peaks of increasing amplitude with ion dose. This indicates that the UO_2 near neighbor structure is susceptible to forming complex U-O features when irradiated with ions. The shoulder forming on the lower R side of the crystallographic oxygen peak and the upcoming separate peak is fit with its own shell of atoms at 1.9 Å. Remarkably, the formation of a shoulder on the lower R side of the original O shell has been seen in oxidation of UO_2 and has been corroborated by EXAFS results on UO_{2+x} and PuO_{2+x}. Although, the oxo-shoulder feature has been previously fit at 1.7 Å, making the irradiation induced oxo-shoulder slightly longer at 1.9 Å in distance than seen in UO_{2+x} . Therefore, there appears to be an oxygen rich region forming in ion irradiated UO_2 which must exist along with an oxygen poor region elsewhere. The local chemistry in the target material is getting modified to incorporate oxygen ions in the interstitial defect sites when irradiated with krypton ions.

In the χ(R) spectra of the samples, there is no peak shift in the crystallographic peaks of U-O and U-U at 2.35 Å and at 3.45 Å respectively. There is however a monotonic decrease in the peak amplitude across all features of each of the sample spectra as the incoming ion dose is increased. This continuous loss of spectral amplitude indicates that the order is decreasing along with the incorporation of oxygen interstitials in the defect sites in UO_2. The only significant variation is the increase in amplitude of the nearest neighbor non-

crystallographic O peak with a U – O distance of 1.9 Å. The non-crystallographic O peak becomes larger with increasing ion dose while simultaneously the crystallographic O peak diminishes such that at the highest dose point, the two O peaks are distinct and very close in peak amplitude.

Therefore, agreeing with the results of the proton irradiated samples, the mid range order is similar to unirradiated UO_2 and doesn't have a significant decrease in overall amplitude. There is loss of peak height in the first U-O shell at 2.36 Å and the U-U shell at 3.86 Å, which can be attributed to lattice disorder. The oxygen shoulder peak is again present at 1.78 - 1.9 Å, which grows with increasing ion dose. The growth in the oxygen shoulder peak and the loss of amplitude in the crystallographic peaks is not as stark as in the H^+ and He^{2+} irradiated samples. Fig. 63-68 shows the Fourier Transform of EXAFS, $\chi(k)$ and the real component of all the studied UO_2 samples. The lowest dose sample (0.18 DPA) has the highest crystallographic peaks and the lowest oxygen shoulder peak while simultaneously the highest dose (3.69 DPA) sample shown in Fig. 68 has the lowest magnitude of the original U-O and U-U shells and the oxygen shoulder is highest. All 6 of the Krypton irradiated samples with varying doses are interrogated in this study.

Sample		U-O (1.8 Å)	U-O (2.36 Å)	U-U (3.85)	U-O (4.5)
Crystal	R		2.36	3.85	4.52
	N		8	12	24
Reference sample	R		2.35	3.87	4.48
	N		8	12	24
	σ		0.047	0.002	0.073
0.18 DPA	R	1.94 ± 0.02	2.36± 0.02	3.86± 0.01	4.45± 0.02
	N	0.12± 0.03	6.12± 1.7	8.46± 2.01	20.66± 5.2
	σ	0.045	0.045± 0.02	0.019± 0.002	0.012± 0.001
0.37DPA	R	1.94± 0.03	2.36± 0.02	3.86± 0.01	4.45± 0.03
	N	0.26± 0.03	4.2± 1.2	7.02± 1.8	18.75± 4.7
	σ	0.05	0.04± 0.02	0.011± 0.001	0.06± 0.018
1.11 DPA	R	1.94± 0.03	2.35± 0.02	3.87± 0.01	4.51± 0.02
	N	0.32± 0.04	4.19± 1.2	7.17± 1.8	17.16± 4.4
	σ	0.05	0.037± 0.014	0.01± 0.001	0.07± 0.018
1.85 DPA	R	1.92± 0.02	2.34± 0.02	3.87± 0.02	4.5± 0.02
	N	0.07± 0.02	5.06± 1.4	6.83± 1.9	16.42± 3.8
	σ	0.05	0.02± 0.012	0.03± 0.007	0.05± 0.015
2.95 DPA	R	1.87± 0.02	2.35± 0.02	3.87± 0.01	4.47± 0.03
	N	0.03± 0.01	3.58± 0.7	6.61± 1.6	14.91± 2.9
	σ	0.05	0.047± 0.02	0.017± 0.001	0.06± 0.016
3.69 DPA	R	1.834± 0.02	2.38± 0.02	3.87± 0.01	4.52± 0.02
	N	1.33± 0.04	3.34± 0.7	5.43± 1.3	12.15± 2.1
	σ	0.05	0.073± 0.019	0.024± 0.016	0.048± 0.02

Table 12: Fitting parameters for the krypton implanted UO_2 samples.

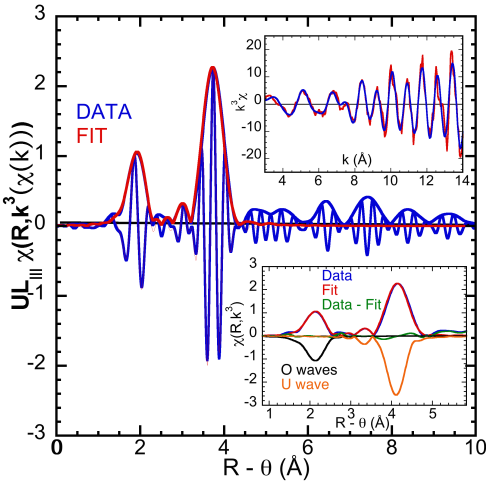

Figure 64: 0.37 DPA sample shows the onset of an oxo shoulder along with distortion of the intermediate order

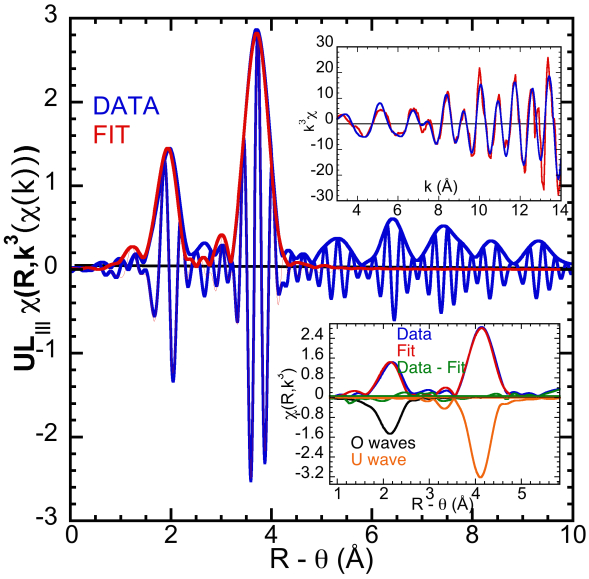

Figure 63: Data from the 0.18 DPA dose in the sample irradiated with Kr ions. Lack of the oxygen shoulder on low R side of the crystallographic shell and the consistent features in the intermediate structure represent the lowest dose sample.

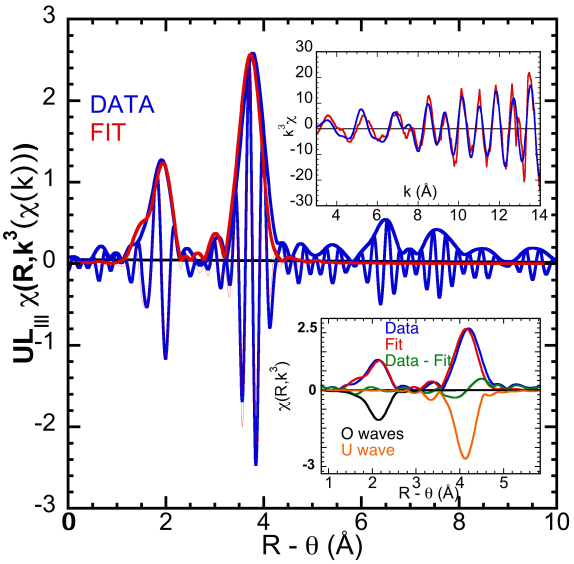

Figure 65: 1.11 DPA sample shows definite growth of an oxo shoulder coupled with relative loss of spectral amplitude

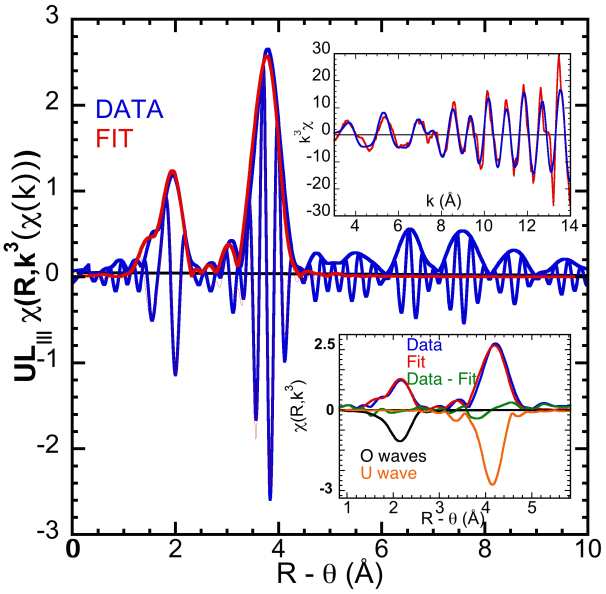

Figure 66: Furthering the dose, the 1.85 DPA sample shows a larger oxo shoulder with reduced peak amplitudes and distorted intermediate range structure

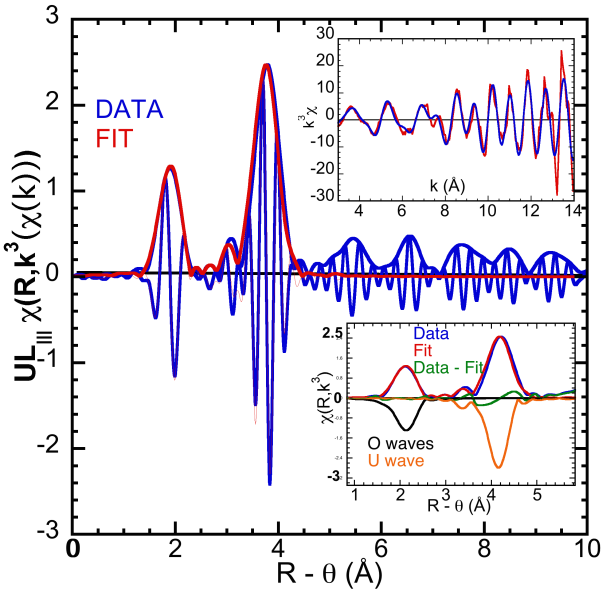

Figure 67: The loss of peak amplitudes continues into the 2.95 DPA sample

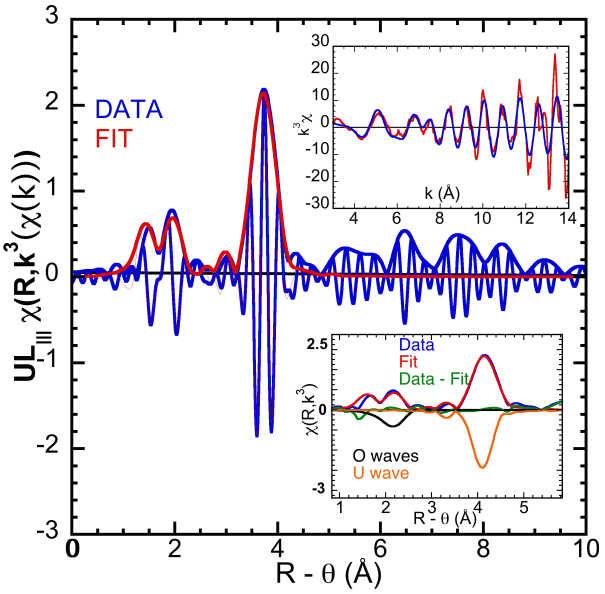

Figure 68: Highest dose sample (3.69 DPA) shows an increasing disorder in the intermediate structure and a decreased peak amplitudes along with a secondary oxygen peak at low R distances that is nearly the same amplitude as the crystallographic peak.

Another interesting effect of the increase in krypton dose is that at the highest dose level of 3.69 DPA (1×10^{15} ions/cm^2), the features as higher R begin to look less like the fluorite structure of UO_2 as seen in the zero dose and at other lower dose samples. This indicates that as the irradiation dose continues to increase, the overall lattice starts to give way to a multisite distribution of atoms. Further, the diminished peak amplitude along with the loss of spectral features gives evidence of non-crystallographic O and U defects invisible to EXAFS. These defects could form clusters in the material thereby reducing the contribution to the overall crystal structure, as its been detected in EXAFS (Fig. 63-69) and altering the fine structure of the material. This is further corroborated by the presence of the two distinct oxygen peaks in the highest dose sample as the oxygen defect cluster is competing in structure with the original crystallographic oxygen shell.

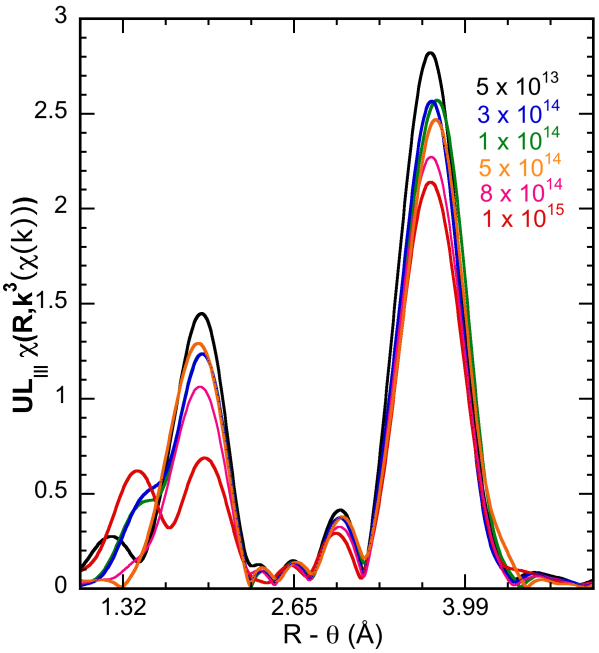

Figure 69: Modulus of Fourier transform of EXAFS fit through 4.5 Å. This image highlights the monotonic spectral amplitude loss and the growth of a non crystallographic O shell at R $<$ 2 Å.

To further highlight the nearest neighbor O peak evolution in the spectra, the region up to R $<$ 2.5 Å was isolated such that both the U-O peaks at 1.9 Å and 2.35 Å were in that region. The ratios of the peak amplitude of the primary O peak and the irradiated sample were taken and these ratios were multiplied to each spectra ensuring a normalized peak height for all the samples for the primary O peak. This normalization reveals the continuous loss of amplitude of the primary O peak coupled with increase in ion dose. More remarkable is the increase in amplitude of the oxo-shoulder on the low R side of the primary O peak. Two distinct changes seem to occur with increasing radiation dose. The primary O peak has shifted 0.01 Å from 2.35 Å to 2.36 Å as the ion dose increases. This change could imply a shift in the lattice parameter to higher numbers, which would be consistent

with EXAFS studies on He^{2+} implanted samples. Another fascinating change is the shift of the oxo shoulder from 1.9 Å to 1.8 Å, where it transforms into a fully resolved independent peak at higher values of incident dose. Coupled with the increase in the amplitude and the transformation into an independent peak, reduction of the U-O_{oxo} distribution shifting to lower R distances could indicate the stabilization of the uranyl type defect clusters, similar to the results from UO_{2+x}.

The formation of a separate peak strongly supports the formation of a secondary phase in the original lattice that doesn't alter the fluorite structure significantly. This formation of domains of defect clusters populated with oxygen is consistently seen in case of UO_{2+x}, supporting the propensity of UO_2 to incorporate U_4O_9 and U_3O_7 type nano domains within the UO_2 lattice at all times. Studies show increased diffusion of oxygen species, specifically oxygen defect clusters, in UO_2 that could further facilitate the formation of smaller UO_{2+x} phases. Without the presence of an active oxidizing mechanism, there ought to be U_2O_3 type O-depleted regions in the material to compensate for UO_{2+x} domains that are detected in XAFS analysis.

Recent studies indicate the formation of photo and radiation stabilized defects in UO_2. Therefore, radiation is enhancing the diffusion of oxo-type defects into aggregation of U(V)/O type structures such that they can be detected via EXAFS measurements. The formation of secondary oxygen peak indicates that the process of oxygen diffusion is in fact preferential and cannot occur in a static unperturbed lattice. This process of oxygen diffusion is high during damage cascades but continues throughout the lifetime of the lattice whenever the oxygen atom has enough energy to migrate and form defect clusters. These defect clusters have been postulated to form U_4O_9 nano domains that consistently exist in the UO_2 lattice.

The COT type defect is the building block of this U_4O_9 structure. The formation of these oxo peaks, in tandem with the preserved overall fluorite structure gives strong evidence of UO_2 retaining its longer range structure with altered short order under irradiation. The idea of UO_{2+x} and UO_{2-x} regions occurring within the lattice due to irradiation supports a recent hypothesis based on Raman spectroscopy measurements performed in He^{2+} implanted UO_3 samples. The study postulates the formation of Magneli type defects that occur due to reorganization of U(III) and U(IV) type domains based on preferential clustering of oxygen atoms. In this case, as in the one discussed in this study, radiation damage proceeds to stabilize small defect clusters that are being detected in experimental measurements.

The decrease in magnitude of the primary oxygen peak is normalized in Fig. 70 so the peak height is identical. By doing this, it can be seen that the oxygen shoulder peak for the highest dose sample (3.69 DPA) has the highest contribution whereas the lowest dose material (0.18 DPA) has the shoulder peak. Not surprisingly, this is consistent with the observations from H^+ and He^{2+} irradiated material. It is important to note the shape and the size of the oxygen shoulder is different from the H^+ and He^{2+} irradiated samples. In the krypton irradiated samples, as the ion dose increases, the shoulder develops into an independent peak fit using an additional shell of oxygen atoms. The difference in the data and the fit of the data is small, which indicates that the new low R peak is indeed a set of oxygen interstitials displaced from their original crystallographic position in the lattice.

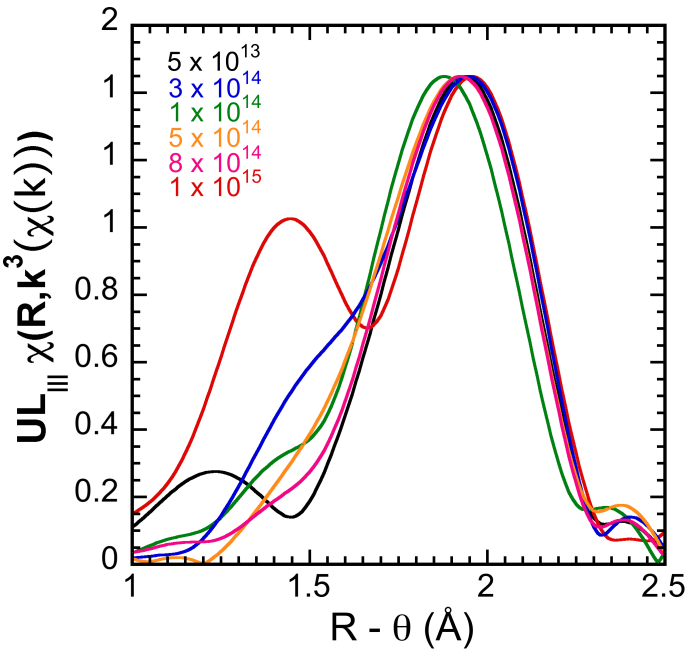

Figure 70: Low R features in He samples compared to two reference samples

To further highlight the nearest neighbor O peak evolution in the spectra, the region up to R $<$ 2.5 Å was isolated such that both the U-O peaks at 1.9 Å and 2.35 Å were in that region. Further, the ratios of the primary O peak for the peak amplitude of the control sample and the irradiated sample were taken and these ratios were multiplied to each spectra ensuring a normalized peak height for all the samples for the primary O peak. Due to correlation between the Debye-Waller factor and the number of atoms being fit in each shell [81], the ratio of the two quantities accurately represents the change due to ion irradiation. Fig. 71 shows the ratio of the number of atoms fit in each shell to the Debye-Waller factor for the respective shells.

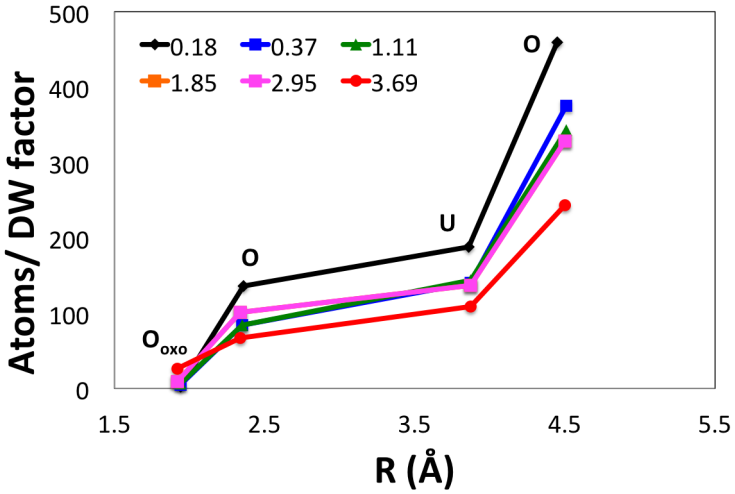

Figure 71: Ratio of number of atoms fit in each shell (including the 1.9 Å shoulder) to the DW factor for each of those shells shows a decrease in this ratio with increasing ion dose except for the U-O shoulder at 1.78 Å.

Table 13 shows the ratio of the number of atoms fit in the oxygen shoulder peak to the DW factor for the shells for varying krypton dose. While the overall effect of krypton irradiation is not clear in the EXAFS spectra, the oxygen peak for each sample still grows with increasing ion dose. The oxygen peak is at a distance of 1.78 Å from the absorbing atom (uranium) which is less than the previously studied samples.

DPA	Atoms / DW
0.18	2.6
0.37	5.2
1.11	6.4
1.85	9.4
2.95	0.6
3.69	26.6

Table 13: Ratio of the number of atoms to the Debye Waller factor increasing in value to indicated the total number of atoms in at the 1.78 Å distance are growing.

6.6 X-ray Diffraction

X-Ray Diffraction measurements were performed on all the krypton implanted samples using the (224) XRD reflection for comparison. The (224) reflection has a high probing length of 1.6 μm, which interrogates the damaged plateau region thus not including effects in the peak region. The measurements were performed in grazing incidence geometry such that only the irradiated damage layer of ~1 µm was interrogated with the sample. With increasing krypton ion dose, lattice peak shift was observed to lower 2θ angles as is shown in Fig. 72. The sample was placed at 2 degrees from the incident x-ray beam and was maintained at this angle to study only the damage region. The measurements reveal a high level of lattice distortion that is increasing with ion dose in the sample. The lowest

dose specimen shows evidence of lattice peak shift and phase transformation to a large extent. Since these measurements were performed at room temperature, the UO_2 structure didn't have the sufficient energy to annihilate the distribution of defects and therefore, the highly complicated lattice damage is seen in the XRD measurements. The XRD studies are somewhat inconsistent with the EXAFS analysis done on krypton implanted UO_2. While there is evidence of phase evolution in EXAFS, there is no clear indication of a highly damage lattice as is seen in the diffraction measurements on these samples. This could primarily be due to the difference in the interrogation volume in UO_2 during EXAFS data collection at the synchrotron beamline. Since EXAFS averages the signal over the volume of the sample, it is possible that the angle of the grazing incidence wasn't small enough to extract the data just from the 1.1µm of krypton damage, but instead measured the signal from the pristine part of the sample that lies beyond the irradiated region.

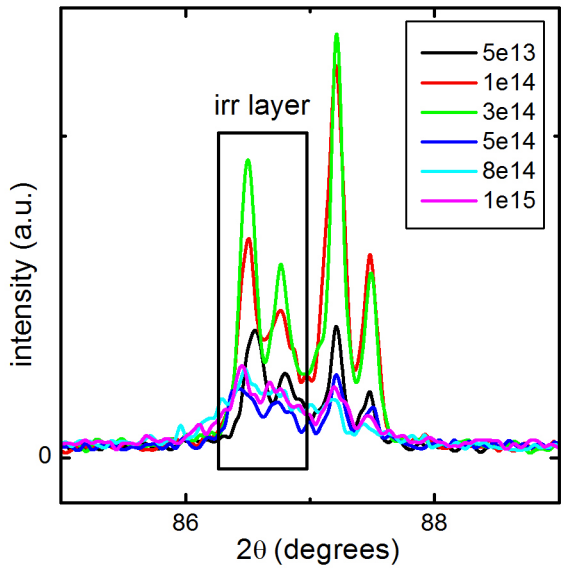

Figure 72: X-ray Diffraction studies on krypton implanted UO_2samples shows that with increasing irradiation damage, the lattice fails to maintain its overall structure

6.7 Transmission Electron Microscopy

6.7.1 Ex-situ TEM samples

Unlike the proton irradiated sample, the microstructure due to krypton implantation is significantly more complicated as it consists of several microstructure features. Krypton, being a heavier atom causes more damage to the sample than the smaller proton and helium atoms. The doses achieved during the krypton irradiation are higher and therefore result in high radiation disorder, which is only further exacerbated by the size of its atoms. The irradiation was also performed at room temperature, which does not allow for coalescence and annihilation of defects and therefore results in isolated defects that are more complicated to understand using microscopy. TEM has revealed the presence of dislocation loops (Fig.

73) and bubbles (Fig. 75) in krypton irradiated UO_2 samples. Fig. 73 shows the presence of dislocations and extended networks in polycrystalline UO_2.

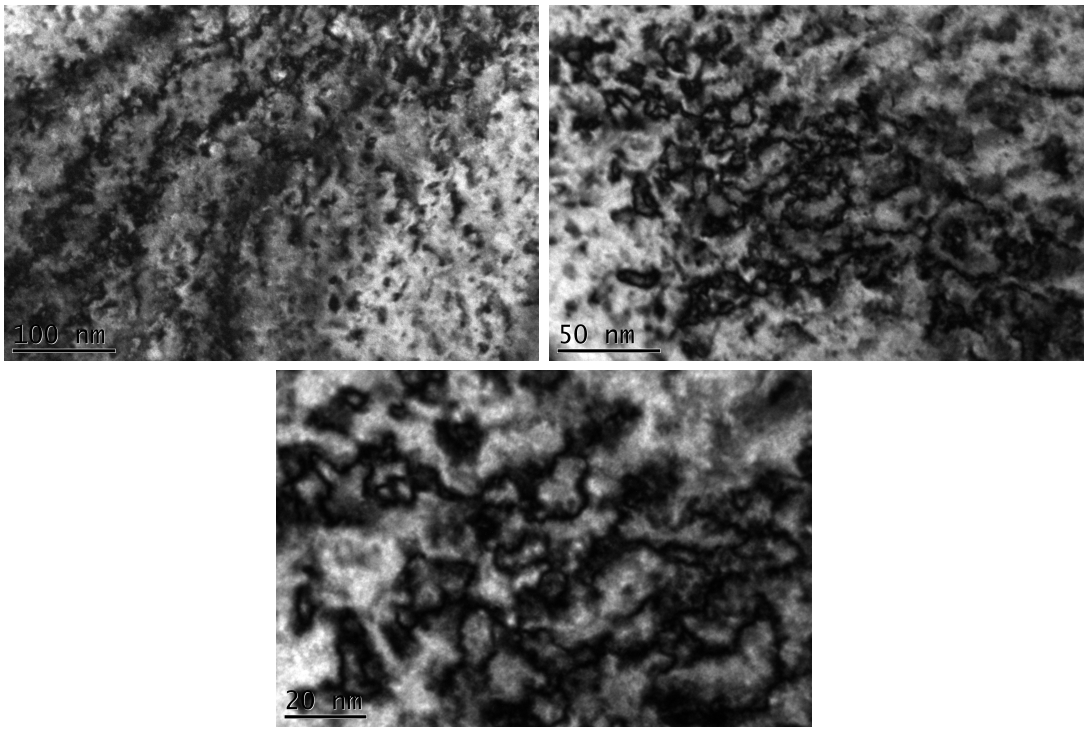

Figure 73: TEM micrographs show the presence of dislocation loops and extended network in krypton implanted UO_2. The network of dislocation grows consistently more complex as the dose of the sample increases.

6.7.2 In-situ TEM samples

TEM measurements for the dislocation observation and characterization was performed by assuming all the dislocations have the same Burgers vector. The measurements of density and loop size were performed manually and each measurement was performed over 5 measurable areas for number density of 50-200 measured features for loop size analysis. The measurements were carried from [111] direction with $g = 220$ reflection. TEM micrographs

in Fig 74. show the dislocation evolution in polycrystalline UO_2 under 1 MeV Kr irradiation at 800^o C. The evolution follows a general (previously observed) trend of small loops $\rightarrow$ big loops $\rightarrow$ dislocation lines$\rightarrow$ dislocation tangles, as the irradiation ion dose increases. Isolating the area around grain boundaries gives insight into the interaction of the dislocations with the sink. Throughout the dose range, there was evidence of a dislocation denuded zone around the grain boundaries of the material.

The increase in the size of the dislocation loops are summarized in Table 14. The assumption is that the dislocations form as a result of interstitial clustering into disk shaped loops that preferentially lie along [111] plane in the UO_2 lattice with a Burgers vector of b = a/2[111]. Therefore, the density of interstitials in the loops can be estimated from the loop area per volume. This loop density has increased significantly as the ion dose reaches a peak value of 1×10^{15} ions/cm^2. It is seen that the number of interstitials in the dislocation loops appear to saturate at the highest dose point.

Dose	Loop Size (nm)	Loop Density (#/m^3)
1×10^{14}	5.67	5.00×10^{22}
3×10^{14}	6.84	5.08×10^{22}
5×10^{14}	7.96	4.38×10^{22}
8×10^{14}	8.06	4.13×10^{22}
1×10^{15}	10.4	3.76×10^{22}
2×10^{15}	12.55	1.78×10^{22}
3×10^{15}	14.35	1.03×10^{22}
4×10^{15}	15.95	9.92×10^{21}
5×10^{15}	16.73	8.68×10^{21}

Table 14: Comparison of loop area and density evolution with increasing krypton ion dose.

Observing the denuded zone in the grain boundaries of the 1 MeV krypton implanted UO_2 is the first known observation of the dislocation denuded zone in UO_2 (Fig. 74). It is also

noted that as the incoming ion dose increases, the relative width of the denuded zone shows a marked increase. Studies have shown the propensity of higher angle grain boundaries to have higher sink strength due to their open structure. Further, higher temperatures create higher diffusion rates that cause the interstitial atoms to migrate to grain boundary sinks. Therefore, dislocation denuded zone are more common at high angle grain boundaries at higher temperatures than in case of low angle boundaries at lower temperatures.

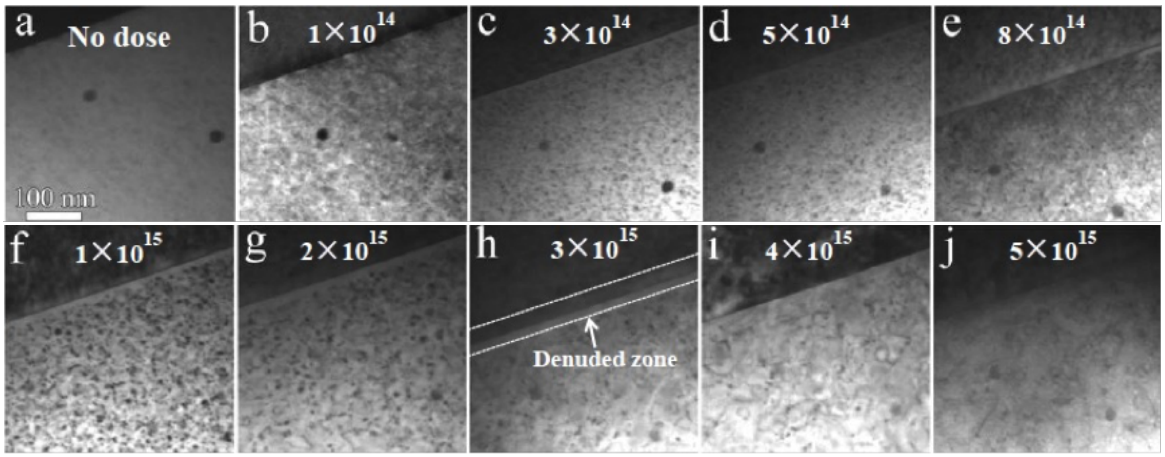

Figure 74: Bright field images show the nucleation and growth of dislocation loops with increasing krypton ion dose

Bubble density, size and evolution were measured for the Kr irradiated UO_2 samples by assuming all the bubbles have a spherical shape. The krypton gas bubbles occupy 1.94% of the sample volume at 800 ^oC with a maximum bubble diameter of 2.1 nm at the highest dose level. The evolution of bubble size and diameter with radiation dose is listed in Table 15. In comparison with literature information on lower temperature Kr implanted UO_2 **[35]**, the bubble swelling and volume are significantly more with increase in temperature of the samples. As an example, the bubbles occupy 0.35% of the sample volume at room

temperature, 1.22% of the volume at 600 ^{o}C and then 1.94% of the volume at 800 ^{o}C. The result of bubble diameter and density evolution is in agreement with the in-pile irradiation measurements done in the past **[75]**. While dislocations dominant regions also had grain boundary dislocation denuted zones, no such observation was made where the Kr gas bubbles aggregated along the grain boundaries in the sample.

Fluence	Bubble Diameter	Bubble Density
1×10^{14}	1.48 ± 0.3 nm	2.4×10^{24} / m^3
3×10^{14}	1.52 ± 0.3 nm	2.6×10^{24} / m^3
5×10^{14}	1.57 ± 0.3 nm	3×10^{24} / m^3
1×10^{15}	1.6 ± 0.3 nm	3.3×10^{24} / m^3
2×10^{15}	1.62 ± 0.3 nm	3.7×10^{24} / m^3
3×10^{15}	1.64 ± 0.3 nm	4×10^{24} / m^3
5×10^{15}	1.67 ± 0.3 nm	4.2×10^{24} / m^3

Table 15: Increase in Kr bubble diameter and size with increasing ion dose

Bubble images were extracted along the edge region of the sample irradiated to 800 ^{o}C. The surface region can absorb more interstitials than vacancies due to the higher mobility of interstitials as compared to vacancies. The region close to the surface also acts as an area for defect sinks. The krypton ions can get trapped in the unbalanced vacancies close to the surface of the sample and form Kr gas bubbles in the edge areas. The preexisting Kr atoms can also migrate to small bubbles and enlarge them by getting absorbed there, relieving the stress arising from ion implantation. The over focus and under-focus image of polycrystalline UO_2 samples irradiated by Kr ions to a temperature of 800 ^{o}C for intermediate dose of 3.7 $\times$ 10^{15} ions/cm^2 and high dose of 5 $\times$ 10^{15} ions/cm^2 is shown in Fig. 75. A high resolution image of the TEM bubbles is shown in Fig. 76.

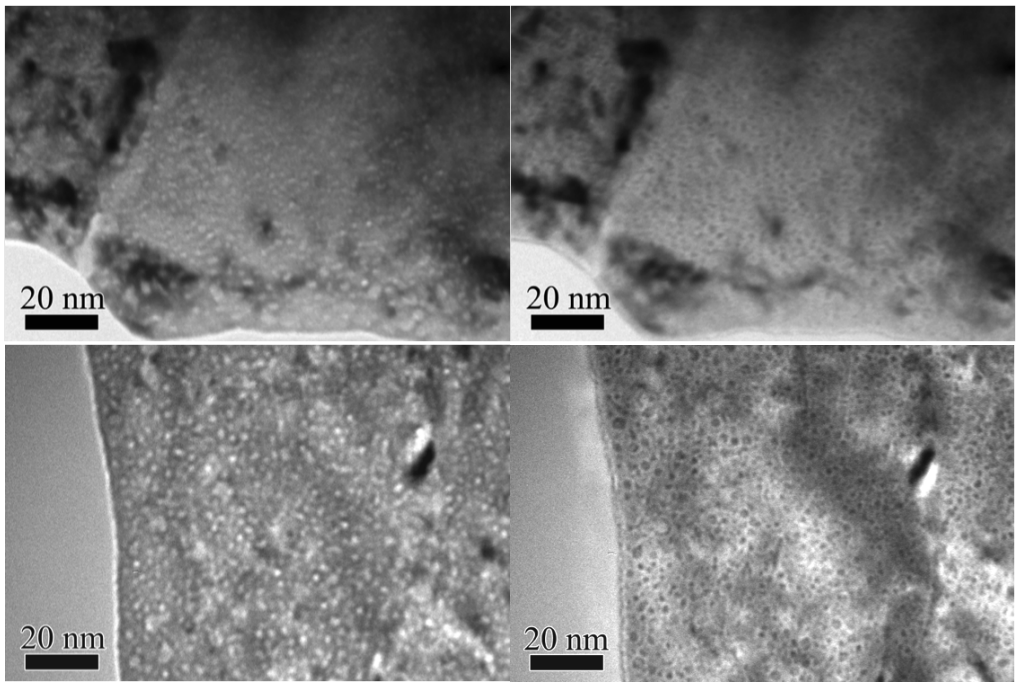

Figure 75: Bubble images at intermediate dose of 3.7×10^{15} ions/cm^2 and final dose of 5×10^{15} ions/cm^2

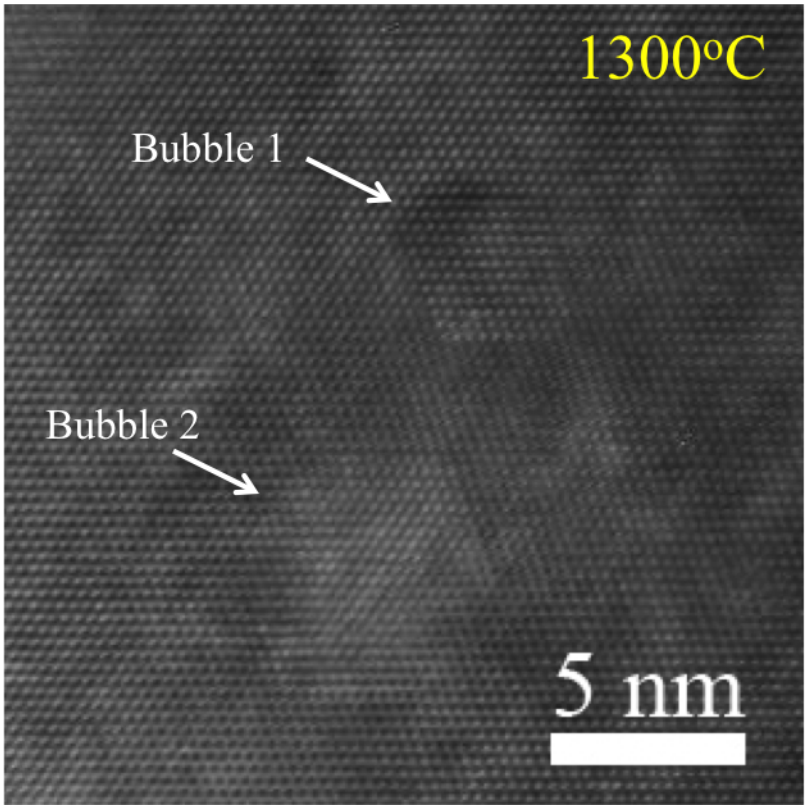

Figure 76: Krypton bubbles found in irradiated sample

The evolution of dislocation microstructure and krypton gas bubbles was analyzed using Transmission Electron Microscopy in in situ and ex situ implanted polycrystalline UO_2. Simultaneously, the samples used for ex situ irradiation were characterized using X-ray Diffraction and Extended Xray Absorption Fine Structure measurements. TEM results show the evolution of dislocation microstructure follows the trend of small loops → big loops → dislocation lines→ dislocation tangles with increasing krypton ion dose.

In case of the room temperature samples, the annealing of the samples wasn't perform, which rendered the damage rather challenging to quantify. Room temperature irradiation does create relatively similar damage to high temperature irradiation, with the exception that

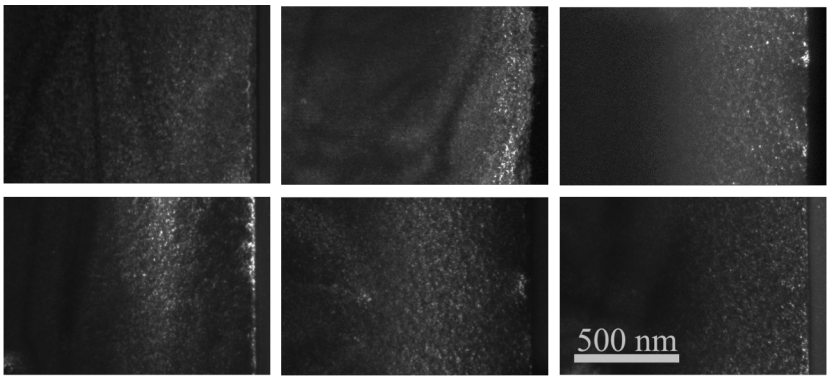

Figure 77: Evolution of defect microstructure in Kr implanted UO_2 at low dose

temperature aided defect annihilation and defect growth is minimized. The micrographs in Fig. 77 show an evolution of dose from 3×10^{15} ions/cm^2 through to 1×10^{15} ions/cm^2 with a visible increase in damage in the material. These images are taken in dark field imaging mode due to enhanced contrast of the damage. Once annealed, these images are expected to resemble the bubble and loop geometry similar to the 800 ^{o}C samples.

The general loop density decreases with increasing ion dose, while the loop size shows an increase. XRD results show an expansion in the lattice with ion dose and suggest the transformation into newer phases due to increased atom mobility. Finally, EXAFS reveals a hyperstoichiometric UO_2 local structure with a distorted near neighbor oxygen distribution along with a conserved overall fluorite structure. The EXAFS results indicate the propensity of UO_2 to exist as UO_{2+x}in the presence of external energy sources, which in this case is given by krypton ion irradiation. The lattice structure evolution is a result of the damaging nature of radiation and is evident in the decreased peak amplitudes of the krypton ions. Overall, krypton ions create zones of high microstructure and local structure damage, while maintaining the fluorite FCC structure in UO_2.

6.8 Summary

Krypton ions were accelerated using an ion accelerator in ex-situ and in-situ irradiation methods to evaluate the effect of radiation damage in UO_2 due to one of the most common fission products. The analysis was done using Xray Diffraction to study the change in lattice parameter and EXAFS was used to probe the local structure distribution along with the clustering of oxygen defects due to irradiation. TEM was used to study the change in microstructure resulting from krypton irradiation. The key results are:

1. XRD reveals an increase in the lattice parameter coupled with altered lattice structure
2. EXAFS collectively reveals
    (a) Oxygen clustering at U-O distance of 1.8 - 1.9 Å, which is a non crystallographic position
    (b) Reduced spectral amplitude for all peaks with increasing dose that indicates a loss of overall structure
    (c) Increased near neighbor distances supporting an increase in the lattice parameter
    (d) With increase in dose, the U-$O_{non-crystallographic}$ distance decreases to more stable uranyl distances
3. TEM results can collectively be summarized as

(a) The microstructure is dominated by dislocation loops and inert gas bubbles.

(b) The dislocations grow with ion dose and follow a general trend of small loops → big loops → dislocation lines→ dislocation tangles.

(c) The bubbles tend to do grow smaller in density but larger in size with increasing ion dose.

(d) There was an observation of defect denuted zone along the grain boundary in krypton implanted UO_2 samples

Overall, the lattice structure and microstructure gets more complicated and less coherent with increasing ion dose and the measurement techniques listed here, demonstrate this change. The discussion of these results is in the Discussion section

7 Discussion

7.1 Summary of H^+ Irradiated Samples

Proton irradiations were performed to simulate radiation damage due to neutron irradiation in a nuclear reactor. The irradiation was performed using an ion accelerator at a proton acceleration energy of 2.6 MeV on the target sample for a set of 6 samples with systematic dose increase from 0.01 DPA through 0.5 DPA. The samples were analyzed using techniques specific to local structure (EXAFS), average structure (XRD) and microstructure (TEM).

Using EXAFS analysis technique, the proton irradiated samples show an increase in the low-R oxo-feature with increasing ion dose. The reference sample in Fig. 78 and the low dose sample (0.01 DPA) have no evidence of the 1.9 Å oxygen peak, which forms as a result of increasing irradiation. With slightly higher doses of 0.05 DPA and 0.1 DPA, this peak increases in magnitude and therefore can be fit by an independent shell of atoms in the UO_2 near neighbor distribution. The increase in size of this oxygen shoulder on the low-R side of the original crystallographic O-peak occurs simultaneously with a decrease in magnitude of the original oxygen peak at 2.36 Å. This indicates that somehow the oxygen atoms in the original peak are rearranging themselves to shorter and more stable distances close to the absorbing ion, uranium. As discussed previously, the uranyl complex of uranium atom double bonded with oxygen has bond distances of approximately 1.7-1.8 Å and is highly stable in its arrangement. Therefore uranyl type bonding is inferred in the structure of irradiated UO_2 and it grows with increasing irradiation dose.

While for radiation doses of 0.01 DPA through 0.4 DPA, the 1.9-1.8 Å oxygen peak grows as the radiation dose increases, the higher R peaks of $R > 4.5$ Å do not show a change in peak positions but they do have a reduced amplitude similar to the first two crystallographic peaks

of oxygen and uranium. As the proton radiation dose increases to 0.5 DPA, the distortion in EXAFS spectra, and hence the lattice structure, shows disorder that isn't localized any longer just to the first nearest neighbors. This can be seen in Fig. 78 where the EXAFS spectra for the 0.5 DPA is seen in orange. The presence of the low R oxygen peak occurs simultaneously with highly disordered midrange structural features and the peaks do not follow the fluorite lattice positions any longer. This implies that at higher radiation doses, the disorder grows and affects the whole lattice rather than just the immediate neighbors.

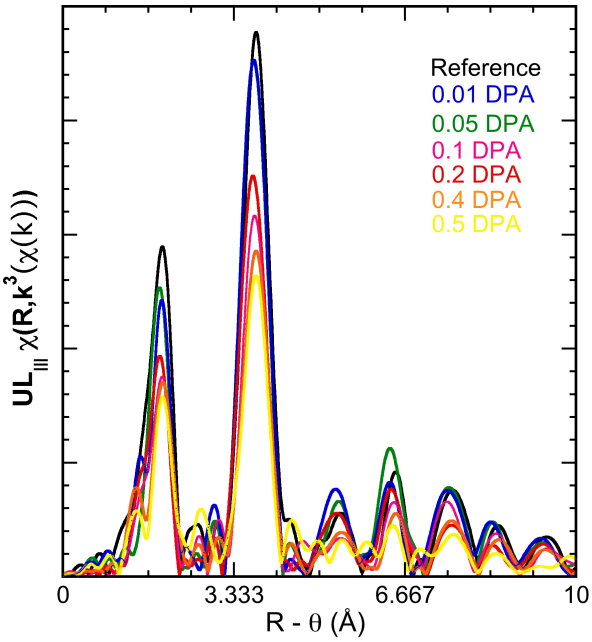

Figure 78: Fourier Transform of k^3-weighted EXAFS for proton irradiated polycrystalline samples through 0.4 DPA - 0.5 DPA dose

X-ray Diffraction studies show a small, albeit consistent, increase in lattice parameter with dose in the material. This increasing lattice parameter is consistent with EXAFS measurements, where the near neighbor atoms are fit 0.01 Å longer than the pristine sample. With increasing dose, the shoulder shifts to shorter U-O distances, while the rest of the lattice expands. Therefore, the O shell is incorporated close to the U atom and supports the theoretical presence of oxygen rich regions in the material, along with oxygen poor regions in the material.

The EXAFS and XRD results can be summarized as:

1. The lattice parameter grows slowly with dose and has been verified by EXAFS and XRD measurements.

2. Monotonic loss of amplitude of the Fourier transform suggests loss of atoms in crystallographic positions along with the presence of systematic (non-glassy) type defects that suggest atomic clustering.

3. The oxygen shoulder consistently grows in prominence and moves to shorter U-O distances while simultaneously the remaining lattice exhibits expansion.

4. At high radiation dose of H^+ ions of 0.5 DPA, the intermediate structure shows significant variation from fluorite structure.

Transmission Electron Microscopy measurements reveal simple radiation induced microstructure due to proton irradiation consisting of dislocations. The dislocation loop dominant

microstructure was studied along the [110] pole and the loops were seen to lie along g = [111]. Most dislocation loops have been confirmed to lie along the [111] plane due to a large empty space in the fluorite lattice that exists as an interstitial defect site along this plane. The incorporation of oxygen interstitial atoms locally not only provides stability to the lattice, but also creates small domains of UO_{2+x} (mostly U_4O_9) type phases [74]. The TEM observed dislocations are shown to be off-stoichiometric due to greater diffusion of oxygen in the material and therefore are oxygen rich in constitution. However, the density of dislocations don't quite justify the larger distortion of the lattice as suggested in EXAFS and XRD. The TEM observations can be summarized as:

1. The dislocation dominant microstructure shows an increase in loop density from 7.06×10^{21} through to 1.4×10^{23} loops / m^3 with increasing ion dose from 0.01 to 0.5 DPA.

2. The size of the dislocation loops first decreases with increasing dose and then saturates at a size of ~ 9 nm.

3. There is a distribution of defect clusters that appear invisible to TEM but are visible and detected by techniques sensitive to the atomic structure.

7.2 Summary of He^{2+} Irradiated Samples

He^{2+} irradiated samples were studied using X-ray Diffraction, Extended X-ray Absorption Fine Structure spectroscopy and Transmission Electron Microscopy. The collective results indicate an expansion of the lattice, a reorganization of constituent lattice atoms and presence

of microstructure defects, all of which get more complicated with increasing ion dose. UO_2 samples in this study were irradiated to 0.006 and 0.035 DPA and were studied along with a pristine sample for control. A summary of the key results and findings has been discussed in this subsection.

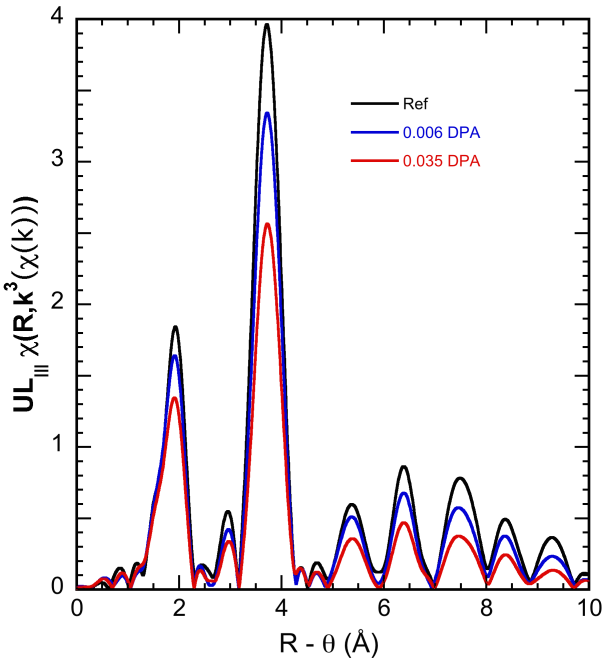

Figure 79: Fourier Transform of k^3-weighted EXAFS for helium irradiated polycrystalline samples through 0.006 DPA - 0.035 DPA dose

X-ray Diffraction studies clearly point to an increase in lattice parameter, consistent with literature, which demonstrates an incremental relationship with dose. EXAFS results in the case of He^{2+} implanted samples (shown in Fig. 79), show a combination of three simultaneous effects due to ion irradiation:

1. The near neighbor distances show an increase, that directly support the XRD results of lattice parameter increase.
2. The overall spectral amplitude monotonically decreases, indicating the variation of irradiated material from pristine UO_2 lattice.
3. An oxygen shoulder peak gains prominence at short U-O distances of 1.9 Å, also consistently with an increase in ion dose.

Transmission Electron Microscopy measurements collectively indicate:

1. The presence of radiation induced gas bubbles resulting from He^{2+} irradiation.
2. The measurements indicate radiation damage induced microstructure in the plateau region is relatively constant and therefore offers a good region for X-ray measurements.
3. The measurements were done close to the (011) pole with g = [-1-11] and showed a large distribution of dislocation loops.
4. The density and the size of the loops grew from 6 $\times 10^{21}$ to 13$\times 10^{21}$ loops/ $m^3$and from 7.3 to 8.5 nm respectively.

7.3 Summary of Kr Irradiated Samples

To understand the impact of one of most common fission products, krypton irradiation in UO_2 was performed using an ion accelerator with in-situ and ex-situ implantation modes.

The krypton ions were accelerated to an energy of 1.8 MeV, providing a short implantation depth of 1.1 µm. This implantation damage required EXAFS and XRD techniques to be altered so as to interrogate only this short damage region. The atomic and lattice structure evolution was studied using EXAFS and XRD and the microstructure was interrogated using the TEM. The cumulative bulk radiation dose of the samples is from 0.18 DPA through to 3.7 DPA. The irradiations were performed at room temperature for ex situ and at 600 ^{o}C for in situ irradiation.

X-ray diffraction suggests a complete loss of phase due to krypton damage in the damage region. EXAFS results, extracted using grazing incidence measurements, consistently point to an increase in the near neighbor spacing in the material along with the appearance of an oxygen shoulder at low R distance of 1.8 Å from the absorbing ion. This shoulder is seen to develop into a fully independent peak at higher dose rates. Similar to H^{+} and He^{2+} EXAFS results, Kr implanted samples demonstrate a loss of spectral amplitude consistent with ion dose increase. The krypton irradiated samples have very little change in the mid range features at all dose levels and mostly show a variation in near neighbor structure. The Fourier Transform of the EXAFS for krypton irradiated samples can be seen in Fig. 80**.** The key EXAFS and XRD results are:

1. Loss of spectral amplitude is seen in both XRD (average structure) and EXAFS (local structure)

2. Increase in lattice parameter (XRD) is consistent with increase in near neighbor distances in EXAFS with the increase of near neighbor distance by 0.02 Å at high Kr dose.

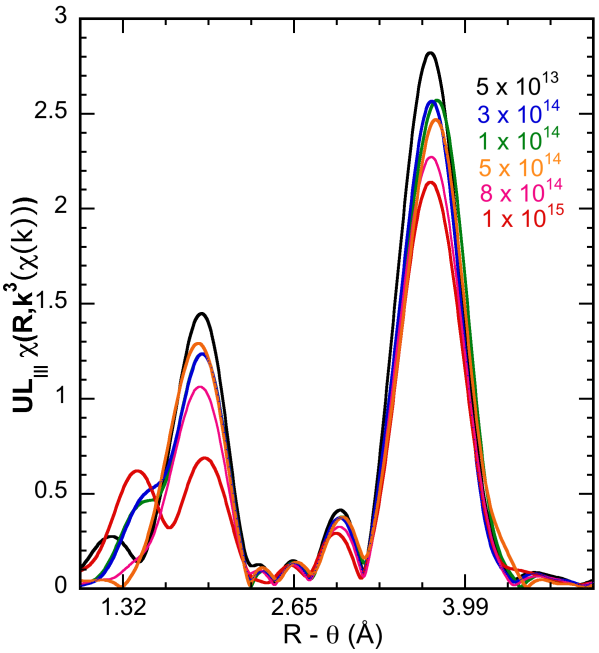

Figure 80: Modulus of Fourier transform of various dose krypton implanted UO_2 samples

3. Near neighbor feature at 1.8 Å can be fit with a shell of oxygen ions indicating a cluster of O defects growing with dose at short distance from U atom.

4. With high dose, the non crystallographic shoulder increases to an independent O peak with nearly the same magnitude as the crystallographic peak.

5. With increase in ion dose, the near neighbor distance between U and the non crystallographic O peak decreases from 1.9 Å to 1.78 Å, while the rest of the near neighbor spacings increase.

The measurements were performed on FIB lamellae that were extracted from the damaged region of 1.1 µm. Transmission Electron Microscopy results indicate

1. The presence of two primary defect types: Dislocation types and inert gas bubbles.
2. The density of the dislocations decreased from 5×10^{22} loops/m^3 to 8.68×10^{21} loops/m^3.
3. The dislocations coalesced to form larger networks that were seen in higher dose samples and therefore, the loop size grew from 5.67 nm to 16.73 nm.
4. In case of bubbles, the overall gas bubble size is approximately 1.6 nm with a density on the order of 10^{24} bubbles/m^3.

The reduction in amplitude of the crystallographic peaks in EXAFS suggests a disappearance of atoms from their original positions to being spread over varying distances from their crystallographic positions. The O atoms tend to form a cluster appearing hyperstoichiometric at short U-O distances of 1.8 Å. The U-$O_{non-crystallographic}$ distance decreased with increasing ion dose. Therefore, the U-O distance moves towards a more stable type configuration with increasing disturbance in the lattice. This short bond has been found in uranyl complexes and in U_4O_9 type structures. These observations are similar to the H and He samples, albeit to different extents.

TEM results overall suggest that dislocation loops coalesce to form dislocation networks that are lower in density but greater in size. This is due to the increased mobility of atoms during ion implantation and therefore, the higher the dose, the greater is the mobility of atoms to form larger defect structures during the irradiation. Inert gas, krypton, coalesces to form bubbles in UO_2 where the size of bubbles is aided by the increase in temperature of

the sample. Therefore, higher the sample temperature, the greater is the mobility of the Kr ion to form larger gas bubbles.

7.4 Similarities and Differences in Irradiation Conditions

One of the key goals of this study is to understand the effects of different irradiation conditions on the resulting microstructure in UO_2. Using three different irradiation species and their range of fluences, this section will attempt to point out the essential microstructure and lattice structure differences. Table 16 and 17 show the estimates of dislocation density, size bubble density and bubble size for all the irradiation species at various radiation doses.

With increasing irradiation species size, there is a consistent increase loop diameter (as shown in Fig. 81). The damage due to ion irradiation is larger at any given dose due to a larger irradiation species. Therefore, at the dose of 0.01 DPA, the loop diameter due to He irradiation is greater than loop diameter due to H irradiation. In case of loop density, H and He irradiation causes the density to increase with irradiation dose. However, Kr irradiation causes loop density to decrease due to loop transition from individual dislocations to dislocation networks. This results in larger and larger loop sizes and lower and lower density of the loop.

Ion	Dose (DPA)	Microstructure	Density	Size (nm)
Kr	0.37	Dislocation Loops	5.0×10^{22} loops/ m^3	5.67 ± 0.3
	1.11	“	5.08×10^{22} loops/ m^3	6.84± 0.3
	1.85	“	4.38×10^{22} loops/ m^3	7.96± 0.3
	2.95	“	4.13×10^{22} loops/ m^3	8.06± 0.3
	3.69	“	3.76×10^{22} loops/ m^3	10.4± 0.3
	Higher doses	Dislocation network	density decreases	> 12
He	0.006	Dislocation loops	6×10^{21} loops/m^3	7.3± 0.3 nm
	0.035	Dislocation loops	8×10^{22} loops/m^3	8.5± 0.3 nm
H	0.01	Dislocation loops	3.06×10^{21} loop/m^3	7.9 ± 0.4
	0.05	“	4.23×10^{21} loop/m^3	8.3 ± 0.4
	0.1	“	7.38×10^{22} loop/m^3	10.5 ± 0.4
	0.4	“	8.02×10^{22} loop/m^3	14.2 ± 0.4
	0.5	“	9.4×10^{22} loop/m^3	15.7 ± 0.4

Table 16: Summary of Dislocation loop features observed using Transmission Electron Microscopy

Ion	Dose (DPA)	Microstructure	Density	Size (nm)
Kr	0.37	Bubbles	$2.4 \pm 0.1 \times 10^{24}$ / m^3	1.48 ± 0.3 nm
	1.11	“	$2.6 \pm 0.1 \times 10^{24}$ / m^3	1.52 ± 0.3 nm
	1.85	“	$3 \pm 0.1 \times 10^{24}$ / m^3	1.57 ± 0.3 nm
	2.95	“	$3.3\pm 0.1 \times 10^{24}$ / m^3	1.6 ± 0.3 nm
	3.69	“	$3.7\pm 0.1 \times 10^{24}$ / m^3	1.62 ± 0.3 nm
He	0.006	Bubbles	$5 \pm 0.3 \times 10^{23}$ / m^3	1.3± 0.3 nm
	0.035	“	$9 \pm 0.3 \times 10^{23}$ / m^3	1.6± 0.3 nm

Table 17: Summary of inert gas bubbles features observed using Transmission Electron Microscopy

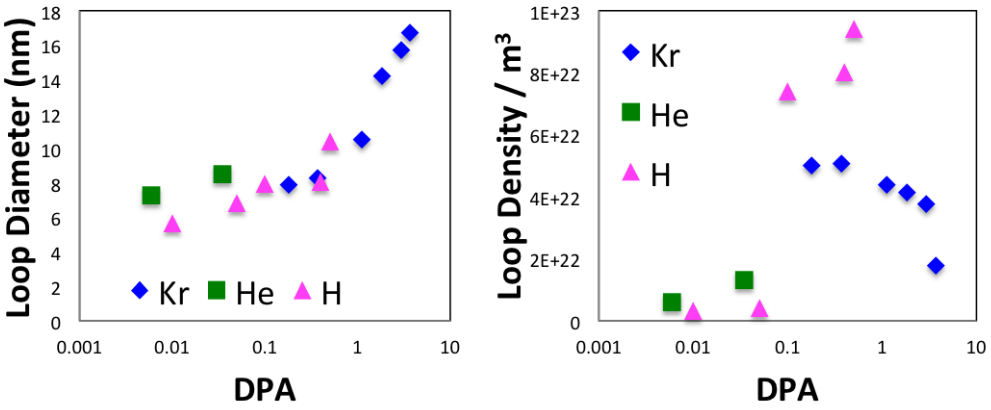

Figure 81: Dislocation loop density and diameter plotted vs Fluence for Kr, He and H implanted samples. The DPA is plotted on a log scale.

Dislocation bubble microstructure increases in size and density consistently with increasing ion dose. In case of Kr ions, the bubbles are greater in size than due to He bubbles at any given dose. Therefore, the bubble nucleation due to Kr ions is larger due to larger atom size of the irradiation species. This is shown in Fig. 82.

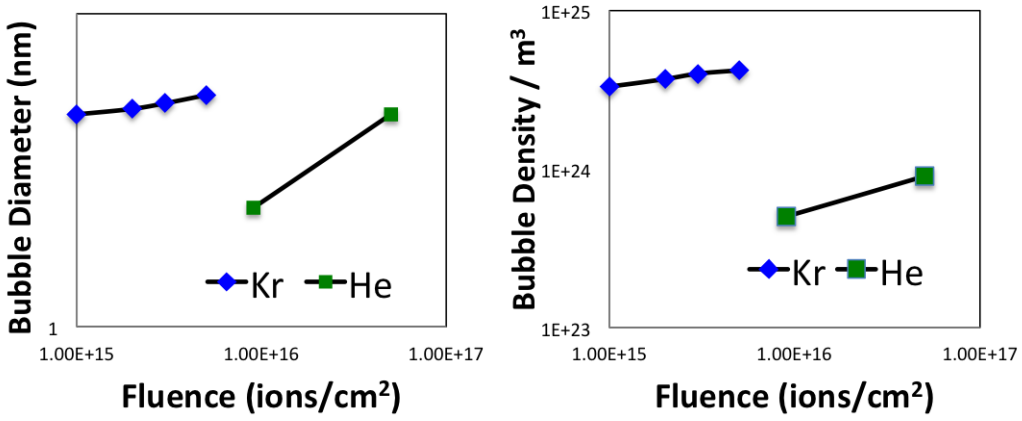

Figure 82: Bubble density and diameter plotted vs Fluence for Kr and He implanted samples. Both the ordinate and abscissa are in natural log scale.

The increase in the size of the lattice parameter has been attributed to the ingrowth of lattice defects in UO_2 following irradiation. During the process of ion irradiation, Frenkel defect pairs are produced at a constant rate that can only be overcome due to temperature assisted annihilation. With increasing DPA, there is a greater production of Frenkel defects that are produced along the path of ion irradiation. Due to the accumulation of Frenkel pairs, there is an overall volume increase in the lattice, resulting in greater lattice parameter. Increase in lattice parameter is seen by the decrease in the relative 2θ position of the (224) reflection in all the UO_2 samples. These observations are consistent with previously performed low dose irradiations in UO_2 that show a consistent increase in lattice parameter. This study, however, is the first comparison between the lattice parameter change due to various irradiation species used in UO_2. The extent of lattice parameter change as shown in Fig. 83, is clearly larger in case of a larger irradiating ion. The percentage increase in the lattice parameter change in the case of He^{2+} irradiation as compared to H^{+} irradiation is ~37%, which is quite significant.

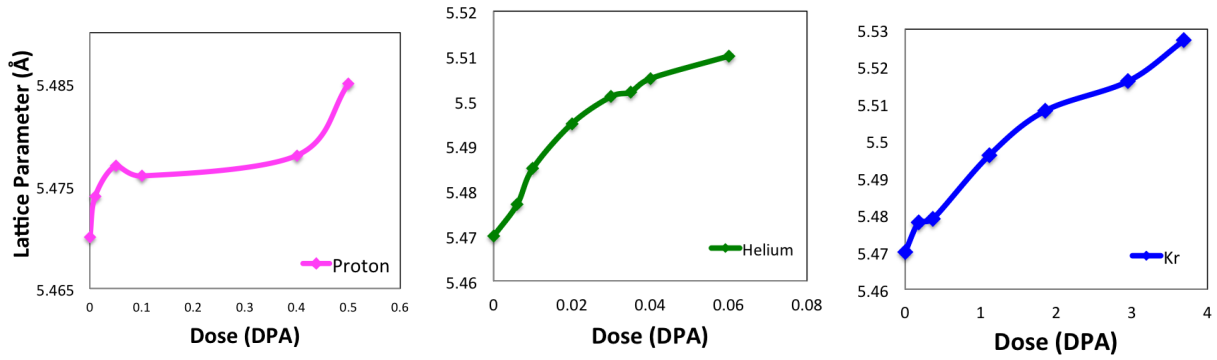

Figure 83: Increase in lattice parameter for H, He and Kr implanted samples as a function of dose in DPA.

There are two factors responsible for distorting the lattice as detected by X-ray Diffraction and EXAFS. The lattice parameter change is higher for krypton ions than for helium ions, which in turn is greater than in the case of proton irradiation. Therefore, the lattice parameter change increases with ion dose and with the type of ion. The % lattice parameter change is ~4 times greater for He^{2+} ion dose than for H^{+} ion dose at the same dose level of 0.1 DPA. This could be a coincidence since He^{2+} is four times the mass of H^{+}, but its nonetheless fascinating. These measurements indicate that the larger the ion, the greater the expansion of the lattice at the same radiation dose. Therefore, in the reactor, bigger fission products create higher damage and challenge fuel integrity even more. This effect is also seen in the case of % variation in the lattice. The percent change was calculated based on EXAFS fit of the number of atoms in the U-U near neighbor shell. The percent change progressively decreases from Kr ions to He^{2+} ions to H^{+} ion irradiated samples at low and comparable doses. Therefore, the size of the atom directly affects the change in lattice integrity, with heavier irradiation species creating larger % change. This is graphically shown in Fig. 84**.** While there is an increase in lattice parameter of the crystallographic lattice, there is a decrease in near neighbor distances in the case of the non crystallographic O peak. With increase in ion dose, the U-O distance consistently decreases, while the remaining original peaks see an expansion. This effect could be attributed to the tendency of U-O to form uranyl complexes that are highly stable within the UO_2 lattice. Therefore, the lattice expansion is concomitant with a decrease of U-$O_{non-crystallographic}$ distance in favor of local structure stability to accommodate the oxygen clustering in the lattice. This decrease is seen in higher doses and heavier ions from 1.9 Å through to 1.78 Å, where it starts to resemble the UO_{2+x} features seen in other studies [19].

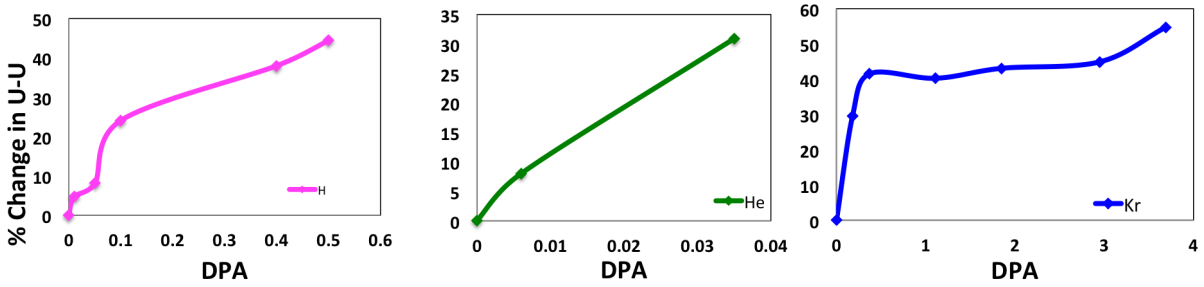

Figure 84: Percentage change in the U-U atoms fit indicating the variation of the irradiated lattice from the pristine one.

7.5 Simulations and Theoretical Studies

It is remarkable that effects similar to oxidation are seen after ion irradiations in UO_2 despite the lack of an active oxidation mechanism during and after ion implantations. Recent Molecular Dynamics and Temperature Accelerated Dynamics simulations done by Aidhy, et al on UO_2 give evidence of interstitial clustering to form Cuboctohedral (COT) type defects [23]. As detailed in the background section, the COT defect clusters occur only in oxygen rich environment, therefore their presence in irradiated material is surprising. In these simulations COT clusters have formed with oxygen interstitial ions while the uranium sub-lattice remains undisturbed. These are similar observations to the data obtained from EXAFS, in which there are shorter U-O bonds forming with higher irradiation doses. In the MD simulations shown in Fig. 85, oxygen interstitials form COT type clusters over time resulting in overall improved stability of the system.

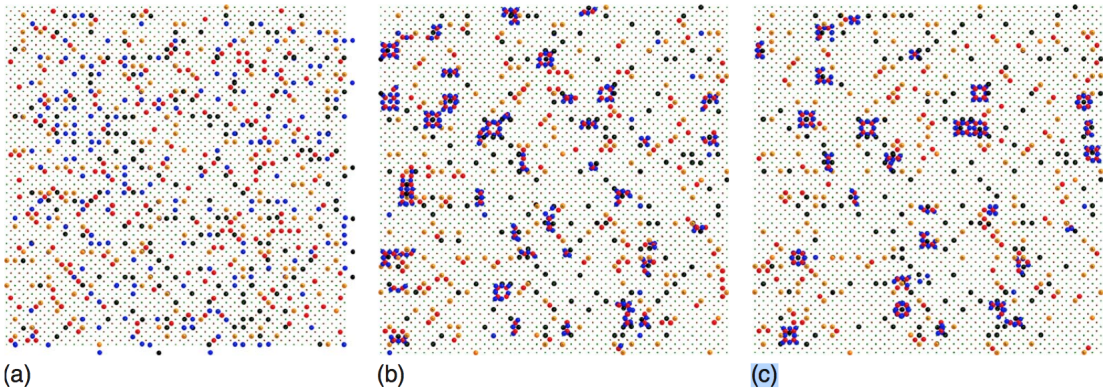

Figure 85: Evolution of the point defects on O and U sub-lattice with orange and black for uranium interstitials and vacancies. Snapshots are taken at a) t = 0 ps, b) t = 40 ps and c) t = 1000 ps. Initially 200 FP were introduced. All the U vacancies are almost undisturbed and all the O defects cluster. [23]

More detailed analysis of the oxygen defect clusters in UO_2 by Andersson, et al [5] using DFT is indicative of higher stability of split-quad interstitials over the COT clusters. An illustration of the split-quad interstitials is shown in Fig. 86. The calculations originate from split di-interstitial clusters of oxygen ions that form the building block of split-quad interstitial clusters. This study was corroborated by recent work published in Nature [38] regarding the greater stability of split-di interstitials over the previously postulated COT type defect clusters (Fig. 87) along certain lattice planes. Therefore, clusters preferentially form in the lattice depending on the availability of oxygen ions in a given geometry.

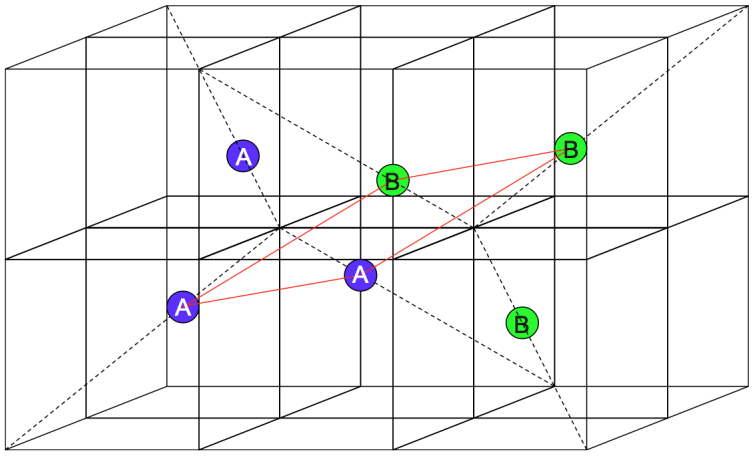

Figure 86: Split-quad interstitial cluster with the oxygen sub-lattice represented as cubes. The oxygen interstitials lie along the diagonals and the two split-di interstitials are represented as A and B which together make the split-quad interstitial.

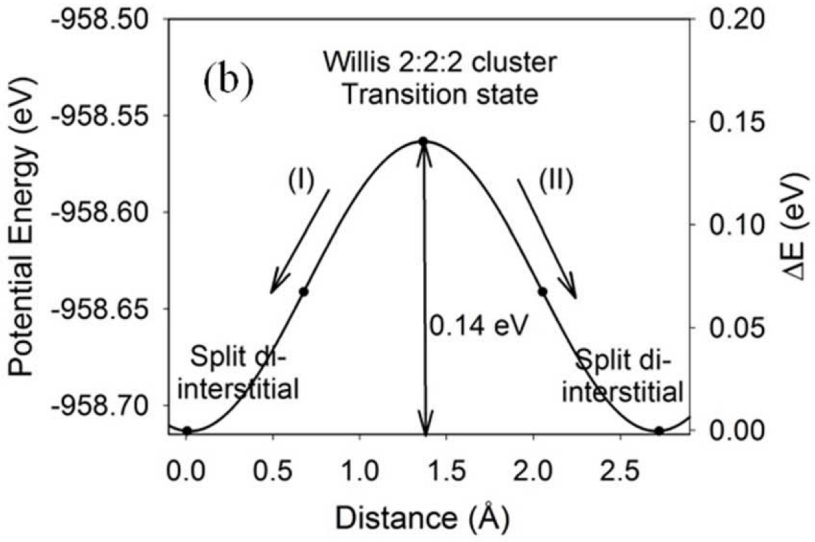

Figure 87: Potential energy of the cluster indicates transition from the Willis COT structure to the split di-interstitial cluster for higher stability.

There is a likely presence of COT defects in H^+, He^{2+} and Kr irradiated samples, since there is evidence of oxygen clustering due to the increasing magnitude of 1.8 Å oxygen shoulder peak. There is also a possibility of a distribution of split-quad interstitial (SQI) clusters, along with some point defects in the lattice. While oxygen defects tend to cluster, there are some point defects in the material. These clusters and point defects alter the local chemistry in the irradiated UO_2 samples, which has been detected via EXAFS measurements. Overall, there exists a distribution of COT, SQI clusters and voids that occur simultaneously in the UO_2 and contribute to the lattice structure evolution.

Radiation induced defect evolution on multiple length scales in UO_2 has been studied using techniques specific to chemistry evolution and also microstructure formation. As it has been previously stated, there are limitations to the experimental data obtained by the various experimental methods that could present inherent scientific gap in explaining the "atom to defect" evolution mechanism in the irradiated material. For this precise reason, the use of simulation methods is absolutely key to verifying the underlying assumptions used for experimental measurements. The ability of simulation software to mimic the onset of radiation damage has proven to be very helpful in understanding the formation of point defect clusters and their stoichiometry and further, the evolution of these clusters with time and temperature. So, using simulation the relative stoichiometry of point defects and the percent of atoms that are damaged can be predicted. However, each simulation performed in complex materials is highly dependent on the potentials used to relax the material. There has been a study that shows that different atomic potentials in irradiated UO_2 result in characteristics of point defects are vastly different from one another [42]. This appears to be an inherent limitation to simulation as the true material potential can be hard to

calculate and can create faulty defect distributions. Therefore, simulation needs to rely on experimental data just like experiment should be verified by simulation.

Cluster dynamics have been used to explain the formation and evolution of radiation induced defects in UO_2 [43]. Cluster dynamics is a highly advanced modeling system that has the capacity to simulate the material conditions during an ion irradiation and the subsequent formation and interaction of point defects. This work seeks to implement atomistically developed cluster dynamics model to investigate various stages of defect clustering in UO_2 including extended defect structures seen via empirical methods. The first step in this method uses first principles calculations based on density functional theory (DFT) to calculate energies of formation and interaction of intrinsic point defects and extended structures such as fission gas bubbles and bulk defect clusters. Previously performed cluster dynamics calculations, while simple, erroneously assumed the stoichiometry of defect clusters. The assumption that all point defect clusters are stoichiometric in UO_2 is incorrect and disagrees with experimental data. The cluster dynamics approach discussed in this study analyses the composition of defect clusters without preconceived assumptions and the evolution of these defect clusters under varying post irradiation conditions.

The results of the atomic and microstructure level experiments were verified by a combination of theoretical and simulation measurements. Along with dealing with the complicated stoichiometry evolution, the methods interrogated the basic science behind the results that were observed using empirical methods. The FEFF calculations listed below give an overview of the software that was used to simulate an EXAFS spectrum for a pristine lattice with crystallographic lattice atom positions. FEFF is used in conjunction with Artemis and Athena codes to simulate the effect of individual vacancies and interstitials on the EXAFS

spectrum. Cluster Dynamics was used to simulate the concentration and distribution of voids and interstitials at various dpa rates, to compare with the experimental data. Basic theoretical calculations were also performed to understand the impact of microstructure formation on the extent of lattice structure variations in the irradiation UO_2 samples. Finally, CrystalMaker software was used to model the defect insertion in the UO_2 lattice, to help visualize the geometry of defects and to use with Artemis and Athena to simulate the EXAFS spectrum.

7.5.1 Basic FEFF calculations

FEFF9 code was used as a part of EXAFS data analysis to generate EXAFS spectra and parameters for a pristine sample [70]. The modulation of the spectra from pristine sample to radiation damaged sample was done as a part of the EXAFS fitting routine. Here, FEFF was used to simulate basic UO_2 lattice with atoms in their theoretical positions based on the FCC fluorite structure. The goal of this study was to simulate the effect of individual point defects on the EXAFS spectra of the lattice.

FEFF is an ab initio multiple-scattering code for calculating excitation spectra and electronic structure of the material being probed. It is based on Green's function approach, by accounting for variation in self-energy shifts, inelastic losses and Debye-Waller factors. The calculation can be done by importing a list of atomic positions or generating this list within the software. Both of these options were attempted to check for any inherent variation in calculation. Within the software, a molecule of UO_2 is specified to generate an ATOMS. INP file, which can further be modified or used as is in various other EXAFS calculation software. One such ATOMS input file was used to generate the Fourier transform spectra

of EXAFS in the case of one, two and more vacancies in the input file. This is done by simply removing an atom of choice, O or U from its position and then running the EXAFS calculation to generate an approximation of the atomic spectra. The results from one such calculation is shown in Fig. 88. With addition of vacancies (removal of atoms) in the lattice, the spectra shows a monotonic loss in amplitude. Therefore, the direct result of the vacancy type point defect is the reduction in EXAFS amplitude.

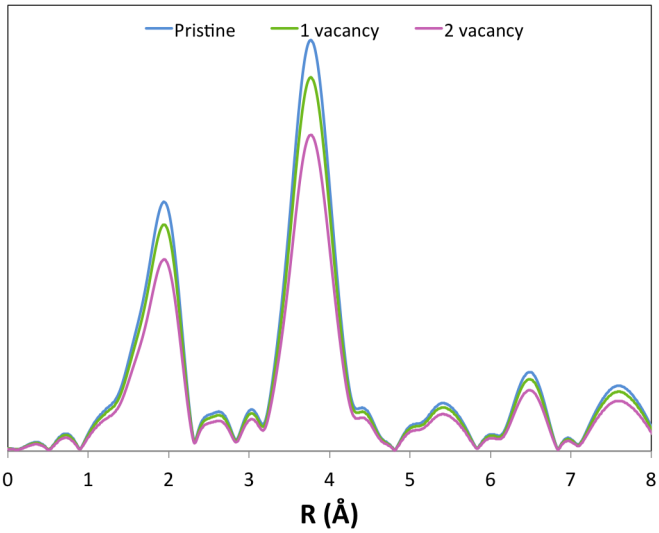

Figure 88: FEFF generated Fourier transforms of pristine UO_2 lattice and UO_2 with one and two oxygen vacancies.

Vacancies, however, imply the removal of atoms from the lattice, which would mean that the target sample is becoming less dense, as a large percentage (5 - 10%) of the atoms are being removed. In the case of radiation damaged samples, the vacancies occur along with interstitial atoms, thereby maintaining the overall density by altering the local structure of the material. Therefore, the effect of interstitials on EXAFS must be individually simulated. This process was more complicated than simulating vacancies as the FEFF software wasn't

designed to handle complicated molecular structures. Artemis, Athena were used and the results for this are shown in Fig. 89. The two softwares were created for EXAFS analysis at the Advanced Photon Source for basic fitting of EXAFS data. The following steps were followed for simulating the effect of multiple oxygen interstitial clusters in UO_2 lattice on the EXAFS of the material:

1. CrystalMaker software was used to generate UO_2 and UO_{2+x} structures.
2. Atoms.xyz file was produced using CrystalMaker software, that could be used as an input to Artemis for extended structure fitting.
3. Athena was used to perform EXAFS fit and produce Fourier transforms in R-space for UO_2 lattice with oxygen interstitials.

7.5.2 Molecular Dynamics and Cluster Dynamics

Cluster dynamics and Monte Carlo methods have been employed in this study to understand the evolution of atomic physics following radiation damage at the mesoscale. While cluster dynamics can be used to simulate radiation damage and thermal imaging on various length scales, it comes with limitations. One of these limitations is that it doesn't allow for direct comparison of results based on the irradiation ion. Therefore, most of the results shown in this case have utilized a normalized dpa rate that describes the onset of the damage cascade in the sample but cannot be separated based on the mass of charge of the irradiating species. While Molecular Dynamics describes the onset of damage in a specific material, Cluster

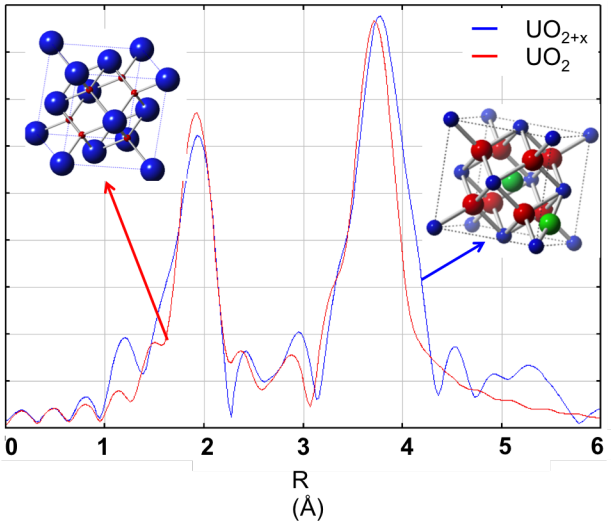

Figure 89: Simulation of oxygen interstitial clusters using CrystalMaker, Artemis and Athena software

Dynamics approximates the scale and type of damage on microstructure and atomic level at any time during and after irradiation. Thermal conditions continuously change from the beginning of the radiation experiment through to the cooling down of the material at the end, and this entire range of material conditions can be simulated using CD.

The CD simulations were done for void (and cluster) size and constituency evolution during ion irradiation in UO_2. To do this, a uniform distribution of defect sinks, voids and dislocation loops, were distribution throughout the UO_2 matrix [43]. The results have been discussed based on change in void/ cluster concentration with evolution in time. A void is expected to grow with the absorption of vacancies and removal of interstitials as a underlying assumption in this study and a cluster of defects grows with absorbing interstitials and emission of vacancies. It was noted that with the distribution of point defects around the defect sinks, the general concentration of vacancies decreased due to the significantly higher mobility of oxygen interstitial defects that would get absorbed in void sinks. It was

found, regardless of the size of the void, the interstitial absorption is efficient at the sinks and drastically reduces the void concentration with increasing time. With the knowledge of decreasing void size due to ion mobility dependence on low migration energy of interstitials, one can make some basic assumptions regarding the general type of defect cluster that can be found in ion irradiated materials. With oxygen atom migration energy of 0.6 eV and uranium migration energy of 2.4 eV, oxygen rich dislocation loops are the most likely type of damage cluster to form. Subsequently, due to higher migration energy of uranium vacancies, most will not migrate to defect sinks and will remain as individual point defects during irradiation.

Cluster Dynamics calculations were done for various dpa rates in the material to simulate the growth of various point defects into clusters and voids. It was noted that with increasing DPA rate, the overall void density in the material grew significantly as shown in Fig. 90. Therefore, the greater the rate of radiation damage, the more will be the resulting concentration of defect voids and clusters. This is in agreement with the results from H^+, He^{2+} and Kr implanted samples where the concentration of defects is higher in case of higher damage rates resulting from larger ion species. The lowest dose Kr loop density is 5×10^{22} loops /m^3, which is greater than loop density for He^{2+} implanted samples is 6×10^{21} loops /m^3, which is further greater than H^+induced loop density of 3×10^{21} loops/ m^3. Further, the order of magnitude of void density is the same for experimental results as for simulation results, where the number density of voids is on the order of 10^{21}loops/ m^3. Thus this study recommends continuing comparisons with CD results as they are a good approximation of empirical data.

Oxygen defects seen in EXAFS can be fit with a low U-O distribution and the relative

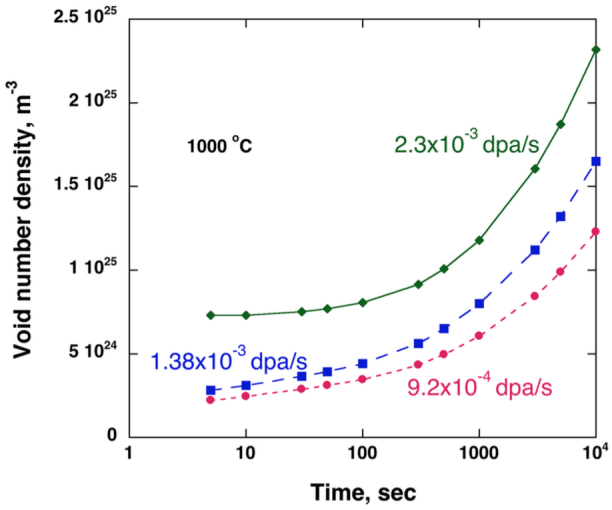

Figure 90: Increase in void number density with increasing DPA rates with time.

increase in the oxo shoulder can be measured in comparison to the original crystallographic oxygen shell to understand the extent of lattice change. Uranium defects were identified to be fit with a decreasing peak height and the log ratio analysis was done to identify the decrease in Debye-Waller factors indicating a symmetric spread in the position of atoms around their crystallographic position due to ion irradiation. EXAFS, however, didn't explain the distribution of original point defects that exist in the irradiated material. CD calculations show that with increasing time during ion irradiation, the concentration of oxygen and uranium vacancies generally show an increase in quantity. This is shown in Fig. 91 where the white dotted line represents the stoichiometric composition of U:O is 1:2. With increasing time, the concentration of number of uranium vacancies and oxygen vacancies shifts from hypostoichiometric to hyperstoichiometric. This change occurs occurs between 300 and 500 sec from the start of the irradiation. Hyperstoichiometric voids indicate the presence of hypostoichiometric clusters elsewhere in the material to balance out the O vacancies and the

O interstitials. Due to low migration energy of oxygen point defects, the voids absorb oxygen vacancies faster and oxygen interstitials cluster to form interstitial rich dislocation loops, leaving behind a distribution of U vacancies and U interstitials. Therefore, most O defects will cluster and more U defects than O defects will exist as individual point defects with a concentration greater than expected from a 1:2 distribution of U to O atoms. According to Fig. 91, the number of U vacancies is $1/4^{th}$ the number of O vacancies in the material.

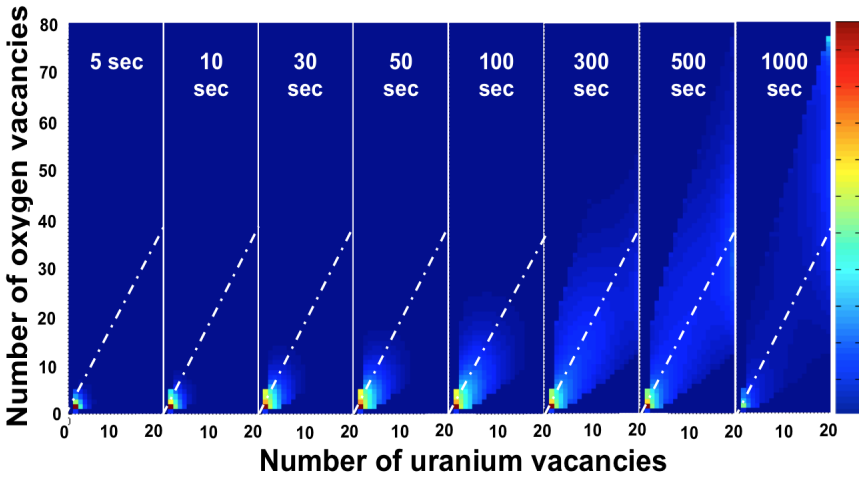

Figure 91: Increase in the vacancy type point defect with increasing time during ion irradiation, as simulated by CD

Cluster Dynamics calculations also suggest that uranium vacancies are the rate limiting factor in the movement and absorption of defects in the defect sinks (clusters, voids). This is because migration energy for the U vacancy is the highest of all the point defect migration energies. It was further found that with increasing time, the clusters with hyperstoichiometric composition are more in abundance in the UO_2 lattice than stoichiometric and hypostoichiometric clusters. Therefore, the overall effect of radiation damage in simula-

tion measurements suggest the presence of hyperstoichiometric composition of defect species that have been detected in EXAFS measurements. Fig. 92 shows the growth in density of hyperstoichiometric clusters with time evolution. It was also found that the clusters grew faster in the direction of the oxygen interstitials and quickly become oxygen rich with point defect ratio of O/U $>$ 2. Therefore, oxygen rich dislocation loops exist during and after ion irradiation. These measurements support the experimental work where the growth of defects is hyperstoichiometric, as demonstrated by the oxygen peak fit of the EXAFS peak at 1.8 Å U-O distance. Similar results were also obtained by Molecular Dynamics simulation that used Basak Potential to model the distribution of vacancy clusters following a damage cascade event. According to this, the fraction of off stoichiometric clusters is much greater than stoichiometric clusters in UO_2. The similarities in the number densities of voids discovered in CD simulations to that of experimental results is discussed in the next section.

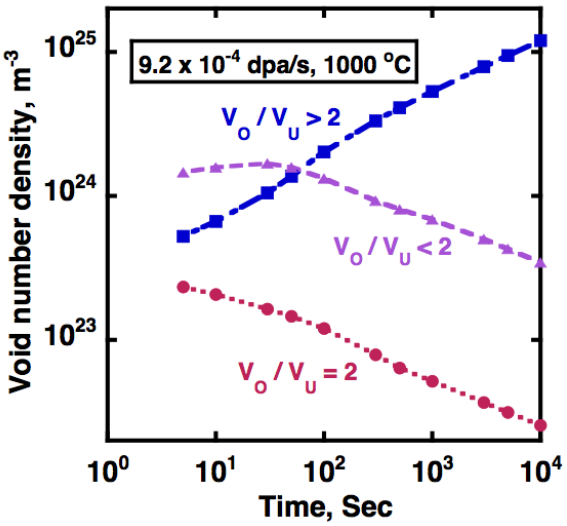

Figure 92: Evolution of clusters of various compositions with time during an ion irradiation.

7.5.3 Basic Theoretical Calculations

So far, the knowledge of defects on multiple length scales is proof that radiation damage exists in various sizes in the material undergoing irradiation. Defects of several nanometers and microns in size can be imaged via TEM by focussing on the specific region, identifying its lattice plane and using the beam to extract images that define the defect's size and shape accurately. In this way, a distribution of defects, such as dislocations, can be adequately characterized. Dislocations in UO_2 have been measured to exist along the [111] plane with their distribution becoming more complicated with increasing ion dose. Simultaneously, lattice specific techniques, EXAFS and XRD, give evidence of oxygen dominant defect clusters existing at short U-O distances with the overall lattice spacing showing an increase. It would therefore make sense to compare the defects of multiple length scales, so as to explain the existence of the various radiation induced features. A basic calculation was then conducted to compare the correlation between the two length scales. This is detailed in Appendix A and B. The following key results were obtained from this analysis:

1. Microstructure damage affects lattice atoms on the scale of 0.1%
2. EXAFS damage detects a change in the spectral loss and atomic positions in the lattice on the order of $>$ 5-7%
3. The microstructure defects, while rich in oxygen interstitials, do not adequately explain the $>$ 5% change in EXAFS.
4. EXAFS damage is a cumulative effect of microstructure damage (0.1%) and point defects and point defect clusters (˜98%)

5. Defect clusters are responsible for the majority of the EXAFS signal that aren't visible in the TEM.

6. Cluster Dynamics calculations provided an approximation of TEM invisible clusters forming in UO_2 and give a total lattice change on the order of $>$ 5-6% which is very similar to basic calculations performed

7. It is also expected from CD results that U vacancy and interstitial defects do not cluster like O defects and tend to exist as individual point defects more than in clusters

8. The general distribution of defects that together contribute to the overall structure variation due to ion irradiation in UO_2 is graphically summarized in Fig. 93.

Figure 93: Graphical representation of defect structure contribution towards UO_2 damage on multiple length scales

For further detail on theoretical analysis, refer to Appendix A for basic comparison of dislocations to TEM results and Appendix B for comparison between Cluster Dynamics simulations and empirical results.

7.5.4 CrystalMaker Dislocation Analysis

Several studies have been performed to understand the process of rapid oxidation of UO_2 to higher, more stable states, which indicate that the additional oxygen ions aren't incorporated randomly, but in fact, form an ordered sub-lattice. Fig. 94 shows the process of incorporation of O ions into a UO_2 unit cell obtained using CrystalMaker software. The gradual addition of the oxygen ions starts in the interstitial defect sites in the UO_2 lattice and progresses to stable clusters that form without distorting the lattice until the U_3O_8 phase is reached. Initially, UO_2 exists as a FCC fluorite with the Fm3m space group, which has been maintained during irradiation and oxidation until U_3O_8 stoichiometry displays a stable phase of P43m [10]. The stability of the Fm3m phase throughout the oxidation and irradiation process confirms the propensity of UO_2 to have a stable and resistant geometry over varying stoichiometries. Additionally, the solidarity of the fluorite structure in UO_{2+x} corroborates the clustering nature of oxygen atoms in the interstitial defect sites in the UO_2 lattice. The [111] axis plane, shown in red in Fig. 94, lies along the empty sites in the lattice of UO_2 where interstitial defects preferentially form [85]. The presence of these interstitials is favorable to the stability of the lattice, since it no longer has a large unoccupied space in the center of it (hence, the negative oxygen interstitial formation energy).

CrystalMaker is a visualization software that was used for conceptualizing the position of various defect types in a radiation damaged lattice. The use of CrystalMaker was further extended to calculating basic EXAFS spectra for small defects that can populate the matrix of UO_2 atoms. First, a pristine UO_2 lattice is produced with known positions and types of atoms. Parameters such as lattice spacing and lattice plane are defined to accurately understand the 3-D spread of the unit cell. Based on literature data and findings in this

study, individual point defects can be inserted along the defect sites in the unit cell. As an example, insertion of oxygen interstitial (green in the second figure) is done in the empty [111] site to demonstrate the stability of the lattice surrounding the point defect insertion. Subsequently, addition of several oxygen interstitials show the transition from Fm3m phase to P43m in U_3O_8. Therefore, the UO_2 and UO_{2+x} lattice tends to maintain its overall fluorite structure till the new phase of P43m is reached.

Using the 3-D geometries of the structures designed in CrystalMaker, the atomic positions of these structures is extracted in a format that is acceptable by EXAFS approximating software. This format is then used as an input and EXAFS spectra for the various defect positions is calculated. Naturally, the effect of one interstitial in a unit cell is rather small and the EXAFS spectra reflects this small change. The overall defects and defect interaction in the actual material is more complicated than isolated effects from point defects. Nonetheless, using isolated defects helps understand the sensitivity of EXAFS on small defects. Since, it is known that oxygen defects tend to cluster in the UO_2 lattice, EXAFS simulations were also performed for 2 oxygen interstitials and for the addition of a cluster of oxygen defects, while maintaining the overall fluorite structure. Therefore, it has now been proven with experimentation and with CrystalMaker structures that the addition of oxygen defect clusters locally distorts the EXAFS of UO_2 lattice and this change is consistently increasing with additional O in UO_2 . Therefore CrystalMaker was used to visualize the various defect structures and also used to generate input files based on approximate atomic positions of atoms that were derived from XAFS results and used for EXAFS approximation software. This is shown in Fig. 85.

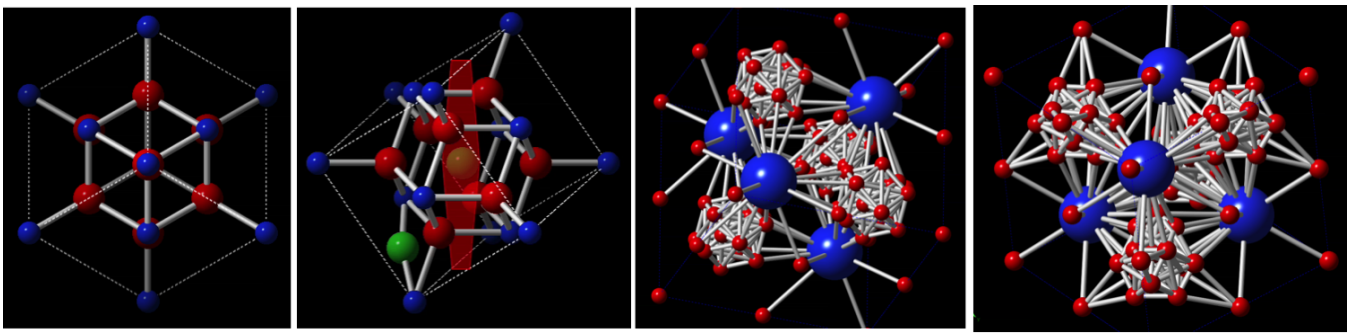

Figure 94: Oxygen interstitial addition to pristine UO_2lattice starts on interstitial defect sites (green). With sufficient addition of oxygen ions, the interstitial cluster size increases till new phases are reached.

7.6 Overall Discussion

X-ray Absorption Fine Structure (XAFS) analysis in irradiated d-UO_2 is sensitive to local structure and chemistry in the target material including, but not limited to, coordination chemistry, near neighbor distances and oxidation state. Focus of this study on these facets of the analysis technique has resulted from complicated microstructure formation as a result of ion irradiation and its correlation to disorder in local chemistry. UO_2 interstitials have negative oxygen interstitial formation energy [37], which results in development of 16 known phases between UO_2 and U_4O_9 by varying values of 'x' in UO_{2+x}. The stoichiometry evolution due to propensity of UO_2 to form UO_{2+x} domains internally has shown to further complicate the analysis of irradiation induced lattice structure changes. The formation of short axial bonds between uranium and oxygen in ion irradiated UO_2 indicates that there is a more stable configuration that can be achieved locally with the addition of energy into the system.

The ion irradiation has shown to disrupt local structure by giving rise to multisite oxygen distribution at approximately 1.8 - 1.9 Å ($\tilde{}$ 0.2 Å longer than in documented UO_{2+x}) similar to oxygen interstitials created in UO_{2+x}, however, there is no known oxidation of the material

during irradiation. One explanation for the reduced U-O bond distance is the multisite distribution resulting from uranyl type bonds 1.8 Å in length, which are highly stable due to their oblate geometry and therefore distort the original local structure [16]. An illustration of this stable bond is shown in Fig. 95 where multiple bonds between the uranium and oxygen ions can be seen [1]. The multisite oxygen distribution at short U-O distances has been seen in UO_2 irradiated with H^+, He^{2+} and Kr ions. The extent of this distribution, evident from the EXAFS amplitude, grows with increasing radiation dose.

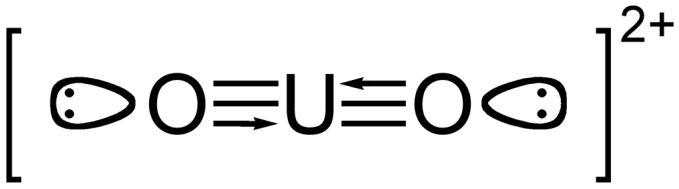

Figure 95: Uranyl bond with multiple bonds between oxygen and uranium have a shorter length than U-O bond in UO_2

X-ray diffraction measurements were performed on all the irradiated UO_2 sample sets. There is a consistent expansion of lattice observed due to the increase in ion irradiation dose. There are two factors that seem to have a great impact on the lattice parameter changes. Firstly, the increase in ion dose for each irradiation study shows that with increasing dose, there is an expansion of the lattice and this is in agreement with the previously done studies in UO_2. Secondly, the diverging lattice parameter is seemingly a function of ion type, which in this case means, the larger the irradiation ion, the greater the expansion of the lattice.

Therefore, even at low helium doses, the effect on the lattice was greater due to helium than due to protons. And further, the effect due to krypton ions on peak shift in XRD was greater than that due to proton and helium ions. Therefore, X-ray Diffraction has been a powerful tool in explaining the lattice evolution with irradiation dose and the type of ion used for radiation damage. The XRD measurements complement the EXAFS technique where increase in near neighbor distances have shown a > 0.01 Å increase in the lattice spacing, along with the presence of oxygen interstitial type defects that have the same effect.

Transmission electron microscopy is an extremely powerful tool in analyzing the structure of radiation induced defects and provide an irrefutable proof of the damage in the target material. Analysis of dislocation microstructures in the three irradiated material show that increasing ion dose perpetuates more complicated defect features in UO_2. Dislocations dominated as the type of microstructure for all the UO_2 irradiation studies. With increase in ion dose, the smaller dislocations coalesced to form loops that further grew into larger networks. Therefore, the general trend for dislocation evolution in krypton implanted UO_2 samples was small loops $\rightarrow$ big loops $\rightarrow$ dislocation lines$\rightarrow$ dislocation tangles. The general trend in H and He samples was that higher dose produced a greater concentration of dislocations. This evolution mechanism was observed in krypton irradiated specimen and in proton irradiated samples.

Dislocation loops present in the three samples certainly modify the local chemistry, but the results in EXAFS measurements detect oxygen defects at a much greater scale. Oxygen being the significantly more mobile ion [**?**] diffuses much faster than uranium defects and therefore, has a greater participation in creating microstructural features with irradiation. A recent study by Chen, et al [13] confirms the presence of oxygen interstitial loops on the

[111] plane when CeO_2 is irradiated with krypton ions. CeO_2, with a fluorite FCC structure and similar lattice constant (5.411 Å) [99] to UO_2, has been used as a surrogate material for many studies to explain microstructure features in UO_2 [34]. The presence of interstitial oxygen loops would result in a reduced near neighbor distance between U and O to certain extent and could be one of the reasons that there is an increase in the oxygen shoulder peak with increasing radiation dose. Fig. 96 shows an illustration of the interstitial loop found on <111> plane by Chen, et al.

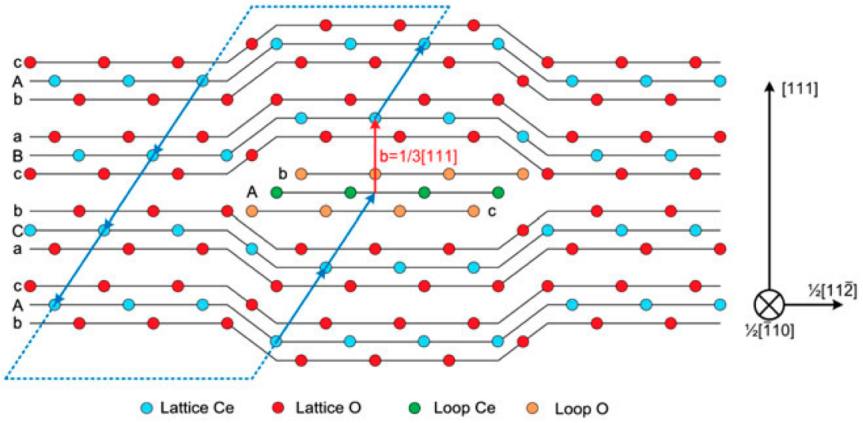

Figure 96: Schematic of interstitial loop forming in CeO_2. The oxygen interstitials are shown in orange in the middle on either sides of the cerium interstitial loop in green [13].

The EXAFS data of the irradiated UO_2 shows a consistent decrease in amplitude of the crystallographic shells with increasing irradiation dose, longer bond distances between near neighbors and the appearance, and increase, of a shoulder on the low R (at 1.9 Å) side of the first crystallographic U-O shell. Random disorder in the material would result in a significant loss of amplitude and further loss of overall spectral features, which isn't seen in this set of samples. Due to the consistent amplitude reduction as shown in Fig. 78, Fig. 79

and Fig. 80 it can be theorized that the defects aren't random but instead seem to cluster such that the overall lattice retains its UO_2 structure even at the higher irradiation doses in this study. This assumption however doesn't take into consideration the dose levels of used nuclear fuel where the high dose could result in larger oxygen clustering and subsequent phase transformation. So far, the radiation resistance of UO_2 is consistent with several studies that indicate that fluorite ceramics in a reactor maintain their lattice structure even at high irradiation doses. A list of the spread of near neighbor distances obtained from EXAFS fits of the three sets of irradiated samples are tabulated in Table 18. The presence of the U-O peak at 1.9 Å is the only significant deviation from the original lattice structure. With increasing irradiation dose, this oxygen shoulder increases in magnitude while the primary O peak at 2.36 Å rapidly diminishes. It seems likely that with higher irradiation doses than the ones studied here, this shoulder will have a greater amplitude contribution to the EXAFS spectra than the crystallographic position. Hence, it can be concluded that the original O peak is redistributing to a multisite distribution of oxygen atoms at low R distances.

Sample info	Dose (DPA)	U-O	U-O	U-U	U-O
UO_2	-	-	2.36	3.85	4.5
$UO_2 + H^+$	0.01-0.5	1.9 - 1.8	2.35 - 2.37	3.85 - 3.87	4.45 - 4.47
$UO_2 + He^{2+}$	0.006-0.035	1.92 - 1.93	2.35 - 2.37	3.85 - 3.87	4.48 - 4.52
UO_2 + Kr	0.18-3.69	1.9 - 1.8	2.36 - 2.38	3.85 - 3.87	4.45 - 4.52

Table 18: Near neighbor distances comparison in d-UO_2 samples analyzed using EXAFS

The decrease in amplitude of the U-U in Fig. 78-80 indicates that the lattice structure is being distorted with higher irradiation dose. Although the decrease in amplitude of the original O peak can be explained via the multisite distribution, the reduction in amplitude of U-U peak suggests distortion of the position of the U atoms in the local structure. The samples are still full density and therefore, the reduction in U atoms in the EXAFS fitting routine was explained through anharmonicity in the lattice following irradiation. This was done using the ratioing method. The U-U waves were separated from the (k) spectrum by subtracting all other waves from the spectrum and extracting the amplitude using Fourier filtering. Studying this amplitude shows that with increasing ion irradiation dose, the amplitudes of the spectra for the irradiated samples diminished. The decrease in amplitude, along with the change in the Debye-Waller factors, is seen throughout the spectrum, even the higher U shells, and is consistent with dose increase. In these samples, the Debye-Waller factors have decreased indicating that the distribution of U-U atoms is likely to be not asymmetric. Therefore, ion irradiation is causing some U atoms to be spread about their crystallographic position such that they do not conclusively cluster in one position, which then cannot be seen in EXAFS analysis. The U atoms tend to spread over 0.4 Å around their position, which did contribute to measurable changes in the EXAFS spectra.

To interrogate the increase in the peak height of the U-O shoulder, the ratio of the atoms to the Debye-Waller factor is shown in Fig. 97 and Fig. 98. This ratio is consistently increasing with greater irradiation dose and indicates that the number of O atoms are in the oxo shell are indeed increasing (and the Debye Waller factor isn't decreasing to cause this effect). The plots show the ratio of atoms to DW factors specifically in the case of the oxo shoulder, thereby demonstrating the increase in the number of atoms fit for the peak

as compared to all the other crystallographic peaks decreasing in amplitude. The number of atoms fit in each shell is seen to increase with increasing ion dose. The ratio of the two quantities proves that while for other crystallographic shells the ratio of Atoms/DW factors is decreasing, in the case of the oxo shoulder, this ratio consistently increases. This indicates a real increase in the atoms fit without dependence on the thermal DW factors.

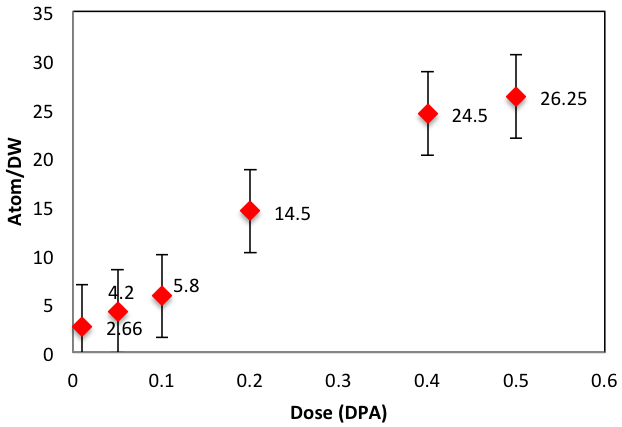

Figure 97: Ratio of number of atoms fit at 1.9 Å shell to the Debye Waller factor increases with increasing H^+ dose.

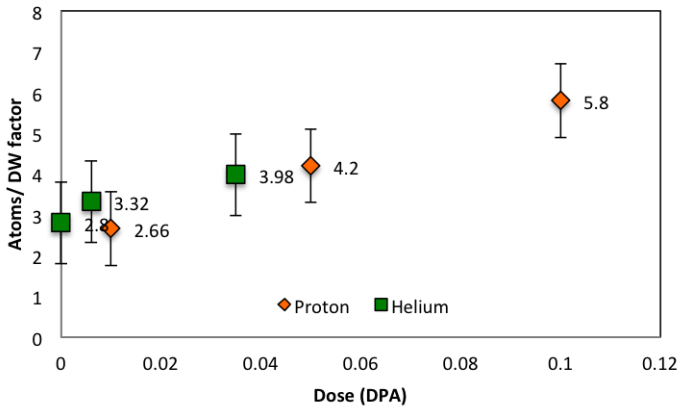

Figure 98: Ratio of number of atoms fit at 1.9 Å shell to the Debye Waller factor for H^+ and He^{2+} irradiated UO_2 samples

A similar chart for the ratio of atoms fit to the DW factor for each shell for the krypton irradiated samples indicates a similar trend (Fig. 99). The ratio increases with increasing krypton ion dose in the UO_2 samples at 1.78 Å distance from the absorbing ion. This distance is less than for H^+ and He^{2+} irradiated samples but follows a similar trend. In both Fig. 97 and Fig. 98, the N/DW ratio increases steadily with dose initially but then the change begins to plateau after a certain dose. In case of krypton implanted samples, one would have expected to see this had the second highest sample not shown a loss of the oxygen shoulder. Its remarkable because the monotonic loss is consistent with other lower dose samples. However, the O shoulder is non existent at this dose. Aside from this data point, all others look similar to the lower dose samples.

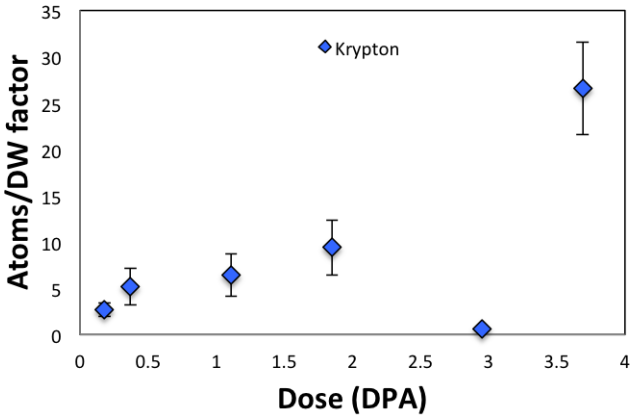

Figure 99: Ratio of number of atoms fit at 1.9 Å shell to the Debye Waller factor increases with increasing Kr dose.

The process involving formation of microstructure is dependent on interstitial and vacancy diffusion in the target material through cluster formation and migration. This process can be understood by studying oxygen clustering that forms spectral features in EXAFS, TEM visible oxygen rich dislocation loops and the spread of uranium atoms away from their crystallographic sites. It is also stated that the diffusion of oxygen interstitials is significantly greater than that of uranium interstitials to form dislocation type microstructure features in UO_2 [?]. It can be concluded that the oxygen interstitial type defects contribute more to forming microstructure defects than uranium interstitials. This is also corroborated by the radiation resistance of the UO_2 lattice, which is primarily maintained by uranium ions remaining in their positions. So, the relatively free oxygen atoms in the UO_2 lattice diffuse more easily around the structure when irradiated with ions and further participate in microstructure formation. The dislocation geometry due to these interstitial defects creates zones in the lattice where damaged ions rearrange closer to each other than their original distances. The decreased distances between U and O atoms create a region for charge transfer

from U to O, creating a stronger uranyl bond at short distances. This (explained graphically in Fig. 95) is discovered in the EXAFS measurements as a small oxo shoulder forming closer to the uranium atoms than the crystallographic oxygen shells. Therefore, point defect diffusion creates a pathway for microstructure formation via small defect cluster formation. However, the microstructure features alone cannot explain the shortened U-O bond distance distribution in irradiated UO_2 and this therefore indicates a different mechanism that is responsible for the EXAFS results.

The microstructure observed in transmission electron microscopy also gives evidence of fission gas bubbles, which are commonly commonly seen in nuclear reactor irradiated fuel. Therefore, ion irradiation creates dislocation type features that form from interstitial type defects and inert gas bubbles form from inert gas implantation, which remain largely unreactive in the target material lattice. The gas bubbles were detected in the case of helium ion implantation and krypton irradiation. The general trend shows a decreasing density of bubbles and increasing size of bubbles with increasing ion dose. This is to be expected, as with increasing ion dose, the instability of the lattice increases, thereby providing gas atoms the needed mobility to combine and form larger features. Therefore, smaller bubbles coalesce to form larger inert gas bubbles as irradiation dose increases and the atom percentage of inert gas in the system is larger.

The presence of inert gas bubbles in the system explains the larger lattice expansion to some extent. In the case of the helium atoms, the concentration of ions due to irradiation first follow a plateau distribution, following which, the nuclear stopping regime results in a peak damage region, where a significantly larger number of helium ions come to a stop in the material. Therefore, the largest concentration of helium atoms are found in the peak

damage region. However, in the case of the krypton implanted samples, the ion damage profile is almost identical throughout the entire damage range. The atom % of krypton is nearly the same throughout the 1.1 µm where the ions are deposited in the material. This implies that the evolution of microstructure with depth in the sample is nearly constant and the lattice expansion seen in the krypton implanted material adequately represents the distortion at any given depth due to krypton ions. Hence, krypton bubbles that form due to ion implantation contribute significantly to lattice expansion and the highly distorted XRD graphs confirm this assumption. The helium atom bubbles on the other hand were observed in the damage plateau region of the sample. XRD was set up so that it sampled the entire damage layer of the sample, which in the case of helium implanted samples is roughly 8 µm. The highest concentration of the helium microstructure damage was in the peak damage region and therefore, if the XRD measurements were conducted in that region, the lattice expansion would have been larger.

The lattice expansion around the damage region further creates an argument for the varying local structure in ion implanted UO_2. The addition of inert gas ions creates bubbles that do not react with the pristine UO_2 lattice. These bubbles therefore locally distort the lattice around them, creating regions of shortened near neighbor distances. Fig. 100, shows an example of krypton adsorption in UO_2 occurs by pushing out the oxygen atoms further away from the surface. Therefore, the region around the bubble is UO_{2-x} and the additional oxygen atoms are pushed further from the bubble and closer to the surface of the sample. This is in agreement with the EXAFS results that show local oxidation and shortened U-O distances, although this does not completely explain the EXAFS results. The oxygen atoms are easily pushed further away from the bubble surface due to the easier

diffusion of oxygen atoms in the lattice. Oxygen, being the smaller ion is removed, creating a region of oxygen vacancies around the bubbles. The uranium lattice thus retains its original structure, albeit some lattice expansion due to the presence of bubbles. So, locally there are hypostoichiometric and hyperstoichiometric regions of UO_2 distributed around the entire damage region in the material.

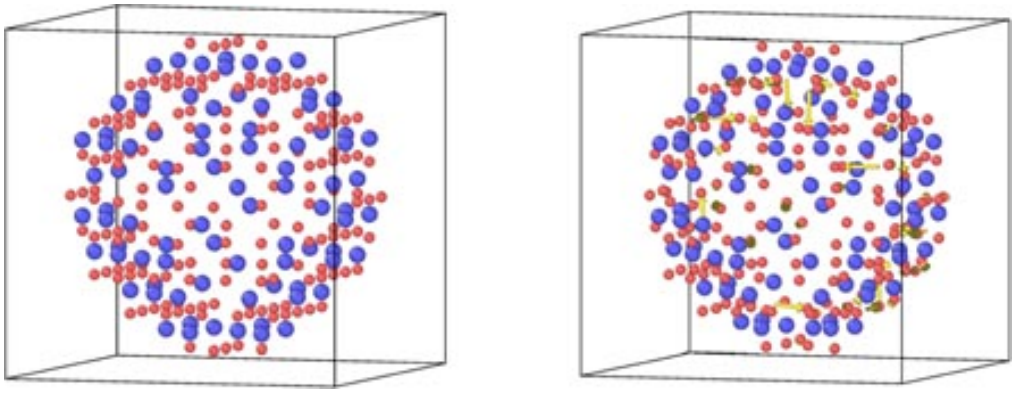

Figure 100: Relaxation of UO_2 lattice on the periphery of the krypton bubble [53]

The relationship between local defects on sub-Å scale and larger defects on nano and micron scale is one of the hardest challenges in this study. While the origination of lattice structure and microstructure defects is due to ion radiation, the growth mechanism for the two different length scales could be very different. Following a damage spike, there is a high concentration of point defects that could produce small isolated defect clusters that are invisible to TEM, or large regions of microstructures that can be easily detected. The original goal was to examine the smaller clusters using EXAFS and comment on the distribution of point defects in the material. However, EXAFS is a technique that averages over several nanometers and microns and detects lattice distortion in average. Therefore, the small isolated clusters of defects still remain isolated and can only be discover by techniques such

as EELS, provided, the location of the cluster is exactly known. Further, the length scales for EXAFS sensitivity is much shorter than that of TEM. EXAFS can detect location of atoms around the target element with hundredths of an Å of precision, which allows for detection of smaller bond distances and the affinity towards certain ligands to be detected. In the case of irradiated UO_2, the presence of short equatorial U-O bonds implies charge imbalance between the two atoms and the possibility of double bonds for increased stability. TEM measurements would be entirely unable to detect such chemistry changes in the material and will fail to explain the oxygen atom distribution following irradiation. The clustering nature of oxygen atoms is largely due to the heavier uranium atom stability in its fluorite lattice and is predicted via theoretical calculations and detected via EXAFS. This study, however, does relate the local structure near neighbor measurements to larger TEM observations, but, it must not be forgotten that the specificity of the two techniques lies on different length and chemistry scales.

X-ray diffraction indicates an expansion of the lattice resulting from radiation induced defects in the He^{2+} irradiated UO_2 samples. This is corroborated by the EXAFS curve fitting results that show an increase in the U-U distances by 0.02 Å for both irradiated samples. This corresponds to a 0.5% increase in the local lattice spacing as seen via EXAFS analysis, which is remarkably consistent with the XRD results. The expansion suggests that the defects that form due to irradiation alter the local and average structure in the X-ray interrogation region. Primary cause of lattice parameter increase has been attributed to the presence of Frenkel pairs on U and O sublattice and small He vacancy clusters, which are expected to form due to ion implantation in the material. However the formation of UO_{2+x}, i.e., U_4O_9 type domains in UO_2, has shown to reduce lattice spacing due to Jahn-Teller

distortion in the molecule. Therefore, the accumulation of irradiation induced defects must be so significant such as to result in the larger lattice parameter seen in EXAFS and XRD. The O clustering resulting from dislocations in He^{2+} implanted samples is negligible due the relatively small number of atoms involved in dislocations and inert gas bubbles (~ .1%) whereas, EXAFS analysis shows greater than 5% change in the relative positions of atoms due to irradiation. Therefore, the biggest contribution to EXAFS spectra is from TEM invisible smaller defect clusters that form due to ion irradiation.

These results are coupled and occur simultaneously with increasing dose. The U-O shoulder at 1.9 Å is similar in position and type to the UO_{2+x} samples studied using EXAFS and indicate the presence of a uranyl type bond. This potentially means that the radiation introduces uranyl type structures as a defect along with the postulated Willis Structure [95] type interstitials and possibly without overall addition of O. One hypothesis could be that either these defects are the first type to form as a result of irradiation from clustering of point defects. A different theory could be that charge accumulation due to ion irradiation causes these to become uranyl type (presence of O at 1.9 Å) at lower temperatures following the irradiation. The Raman spectroscopy measurements [22] suggest the creation of a polaron during the irradiation process that over time results in oxygen rich and oxygen poor regions along the U sublattice, support the existance of U (IV) and (UIII) structures. Along with the presence of the Willis type cuboctohedral defects, the stability of split quad interstitial (SQI) defect is demonstratively greater in the UO_2 lattice [38]. Recent studies have discussed the stability of specific clusters (E.g., SQI, COT, etc) as a function of different lattice planes. This means, if the COT defect has greater stability along the [111] plane, the SQI cluster has statistically higher chance of existing along [100]. Therefore, radiation damage in UO_2

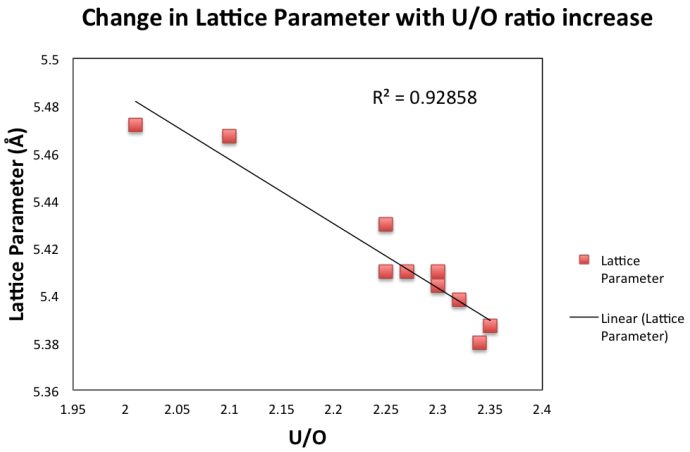

Figure 101: The decrease in lattice parameter is plotted against increasing values of 'x' in UO_{2+x}

results in a predominant distribution of small point defect clusters with varying geometries that are not visible in the TEM observations. These clusters are large enough in distribution that EXAFS and XRD techniques can detect their presence and their subsequent affect on the integrity of the lattice.

The presence of hyperstoichiometric regions in irradiated UO_2 without the affect of an oxidizing mechanism indicates that there must exist hypostoichiometric regions elsewhere in the material. A stark difference in the oxidization effect and the radiation effect is the change in lattice parameter under the two environments. Oxidization of UO_2 results in a decrease in the lattice parameter, due to complex uranyl type molecules, U_4O_9 phases with short U-O distances, Jahn- Teller distortions or the presence of interstitial defect clusters. Radiation results in an increase in the lattice and near neighbor space, increasing with irradiation dose. The decrease in the lattice parameter due to oxidation is shown in Fig. 101. Simultaneously, the lattice parameter from irradiation experiences an increase as shown in Fig. 83.

The significant result from this study is the corroboration of the Raman experiments on He^{2+} irradiation UO_2 showing evidence of O displacements and clustering to give U(III)- and U(V)-enriched domains. This study demonstrate two significant extensions; the O-enriched domains occupy a significant fraction of the material even at extremely modest integrated doses and that the local O concentration is sufficiently high enough to result in U-oxo type bonds indicative of U_4O_9 -type clusters. This means that the detailed information on species and local structure and their trends, with increasing ion dose found by EXAFS almost, duplicate those that occur with oxidation. The implication then, is that the ion irradiation-induced defects produce fluctuations in the local oxygen concentration to give O-enriched and depleted nano-domains in UO_2 resulting in the regions with locally high O concentrations emulating oxidation and the formation of U_4O_9-like domains in UO_{2+x}.

This O shell and U-O non-crystallographic distance can be compared with the similar shell found in UO_{2+x}, where the distance is 0.2 Å shorter than the one in this study, and therefore almost identical to the U-oxo bond in α-UO_3 [9]. Although 1.8-1.9 Å might still be considered a multiply bound uranyl type of O, it is significantly longer than the typical distance seen in UO_{2+x} EXAFS measurements. It is nevertheless shorter than bridging type oxo bonds in, e.g., U_3O_8 [10]. The 0.03 Å expansion of the oxo bond in U(VI) hydroxide molecular complexes shows that U-O_{oxo} distances are subject to chemical effects, caused in that case by the π-donor capacity of the OH– ligand [16]. The observed 0.2 Å expansion from α-UO3 is, however, much too long to originate solely in this effect, suggesting an asymmetric bridge or perhaps a U(V)-oxo. Since irradiation cannot oxidize the material it is not surprising that this short bond is longer than that in a typical U(VI)-oxo compound. Nonetheless, it is much shorter than the 2.2 Å U(V)-O single bonds found by neutron scattering measurements in

U_4O_9 and U_3O_7 . The other distinct similarity to an EXAFS-derived structural property of UO_{2+x} is the disappearance of all of the other non-crystallographic atoms at longer distances manifested as the even reduction in amplitude of all of the features without the appearance of new ones, leaving a multisite nearest neighbor U-O distribution as the only addition to the spectrum. This poses the question of whether the combined oxo-type neighbor and U amplitude loss are directly caused by static radiation-induced defects or if instead they result from the same type of dynamical polaron as in UO_{2+x} [18]. An essential part of this mechanism would be the movement the adventitious O (or of the photo-induced U(V)) and its subsequent aggregation into O/U(V)-enriched domains where the dynamical charge-transfer occurs. This subsequently implies that a mechanism exists whereby the dynamical polaron is stabilized beyond the amount that would occur in the static system. Such stabilization, and the corollary propensity in tandem with the transport to propagate the composition fluctuations beyond the narrow peak of the damage profile, would explain why there are a sufficient number to be visible in the EXAFS despite the varying integrated radiation doses. It would also explain not only the efficiency but also the ease with which this process occurs. The irradiation with H^+ and He^{2+} and other light ions create displacements indicating that the product of such displacements, the formation of the O-enriched domains via clustering, are energetically favored so as to stimulate this process in excited UO_2. This corroborates the unusual results obtained with optical pumping that were interpreted as the creation of ordered, in fact coherent, states [18].

7.7 Summary of Discussion

Uranium Dioxide is widely used as a nuclear fuel and is simultaneously the focus of several scientific experiments to better understand the rapid oxygen mobility and stoichiometry evolution in the material. This study has tackled the radiation induced structure progression in UO_2, while carefully studying the oxygen species clustering mechanism in the material. H^+ atoms were used to study the radiation damage due to neutrons and to potentially identify a method to create simple TEM visible microstructures. He^{2+} atoms were used due to their high population in a nuclear reactor and the resultant damage to the fuel and were also included, due to the self irradiation of used nuclear fuel while in storage. Kr ions are one of the most common fission products in the reactor and possess the ability to significantly alter the microstructure in the fuel due to Kr gas bubbles and the their potential of release at high temperatures. Therefore, Kr ions were chosen as one of the irradiation species that were deposited in UO_2 using an ion accelerator. The key lattice measurements that stand true for all the irradiation species can be summarized as:

1. For low doses in the case of all irradiation species, the overall fluorite structure is maintained. The Fourier transform features in irradiated samples occur in the same positions as the pristine samples. This trend is broken only in the case of the highest dose H^+ and Kr irradiated samples, where there is loss of intermediate structure and the peaks at $R > 4.5$ Å no longer follow the reference UO_2 samples.

2. A consistent expansion in lattice is observed and is corroborated by EXAFS and XRD results. This expansion grows with ion dose and also with ion size.

3. A monotonic loss of amplitude of the crystallographic peaks across the Fourier transform of EXAFS is seen in all of the samples. This loss is greater with higher dose, and again with ion size.

4. With the increase in dose, there is an increase in prominence of the non-crystallographic peak at 1.8-1.9 Å. This peak is successfully fit by a shell of oxygen atoms, indicative of oxygen clustering in the samples.

Microstructure measurements were successfully performed using various imaging techniques in the TEM. Bright field two beam imaging condition used on the dislocation loops can detect the lattice plane, size and density of the loops at each irradiation condition. Bubble measurements were made in the case of He^{2+} and Kr irradiated samples along the edge region. Bubble density and diameter is shown to increase with increasing ion dose in both samples. Additionally, the Kr bubbles have a larger diameter than the He^{2+} bubbles. The TEM measurements are summarized as:

1. As the ion dose increases, the dislocation distribution increases in size and density. As noted in the case of Kr implanted samples, dislocations evolve as small loops $\rightarrow$ big loops $\rightarrow$ dislocation lines$\rightarrow$ dislocation tangles.

2. The dislocation loops are consistently seen to lie along the [111] plane in the UO_2 samples. This is because the [111] plane offers a large empty space in the lattice and is known as interstitial cuboctohedral site. Since, this site typically forms interstitial clusters and because oxygen atoms tend to participate readily in microstructure defect

formation, the dislocation loops are likely rich in oxygen and form a hyperstoichiometric region in the lattice.

3. The bubble measurements for both the He^{2+} and the Kr irradiated samples reveal an increase in bubble density and size with increasing dose. With increase in ion dose, there is a greater population of vacancies and vacancy clusters, which form nucleation sites for inert gas bubbles.

Simulation and theoretical techniques are employed in this study to relate the empirical results to calculations. This is crucial to create a predictive basis for the performance of fuel materials under irradiation. In this work, the calculations have successfully verified the experimental results and have potential to be used exclusively to model fuel materials in the future. It has also been shown with basic theoretical calculations that the predominant atomic defect resulting from irradiation in UO_2 is small point defect clusters, largely rich in oxygen interstitials. The key points that are found using simulation measurements are:

1. To study basic defect dependence of EXAFS, FEFF9 based code can be utilized. This code successfully simulates EXAFS patterns based on singular vacancy insertions in a list of atomic positions of a UO_2 lattice. With the addition of vacancies in the lattice, the Fourier transforms monotonically reduced in amplitude. Thus, consistent with empirical results, the loss of vacancies implies loss of overall structure that is shown in simulation measurements.

2. Artemis and Athena software can then be used in conjunction with FEFF to simulate

the effect of interstitials in the UO_2. With addition of oxygen interstitials, the O shoulder begins to grow on the low R side of the Fourier transform, at the U-O length that the interstitial was inserted.

3. CrystalMaker software is a graphic presentation software that was used to create models of the pristine and oxygen rich UO_2 lattices. The software not only helps in visualizing the arrangement of defects, but also can be used to generate atomic positions that were used as an input in the Artemis and Athena software to simulate the effect of interstitials.

4. Cluster Dynamics was used to predict the characteristics of voids and clusters resulting from ion irradiation at various DPA rates and after different times following the ion irradiation. The extent of defect clustering resulting from O and U atoms was used to predict the distribution of defects in an irradiated UO_2 lattice. These results, predicting hyperstoichiometric clusters and oxygen rich and oxygen poor regions are consistent with EXAFS measurements.

5. Finally, these simulations can be used to model the final radiation induced structure breakdown. The basic theoretical calculations used the dislocation and bubble density and size to understand the effect of microstructure on lattice structure changes. Microstructure was used to calculate its effect on the lattice structure on the order of 0.1 %, whereas, EXAFS measurements reveal a change in the structure around 5%. Therefore, basic calculations from Appendix A and B show that ~98% of the defects are small point defect clusters rich in oxygen interstitials. The remaining ~1.99% is contribution from single point defects that are likely rich in U interstitials and vacancies.

Together with the three methods, lattice structure, microstructure and simulation techniques, this study was able to understand the differences in damage structure resulting from various irradiation species on multiple length scales.

8 Conclusions

The study has evaluated the evolution of defects on multiple length scales in UO_2 due to H^+, He^{2+} and Kr irradiation. The experimental results have been corroborated with simulation studies to provide a detailed understanding of defect distribution from singular atoms through to microstructure on the micron length scale. With ion irradiation using accelerators at the University of Wisconsin-Madison and University of Illinois Urbana-Champagne, atomic structure and microstructure defects were introduced in the UO_2 samples. The primary experimental methods to probe the lattice structure are Extended X-ray Absorption Fine Structure (EXAFS) measurements along with X-ray Diffraction (XRD) and Transmission Electron Microscopy, which provided detailed information on the type and characteristics of defects on multiple length scales in UO_2. The results are described in the following subsections:

8.1 Irradiated UO_2 resembles oxidation however increased lattice parameters indicates microstructure changes.

Irradiation of UO_2 creates changes with some similarity to oxidation, but the increase in lattice parameter (as compared to oxidation) indicates differences in microstructure.

- EXAFS analysis reveals the presence of oxygen defect clusters at U-O distance of 1.8 Å.
- Similar to oxidation, UO_2 maintains its overall fluorite structure at low and intermediated radiation doses.

- Unlike UO_{2+x}, radiation damage in UO_2 causes an increase in lattice parameter, due to an accumulation of Frenkle defects and small clusters.
- The distribution of small clusters, that cannot be detected at the TEM level, are primarily responsible for lattice change detected by EXAFS in irradiated UO_2.

Concomitant with the loss of amplitude of the crystallographic features with radiation damage, there is a significant increase in the prominence of the non-crystallographic oxygen shoulder at 1.8 - 1.9 Å from the absorbing ion uranium. This oxygen shoulder is also seen to grow in UO_{2+x} for increasing values of 'x'. The short U-O distance of 1.7 - 1.9 Å is characteristic of the uranyl bond, which is a U double bonded with two O atoms and an overall net 2+ positive charge. These bonds are highly stable in nature due to their oblate geometry and form complex molecules with actinides in used nuclear fuel storage. The presence of the O shoulder also verifies the preference of O cluster of defects that appear as stabilizing features in the U-O near neighbor distribution and a sub-structure that forms in the UO_2 lattice. This process also occurs in UO_{2+x} , where the excess O atoms cluster so as to stabilize the lattice. This shoulder was linked to the presence of uranyl compounds that are highly stable and exist in in U_4O_9 phase. Therefore, small domains of U_4O_9 exists in UO_{2+x} by altering the local structure of the material.

With ion irradiation at low and intermediate doses, there is no evidence of loss of overall fluorite structure in UO_2. In fact, the features of the spectra of the Fourier transforms are in the same positions as the crystallographic samples for all the ion doses except the highest proton ion dose. This is in agreement with historical data indicating that UO_2 maintains its overall fluorite structure during oxidation and nuclear reactor irradiation.

Lattice parameter has been shown to decrease in UO_{2+x} with increasing values of 'x'. This is due to the Jahn-Teller distortion in UO_2 due to accumulation of additional oxygen interstitials in the fluorite lattice. Radiation damage, however, has shown to increase the lattice parameter in UO_2 as seen in XRD and EXAFS experiments. This is because irradiation creates a distribution of Frenkel defects and small defect clusters that together contribute to lattice expansion with increasing ion dose in the material.

While atomic structure and local structure defects show the chemistry evolution in the irradiated material, microstructural features show the extent of accumulated and larger length scale damage. Transmission Electron Microscopy measurements have been made to study larger scale defects in irradiated UO_2 and EXAFS and XRD measurements give insight into collective atomic defects.

XRD and EXAFS measurements reveal differences in the lattice structure by an 0.5 % increase in the lattice parameter and $> 5\%$ of the overall atoms fit in the UO_2 samples. Local structure measurements also reveal an oxygen cluster distribution at short (1.8 - 1.9 Å) distance from U atoms. Therefore, the local structure has significantly been altered due to ion irradiation. TEM data reveals dislocation loops and bubbles that locally alter the structure of the lattice due to the defect itself and the neighboring atoms around the defect.

Theoretical comparison between the extent of microstructure and TEM visible damage was made to local structure damage using basic mathematical calculations. This revealed that the TEM defects could potentially contribute up to 0.01 % of the total damage seen in EXAFS. The remaining local structure damage is due to TEM invisible defects that contribute to the local structure variations seen in EXAFS and TEM. Therefore, it was established that the primary cause of local structure changes and lattice variations are due

to small defect clusters, 4-30 atoms in size that cannot be seen in the TEM and cause large changes to the lattice. The overall effect of TEM changes in UO_2 lattice is on the order of 0.01 %.

Therefore, the general distribution of defects can be attributed partly to individual point defects that exist from irradiation on the order of 1-2% of the overall damage. A large percentage of the damage is point defects coalescing to form defect clusters, that are still too small to be visible in TEM. These constitute 98% of the defects in ion irradiated UO_2. Finally, some defect clusters coalesce to form larger defects that are microstructures visible in TEM, which can be characterized and measured using microscopy techniques. These defects contribute to lattice change on the order of 0.01 % of total damage.

8.2 Multiple measurement and modelings techniques concur with the existence of hyper and hypo stoichiometric regions

The combination of EXAFS, Cluster Dynamics, CrystalMaker Analysis, MD and Raman measurements support the existence of hyper and hypo-stoichiometric regions in the material after irradiations.

- Shows an increase in non crystallographic oxygen distribution at 1.8 Å (hyper)
- Shows a decrease of crystallographic oxygen distribution at 2.35 Å (hypo)

Cluster Dynamics

- Shows an increase in concentration of hyper stoichiometric clusters during irradiation

Raman Measurements

- Suggest the existence of Magneli type defects which give rise to oxygen rich and oxygen poor regions within the uranium sub lattice

Therefore radiation damage creates oxygen rich and oxygen poor regions within the overall stoyichometric lattice.

In case of irradiated UO_2, there exists no active oxidation mechanism that caused the creation of UO_{2+x} type features. Therefore, irradiation was seen to result in local segregation of structure by creating hyperstoichiometric and hypostoichiometric regions in the sample. This was seen in EXAFS results, where the non crystallographic oxygen peak existed along with the decrease in magnitude of the crystallographic oxygen shell. The two U atoms bonded to these oxygen atoms, therefore existed as U^+ and U^-, indicating oxygen rich and oxygen poor regions. These measurements were verified by simulation results in Cluster Dynamics. CD calculated the concentration and constitution of defect clusters and voids during the course of ion irradiation The simulation results show hyperstoichiometric voids and clusters grow in number density with time, as compared to hypostoichiometric and stoichiometric voids and clusters. Therefore, while radiation damage doesn't oxidize the UO_2 samples, it creates regions of hyperstoichiometry that give the appearance of UO_{2+x}. This also means,

that in order to have regions of UO_{2+x} , non-crystallographic oxygen ions must rearrange into defect clusters, similar to UO_{2+x} and align themselves in the UO_2 interstitial defect sites, so as to not alter the overall lattice shape. Raman measurements performed on He^{2+} irradiated samples further give evidence of U^+ and U^-regions in the UO_2 lattice. The group that performed these measurements theorized the existence of complicated O defects called Magneli type structures that render regions in the lattice oxygen rich and oxygen poor. These observations are consistent with empirical and simulation work shown in this study.

8.3 Consistent damage structure complexity with increasing DPA

The lattice parameter, the microstructure visible to TEM and the lattice structure invisible to TEM all scale with DPA. No conclusive evidence was seen on microstructure evolution of the material due to DPA rate.

- The oxo-shoulder moves to shorter U-O distances (˜1.8 Å) with increasing ion dose. This is in agreement with UO_{2+x} EXAFS measurements where the non-crystallographic O shell is fit at very short distance of 1.7 Å.
- Inert gas bubbles are seen to grow in size and density with increasing irradiation dose.
- Increase in ion dose results in larger size and number density of dislocation loops under H and He irradiation
- For the Kr implanted samples, the dislocation density decreases as a function of dose. However, the dislocation size grows as small loops → big loops → dislocation lines→

dislocation tangles

- Lattice expansion is demonstrated to be a function of radiation dose.

The differences in the resulting atomic structure defects from varying irradiating ions is key to understanding defect structure evolution in a nuclear reactor where several different ions constantly damage the nuclear fuel lattice. A tabulated list of differences in microstructures and EXAFS fits is shown in Table 16, 17 and 18. One of the notable difference was the position of the oxygen shoulder peak. For He^{2+} irradiated samples, the peak was located closer to 1.9 Å whereas for higher dose H^{+} samples, this was closer to 1.78 Å. The krypton irradiated samples also showed an oxygen shoulder fit at distances decreasing with increasing dose from 1.9 Å through to 1.78 Å. This indicates the propensity of the oxygen shoulder to form at shorter U-O distances in favor of greater stability of the system. Therefore, the O defect cluster ought to be chemically stable near U atoms, located in the void in the UO_2 lattice along the [111] plane. This stability occurs at greater ion doses and with larger DPA (resulting from larger ions) so as to provide the necessary energy to the lattice to break the original O bonds to form non crystallographic O positions. Therefore, the distance at which the oxygen defect cluster is located in regards to the U atom in the lattice is inversely proportional to the ion dose. Also, for larger DPA rates, the U-$O_{non-crystallographic}$ will stabilized to shorter distances quicker.

With increasing ion dose and increasing size of the damaging species, the resulting defect structure gets continually more complicated. Increase in ion dose results in larger loss of monotonic amplitude in the EXAFS spectra for all the samples. Along with the loss of spectral amplitude, there is an increase in the amplitude of the non-crystallographic oxygen

shoulder, which consistently grows with increasing dose. Since the shoulder has been related to the formation of uranyl type bonds and oxygen interstitial cluster formation, the radiation dose increase complicates the local structure distribution with increasing dose. The increase in the oxygen interstitials leads to the formation of multiples of the cuboctohedral cluster or the split quad interstitial cluster, therefore, the resulting cluster is a complicated defect cluster, larger than 6 point defects (which is what the classic COT cluster consists of). The $>$ 5% change in the lattice disorder increases to 30% change in case of highest dose Kr implanted samples, indicating that with increasing ion dose, the lattice structure is significantly affected by the radiation damage in terms of damage cluster and microstructure formation.

This structure evolution into more complex features continues into the microstructure distribution with increasing ion dose. The bubble distribution grows larger and higher in number density, thereby affecting the integrity of the lattice further. Simultaneously, the dislocation loops coalescing to form larger, more complex networks of dislocations becomes harder to characterize with increasing dose. This further indicates that radiation dose continues to create complicated structures on multiple length scales in the material that could significantly alter the mechanical and thermal transport properties of the fuel.

Further, the overall % change in the number of atoms fit in each shell (indicative of the extent to which the lattice looses its original structure) is also directly linked to the irradiating ion size. This is to be expected, however, this study gives conclusive proof of the extent to which large ions damage the structure more than smaller ions. Therefore, in a nuclear reactor, fission gases are hugely responsible for the compromise of the nuclear fuel radiation damage.

The EXAFS and XRD analysis reveals that the lattice parameter increase is directly linked to the ion dose and ion size of the irradiating species. The rate of change of the lattice parameter is much larger in case of Kr ions than for He ions, which is greater than H ions. This is because, irradiation creates a distribution of Frenkel pairs in the process of radiation damage, that together contribute to lattice expansion. Therefore, larger the irradiating species, greater will be the distribution of defects, and hence the lattice parameter will grow faster.

9 Future Work

9.1 Advanced Test Reactor Irradiation

To compare the ion irradiations performed in this study to nuclear reactor irradiation, the Advanced Test Reactor (ATR) will be used to perform an irradiation experiment with similar parameters as the ion accelerator study, albeit in a nuclear reactor. This experiment seeks to put several samples of depleted UO_2 in Idaho National Lab's (INL) ATR for varying lengths to study the effect of irradiation on microstructure evolution and thermal conductivity of UO_2. The sample will be placed in the B-7 position of the ATR. This position uses the Hydraulic Shuttle Irradiation System (HSIS) that allows a train of 16 capsules to be inserted and removed from the reactor while it is operating. Each titanium capsule in this system is 2.25" long and has on outer diameter of 0.625", with a maximum weight of 27.0 grams [68]. It is intended for the capsules to be in the reactor from a few hours to a maximum of 90 days. The approximate thermal and fast (E $>$ 1 MeV) fluxes in the B-7 location is $2.5 \cdot 10^{14}$ and $8.1 \cdot 10^{13}$ n/cm^2-s, respectively [68]. An illustration of the ATR reactor core with various irradiation positions and control mechanisms used are shown in Fig. 60.

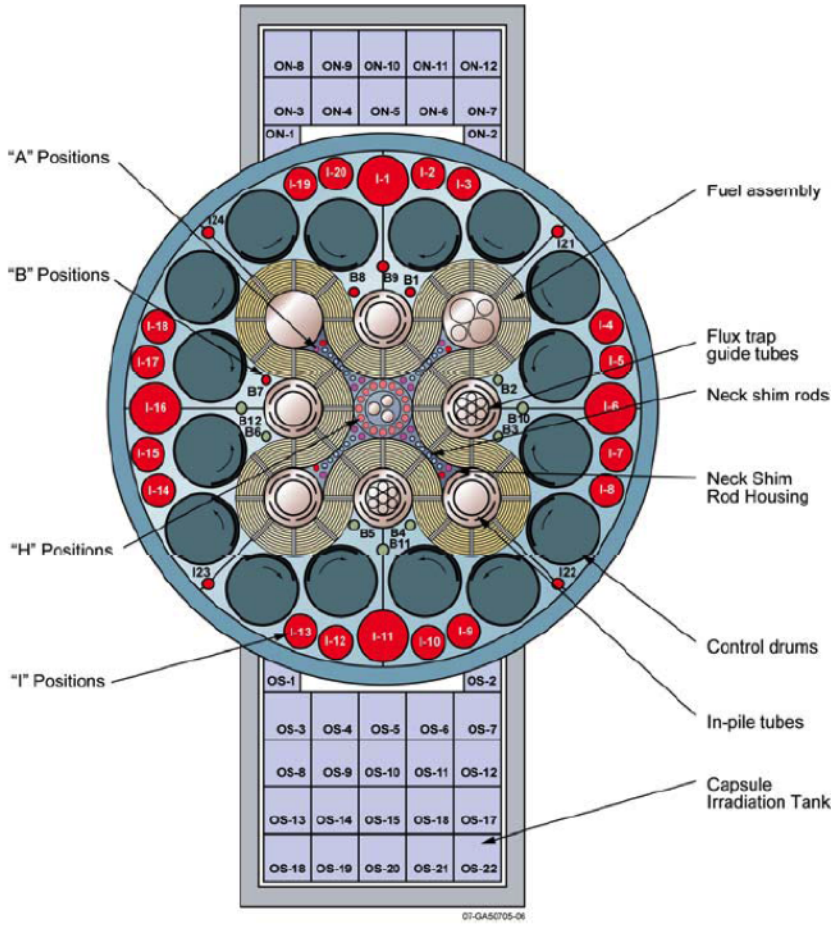

Figure 102: Schematic of ATR showing irradiation test positions. The B-7 position will be used for this experiment.

Depleted UO_2 is used in this experiment to avoid complex microstructure formation due to fission; properties of d-UO_2 are used in the calculations. A suitable material to surround the UO_2 would fulfill a few key characteristics. First, it would be practical to handle and put in a capsule to put in the ATR. Also, the material would undergo a reaction that releases particles with high enough energy to sufficiently penetrate the UO_2 and cause significant

damage. Three types of reactions are explored for viability:

1. Neutron irradiation of incident energy comparable to proton irradiations done at UW-Madison
2. An (n, α) reaction where both an α particle and a daughter particle would be incident on the UO_2 target.
3. A Krypton implantation with neutrons to drive the implanted ions to increasing depths

9.1.1 Neutron Irradiation

The ATR has high fast neutron flux of $8.1 \cdot 10^{13}$ n/cm^2-s and therefore can sufficiently irradiate the d-UO_2 samples in the Hydraulic Shuttle Irradiation System. Neutron irradiation is bulk irradiation which means that the target sample will have consistent damage and not like ion beam damage that forms a damage plateau and a damage peak. Consistent radiation damage provides the ability to comment on the thermal transport decrease, the stoichiometry evolution throughout the sample and the extended microstructure defects. The high energy neutrons can be used to compare to proton irradiation damage as well.

9.1.2 Alpha Irradiation

Data collected for potential (n, α) reaction targets include cross sections at various energies, abundance of the isotope, mass of the target and daughter, density, and penetration depth into UO_2 target. The (n, α) reaction takes the form shown in equation 3.

$$ {}^{A}_{Z}X + {}^{1}_{0}\,n \rightarrow {}^{4}_{2}\,\alpha + {}^{A-3}_{Z-2}\,D + Q $$

where X is the target isotope with mass number A and atomic number Z, D is the daughter isotope, and Q is the reaction energy (Q-value) release by the reaction. After calculating the Q-value from the masses of the target isotope, neutron, α particle and daughter isotope, the kinetic energies of the daughter and α particles by using classical momentum and kinetic energy conservation. These formulas for the kinetic energies of the resultant α particle and daughter isotope are shown in equations 4 and 5, respectively.

$$ T_{\alpha} = \frac{Q+T_n}{(1+m_{\alpha}/M_D)} $$

$$ T_D = \frac{Q+T_n}{(1+M_D/m_{\alpha})} $$

Where T is the kinetic energy of the daughter particle, α particle, or neutron, MD is the mass of the daughter particle, and mα is the mass of the α particle. Additionally, the macroscopic cross section is calculated for each isotope using equation 6 to determine the yield of each (n, α) reaction.

$$ \Sigma = \frac{\sigma \cdot \rho \cdot N_A v}{MM} $$

where σ is the microscopic cross section (cm-2), ρ is the density of the target material (kg/m3), N_{Av} is Avogadro's number ($6.022 \cdot 10^{23}$ mol^{-1}), and MM is the molecular mass (g/mol). Cross-section data is used as collected from Brookhaven National Laboratory's National Nuclear Data Center [86]. Finally, the energy and isotope information is used to

calculate the depth the daughter and α particles penetrate in the UO_2 with the Stopping and Range of Ions in Matter [104] program. Table 14 shows data from four of the most energetic reactions of the 42 reactions studied.

Reaction	E	σ_{res} (b)	T_D	T_α	Σ	$Depth_D$	$Depth_\alpha$	Abund.
		(b)	(MeV)	(MeV)	$\left(\frac{1}{cm^2}\right)$	(μm)	(μm)	%
^{6}Li (n, α) ^{3}H	thermal	944	3.31	2.49	50.6	4.2	5	7.60
^{10}B (n, α) ^{7}Li	thermal	3690	1.38	2.42	546	1.5	5	19.90
^{58}Ni (n, α) ^{55}Fe	2 MeV	$6.8{\cdot}10^{-4}$	0.402	12	$6.4{\cdot}10^{-5}$	0.25	15	68.10
^{59}Ni (n, α) ^{56}Fe	204 eV	140	0.408	5.71	12.7	0.25	15	0

Table 19: Data for four energetic (n, α) reactions.

9.1.3 Krypton Implants

Another potential method for implanting particles in UO_2 is the (n, scatter) reaction. An advantage of the scatter reaction over the (n, α) reaction is that only one particle is implanted in the UO_2. Energy and momentum balances are used to calculate the final energy of the target particle. The result is shown in equation.

$$T_X = \frac{T_{n1} \cdot m_n (2m_n + m_X + 2\sqrt{(m_n m_X)})}{4m_n^2 + m_X^2}$$

where T_X is the final kinetic energy of the target particle, T_{n1} is the energy of the incoming neutron, m_n is the neutron mass, and m_X is the mass of the target particle. The elements studied for the (n, scatter) include neon, argon, krypton, xenon, lithium, bromine, rubidium, yttrium, zirconium, cesium, barium, and iodine. Energy and macroscopic cross-section calculations are done for resonances at high energies. Of the 13 isotopes with multiple

resonances studied, only three of the reactions yielded particles with penetration depths exceeding 20 nm. To allow for material analysis, particles need to penetrate about 20 nm. Table 15 shows these three target particles, the relevant resonances and cross-sections, the resultant energy of the target, the penetration depth, and the atomic abundance.

Target	E_{res}	σ_{res}	T_X	Σ	$depth_X$	Abund.
		(b)		$\left(\frac{1}{cm^2}\right)$	(nm)	%
^{7}Li	261 keV	12	70.9 keV	0.551	400	92.40
^{7}Li	4.6 MeV	2.2	1.2 MeV	0.101	2300	92.40
^{40}Ar	77 keV	35	70.6 keV	$1.69{\cdot}10^{-4}$	70	99.60
^{79}Br	2 MeV	2.3	32.0 keV	$5.48{\cdot}10^{-2}$	25	50.70
^{84}Kr	2 MeV	3.1	29.0 keV	$8.34{\cdot}10^{-5}$	24	57.00
^{129}Xe	2 MeV	4.3	18.7 keV	$1.19{\cdot}10^{-5}$	12	26.40

Table 20: Data for three (n, scatter) reactions with highest penetration depths.

Ideally, the heavier isotopes listed in Table 14 would be used in the experiment because they have significant fission product abundance. The (n, scatter) reactions are studied with incoming neutron energies of 2 MeV (the average fission neutron energy) to obtain higher resultant energies and larger penetration depths. Since the densities used for these experiments are at atmospheric pressure, the densities of the gasses could be increased in the experiment sample to increase the yield of the reaction. Due to its significant fission product abundance and penetration depth exceeding 20 nm, the 84Kr is the most relevant scattering reaction.

Due to the uncertainty in the reaction products' incidence rate on the sample surface, a new method for krypton irradiation was proposed. Krypton ions will be implanted into the d-

UO_2 samples at an ion accelerator facility prior to the neutron irradiation in the reactor. The neutron flux will eventually drive the implanted Kr ions further into the sample to create a uniform and deeper implant layer. This would be ideal for thermal transport measurements and EXAFS analysis. Handing these samples prior to the ATR irradiation and inserting them into the HSIS capsule will also be significantly simplified. Fig. 61 and Fig. 62.

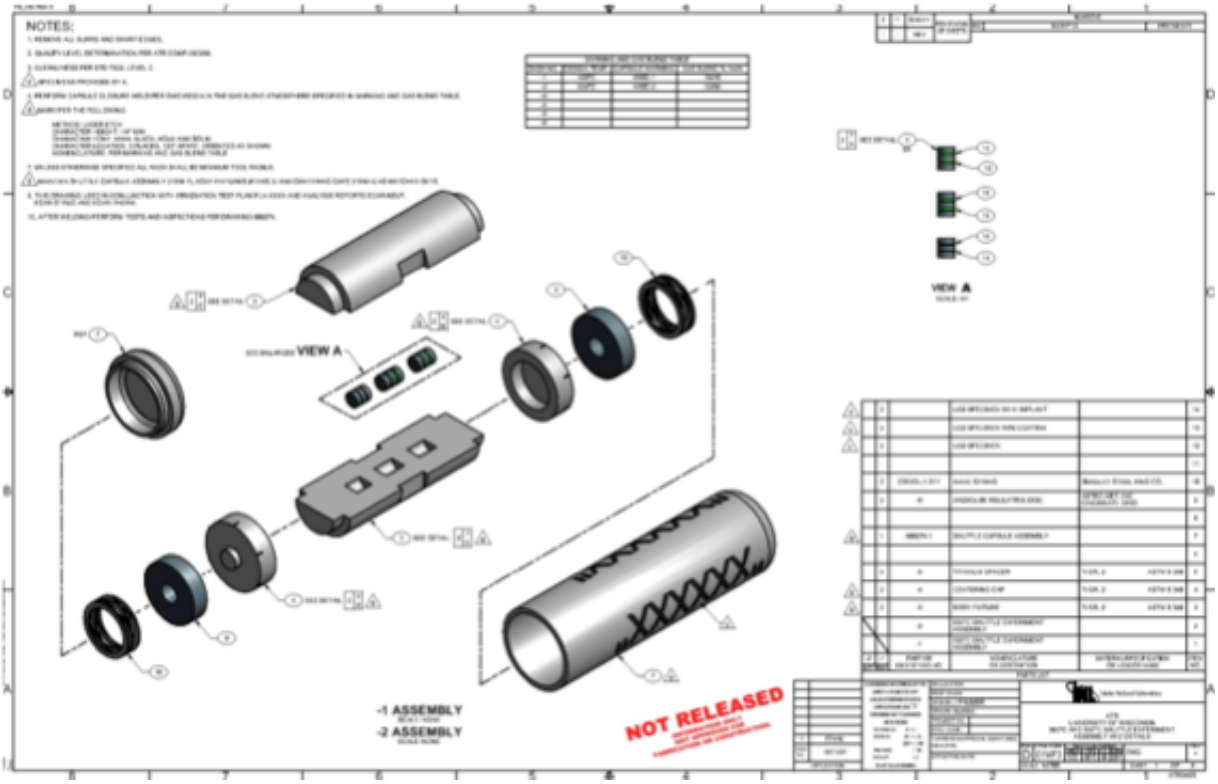

Figure 103: HSIS capsule design for the three sets of d-UO_2 ATR irradiations.

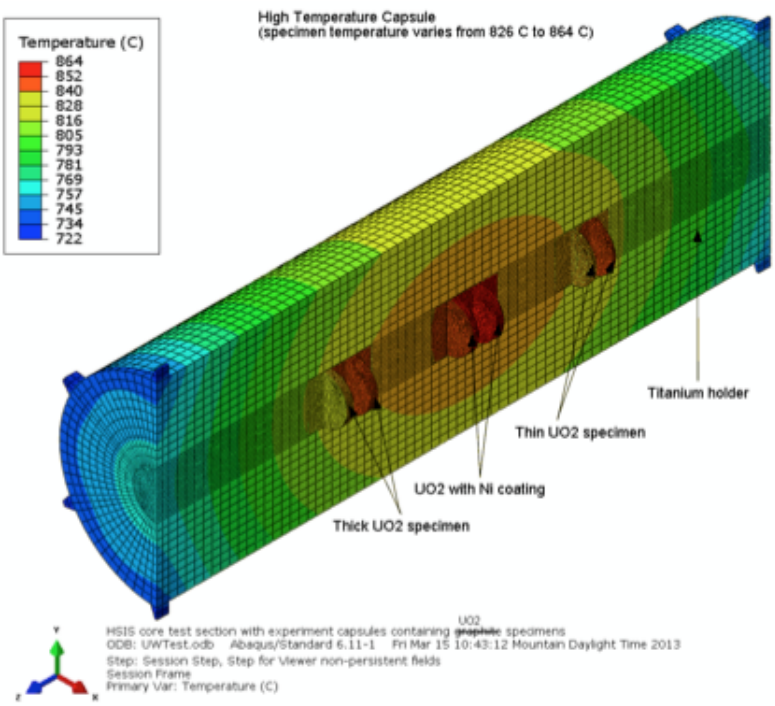

Figure 104: Heating in the HSIS capsule during ATR irradiation. The sample temperatures can be lowered using a gas mixture in the irradiation capsule

A summary of all the neutron, alpha and krypton irradiation is given in Table 16. Three temperatures for the irradiation ensures that there is comparison between all the ion beam implanted irradiations. Also, with increasing temperatures, microstructures and chemistry evolve to result in different damage features. These features will be explored and using post irradiation examination (PIE) techniques including TEM, EXAFS, XRD and thermal transport measurements. A total of 54 samples will be irradiated and studied using varying irradiation doses, temperatures and ion types.

Specimen types	Kr implant
	Alpha Implant
	PC UO2
Specimen size	3 mm id X 500 um thick
# At each dose	6 (2 each at 150 C, 500 C, 800 C)
Fluence levels	Kr: $1{\cdot}10^{15}$, $5{\cdot}10^{15}$, $1{\cdot}10^{16}$
	α : 1E16, 5E16, 1E17
	n: 1E18,

Table 21: Summary of all the ATR samples to be irradiated along with their ion types, doses and temperatures

The entirety of this experiment will be funded by the Advanced Test Reactor to encourage new users to perform novel experiments and to enrich the existing sample inventory with fuel related samples.

Appendix A

Relating the microstructure to lattice structure was approached by first performing basic calculations to compare the TEM observable defects to the EXAFS visible lattice structure change. This was done by comparing EXAFS information to TEM dislocation information in case of He^{2+} irradiated UO_2. This analysis is given below.

- Dislocation loop density in UO_2 is 6×10^{21} loops/m^3
- Average loop diameter is 7.3 nm

Assuming a stoichiometric composition of dislocation loops

- Total UO_2 molecule length is ~ 306 pm or 3.06 Å
- Using loop diameter, the total circumference of the loop can be calculated as

$$\text{Circumference} = 2\pi r$$

$$\therefore \text{Circumference of dislocation} \approx 23 \text{ nm}$$

- Dividing the total circumference by the molecule length of UO_2

$$\text{Number of } UO_2 \text{ units in each dislocation} = \frac{2\pi r}{UO_2 molecule}$$

$$\therefore \text{Number of } UO_2 \text{ units in each dislocation} \approx \frac{23nm}{3.06\mathring{A}}$$

$$\approx 76 \text{ units of } UO_2 \text{ per dislocation}$$

- Using loop density, the total number of units of UO_2 can be calculated in $1m^3$ of space

$$\text{Number of } UO_2 \text{ units/m}^3 = \text{Loop density} \times \text{Number of } UO_2 \text{ units per dislocation}$$

$$\Rightarrow \text{Number of } UO_2 \text{ units/m}^3 = 6\times10^{21} \text{ loops/m}^3 \times 76 \text{ units of } UO_2 \text{ per dislocation}$$

$$\Rightarrow \text{Number of } UO_2 \text{ units/m}^3 = 4.56\times10^{23} \text{loops/m}^3$$

- EXAFS interrogation depth in UO_2 is approximately 4µm
- Total analysis volume for each sample can be calculated using volume of cylinder equation

$$\text{Total interrogation volume} = 2\pi r^2 h$$

$$\Rightarrow \text{Total interrogation volume} = 2\pi \left(\frac{5.2mm}{2}\right)^2 (4\mu m)$$

$$\Rightarrow \text{Total interrogation volume} = 0.17 \text{ mm}^3$$

- Using number of dislocations in $1m^3$

Total number of dislocated units of UO_2in the interrogation volume = Number of UO_2 units/m^3× Interrogation volume

⇒Total number of dislocated units of UO_2in the interrogation volume = 4.56×10^{23} units/m^3× 0.17 mm^3

⇒Total number of dislocated units of UO_2in the interrogation volume = 7.752×10^{13}units

- Using Avogadro's number, the total number of UO_2 molecules in the interrogation volume can be calculated as

$$\text{Number density of } UO_2 = \frac{N_A}{M} \cdot \rho$$

Where, N_A= Avogadro's number = 6.022×10^{23}, M = Molar mass in grams and ρ = density of UO_2 = 10.97 g/cm^3

Therefore,

$$\text{Number density of } UO_2 = \frac{6.022 \times 10^{23}}{270.03 g/mol} \cdot (10.97 g/cm^3)$$

⇒Number density of UO_2 = 2.446×10^{22} molecules/cm^3

- Using number density of UO_2, the number of UO_2 molecules in the interrogation volume can be calculated as

$$\text{Total number of } UO_2 \text{ molecules} = 2.446 \times 10^{22} \text{ molecules/cm}^3 \times 0.17 \text{ mm}^3$$

$$\Rightarrow \text{Total number of } UO_2 \text{ molecules} = 4.158 \times 10^{18} \text{ molecules}$$

- The atoms surrounding the dislocation are also affected by the presence of the dislocation.
- Assuming the dislocation affects 2 lattice planes around it on each side, the total number of dislocated units can be multiplied by 4

$$\Rightarrow \text{Total affected } UO_2 \text{ units} = 3.10 \times 10^{14} \text{molecules}$$

- Using this number, the total percentage of the UO_2 sample that is either a dislocation or affected by a dislocation can be approximated as,

$$\text{Percentage of total sample that is dislocated or affected by a dislocation} = \frac{3.10 \times 10^{14} molecules}{4.158 \times 10^{18} molecules} \times 100$$

$$\Rightarrow 0.007 \text{ \% of the total population}$$

- Therefore, approximately, 0.007% of the total population is affected due to TEM visible dislocations
- Similar analysis was done for He^{2+}bubbles found in the samples.
- Approximate number of atoms that are affected by bubbles in the lattice are 0.00254% of population of the sample

Therefore, only about ***0.01%*** of the total constituent molecules will exhibit a change in the near neighbor structure due to the presence of TEM visible defects.

Appendix B

This section aims to develop a basic correlation between simulation results and the EXAFS observed results. The ultimate goal being the distribution of defect types resulting from ion irradiation.

- The total interrogation volume in UO_2 during EXAFS was calculated to be 0.17 mm^3.
- The total number of UO_2 molecules in the interrogation volume are approximately 4.158×10^{18} molecules.
- It was also determined from Appendix A, percentage of molecules affected by TEM visible defects is approximately **0.01%**
- Further, EXAFS detects a 5% change in the number of atoms affected by radiation for this dose level.
- Therefore, 4.99% of the change is yet unaccounted for
- Assuming there exist damage clusters smaller than TEM visibility on the scale of 2-30 atoms in size, these atoms would then be responsible for majority of the damage.
- 5% of the change in EXAFS corresponds to

$$5\% \text{ of atoms in interrogation volume} = 0.05 \times 4.158 \times 10^{18} \text{ molecules}$$

$$\Rightarrow 5\% \text{ of atoms in interrogation volume} = 2.08 \times 10^{17} \text{ molecules}$$

- Void and cluster density in Cluster Dynamics simulation was calculated to be 1.2 $\times 10^{27}$clusters/m^3 at the end of the ion irradiation
- This number was obtained based on CD calculations, taking into account $U_{vacancy}$, $U_{interstitial}$, $O_{vacancy}$ and $O_{interstitial}$ concentration in damage clusters
- Further, these numbers were calculated using average migration energy of point defects verified through multiple references.
- Therefore, the total number of clusters in EXAFS interrogation volume can be calculated as

Total CD generated voids and clusters in EXAFS volume = 1.2$\times$ 10^{27}clusters/m$^3\times$ 0.17 mm^3

$\Rightarrow$Total CD generated voids and clusters in EXAFS volume = 2.04 $\times$ 10^{17}clusters

- According to CD simulations, there is an even spread of clusters and voids in the material
- This number is very similar to the 5% change in lattice detected in EXAFS
- The percent contribution of CD calculated damage clusters to the 5% change can be estimated as follows

$$\% \text{ Contribution of CD clusters towards lattice change} = \frac{2.04\times10^{17}}{2.08\times10^{17}} \times 100$$

$$\Rightarrow \mathbf{98.07\ \%}$$

- 98% is an expected contribution of damage clusters towards 5% lattice structure change in UO_2
- Therefore, Cluster Dynamics models are a good approximation towards understanding the approximate percentage breakdown of radiation induced structures that alter the overall material lattice.
- 98% of 5% is approximately **4.9%** of the total lattice change.
- This implies, the remaining 0.09 % of the defects are due to point defects and other miscellaneous defect types.
- Proceeding further, O defects tend to have a significantly less migration energy (0.3 eV for $O_{vacancy}$) as compared to U defects (2.4 for $U_{vacancy}$)
- Therefore, O defects tend to be more mobile and quickly get absorbed in the vacancy and interstitial defect clusters
- On the other hand, U defects are rate limiting defects and can reduce/ increase the rate of O defect absorption
- Therefore, of the remaining point defects are predominantly uranium type defects and a small distribution of oxygen point defects

- This agrees with the O clustering results from EXAFS analysis, where O rich and O poor regions collectively demonstrate O point defects getting absorbed to form clusters and voids
- On the other hand, U defects in EXAFS show a spread around their crystallographic position in no clear sub-structure that could indicate clustering comparable to oxygen.

End

References

[1] Uranyl, 2013.

[2] T et al Abe. *Comprehensive Nuclear Materials*. Elsevier, 2012.

[3] G C Allen and P A Tempest. Ordered Defects in the Oxides of Uranium. *Proceedings of the Royal Society of London. A. Mathematical and Physical Sciences*, 406(1831):325–344, 1986.

[4] D A Andersson, G Baldinozzi, L Desgranges, D R Conradson, and S D Conradson. Density Functional Theory Calculations of UO2 Oxidation: Evolution of UO2+x, U4O9–y, U3O7, and U3O8. *Inorganic Chemistry*, 52(5):2769–2778, 2013.

[5] D A Andersson, J Lezama, B P Uberuaga, C Deo, and S D Conradson. Cooperativity among defect sites in in AO2+x and A4O9 (A=U,Np,Pu): Density functional calculations. *Phys. Rev. B*, 79(2):24110, January 2009.

[6] S. Aronson, R. B. Roof, and J. Belle. Kinetic Study of the Oxidation of Uranium Dioxide. *The Journal of Chemical Physics*, 27(1):137, 1957.

[7] Xian-Ming Bai, Anter El-Azab, Jianguo Yu, and Todd R Allen. Migration mechanisms of oxygen interstitial clusters in uo2. *Journal of physics. Condensed matter*, 25(1), January 2013.

[8] C B Basak, A K Sengupta, and H S Kamath. Classical molecular dynamics simulation of {UO2} to predict thermophysical properties. *Journal of Alloys and Compounds*, 360:210–216, 2003.

[9] Nicholas A Brincat, Stephen C Parker, Marco Molinari, C Allen, and Mark T Storr. Ab Initio Investigation of the UO3 Polymorphs : Structural Properties and Thermodynamic Stability. *Inorganic Chemistry*, 53(Vi):12253–12264, 2014.

[10] Nicholas a Brincat, Stephen C Parker, Marco Molinari, Geoffrey C Allen, and Mark T Storr. Density functional theory investigation of the layered uranium oxides U3O8 and U2O5. *Dalton transactions (Cambridge, England : 2003)*, November 2014.

[11] Lewis T Chadderton. *Radiation damage in crystals*. Methuen London, 1965.

[12] Wei-Ying Chen, Jianguo Wen, Marquis a. Kirk, Yinbin Miao, Bei Ye, Brian R. Kleinfeldt, Aaron J. Oaks, and James F. Stubbins. Characterization of dislocation loops in CeO 2 irradiated with high energy Krypton and Xenon. *Philosophical Magazine*, 93(36):4569–4581, December 2013.

[13] Wei-Ying Chen, Jianguo Wen, Marquis A Kirk, Yinbin Miao, Bei Ye, Brian R Kleinfeldt, Aaron J Oaks, and James F Stubbins. Characterization of dislocation loops in CeO2 irradiated with high energy Krypton and Xenon. *Philosophical Magazine*, 93(36):4569–4581, 2013.

[14] Horst Geckeis Christophe Poinssot. *Radionuclide Behaviour in the Natural Environment*. Elsevier, 2012.

[15] Tatiana Shvareva Ginger E. Sigmon Peter C. Burns Alexandra Navrotskya Christopher R. Armstrong, May Nyman. Uranyl peroxide enhanced nuclear fuel corrosion in seawater. *Proceedings of the National Academy of Sciences of the United States of America*, 109:1874–1877, January 2012.

[16] David L Clark, Steven D Conradson, Robert J Donohoe, D Webster Keogh, David E Morris, Phillip D Palmer, Robin D Rogers, and C Drew Tait. Chemical Speciation of the Uranyl Ion under Highly Alkaline Conditions. Synthesis , Structures , and Oxo Ligand Exchange Dynamics. *Inorganic Chemistry*, 38(7):1456–1466, 1999.

[17] Steven D. Conradson, Bruce D. Begg, David L. Clark, Christophe den Auwer, Mei Ding, Peter K. Dorhout, Francisco J. Espinosa-Faller, Pamela L. Gordon, Richard G. Haire, Nancy J. Hess, Ryan F. Hess, D. Webster Keogh, Gerard H. Lander, Dario Manara, Luis a. Morales, Mary P. Neu, Patricia Paviet-Hartmann, Jean Rebizant, Vincenzo V. Rondinella, Wolfgang Runde, C. Drew Tait, D. Kirk Veirs, Phillip M. Villella, and Franck Wastin. Charge distribution and local structure and speciation in the UO2+x and PuO2+x binary oxides for xâ©œ0.25. *Journal of Solid State Chemistry*, 178(2):521–535, February 2005.

[18] Steven D. Conradson, Tomasz Durakiewicz, Francisco J. Espinosa-Faller, Yong Q. An, David a. Andersson, Alan R. Bishop, Kevin S. Boland, Joseph a. Bradley, Darrin D. Byler, David L. Clark, Dylan R. Conradson, Leilani L. Conradson, Alison L. Costello, Nancy J. Hess, Gerard H. Lander, Anna Llobet, Mary B. Martucci, Jose Mustre de Leon, Dennis Nordlund, Juan S. Lezama-Pacheco, Thomas E. Proffen, George Rodriguez, Daniel E. Schwarz, Gerald T. Seidler, Antoinette J. Taylor, Stuart a. Trugman, Trevor a. Tyson, and James a. Valdez. Possible Bose-condensate behavior in a quantum phase originating in a collective excitation in the chemically and optically

doped Mott-Hubbard system UO_{2+x}. *Physical Review B*, 88(11):115135, September 2013.

[19] Steven D Conradson, Dario Manara, Franck Wastin, David L Clark, Gerard H Lander, Luis A Morales, Jean Rebizant, and Vincenzo V Rondinella. Local Structure and Charge Distribution in the UO2 U4O9 System. *Inorganic Chemistry*, 43(22):6922–6935, 2004.

[20] Jean-Paul Crocombette. Influence of charge states on energies of point defects and clusters in uranium dioxide. *Physical Review B*, 85(144101), April 2012.

[21] Jesse Johns Melissa Teague Michael Tonks Robert Youngblood Curtis Smith, Heather Chichester. Accident tolerant fuel analysis. Technical report, Idaho National Lab, September 2014.

[22] L. Desgranges, G. Guimbretière, P. Simon, C. Jegou, and R. Caraballo. A possible new mechanism for defect formation in irradiated UO2. *Nuclear Instruments and Methods in Physics Research Section B: Beam Interactions with Materials and Atoms*, 315:169–172, November 2013.

[23] Tapan Desai Dieter Wolf Dilpuneet Aidhy Paul C. Millett and Simon R Phillpot. Kinetically evolving irradiation-induced point defect clusters in UO2 by molecular dynamics simulation. *Physical Review B*, 80(10), 2009.

[24] S L Dudarev, D Nguyen Manh, and A P Sutton. Effect of Mott-Hubbard correlations on the electronic structure and structural stability of uranium dioxide. *Philosophical Magazine Part B*, 75(5):613–628, 1997.

[25] R M Ibberson L Nowicki B T M Willis Frédérico Garrido A.C. Hannon. Neutron Diffraction Studies of U4O9: Comparison with EXAFS Results. *Physical Review B*, 74(18), 2006.

[26] V. Fritzsche. A new spherical-wave approximation for photoelectron diffraction, exafs and meed. *Journal of physics. Condensed matter 2*, 2, 1990.

[27] Lionel Thome G. Sattonnay, F. Garrido. Behaviour of helium in uo2 single crystals: a transmission electron microscopy investigation. *Journal of Nuclear Materials*, 84:109–115, 2011.

[28] F Garrido, R M Ibberson, L Nowicki, and B T M Willis. Cuboctahedral oxygen clusters in U3O7. *Journal of Nuclear Materials*, 322(1):87–89, 2003.

[29] N R Holmes GC Allen NR Holmes GC Allen NR Holmes G.C. Allen. Mixed Valencey Behaviour in Some Uranium Oxides Studied by X-Ray Photoelectron Spectroscopy. *Canadian Journal of Applied Spectroscopy*, 38:124–130, 1993.

[30] Hua Y Geng, Ying Chen, Yasunori Kaneta, and Motoyasu Kinoshita. Stability mechanism of cuboctahedral clusters in UO2+x: First-principles calculations. *Phys. Rev. B*, 77(18):180101, May 2008.

[31] Francesco P. Ballistreri Andrea Pappalardo Giuseppe Trusso Sfrazzetto Gaetano A. Tomaselli Rosa M. Toscanoc Francesco Punzo Giuseppe M. Lombardo, Amber L. Thompson. An integrated x-ray and molecular dynamics study of uranyl-salen structures and properties. *Dalton transactions*, 41:1951–1960, December 2012.

[32] R W Grimes and C R A Catlow. The Stability of Fission Products in Uranium Dioxide. *Philosophical Transactions of the Royal Society of London. Series A: Physical and Engineering Sciences*, 335(1639):609–634, 1991.

[33] T Allen E.A Kenik A Jensson S.M Bruemmer J Gan A.D Edwards P.M Scott P.L Anderson G.S Was, J.T Busby. Emulation of neutron irradiation effects with protons: validation of principle. *Journal of Nuclear Materials*, 300:198–216, 2002.

[34] Aurore Guglielmetti, Alain Chartier, Laurent van Brutzel, Jean-Paul Crocombette, Kazuhiro Yasuda, Constantin Meis, and Syo Matsumura. Atomistic simulation of point defects behavior in ceria. *Nuclear Instruments and Methods in Physics Research Section B: Beam Interactions with Materials and Atoms*, 266(24):5120–5125, 2008.

[35] L.F. He, B. Valderrama, A.-R. Hassan, J. Yu, M. Gupta, J. Pakarinen, H.B. Henderson, J. Gan, M.A. Kirk, A.T. Nelson, M.V. Manuel, A. El-Azab And, and T.R. Allen. Bubble formation and Kr distribution in Kr-irradiated UO2. *Journal of Nuclear Materials*, 2014.

[36] Henry R Hoekstra, Stanley Siegel, and Francis X Gallagher. The uranium-oxygen system at high pressure. *Journal of Inorganic and Nuclear Chemistry*, 32(10):3237–3248, 1970.

[37] Misako Iwasawa, Ying Chen, Yasunori Kaneta, Toshiharu Ohnuma, Hua-Yun Geng, and Motoyasu Kinoshita. First-Principles Calculation of Point Defects in Uranium Dioxide. *Materials Transactions*, 47(11):2651–2657, 2006.

[38] Rodney C Ewing & Udo Becker Jianwei Wang. Average structure and local configuration of excess oxygen in UO2+x. *Nature Scientific Report*, March 2014.

[39] R.C. Albers J.J. Rehr, S.I. Zabinsky. Ifeffit license. *Phys. Rev. Lett.*, 69, 1992.

[40] Deborah J Jones, Jacques Roziere, Geoffrey C Allen, and Paul A Tempest. The structural determination of fluorite-type oxygen excess uranium oxides using EXAFS spectroscopy. *The Journal of chemical physics*, 84(11):6075–6082, 1986.

[41] A T Nelson J.T. White. Thermal conductivity of UO2+x and U4O9-y. *Journal of Nuclear Materials*, 443:342–350, November 2013.

[42] Meiying Hou M. Verwerft Kevin Govers, Sergei Lemehov. Comparison of interatomic potentials for uo2. part i: Static calculations. *Journal of Nuclear Materials*, 366:161–177, 2007.

[43] Sarah Khalil. *Multiscale Modeling of Nucleation and Growth of Defect clusters in UO2*. PhD thesis, University of Wisconsin-Madison, February 2014.

[44] R de L Kronig and W G Penney. Quantum mechanics of electrons in crystal lattices. *Proceedings of the Royal Society of London. Series A*, 130(814):499–513, 1931.

[45] Konstantin N Kudin, Gustavo E Scuseria, and Richard L Martin. Hybrid Density-Functional Theory and the Insulating Gap of UO2. *Phys. Rev. Lett.*, 89(26):266402, December 2002.

[46] W. Van Lierde, J Pelsmaekers, and A. Lecocq-Robert. On the Phase Limits of U4O9. *Journal of Nuclear Materials*, 37:176–285, 1970.

[47] Lee Meng Lung Liew Kaeng Nan. Study of fib milling induced damage and contamination on ex-situ lift-out tem specimen and methodology to reduce the artifacts. *Physical and Failure Analysis of Integrated Circuits (IPFA), IEEE Symposium*, pages 404–407, 2013.

[48] Clarissa Yablinsky Lingfeng He, Mahima Gupta. In-situ tem observation of dislocation evolution in kr-irradiated uo2 single crystals. *Journal of Nuclear Materials*, pages 1–19, 2014.

[49] P. Lucuta, H. Matzke, and I. Hastings. A pragmatic approach to modelling thermal conductivity of irradiated UO2 fuel: review and recommendations. *Journal of Nuclear Materials*, 232:166, 1996.

[50] D G Madland. Total prompt energy release in the neutron-induced fission of 235U, 238U, and 239Pu. *Nuclear Physics A*, 772:113–137, May 2006.

[51] a. Magnéli. -Type With Recurrent Dislocations of Atoms: 'Homologous Series' of Molybdenum and Tungsten Oxides. *Acta Crystallographica*, 6(1951):495–500, 1953.

[52] R.J. McEachern and P. Taylor. A review of the oxidation of uranium dioxide at temperatures below 400 °C. *Journal of Nuclear Materials*, 254(2-3):87–121, April 1998.

[53] Fabienne Ribeiro Mehdi Colbert, Guy Tréglia. Theoretical study of xenon adsorption in uo2 nanoporous matrices theoretical study of xenon adsorption in uo2 nanoporous matrices. *Journal of Physics: Condensed Matter*, 26(48), September 2014.

[54] Zhi-Gang Mei, Marius Stan, and Jiong Yang. First-principles study of thermophysical properties of uranium dioxide. *Journal of Alloys and Compounds*, (0):–, 2014.

[55] C Meis and A Chartier. Calculation of the threshold displacement energies in {UO2} using ionic potentials. *Journal of Nuclear Materials*, 341(1):25–30, 2005.

[56] Michael Texier Michael Jublot. Sample preparation by focused ion beam micromachining for transmission electron microscopy imaging in front-view. *Micron*, 56(63-67), 2014.

[57] Yasunori Kaneta Toshiharu Ohnuma Hua-Yun Geng Misako Iwasawa Ying Chen and Motoyasu Kinoshita. First-Principles Calculation of Point Defects in Uranium Dioxide. *Materials Transactions*, 47(11):2651–2657, 2006.

[58] M.A Kirk M.L Jenkins. *Characterisation of Radiation Damage by Transmission Electron Microscopy*. CRC Press, November 2001.

[59] T. Diaz de la Rubiab N. Sonedaa. Defect production, annealing kinetics and damage evolution in alpha-fe: An atomic-scale computer simulation. *Philosophical Magazine A*, 78(5):995–1019, 1998.

[60] K Naito and K Kamegashira. High temperature chemistry of ceramic nuclear fuels with emphasis on non-stoichiometry. *Advances in Nuclear Science and Technology*, 9:99–180, 1976.

[61] Nuclear News. Evolution of Spent Nuclear Fuel in Dry Storage Conditions, 2014.

[62] Matthew Newville. EXAFS analysis using FEFF and FEFFIT. *Journal of synchrotron radiation*, 8(2):96–100, 2001.

[63] Matthew Newville. Fundamentals of XAFS. *Consortium for Advanced Radiation Sources, University of Chicago (USA)[http://xafs. org]*, 2004.

[64] Kazuhiro Nogita and Katsumi UNE. Thermal Recovery of Radiation Defects and Microstructural Change in Irradiated UO2 Fuels. *Journal of Nuclear Science and Technology*, 30(9):900–910, 1993.

[65] D I R Norris. Voids in irradiated metals (Part I). *Radiation Effects*, 14(1-2):1–37, 1972.

[66] D R Olander. *Fundamental aspects of nuclear reactor fuel elements: solutions to problems*. 1976.

[67] A. A. Borovoi P.A. Sterne, A. Gonis. *Actinides and the Environment*, volume 41. Springer Science and Business Media, 1998.

[68] A Joseph Palmer, Gerry L McCormick, and Shannon J Corrigan. Hydraulic Shuttle Irradiation System (HSIS) Recently Installed in the Advanced Test Reactor (ATR). *Proceedings of ICAPP '10, Paper*, 10354:13–17, 2010.

[69] Alain Chartier Christine Gueneau Ann E Mattsson Veena Tikare Timothy Bartel Theodore Besmann Marius Stan Ram Devanathan Laurent Van Brutzel and Paul Van Uffelen. Modeling and simulation of nuclear fuel materials. *Energy and Environmental Science*, 3:1406–1426, June 2010.

[70] John J Rehr, Joshua J Kas, Fernando D Vila, Micah P Prange, and Kevin Jorissen. Parameter-free calculations of X-ray spectra with FEFF9. *Phys. Chem. Chem. Phys.*, 12(21):5503–5513, 2010.

[71] Douglas Rigby. Evaluation of the technical basis for extended dry storage and transportation of used nuclear fuel. Technical report, United States Nuclear Waste Technical Review Board, December 2010.

[72] Vincenzo V. Rondinella and Thierry Wiss. The high burn-up structure in nuclear fuel. *Materials Today*, 13(12):24–32, December 2010.

[73] E. Rothwell. High temperature substoichiometry in uranium dioxide,. *United Kingdom Atomic Energy Authority*, 1961.

[74] G. Rousseau, L. Desgranges, F. Charlot, N. Millot, J.C. Nièpce, M. Pijolat, F. Valdivieso, G. Baldinozzi, and J.F. Bérar. A detailed study of UO2 to U3O8 oxidation phases and the associated rate-limiting steps. *Journal of Nuclear Materials*, 355(1-3):10–20, September 2006.

[75] K. Nogita S. Kashibe, K. Une. Formation and growth of intragranular fission gas bubbles in uo2 fuels with burnup of 6–83 gwd/t. *Journal of Nuclear Materials*, 206(1):22–34, 1993.

[76] T. Gouder B. Gaudreau M. Verwerft S. Van den Berghe, F. Miserque. X-ray photon spectroscopy on uranium oxides: A comparison between bulk and thin layers. *Journal of Nuclear Materials*, 294:168–174, 2001.

[77] P Scherrer. Bestimmung der grosse und der inneren struktur von kolloidteilchen mittels rontgenstrahlen, nachrichten von der gesellschaft der wissenschaften, gottingen. *Mathematisch-Physikalische Klasse*, 2:98–100, 1918.

[78] Georg Schreckenbach, P Jeffrey Hay, and Richard L Martin. Density functional calculations on actinide compounds: Survey of recent progress and application to UO2X4 and AnF6 (modified title). *Journal of Computational Chemistry*, 20(1):70–90, 1999.

[79] R Schueneman and L Burgraff. Oxidation at Surfaces of Uranium Oxide Particles. *APS Ohio Sections Spring Meeting Abstracts*, April 2001.

[80] E M Schulson, M L Swanson, and S R Macewen. Point defect annihilation kinetics and irradiation creep in ordered alloys. *Philosophical Magazine A*, 37(5):575–589, 1978.

[81] E Sevillano, H Meuth, and J J Rehr. Extended x-ray absorption fine structure Debye-Waller factors. I. Monatomic crystals. *Phys. Rev. B*, 20(12):4908–4911, December 1979.

[82] Francisco J Espinosa-Faller Yong Q An David A Andersson Alan R Bishop Kevin S Boland Joseph A Bradley Darrin D Byler Steven D. Conradson Tomasz Durakiewicz. Possible Bose-condensate behavior in a quantum phase originating in a collective excitation in the chemically and optically doped Mott-Hubbard system UO2+x. *Physical Review B*, 88(11), 2013.

[83] Nicholas C. Handy Andrew G. Ioannou Chris-Kriton Skylaris Andrew Willetts Adrian M. Simper Steven Spencer, Laura Gagliardi. Hydration of uo22+ and puo22+. *Journal of Physical Chemistry*, 103:1831–1837, 1999.

[84] R E Stoller, M B Toloczko, G S Was, A G Certain, S Dwaraknath, and F A Garner. On the use of {SRIM} for computing radiation damage exposure. *Nuclear Instruments and Methods in Physics Research Section B: Beam Interactions with Materials and Atoms*, 310(0):75–80, 2013.

[85] Kurt E. Sickafus Yasumasa Nishiura Mitsuhiro Itakura Ying Chen Yasunori Kaneta Motoyasu Kinoshita Takashi Ichinomiya, Blas P. Uberuaga. Temperature accelerated dynamics study of migration process of oxygen defects in uo2. *Journal of Nuclear Materials*, 384:315–321, 2009.

[86] Jagdish K Tuli and Alejandro Sonzogni. NNDC Data Services. Technical report, BROOKHAVEN NATIONAL LABORATORY (BNL), 2010.

[87] Kaye Savage Tyler Womble, Wenyi Shu. Uranium distribution in geochemically diverse sediments. *Journal of South Carolina Academy of Science*, 9:18–22, 2011.

[88] Michael Ortiz Vikram Gavini, Kaushik Bhattacharya. Vacancy clustering and prismatic dislocation loop formation in aluminum. *Phys. Rev. B*, 76(180101):1–4, 2007.

[89] Dimitrios Papaioannoi Ramil Nasyrow Vincenzo Rondinella, Thierry Wiss. Microstructure and macroscopic alteration affecting nuclear fuel during extended storage. *Proceedings of High-Level Radioactive Waste Management Conference*, 1083-1088, 2012.

[90] Gary S Was. *Fundamentals of Radiation Materials Science Fundamentals of Radiation Materials Science Fundamentals of Radiation Materials Science*. Springer Berlin Heidelberg, Nuclear Engineering and Radiological Sciences Materials Science and Engineering, University of Michigan, 1921 Cooley Bldg. 2355 Bonisteel Blvd, Ann Arbor, MI, 48109-2104, USA, 2007.

[91] W J Weber. Ingrowth of lattice defects in alpha irradiated {UO2} single crystals. *Journal of Nuclear Materials*, 98:206–215, 1981.

[92] W J Weber. Alpha-irradiation damage in CeO2, UO2 and PuO2. *Radiation Effects*, 83(1-2):145–156, 1984.

[93] A D Whapham and B E Sheldon. Radiation damage in uranium dioxide. *Philosophical Magazine*, 12(120):1179–1192, 1965.

[94] David B Williams and C Barry Carter. *The Transmission Electron Microscope*. Springer, 1996.

[95] B T M Willis. Structures of UO2, UO2+x andU4O9 by neutron diffraction. *J. Phys. France*, 25(5):431–439, 1964.

[96] B T M Willis. The defect structure of hyper-stoichiometric uranium dioxide. *Acta Crystallographica Section A*, 34(1):88–90, January 1978.

[97] Dong-Seong Sohn Yang-Hyun Koo, Byung-Ho Lee. Analysis of fission gas release and gaseous swelling in uo2 fuel under the effect of external restraint. *Journal of Nuclear Materials*, 280:86–98, 2000.

[98] Saito Yasutoshi. Nonstoichiometry in uranium dioxide. *Journal of Nuclear Materials*, 51(1):112–125, 1974.

[99] Bei Ye. *Formation and growth of irradiation-induced defect structures in ceria*. PhD thesis, University of Illinois at Urbana-Champaign, 2011.

[100] T.R. Allen Yina Huang, Benjamin Maier. Irradiation-induced effects of proton irradiation on zirconium carbides with different stoichiometries. *Nuclear Engineering and Design*, pages 55–63, 2014.

[101] Hunhawa Lim Younsuk Yun Hanchul Kim and Kwangheon Park. Electronic structure of UO2 from the density functional theory with on-site coulomb repulsion. *Journal of the Korean Physical Society*, 50(5):5, 2007.

[102] Robert Montgomery Fei Gao Xin Sun Yulan Li, Shenyang Hu. Enhanced generic phase-field model of irradiation materials: Fission gas bubble growth kinetics in polycrystalline uo2. Technical report, Pacific Northwest National Laboratory, May 2012.

[103] W.H. Zachariasen. Crystal chemical studies of the 5f-series of elements. XXIII. On the crystal chemistry of uranyl compounds and of related compounds of transuranic elements. *Acta Crystallographica*, 7:795–799, 1954.

[104] James F Ziegler, M D Ziegler, and J P Biersack. SRIM–The stopping and range of ions in matter (2010). *Nuclear Instruments and Methods in Physics Research Section B: Beam Interactions with Materials and Atoms*, 268(11):1818–1823, 2010.